Evidence and cross section measurement of the process $pp \to t\bar{t}\gamma$ at a center-of-mass energy of 7 TeV with the ATLAS experiment

Dissertation
zur Erlangung des Grades eines Doktors
der Naturwissenschaften

vorgelegt von
M.Sc. Oliver Rosenthal

eingereicht bei der Naturwissenschaftlich-Technischen Fakultät
der Universität Siegen
Siegen 2013

Gutachter der Dissertation:	Prof. Dr. Ivor Fleck
	PD Dr. Kevin Kröninger
Datum der Disputation:	15.Oktober 2013

Gedruckt auf alterungsbeständigem holz- und säurefreiem Papier.

Contents

0 Introduction **1**

1 Particle Physics **3**
1.1 Standard Model of Particle Physics . . . 3
1.2 Quantum Electrodynamics and electroweak unification . . . 5
1.3 CKM matrix . . . 7
1.4 The Brout-Englert-Higgs mechanism . . . 9
1.5 The BEH boson . . . 10
1.6 Yukawa coupling . . . 13
1.7 Quantum Chromodynamics . . . 14

2 The Top Quark **17**
2.1 Top quark pair production . . . 17
2.2 Single top quark production . . . 21
2.3 Top quark decay . . . 23
2.4 Background processes for top quark pair events . . . 26
2.5 Top quark properties . . . 29
2.5.1 Mass . . . 29
2.5.2 Electric charge . . . 29
2.5.3 Polarization of the W boson in top quark decay . . . 30
2.5.4 Spin correlations in $t\bar{t}$ production . . . 30
2.5.5 Asymmetry in $t\bar{t}$ production . . . 32
2.6 Top quark pair events associated with an additional photon . . . 33

3 The LHC and the ATLAS experiment **37**
3.1 The Large Hadron Collider . . . 37
3.2 ATLAS Detector Layout . . . 41
3.3 ATLAS Coordinate System . . . 42
3.4 The Magnet System . . . 42
3.5 The Inner Detector . . . 43
3.6 The Calorimeter System . . . 45
3.7 The Muon System . . . 46
3.8 The ATLAS Trigger System . . . 48

4 Physics objects **51**
4.1 Jet . . . 51
4.1.1 Reconstruction . . . 51
4.1.2 Energy calibration . . . 52
4.1.3 Quality criteria . . . 53
4.1.4 b-tagging . . . 54

4.1.5 Object defintion . . . 55
4.2 Electron . . . 56
4.2.1 Reconstruction . . . 56
4.2.2 Energy scale and energy resolution . . . 57
4.2.3 Identification . . . 58
4.2.4 Isolation . . . 59
4.2.5 Trigger . . . 61
4.2.6 Object defintion . . . 63
4.3 Muon . . . 64
4.3.1 Reconstruction . . . 64
4.3.2 Momentum resolution . . . 64
4.3.3 Trigger . . . 66
4.3.4 Object definition . . . 67
4.4 Missing transverse energy . . . 68
4.5 Photon . . . 69
4.5.1 Reconstruction . . . 69
4.5.2 Identification . . . 70
4.5.3 Object defintion . . . 73

5 Data sample and Monte Carlo modeling 75
5.1 Dataset . . . 75
5.2 Data streams . . . 77
5.3 Event simulation . . . 77
5.4 $t\bar{t}\gamma$ simulation . . . 78
5.4.1 WHIZARD . . . 79
5.5 Background simulation . . . 80
5.5.1 Top quark pair production . . . 80
5.5.2 W boson production with additional partons . . . 80
5.5.3 W boson production associated with a photon and additional partons 81
5.5.4 Z boson production with additional partons . . . 81
5.5.5 Single Top Quark Production . . . 82
5.5.6 Diboson production . . . 82
5.6 Signal phase space overlap . . . 82
5.7 Monte Carlo event weights . . . 82

6 Event selection and event yield 85
6.1 Event selection . . . 85

7 Analysis strategy to estimate the $t\bar{t}\gamma$ cross section 91
7.1 Discriminating variable . . . 92
7.2 Template fitting . . . 93
7.3 Cross section calculation . . . 94

8 Derivation of signal and background templates **97**
8.1 Signal template . . . 97
8.2 Background template . . . 102

9 Estimation of the $e \to \gamma$ misidentification rate **109**
9.1 Estimation of the $e \to \gamma$ misidentification rate . . . 109
9.2 Derivation of the $e \to \gamma$ misidentification scale factors . . . 113

10 Background contributions with a prompt photon **119**
10.1 QCD multijet+γ contribution . . . 119
10.1.1 QCD multijet estimation with the matrix method . . . 120
10.1.2 QCD multijet estimation with a prompt photon in the final state . 121
10.2 W+jets+γ contribution . . . 124
10.3 Top quark pair background . . . 132
10.3.1 $t\bar{t}$ events with a misidentified electron in the final state . . . 132
10.3.2 $t\bar{t}\gamma$ events outside of signal phase space . . . 133
10.3.3 $t\bar{t}\gamma$ events outside of fiducial region . . . 133
10.4 Other contributions . . . 136

11 Measurement of the $t\bar{t}\gamma$ cross section **139**

12 Systematic uncertainties **143**
12.1 Template Modeling . . . 144
12.1.1 Signal template . . . 144
12.1.2 Background template . . . 145
12.2 Prompt photon background . . . 146
12.3 Monte Carlo modeling . . . 147
12.4 Detector Modeling . . . 149
12.4.1 Jet . . . 149
12.4.2 Leptons & photon . . . 151
12.4.3 Missing transverse energy . . . 153
12.5 Pileup dependence . . . 153
12.6 Luminosity . . . 153
12.7 Total systematic uncertainty . . . 154

13 Signal significance **157**

14 Summary and Outlook **159**

A Monte Carlo samples **161**
A.1 $t\bar{t}$ Monte Carlo samples . . . 161
A.2 W+jets+γ Monte Carlo samples . . . 163
A.3 W+jets Monte Carlo samples . . . 164
A.4 Z+jets Monte Carlo samples . . . 167
A.5 Diboson Monte Carlo samples . . . 170

A.6 Single top Monte Carlo samples 171
A.7 Dijet Monte Carlo samples 172

B Additional plots **173**
B.1 Additional plots of Chapter 6 173
B.2 Additional plots of Chapter 8 178
B.3 Additional plots of Chapter 9 181
B.4 Additional plots of Chapter 10 184
B.5 Additional plots of Chapter 12 187

Bibliography **201**

List of Tables

1.1 Overview of Standard Model gauge bosons. 4
1.2 Overview of Standard Model fermions. 5

4.1 Shower variables used for electron identification. 60
4.2 Single electron trigger chains for 2011 data. 62
4.3 Single muon trigger chains for 2011 data. 66
4.4 Shower variables used for photon identification. 72

5.1 Overview of datas periods recorded by ATLAS in 2011. 76

6.1 Data event selection. 86
6.2 $t\bar{t}\gamma$ event selection and selection efficiencies 88

8.1 Relative weights of correction factors used to derive prompt photon template. 101
8.2 Weights to derive background template. 104

9.1 $e \to \gamma$ misidentification scale factor uncertainties for all photons. 116
9.2 $e \to \gamma$ misidentification scale factor uncertainties for unconverted photons. 117
9.3 $e \to \gamma$ misidentification scale factor uncertainties for converted photons. . 118

10.1 QCD+γ background yield estimation. 122
10.2 Uncertainties of QCD+γ estimation. 124
10.3 Template fit results in W+jets+γ control region. 125
10.4 Estimated total data yields in W+jets+γ control region. 126
10.5 Background estimation of W+jets+γ control region in muon channel. . . . 127
10.6 W+jets+γ extrapolation factors and final background yield estimation. . . 132
10.7 $t\bar{t}$ background with a misidentified electron. 134
10.8 $t\bar{t}\gamma$ background outside of signal phase space. 135
10.9 $t\bar{t}\gamma$ background outside of fiducial regio. 136
10.10 Remaining background contributions. 137

11.1 Process yields included in the template fit. 140

12.1 Overview of Monte Carlo modeling uncertainties 149
12.2 Overview of all systematic uncertainties. 156

A.1 WHIZARD $t\bar{t}\gamma$ Monte Carlo sample 161
A.2 MC@NLO $t\bar{t}$ Monte Carlo sample 161
A.3 POWHEG $t\bar{t}$ Monte Carlo samples 162
A.4 ACERMC $t\bar{t}$ Monte Carlo samples 162
A.5 ALPGEN W+jets+γ Monte Carlo samples with up to five partons 163
A.6 SHERPA W+jets+γ Monte Carlo samples with up to three partons . . . 163

A.7 $W(\to e\nu)$+jets Monte Carlo samples with up to five partons 164
A.8 $W(\to \mu\nu)$+jets Monte Carlo samples with up to five partons 164
A.9 $W(\to \tau\nu)$+jets Monte Carlo samples with up to five partons 165
A.10 $W + b\bar{b}$+jets Monte Carlo samples with up to three partons 165
A.11 $W + c\bar{c}$+jets Monte Carlo samples with up to three partons 166
A.12 $W + c$+jets Monte Carlo samples with up to four partons 166
A.13 $Z(\to ee)$+jets Monte Carlo samples with up to five partons 167
A.14 $Z(\to \mu\mu)$+jets Monte Carlo samples with up to five partons 167
A.15 $Z(\to \tau\tau)$+jets Monte Carlo samples with up to five partons 168
A.16 $Z + b\bar{b}$+jets Monte Carlo samples with up to three partons 169
A.17 Diboson Monte Carlo sample 170
A.18 Single top production Monte Carlo sample 171
A.19 Dijet Monte Carlo sample 172

List of Figures

1.1 Unitary triangle describing CKM matrix. 9
1.2 BEH potential. 10
1.3 BEH production cross sections 11
1.4 BEH boson measurements by ATLAS: significance and signal strength. . 12
1.5 BEH boson measurements by ATLAS: diphoton and four-lepton invariant mass. 13
1.6 Running strong coupling. 15

2.1 CTEQ6L1 parton density functions. 18
2.2 Top quark pair production diagrams. 19
2.3 Top quark pair cross section vs. $\sqrt{s}$. 20
2.4 Top quark pair cross section results by ATLAS and CMS. 21
2.5 Single Top quark production diagrams 22
2.6 Single top quark cross section results by ATLAS. 23
2.7 Top quark pair decay channels and branching fractions. 25
2.8 Diagram of semileptonic top quark pair event. 26
2.9 QCD predictions for hard scattering cross sections. 27
2.10 W+jets and Z+jets production diagrams. 28
2.11 Diboson production diagrams. 28
2.12 Top quark mass measurements by the ATLAS and CMS. 29
2.13 W boson polarization measurements by ATLAS and CMS. 31
2.14 $t\bar{t}$ forward backward asymmetry results by CDF. 33
2.15 Radiative top quark pair production diagrams. 35
2.16 Radiative top quark pair decay diagrams. 36

3.1 Schematic view of the CERN accelerator. 38
3.2 Overall view of LHC and four main experiments. 39
3.3 Cumulative integrated luminosity and maximum instantaneous luminosity of LHC. 40
3.4 Overall layout of the ATLAS detector 41
3.5 Illustration of ATLAS magnet system. 43
3.6 Cut-away view of ATLAS inner detector. 44
3.7 Transverse section of ATLAS inner detector. 45
3.8 Cut-away view of ATLAS calorimeter system 46
3.9 Overview of the muon system of ATLAS detector. 48
3.10 Schematical representation of ATLAS trigger system. 49

4.1 Average energy of jets calibrated at EM scale with respect to the truth jet energy. 53
4.2 Rejection factors as a function of the tagging efficiency for different algorithms. 55

4.3 b-jet tagging efficiency from data and Monte Carlo simulation and resulting scale factors. . . . 56
4.4 Calibrated $Z \rightarrow$ invariant mass in 2011 data. . . . 58
4.5 EF trigger rates and efficiencies of single electron triggers used for 2011 data. 62
4.6 Electron identification scale factors for 2011 data. . . . 64
4.7 $Z \rightarrow \mu\mu$ mass distribution after resolution correction. . . . 65
4.8 Electron identification scale factors for 2011 data. . . . 68
4.9 R_η, $w_{\eta 2}$ distributions in data and Monte Carlo simulation. . . . 73
4.10 Photon identification efficiencies for 2011 data. . . . 74

5.1 Mean number of interactions per bunch crossing for 2011 data. . . . 76

6.1 Data vs. Monte Carlo control plots after final selection (I). . . . 89
6.2 Data vs. Monte Carlo control plots after final selection (II). . . . 90

7.1 $t\bar{t}$ vs. $t\bar{t}\gamma$ comparison of photon isolation. . . . 92
7.2 Signal efficiency vs. background rejection for different isolation variables. . 93

8.1 Invariant mass distribution of the electrons from data. . . . 97
8.2 p_T^{cone20} distributions from $Z \rightarrow e^+e^-$ data. . . . 98
8.3 p_T^{cone20} distributions of electrons and photons (I). . . . 100
8.4 p_T^{cone20} distributions from $Z \rightarrow e^+e^-$ data with additional jets. . . . 101
8.5 Final signal templates. . . . 102
8.6 p_T^{cone20} distributions from background photon candidates. . . . 103
8.7 p_T distributions from background photon candidates in simulated $t\bar{t}$ events. 105
8.8 p_T and $|\eta|$ distributions from background photon candidates in data. . . . 106
8.9 Final background templates. . . . 107

9.1 $Z \rightarrow ee.\, e\gamma_{\text{misId}}$ invariant mass distribution. . . . 111
9.2 $Z \rightarrow ee.\, e\gamma_{\text{misId}}$ p_T distribution. . . . 112
9.3 Measured ratio of $Z \rightarrow e\gamma_{\text{misId}}$ and $Z \rightarrow ee$ events. . . . 114
9.4 $e \rightarrow \gamma$ scale factors. . . . 115

10.1 Template fit results for QCD multijet background. . . . 123
10.2 Data vs. Monte Carlo control plots in W+jets+γ control region (I). . . . 129
10.3 Data vs. Monte Carlo control plots in W+jets+γ control region (II). . . . 130
10.4 Template fit results for W+jets+γ background. . . . 131
10.5 Reconstructed photon p_T and $|\eta|$ versus corresponding truth values. . . . 136

11.1 Result of the template fit. . . . 141

12.1 Sytematic uncertainty from jet energy scale. . . . 144
12.2 Systematic background templates from p_T and $|\eta|$ reweighting. . . . 145
12.3 Systematic background templates to estimate prompt photon contamination. 146
12.4 Jet energy scale and b-jet energy scale uncertainties. . . . 152
12.5 Pileup dependence of $t\bar{t}\gamma$ selection efficiencies. . . . 154

13.1 Probability distribution of the observed number of events for the background only hypothesis. 157

B.1 Data vs. Monte Carlo control plots after final selection (III). 173
B.2 Data vs. Monte Carlo control plots after final selection (IV). 174
B.3 Data vs. Monte Carlo control plots after final selection (V). 175
B.4 Data vs. Monte Carlo control plots after final selection (VI). 176
B.5 Data vs. Monte Carlo control plots after final selection (VII). 177
B.6 p_T^{cone20} distributions of electrons and photons (II). 178
B.7 p_T^{cone20} distributions of electrons and photons (III). 179
B.8 p_T^{cone20} distributions of electrons and photons (IV). 180
B.9 $Z \to ee.e\gamma_{\text{misId}}$ invariant mass distributions (I). 181
B.10 $Z \to ee.e\gamma_{\text{misId}}$ invariant mass distributions (II). 182
B.11 $Z \to ee.e\gamma_{\text{misId}}$ invariant mass distributions (II). 183
B.12 Data vs. Monte Carlo control plots in W+jets+γ control region (III). . . 184
B.13 Data vs. Monte Carlo control plots in W+jets+γ control region (IV). . . 185
B.14 Data vs. Monte Carlo control plots in W+jets+γ control region (V). . . . 186
B.15 Sytematic uncertainties (II). 187
B.16 Sytematic uncertainties (III). 188
B.17 Sytematic uncertainties (IV). 189
B.18 Sytematic uncertainties (V). 190
B.19 Sytematic uncertainties (VI). 191
B.20 Sytematic uncertainties (VII). 192
B.21 Sytematic uncertainties (VIII). 193
B.22 Sytematic uncertainties (IX). 194
B.23 Sytematic uncertainties (X). 195
B.24 Sytematic uncertainties (XI). 196
B.25 Sytematic uncertainties (XII). 197
B.26 Sytematic uncertainties (XIII). 198
B.27 Sytematic uncertainties (XIV). 199

Chapter 0

Introduction

Since the discovery of the top quark in 1995, many of its properties have been measured with high precision by the D0 and CDF experiments at the Tevatron collider. These properties include the mass, spin properties and the electromagnetic charge, verifying experimentally that the top quark is indeed completing the third quark generation predicted by the Standard Model of particle physics.
The top quark is of particular interest, since it is the only quark that decays before it can hadronize. It provides the unique opportunity to study the properties of the bare quark itself, which passes on its properties directly to its decay products. This opens up the possibility to study the coupling structure and strength of the top quark to the neutral electroweak gauge bosons, the photon and the Z boson. Especially the measurement of the top-photon coupling will provide an important validity check of the Standard Model and possibilities for the search of new physics, described by an anomalous $t\gamma$ vertex structure with additional electromagnetic or weak dipole moments. This is one of the questions regarding the top quark, which could not be answered by the Tevatron collaborations. However, the Large Hadron Collider will allow to investigate such topics in the future, which started a new era in particle physics with the first proton-proton collisons at a center-of-mass energy of $\sqrt{s} = 7\,\text{TeV}$ in 2010.
A first important step towards a test of the top-photon coupling is the measurement of the top quark pair production cross section with an additional prompt photon in the final state ($t\bar{t}\gamma$). This thesis presents the measurement of the $t\bar{t}\gamma$ cross section at a center-of-mass energy of $\sqrt{s} = 7\,\text{TeV}$, performed with the total proton-proton collison data of $\mathcal{L}_{\text{int}} = 4.7\,\text{fb}^{-1}$ collected in 2011 by the ATLAS detector. Events are selected in the single lepton channels, featuring a high energetic muon or electron, large missing transverse energy, at least four jets and one photon. An analysis strategy is developed to distinguish $t\bar{t}\gamma$ signal events from background contributions, which are dominated by events with a hadron from jet fragmentation misidentified as a photon. The final result of this analysis states the $t\bar{t}\gamma$ cross section times branching ratio for the non-full-hadronic decay channels for photons with a transverse momentum of $p_T > 20\,\text{GeV}$ and pseudorapidity $|\eta| < 2.37$. Further, the signal significance of the $t\bar{t}\gamma$ signal is estimated, since no evidence of this process could be measured at the LHC so far.
This thesis is subdivided into 14 chapters. An overview of the current theoretical understanding of particle physics is given in chapter 1, followed by current predictions and measurements of the top quark with an emphasis on $t\bar{t}\gamma$ events. Chapter 3 introduces the experimental setup at the Large Hadron Collider and the ATLAS experiment. Chapter 4 defines the modeling, reconstruction and identification of all relevant physics objects, followed by the description of the analyzed dataset as well as the signal and background

modeling in Monte Carlo simulated events. The developed $t\bar{t}\gamma$ event selection is defined in chapter 6. In chapter 7, the analysis strategy is outlined, which is then described in detail in chapters 8 to 11. The derivation of the systematic uncertainties is listed in chapter 12. After the estimation of the signal significance in chapter 13, the thesis concludes with a summary of the $t\bar{t}\gamma$ cross section result and an outlook for possible further studies of the $t\bar{t}\gamma$ signal.

Chapter 1

Particle Physics

1.1 Standard Model of Particle Physics

The Standard Model of particle physics provides a theoretical description of all known subatomic particles and their interactions via three fundamental forces [1, 2, 3, 4]. This theory explains almost all experimental results and precisely predicts a wide variety of phenomena. Over time and by conducting many experiments, the Standard Model has proven to be a well-tested physics theory.

The Standard Model is based on the combination of local gauge symmetries, leading to conservation laws according to the Noether Theorem [5]. The Standard Model introduces the three fundamental forces as gauge fields which model the interactions of the particles and conserve local symmetries. Measured at a typical energy scale of 1 GeV, the forces can be characterized by widely different ranges and strengths. The weak force, which is responsible for radioactive decay, has a range of 10^{-18} m and is about 10^5 times weaker than the electromagnetic force. Electromagnetic interactions occur between electrically charged particles, explaining most macroscopic physics phenomena. The electromagnetic force has infinite range and strength determined by the fine structure constant $\alpha \approx \frac{1}{137}$. The strong nuclear force binds all constituents of a nucleus and has a range of about 10^{-15} m and a strength 100 times that of the electromagnetic force. These constituents are quarks carrying color charge, which is unrelated to visual perception of color. The color charge is characterized by three values, red, green and blue, as well as the corresponding anticolors. The fourth force is gravity, which also has infinite range, but due to its low energy coupling of about 10^{-38}, gravity is too weak to be observed in particle physics experiments and is therefore not included in the Standard Model. Electromagnetism and weak interactions are unified in a single gauge group, the theory of strong interactions remains in a separate gauge group. Gauge bosons are the carriers of the fundamental interactions. The photon is a massless and chargeless particle transmitting electromagnetic interactions, the massive vector bosons W^+, W^- and Z^0 mediate the weak force, while eight different gluons can be exchanged between quarks in the strong interaction. These particles have integer spin values and hence obey Bose-Einstein statistics. An overview of all gauge bosons including their masses and electric charges is shown in Table 1.1.

Observable matter consists of only a few fundamental fermions, i.e spin-$\frac{1}{2}$ particles which follow Fermi-Dirac statistics. The class of fermions consists of a total of 12 particles and their respective antiparticles, which are subdivided into leptons and quarks as listed in Table 1.2. Antiparticles have the same masses as their corresponding particles, but opposite quantum numbers, like charges and the weak isospin. Both types of fermions can be grouped together in three families, each consisting of two leptons and two quarks: a

Bosons

Photon γ	mass: $< 1 \times 10^{-18}$ eV electric charge: 0
Gluon	mass: 0 electric charge: 0
$W^{\pm}$	mass: 80.385 ± 0.015 GeV electric charge: $\pm e$
Z^0	mass: 91.1876 ± 0.0021 GeV electric charge: 0

Table 1.1: Overview of all gauge bosons represented in the Standard Model including their masses and electric charges [6].

massive lepton with the electric charge of -1e, with e being the elementary charge, and an almost massless neutrino without any electric charge, and finally, a pair of quarks with an electric charge of $+\frac{2}{3}e$ and -$\frac{1}{3}e$. These two quarks are generally called up-type and down-type quark with respect to the names of the first family. In one family, the two leptons and quarks each form weak isospin doublets, since they are identical with regard to the weak interaction.
Ordinary atoms consist only of fermions of the first family with up and down quarks composing the nucleus and electrons filling the shell, as the other charged fermions are each much heavier than the corresponding first-family particles.
The elementary particles and fundamental forces described by the Standard Model explain only around 5% of the total mass-energy of the universe. The remaining 95% are composed from dark matter and dark energy, which are still unknown.
The local gauge theory can be written as the gauge symmetry group

$$SU(3)_C \times U(2)_L \times U(1)_Y,$$

including color charge (C), weak isospin (L) and hypercharge (Y) gauge groups. The Lagrangian, which describes the Standard Model, is composed of terms for the strong interactions $\mathcal{L}_{\mathrm{QCD}}$, the electroweak interactions $\mathcal{L}_{\mathrm{EW}}$, the Brout-Englert-Higgs mechanism $\mathcal{L}_{\mathrm{BEH}}$ and the Yukawa coupling $\mathcal{L}_{\mathrm{Yukawa}}$.

Quarks

Up ($\boldsymbol{u}$)	mass: $2.3^{+0.7}_{-0.5}$ MeV electric charge: $+\frac{2}{3}e$ I_z: $+\frac{1}{2}$	**Down** ($\boldsymbol{d}$)	mass: $4.8^{+0.7}_{-0.3}$ MeV electric charge: $-\frac{1}{3}e$ I_z: $-\frac{1}{2}$
Charm ($\boldsymbol{c}$)	mass: 1.275 ± 0.025 GeV electric charge: $+\frac{2}{3}e$ I_z: $+\frac{1}{2}$	**Strange** ($\boldsymbol{s}$)	mass: 95 ± 5 MeV electric charge: $-\frac{1}{3}e$ I_z: $-\frac{1}{2}$
Top ($\boldsymbol{t}$)	mass: 173.3 ± 1.0 GeV electric charge: $+\frac{2}{3}e$ I_z: $+\frac{1}{2}$	**Bottom** ($\boldsymbol{b}$)	mass: 4.18 ± 0.03 GeV electric charge: $-\frac{1}{3}e$ I_z: $-\frac{1}{2}$

Leptons

Electron ($\boldsymbol{e^-}$)	mass: 0.511 MeV electric charge: $-e$ I_z: $-\frac{1}{2}$	**Electron neutrino** ($\boldsymbol{\nu_e}$)	mass: $<$ 2 eV electric charge: 0 I_z: $+\frac{1}{2}$
Muon ($\boldsymbol{\mu^-}$)	mass: 105.66 MeV electric charge: $-e$ I_z: $-\frac{1}{2}$	**Muon neutrino** ($\boldsymbol{\nu_\mu}$)	mass: $<$ 0.19 MeV electric charge: 0 I_z: $+\frac{1}{2}$
Tau ($\boldsymbol{\tau^-}$)	mass: 1776.82 MeV electric charge: $-e$ I_z: $-\frac{1}{2}$	**Tau neutrino** ($\boldsymbol{\nu_\tau}$)	mass: $<$ 18.2 MeV electric charge: 0 I_z: $+\frac{1}{2}$

Table 1.2: Overview of all fermions represented in the Standard Model including their masses, electric charges and third components of the weak isospin [6].

1.2 Quantum Electrodynamics and electroweak unification

The gauge theory representing electromagnetic interactions is described by quantum electrodynamics (QED). The theory is based on the unitary group $U(1)_Q$ with the electric charge Q. The coupling of charged fermion fields ψ to the photon field A_μ is described by

the Lagrangian density:

$$\mathscr{L}_{\mathrm{QED}} = -\frac{1}{4}F_{\mu\nu}F^{\mu\nu} + \sum_n \bar{\psi}_n(i\gamma^\mu D_\mu - m_n)\psi_n\,,$$

with ψ_n describing the bispinor field of one of the n fermions (quarks or electrically charged leptons). The field tensor of the electromagnetic field $F^{\mu\nu}$ and the covariant derivative D_μ are given by:

$$F_{\mu\nu} = \partial_\mu A_\nu - \partial_\nu A_\mu\,,$$
$$D_\mu = \partial_\mu + iqA_\mu\,.$$

Further, γ_μ are the Dirac matrices and e is the elementary charge. The Lagrangian density does not include any mass term, i.e. photons are massless and do not interact with each other.

In the 1960s, Glashow, Salam and Weinberg proposed an unification theory of the QED with the theory of weak interactions [7, 8, 9]. It combines two unitary groups $SU(2)_L$ and $U(1)_Y$ into a $SU(2)\otimes U(1)$ symmetry group. The $SU(2)_L$ group is generated by the weak isospin

$$I_i = \frac{\tau_i}{2} \text{ with } i = 1,2,3\,,$$

with the Pauli-matrices τ_i, while the hypercharge

$$Y = 2(Q - I_3)$$

is the generator of the Abelian $U(1)$ group. The gauge field of the electromagnetic interaction is described by $B_{\mu\nu}$, while the weak gauge field is given by $W^i_{\mu\nu}$:

$$\begin{aligned} B_{\mu\nu} &= \partial_\mu B_\nu - \partial_\nu B_\mu\,, \\ W^i_{\mu\nu} &= \partial_\mu W^i_\nu - \partial_\nu W^i_\mu + g\varepsilon_{ijk}W^j_\mu W^k_\nu \text{ with } i = 1,2,3\,. \end{aligned}$$

The fermion fields can be represented by left handed and right handed components:

$$\psi_L = P_L\psi = \frac{1-\gamma_5}{2}\psi$$
$$\psi_R = P_R\psi = \frac{1+\gamma_5}{2}\psi$$

Left handed leptons and quarks are assigned to doublets

$$L_{\mathrm{lepton}} = \begin{pmatrix} \nu_e \\ e \end{pmatrix} \qquad L_{\mathrm{quark}} = \begin{pmatrix} u \\ d \end{pmatrix}$$

with isospin $I_3 \neq 0$, resulting in the hypercharges $Y_{\mathrm{lepton}} = -\frac{1}{2}$ and $Y_{\mathrm{quark}} = \frac{1}{6}$. Right handed fermions only appear as singlets with $I_3 = 0$ and do not transform under the $SU(2)$ symmetry. As fermions of both helicity states transform under the $U(1)$ symmetry, separate covariant derivatives have to be formed for left-handed and right-handed fermions:

$$D_{\mu,L} = \partial_\mu + i\tau_i\frac{g}{2}W^i_\mu + iY\frac{g'}{2}B_\mu\,,$$
$$D_{\mu,R} = \partial_\mu + iY\frac{g'}{2}B_\mu\,,$$

with the coupling constants g and g' of the weak and electromagnetic interactions, respectively. These constants are related by the weak mixing angle θ_w:

$$\begin{aligned} \sin\theta_w &= \frac{g'}{\sqrt{g^2+g'^2}}\,, \\ \tan\theta_w &= \frac{g'}{g}\,. \end{aligned}$$

The angle is not predicted by the Standard Model, but has been determined experimentally [6]:

$$\sin^2\theta_w = 0.23116 \pm 0.00013\,.$$

The two coupling constants are also related to the elementary charge e via

$$e = g\sin\theta_w = g'\cos\theta_w\,.$$

Overall, the Langragian density of the electroweak theory is

$$\mathscr{L}_{\mathrm{EW}} = -\frac{1}{4}B_{\mu\nu}B^{\mu\nu} - \frac{1}{4}W_{\mu\nu}W^{\mu\nu} + \bar{\psi}_L\gamma^\mu D_{\mu,L}\psi_L + \bar{\psi}_R\gamma^\mu D_{\mu,R}\psi_R\,.$$

The first two terms describe the interactions between the gauge fields themselves, whereas the second two terms discribe the interactions of left-handed particles and right-handed particle interactions, respectively.
The physical fields of the four mediators are described in the electroweak theory by combinations of the gauge fields and the weak mixing angle:

$$\begin{aligned} Z_\mu &= \cos\theta_w W_\mu^3 + \sin\theta_w B_\mu\,, \\ A_\mu &= \sin\theta_w W_\mu^3 + \cos\theta_w B_\mu\,, \\ W_\mu^\pm &= \frac{1}{\sqrt{2}}(W_\mu^1 \pm iW_\mu^2)\,. \end{aligned}$$

These three linear combinations consist of massless gauge fields, which implies that all gauge bosons are considered massless in electroweak interactions. While this is the case for the photon, these assumptions are in contradiction with the discoveries of the massive $W^\pm$ and Z bosons in the 1980s by the UA1 and UA2 experiments [10, 11, 12, 13]. The electroweak theory has to be extended by a new field to account for the mass of the weak gauge bosons, which is described by the widely accepted Brout-Englert-Higgs mechanism.

1.3 CKM matrix

The electroweak theory also describes the mixing of weak quark eigenstates in the Cabibbo-Kobayashi-Maskawa (CKM) matrix [14, 15]. Quarks change their flavors only in weak interactions via coupling to $W^\pm$ bosons. The quark flavor eigenstates transform to the mass eigenstates with

$$V_{CKM}\begin{pmatrix} |d\rangle \\ |s\rangle \\ |b\rangle \end{pmatrix} = \begin{pmatrix} V_{ud} & V_{us} & V_{ub} \\ V_{cd} & V_{cs} & V_{cb} \\ V_{td} & V_{ts} & V_{tb} \end{pmatrix}\begin{pmatrix} |d\rangle \\ |s\rangle \\ |b\rangle \end{pmatrix} = \begin{pmatrix} |d'\rangle \\ |s'\rangle \\ |b'\rangle \end{pmatrix}\,.$$

The CKM matrix can be fully defined by four independent parameters. The standard parameterization of the CKM matrix uses three Euler angles $\Theta_{12}, \Theta_{23}, \Theta_{13}$ and a CP-violating phase δ:

$$V_{\mathrm{CKM}} = \begin{pmatrix} c_{12}c_{13} & s_{12}c_{13} & s_{13}e^{-i\delta} \\ -s_{12}c_{23} - c_{12}s_{23}s_{13}e^{i\delta} & c_{12}c_{23} - s_{12}s_{23}s_{13}e^{i\delta} & s_{23}c_{13} \\ s_{12}s_{23} - c_{12}c_{23}s_{13}e^{i\delta} & -c_{12}s_{23} - s_{12}c_{23}s_{13}e^{i\delta} & c_{23}c_{13} \end{pmatrix}$$

with $s_{ij} = \sin\Theta_{ij}$ and $c_{ij} = \cos\Theta_{ij}$. Another common representation of the matrix uses the Wolfenstein parameterization [16]:

$$V_{\mathrm{CKM}} = \begin{pmatrix} 1 - \lambda^2/2 & \lambda & A\lambda^3(\rho - i\eta) \\ -\lambda & 1 - \lambda^2/2 & A\lambda^2 \\ A\lambda^3(1 - \rho - i\eta) & -A\lambda^2 & 1 \end{pmatrix} + \mathcal{O}(\lambda^4)$$

The four parameters λ, A, ρ and η are related to the standard parameterization by

$$s_{12} = \lambda\,, \qquad s_{23} = A\lambda^2\,, \qquad s_{13}e^{-i\delta} = A\lambda^3(\rho - i\eta)\,.$$

Due to the unitary requirement of the CKM matrix, i.e. $V_{\mathrm{CKM}}V_{\mathrm{CKM}}^{*} = \mathbb{1}$, six triangles can be defined in a complex plane. One particular triangle is described by the unitary constraint

$$\begin{aligned} & V_{ud}V_{ub}^{*} + V_{td}V_{tb}^{*} + V_{cd}V_{cb}^{*} = 0 \\ \Leftrightarrow\ & \frac{V_{ud}V_{ub}^{*}}{V_{cd}V_{cb}^{*}} + \frac{V_{td}V_{tb}^{*}}{V_{cd}V_{cb}^{*}} + 1 = 0\,. \end{aligned}$$

This equation describes a closed triangle in the $(\bar{\rho}, \bar{\eta})$ plane with its corners $(0,0)$, $(0,1)$ and $(\bar{\rho}, \bar{\eta}) = \left(\rho - \frac{\lambda^2}{2}, \eta - \frac{\lambda^2}{2}\right)$. The included angles are defined by

$$\alpha \equiv -\frac{V_{td}V_{tb}^{*}}{V_{ud}V_{ub}^{*}}, \qquad \beta \equiv -\frac{V_{cd}V_{cb}^{*}}{V_{td}V_{tb}^{*}}, \qquad \gamma \equiv -\frac{V_{ud}V_{ub}^{*}}{V_{cd}V_{cb}^{*}}$$

Hence, this unitary triangle can be constrained with two parameters, either two angles or the coordinates of the corner $(\bar{\rho}, \bar{\eta})$. Various measurements are being combined in a global fit to measure the properties of the triangle and subsequently the individual entries of the CKM matrix, as illustrated in Figure 1.1.
The estimated values of the CKM matrix are [6]:

$$V_{\mathrm{CKM}} = \begin{pmatrix} 0.97427 \pm 0.00015 & 0.22534 \pm 0.00065 & 0.00351^{+0.00015}_{-0.00014} \\ 0.22520 \pm 0.00065 & 0.97344 \pm 0.00016 & 0.0412^{+0.0011}_{-0.0005} \\ 0.00867^{+0.00029}_{-0.00031} & 0.0404^{+0.0011}_{-0.0005} & 0.999146^{+0.00021}_{-0.00046} \end{pmatrix}.$$

The measured values are in agreement with the prediction of the unitary matrix, otherwise the triangle in the complex plane would not be closed.

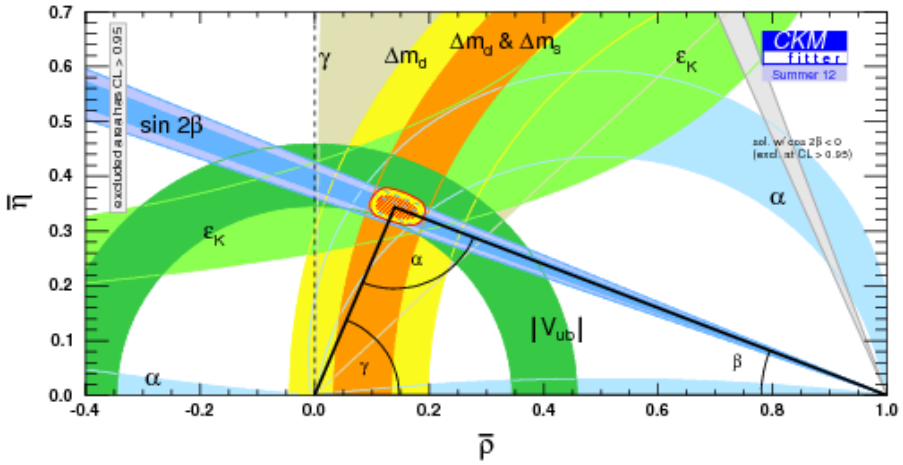

Figure 1.1: Illustration of the individual measurements and the global combination (red hashed region, corresponds to 68% confidence level) in the $(\bar{\rho}, \bar{\eta})$ plane for the calculation of the unitary triangle describing the CKM matrix [17].

1.4 The Brout-Englert-Higgs mechanism

Since the electroweak theory does not include any mass terms for the gauge bosons, a new theory had to be introduced which acknowledges the boson masses while conserving the local gauge invariance. This has been achieved by the Brout-Englert-Higgs (BEH) mechanism through spontaneous symmetry breaking [18, 19, 20].
The BEH mechanism introduces a doublet of two scalar fields

$$\Phi = \frac{1}{\sqrt{2}} \begin{pmatrix} \phi_1 + i\phi_2 \\ \phi_3 + i\phi_4 \end{pmatrix} = \begin{pmatrix} \phi^+ \\ \phi^0 \end{pmatrix} ,$$

and a Lagrangian:

$$\mathscr{L}_{\mathrm{BEH}} = \frac{1}{2}\partial_\mu \Phi^\dagger \partial^\mu \Phi - \mu^2 \Phi^\dagger \Phi + \lambda (\Phi^\dagger \Phi)^2 .$$

The second and third term resemble the BEH potential $V(\Phi^\dagger\Phi)$. The self-coupling λ has to be larger than zero, otherwise the potential is not bounded from below and has therefore no state of minimum energy. If the mass term μ^2 is positive, the potential and the minimum of the potential is obtained for $\langle 0|\phi|0\rangle = \phi_0 = 0$, as shown in Figure 1.2. $\mathscr{L}_{\mathrm{BEH}}$ is then the Lagrangian of a spin-zero particle of mass μ [21]. If μ^2 is negative, $V(\Phi^\dagger\Phi)$ has a minimum, when

$$\langle 0|\phi^2|0\rangle = \phi_0^2 = -\frac{\mu^2}{\lambda} = v^2 ,$$

with the vacuum expectation value v. A non-zero quantity v is equivalent to spontaneous symmetry breaking and results in the generation of a massive scalar boson with a mass of $m_H = \mu\sqrt{2}$ and spin 0. After the extension of the electroweak theory, the gauge boson

masses have been included, expressed in terms of the vacuum expectation value, the weak coupling constant and the weak mixing angle:

$$\begin{aligned} m_W &= \frac{gv}{2}\,, \\ m_Z &= \frac{gv}{2\sqrt{2}\cos\theta_w}\,, \\ m_A &= 0\,. \end{aligned}$$

The value of v is fixed by the Fermi constant G_F, which has been measured from muon decays [6]:

$$v = \sqrt{\sqrt{2}G_F} \simeq 246.22\,\text{GeV}\,.$$

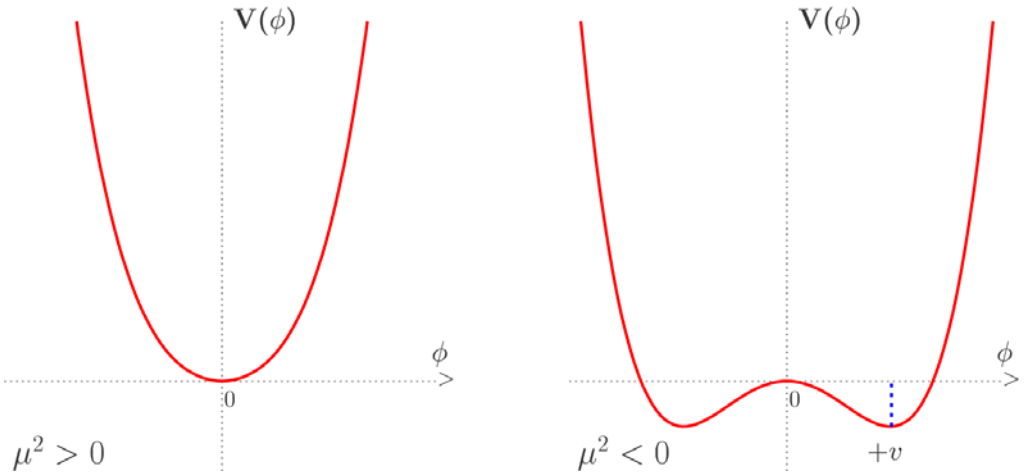

Figure 1.2: Illustrated potential V of the scalar field ϕ in the case $\mu^2 > 0$ (left) and $\mu^2 < 0$ (right) [21].

1.5 The BEH boson

After a search lasting decades, a new milestone in particle physics was set on July 4th, 2012, when the ATLAS and CMS collaborations announced the discovery of a new particle, which was believed to be the long-sought BEH boson [22, 23]. The latest results released at the Moriond conference in March 2013 tentatively confirmed this assumption. In the following, the presented results are restricted to measurements of the ATLAS collaboration, which are all in agreement with the published results of the CMS experiment. Five main decay channels are being analyzed in the search of the scalar boson H, with their cross sections times branching ratios illustrated as a function of the boson mass in

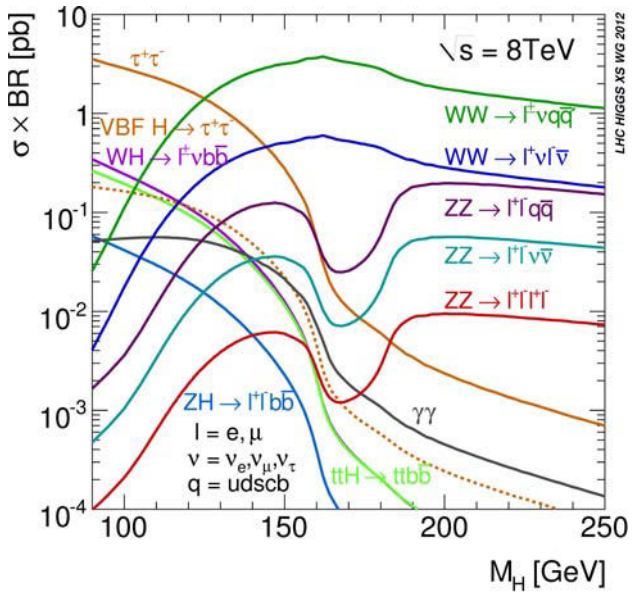

Figure 1.3: Standard Model BEH boson production cross section times branching ratio at a center-of-mass energy of 8 TeV for various decay channels, which are analyzed by the two LHC collaborations ATLAS and CMS [24].

Figure 1.3:

$$
\begin{aligned}
&H \to \gamma\gamma \\
&H \to ZZ \qquad \to l_1^+ l_1^- l_2^+ l_2^- \quad \text{with } l = e, \mu \\
&H \to W^- W^+ \to l_1^+ \nu_{l_1} l_2^- \bar{\nu_{l_2}} \quad \text{with } l = e, \mu \\
&H \to b\bar{b} \\
&H \to \tau^- \tau^+
\end{aligned}
$$

The first goal has already been accomplished by the discovery of an unknown particle with a signal access of above $5\,\sigma$ significance. Combining the total datasets of 2011 and 2012, the ATLAS analyses reach a significance of almost $10\,\sigma$, as shown in Figure 1.4. Hence, the analysis groups have already moved on to the next chapter of BEH physics at the LHC, the precise measurements of properties of the new scalar boson.
The scalar boson mass was derived from measurements in the $\gamma\gamma$ and ZZ channel resulting in [26]

$$m_H = (125.5 \pm 0.2(\text{stat.})^{+0.5}_{-0.6}(\text{syst.}))\,\text{GeV}\,.$$

These two channels were chosen due to the high precision measurements of photon and lepton momenta resulting in the best experimental mass resolution. The invariant mass distributions of both channels are illustrated in Figure 1.5. The observed mass difference between both channels of

$$\Delta m_H = m_H^{\gamma\gamma} - m_H^{ZZ} = (2.3^{+0.6}_{-0.7}(\text{stat.}) \pm 0.6(\text{syst.}))\,\text{GeV}$$

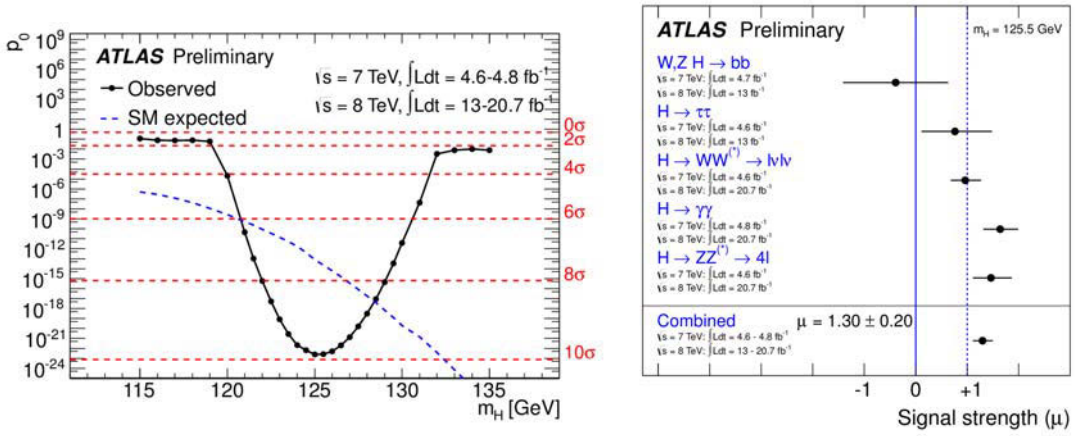

Figure 1.4: The left plot shows the local probability p_0 for a background-only experiment to be more signal-like than the observation as a function of BEH mass for the combination of all channels. The dashed curve shows the median expected local p_0 under the hypothesis of a Standard Model BEH boson production at the corresponding mass. The horizontal dashed lines indicate the p-values corresponding to significances of $0\,\sigma$ to $10\,\sigma$. The right plot shows the measurements results of the signal strength parameter μ for a boson mass of 125.5 GeV for the individual channels and their combination, as well as the Standard Model expectation of $\mu = 1$ [25].

is still under investigation. At the moment, the compatibility of both measurements is at a $2.4\,\sigma$ level.
The results of all five channels are combined by the signal strength, which is the ratio of observed signal events to the expected data yield predicted by the Standard Model for a fixed scalar boson mass. The latest numbers are shown in Figure 1.4 with a combined signal strength of [25]

$$\mu = (1.30 \pm 0.13(\text{stat.}) \pm 0.14(\text{syst.}))\,.$$

In the Standard Model, the BEH boson is predicted to be a CP-even, spin-0 particle, i.e. $J^P = 0^+$. The Landau-Yang theorem [29] forbids the direct decay of a spin-1 particle into a pair of photons. Hence, the spin-1 hypothesis is strongly disfavoured by the observation of the $H \to \gamma\gamma$ decay. Analyses in the $\gamma\gamma$, ZZ and WW channels have focused on the discrimination between the Standard Model assignment and a specific $J^P = 2^+$ graviton-inspired model with minimal couplings to Standard Model particles. The spin-2 model was excluded at 99.9% confidence level [30]. Further, the analysis in the ZZ channel has excluded $J^P = 0^-$,1^+ and 1^- at a $> 96.9\%$ confidence level [28].
With full statistics from 2011 and 2012, the analyses in the different channels have started to categorize their measurements into different production modes of the BEH boson. A first evidence of the vector boson fusion production was found with a significance of $3.1\,\sigma$ [25]. Furthermore, no hints for new physics have been found so far, e.g. in rare decay channels like $H \to Z\gamma$ and $H \to \mu^+\mu^-$ [31, 32].

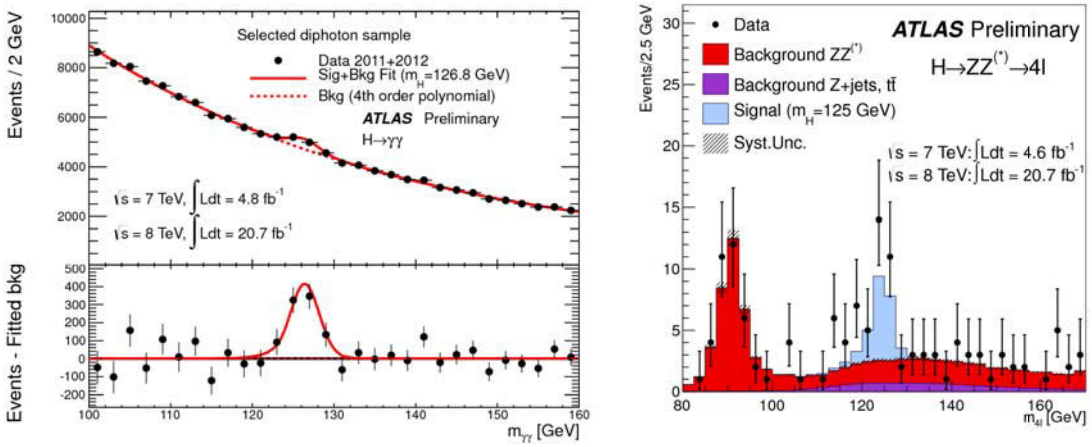

Figure 1.5: The distributions of the diphoton (left) and four-lepton invariant mass (right) for selected candidates of the combined $\sqrt{s} = 8\,\text{TeV}$ and $\sqrt{s} = 7\,\text{TeV}$ datasets. The left plot shows the combined signal+background fit to estimate the number of signal events with the background described by a fourth-order Bernstein polynomial. In the right plot, the data distribution is compared with the Standard Model prediction for a scalar boson mass of 125 GeV [27, 28].

1.6 Yukawa coupling

The BEH mechanism is not only responsible for the generation of the gauge boson masses, but also the masses of all fermions using the same scalar field Φ. For each of the three fermion generations, a Yukawa Langrangian is introduced:

$$\mathscr{L}_{\text{Yukawa}} = -\lambda_e \bar{L}\Phi e_R - \lambda_d \bar{Q}\Phi d_R - i\tau_2 \lambda_u \bar{Q}\Phi u_R + [h.c.]\,.$$

Q are the left-handed quark doublets, d_R and u_R the right-handed down- and up-type quark singlets, L the left handed lepton doublet and e_R the right handed singlet of the charged lepton. The abbreviation $h.c.$ stands for hermetian conjugate. The coupling of the fermion to the BEH field is called Yukawa coupling λ, which is related to the vacuum expectation value v and the resulting masses of the leptons and quarks:

$$m_e = \frac{\lambda_e v}{\sqrt{2}}\,, \qquad m_u = \frac{\lambda_u v}{\sqrt{2}}\,, \qquad m_d = \frac{\lambda_d v}{\sqrt{2}}\,.$$

The Yukawa coupling of most fermions is very small, except for that of the top quark. Due to its very high mass, the coupling of the top quark is given by:

$$\lambda_{\text{top}} = \frac{m_{\text{top}}\sqrt{2}}{v} \approx 1\,.$$

The Standard Model assumes that neutrinos are massless, since no right-handed neutrinos exist. However, the experimentally observed phenomenon of neutrino oscillation requires massive neutrinos [33, 34], which is acknowledged by an extension of the Standard Model called seesaw mechanism [35, 36, 37, 38].

1.7 Quantum Chromodynamics

Strong interactions between quarks are described by Quantum Chromodynamics (QCD), postulated by Gell-Mann, Fritzsch and Leutwyler in 1973 [39]. This gauge theory is based on the non-abelian local gauge symmetry group $SU(3)_C$. The quantum number of the strong nuclear force is called color, occuring in three types (red, green, blue) and their respective anticolors. The interaction is mediated by massless gluons which carry a color-anticolor charge. These gauge bosons are grouped as an octet of linear combinations of the three colors, while a ninth possible combination, a color singlet, does not exist in nature. The Langrangian density of QCD with the quark field ψ_q is given by

$$\mathscr{L}_{\mathrm{QCD}} = -\frac{1}{4} F^a_{\mu\nu} F^{\mu\nu,a} + \sum_{q=1}^{6} \bar{\psi}_{q,c} (i \not{D} - m) \psi_{q,c} \,,$$

with the covariant derivative

$$D_\mu = \partial_\mu + i g_s \frac{\lambda}{2} G^a_\mu \,.$$

The derivative includes the gluon fields G^a_μ, the coupling constant of strong interactions g_s as well as the Gell-Mann matrices λ_a. These eight 3×3 matrices with $a = 1, 2...8$ act as generators of the $SU(3)$ symmetry group, in analogy to the Pauli matrices for weak interactions. The QCD field strength tensor $F^a_{\mu\nu}$ is given by

$$F^a_{\mu\nu} = \partial_\mu G^a_\nu - \partial_\nu G^a_\mu - g_s f_{abc} G^b_\mu G^c_\nu \,,$$

which include a term describing the self-interaction between the gluon, since they carry color charge and can couple to the gauge field themselves. The structure constants f_{abc} is defined by the Gell-Mann matrices via

$$[\lambda_a, \lambda_b] = 2 i f_{abc} \lambda_c \,.$$

One prominent feature of QCD is color confinement. Only color singlets can exist as free particles. As a consequence, quarks cannot exist unbound, but only in colorless bound states, called hadrons. Otherwise, one would face a long range color force field, which does not occur in nature. Hadrons consist of a quark-antiquark pair (meson) or are formed from three quarks or antiquarks (baryon). If two quarks are separated, an energy density flux between the quark pair is created by the gluon field. The energy stored in the flux increases lineary with the length of the flux, until it is energetically more favorable for a new quark-antiquark pair to appear spontaneously, than to allow the flux to extend further. Hence, new hadrons are formed, before quarks become unbound. Results of this can be seen in particle accelerators, where jets of many hadrons and gluons are detected instead of single quarks. This process is called hadronization.
Another property of QCD is described by asymptotic freedom, which states that the interaction strength $\alpha_s = \frac{g_s^2}{4\pi}$ between quarks becomes smaller with decreasing distance and increasing energy. This can be explained in QCD by virtual quark-antiquark pairs screening the color charge and gluon loops, which have an antiscreening effect. While the quark loops render the interaction stronger at shorter distance, the opposite contributions

from the gluon self-coupling is much larger, resulting in an interaction strength at an energy scale $Q >> \Lambda_{\mathrm{QCD}}$ of

$$\alpha_s(Q^2) = \frac{12\pi}{(33 - 2n_f)\ln\left(\frac{Q^2}{\Lambda^2_{\mathrm{QCD}}}\right)}.$$

The strong interaction $\Lambda_{\mathrm{QCD}} \approx 250\,\mathrm{MeV}$ sets the scale at which the coupling constant becomes large and the physics becomes nonperturbative. The equation shows that α_s converges to 0 with increasing energy or a distance approaching 0. This behaviour has been verified in high-energy experiments, as shown in Figure 1.6. Hence, quarks can be considered as free particles at high energies and strong interaction physics can be calculated in perturbation theory.

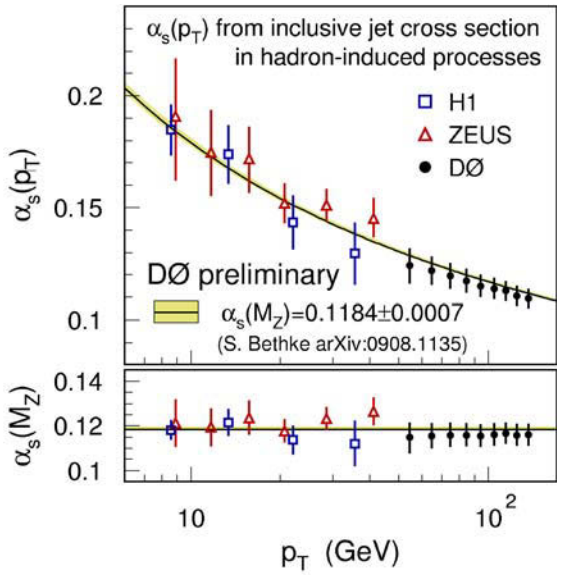

Figure 1.6: The running strong coupling α_s as a function of the transverse momentum (top) and at an energy scale equal to the Z boson mass (bottom). Results are shown from two experiments at the *ep*-collider HERA, H1 and ZEUS, as well as from the D0 experiment, located at the $p\bar{p}$-collider Tevatron. All data points are shown with their total uncertainties and are in agreement with the theoretical prediction (yellow band) [40].

Chapter 2

The Top Quark

The existence of the top quark was well expected since the bottom quark was experimentally discovered in 1977 [41], but due to its high mass, it took almost twenty years until it was discovered. Searches at various e^+e^-−colliders as well as the $p\bar{p}$−collider Sp$\bar{\text{p}}$S at CERN did not provide the possibility of a direct search in the 1980s and early 1990s, but the lower limit on the top quark mass could be increased up to 69 GeV in 1990 [42]. In 1988, the CDF detector at the Tevatron proton-antiproton-collider in Michigan, USA, started data taking at a center-of-mass energy of $\sqrt{s} = 1.8$ TeV. First results of the top quark search were published in 1991 and exceeded the results of the other experiments with a lower mass limit of 77 GeV [43]. In 1992, the D0 detector was commissioned at the Tevatron, which had similar sensitivity to the top quark as the CDF detector. With increasing integrated luminosity and by adding more search channels, the top quark was finally discovered by both collaborations in 1995 [44, 45].
Due to its high mass, the top quark is short-lived with a predicted lifetime of only $5{\cdot}10^{-25}$ s, so that the parton does not form hadrons before the decay, in contrary to the other five quarks. This provides the unique opportunity to study the properties of the bare top quark itself, which passes on its properties directly to its decay products.
The top quark decays almost exclusively into a W boson and a bottom quark with a probability according to the CKM matrix of [6]

$$|V_{tb}|^2 = |0.999146^{+0.000021}_{-0.000046}|^2 \,.$$

Furthermore, top quark physics provides a sensitive probe of the validity of the Standard Model and possible new physics. The LHC produces top quarks abundantly due to high luminosities and high center-of-mass energies, to finally measure all properties with such precision that deviations from the Standard Model will lead to sources of new physics.

2.1 Top quark pair production

The production of top quark pairs at hadron colliders is described by perturbative Quantum Chromodynamics (pQCD). The collisions themselves cannot be described by point-like protons, but by the interactions of their constituents: three valence quarks (uud) and numerous gluons which can split into virtual quark-antiquark pairs, so called sea quarks, are confined in one proton. The $t\bar{t}$ production cross section in hadron collisions can be separated into a short distance partonic cross section for the incoming partons i and j, $\hat{\sigma}(ij \to t\bar{t})$, and into a long distance term consisting of the parton distribution functions $f_i(x_i, \mu_F^2)$ and $f_j(x_j, \mu_F^2)$. This separation between pQCD from non-perturbative effects is set by the factorization scale μ_F, while the parton distribution function of the particle

i describes the probability that parton i carries a certain fraction of the overall proton momentum. They are obtained by fitting theoretical predictions to various sets of experimental measurements from deep inelastic scattering experiments like ZEUS and H1 at HERA [46]. Exemplary, parton distribution functions of the CTEQ6L1 set [47] are shown in Figure 2.1. In higher order calculations, infinities such as ultraviolet divergences appear, which are removed by a renormalisation procedure, set at the renormalization scale μ_R. The total top quark pair production cross section for hard scattering processes is given by:

$$\sigma_{pp\to t\bar{t}} = \sum_{i,j=q,\bar{q},g} \int dx_i dx_j f_i(x_i, \mu_F^2) f_j(x_j, \mu_F^2) \hat{\sigma}(ij \to t\bar{t}, \hat{s}, \mu_R^2)$$

The partonic cross sections $\hat{\sigma}(ij \to t\bar{t})$ have to be evaluated for all possible combinations of i and j, depending on the partonic center-of-mass energy $\hat{s}$.
On tree level, top quark pairs can be produced either via gluon fusion or via quark-antiquark annihilation. Feynman diagrams of both mechanisms are shown in Figure 2.2. At the LHC, gluon fusion is the predominant production process, occuring four times more often than $q\bar{q}$-annihilation. The ratio between both mechanism was reverted at the Tevatron $p\bar{p}$-collider, which can emerge due to two reasons: $q\bar{q}$-annihilation is not favored at a pp-collider like the LHC, because antiquarks are only available as sea quarks, which are carrying significantly less energy than valence quarks. Further, gluon fusion is dominating at the LHC due to its considerably higher center-of-mass energy. This can be explained by a simple calculation. The minimal collison energy of two partons to produce a top quark pair is given by

$$\sqrt{x_i x_j s} \geq 2m_{\text{top}}$$

with m_{top} being the top quark mass, and using the assumption $x_i \approx x_j \approx x$, each parton

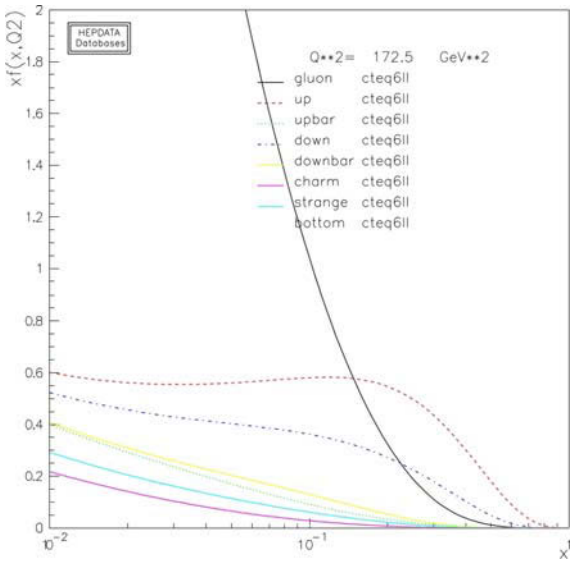

Figure 2.1: Parton density functions ($xf(x)$) of all quarks and the gluon as a function of the proton momentum fraction x in the CTEQ6L1 set for an energy $Q = m_{\text{top}}$ [48].

carries a proton fraction momentum of

$$x \geq \frac{2m_{\text{top}}}{\sqrt{s}} .$$

For the LHC and its center-of-mass energy of $\sqrt{s} = 7\,\text{TeV}$, the equation results in a value of $x \approx 0.05$. Figure 2.1 shows that the parton density function of gluons is significantly higher than any other distribution in the corresponding x-range, i.e. gluon fusion is the favored production process. The Tevatron had a center-of-mass energy of $\sqrt{s} = 1.96\,\text{TeV}$ during Run II and hence, the typical x value was around 0.2. In this case, the production of top quark pairs is dominated by quark-antiquark annihilation processes, in particular involving up and down valence quarks as incoming partons. These two arguments also explain the theoretical top quark pair cross section predictions for pp- and $p\bar{p}$-collisions as a function of $\sqrt{s}$, illustrated in Figure 2.3. At low collision energies, $\sigma(t\bar{t})$ is significantly higher for $p\bar{p}$-collisions due to the prefered $q\bar{q}$-annihilation production processes, while top quark physics would be impossible at the pp-collider like the LHC. Both predictions converge for increasing $\sqrt{s}$ as gluon fusion becomes the predominant production mechanism.

The total top quark pair cross section at the LHC with $\sqrt{s} = 7\,\text{TeV}$ is predicted by an approximate next-to-next-to-leading order calculation [49, 50, 51]:

$$\sigma_{t\bar{t}}^{\text{theo}} = 165^{+4}_{-9}(\text{scale})^{+7}_{-7}(\text{PDF})\,\text{pb}.$$

The top quark mass was set to $m_{\text{top}} = 172.5\,\text{GeV}$ and the renormalization and factorization scales to $\mu = m_{\text{top}}$, while the CTEQ66 parton distribution function set was used. The scale uncertainties are derived by varying both scales by factors of 2 and 0.5, while the PDF uncertainties are obtained using the error set of CTEQ66.

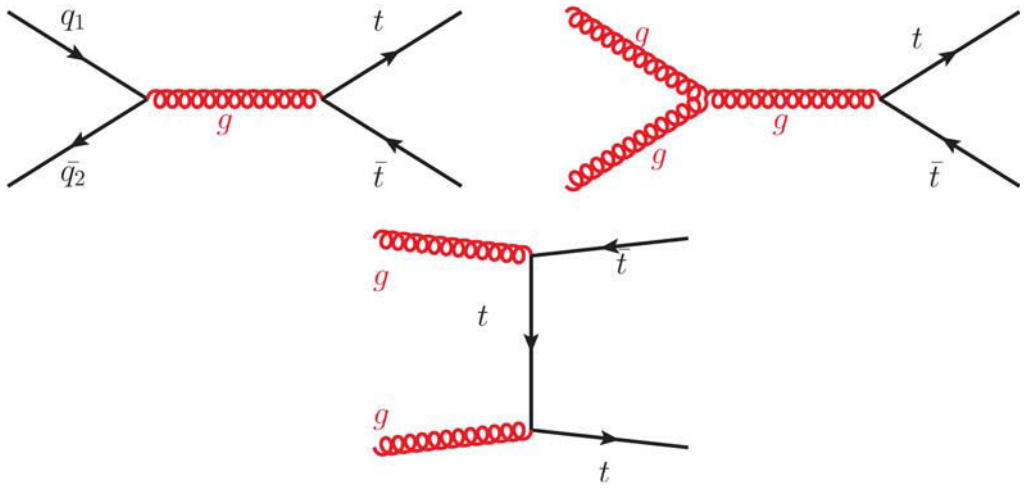

Figure 2.2: Feynman diagrams representing both top quark pair production mechanisms. The upper left diagram shows the quark-antiquark annihilation with the incoming partons being both up-type or down-type quarks. The other two diagrams show gluon fusion processes. The top quark pair is produced by gluon gluon splitting (upper right) or via an exchange of an virtual top quark between the two incoming gluons (lower row).

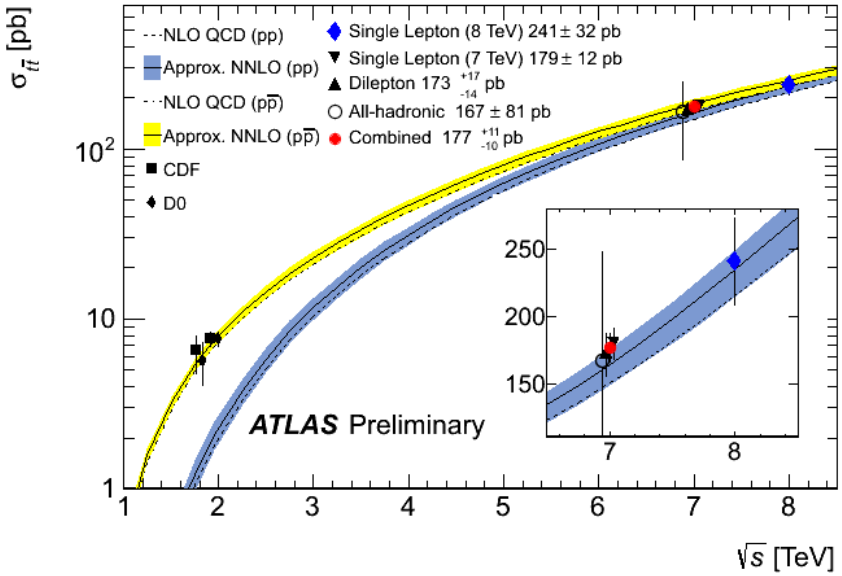

Figure 2.3: Theoretical prediction of the top quark pair cross section as a function of the center-of-mass energy for pp- (blue graph) and $p\bar{p}$-collisions (yellow graph) including uncertainties. The plot also includes experimental results of the CDF and D0 experiments at Tevatron as well as results from the ATLAS experiment at the LHC, all agreeing well with the prediction [53].

Various cross section measurements were performed by members of the ATLAS and CMS experiments until now, using different final states and methods. An official combination of multiple results yields [52]:

$$\sigma_{t\bar{t}} = 173.3 \pm 2.3(\text{stat.}) \pm 9.8(\text{syst.})\,\text{pb},$$

which is in agreement with the theoretical prediction. Figure 2.4 illustrates the individual results used for the combination, which agree with the prediction within systematic uncertainties.

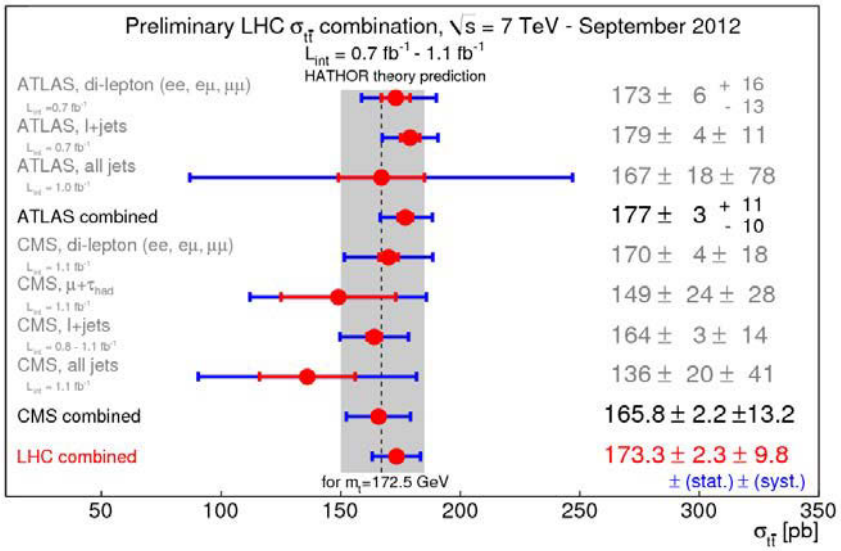

Figure 2.4: Illustration of all top quark pair cross section results by the ATLAS and CMS experiments, used for the first LHC combined result, including statistical (red bars) and systematic uncertainties (blue bars) [52]. All measurements agree with the theoretical prediction (vertical grey band). Furthermore, it is visible that almost all results are dominated by systematic uncertainties.

2.2 Single top quark production

Single top quark events were first observed at both Tevatron experiments, CDF and D0 [54, 55]. Measurements of these processes offer a direct access to the CKM matrix element $|V_{tb}|$ as well as to the $V-A$ structure of the electroweak coupling of the top quark. Three types of production modes contribute to the production of single top quarks, which all occur via the weak interaction:

- t-channel: A space-like W boson ($q^2 \leq 0$) interacts with a b quark from the sea quark of the proton. This process is also called Wg fusion, since the b quark originates from a gluon splitting into a $b\bar{b}$ pair.
- Wt-channel: A b quark is promoted to a top quark and radiates an on-shell W boson ($q^2 = M_W^2$). It is also called the associated production mode.
- s-channel: A time-like W boson ($q^2 \geq (m_t + m_b)^2$) is produced in quark-anti-quark annihilation. The W boson decays into a top quark and an $\bar{b}$ quark ($W \to t\bar{b}$).

The production modes, which are illustrated in Figure 2.5, are listed above according to their cross section at the LHC. The t channel has the largest cross section, which is around 1/3 of that of the top quark pair production, with a sizable contribution of the Wt-channel and only small contributions from the s-channel. The cross sections of all three single top quark production processes have been calculated for pp-collisons at $\sqrt{s} = 7\,\text{TeV}$

with approximate next-to-next-to-leading order precision [56, 57, 58]:

$$\sigma_t^{t-\text{channel}} = 41.9^{+1.8}_{-0.8}\,\text{pb}, \qquad \sigma_{\bar{t}}^{t-\text{channel}} = 22.7^{+0.9}_{-1.0}\,\text{pb},$$
$$\sigma_t^{s-\text{channel}} = 3.1 \pm 0.1\,\text{pb}, \qquad \sigma_{\bar{t}}^{s-\text{channel}} = 1.4 \pm 0.1\,\text{pb},$$
$$\sigma_{t,\bar{t}}^{Wt-\text{channel}} = 15.7 \pm 1.1\,\text{pb}.$$

While the Wt production is charge symmetric, almost two times more top quarks than antitop quarks are produced in the other two production mechanisms. In both cases, the cross sections are dominated by contributions of valence quarks as incoming partons, as they carry significantly higher fractions of the proton momentum than sea quarks. Due to the structure of the proton, two up quarks are available for top quark production, whereas only one down quark is present for the antitop quark production.
Recent results for the t-channel cross section by the ATLAS experiment agree with the theoretical predictions [59]:

$$\sigma_t^{t-\text{channel}} = 53.2 \pm 1.7(\text{stat.}) \pm 10.6(\text{syst.})\,\text{pb},$$
$$\sigma_{\bar{t}}^{t-\text{channel}} = 29.5 \pm 1.5(\text{stat.}) \pm 7.3(\text{syst.})\,\text{pb},$$

Evidence was found for the Wt-channel with a significance of $3.4\,\sigma$ and a cross section was measured by the ATLAS experiment, which also agrees with the prediction [60]:

$$\sigma_{t,\bar{t}}^{Wt-\text{channel}} = 16.8 \pm 2.9(\text{stat.}) \pm 4.9(\text{syst.})\,\text{pb}.$$

Due to the low production rate, only a upper limit could by set for the cross section in the s-channel [61]. All ATLAS results are illustrated in Figure 2.6.

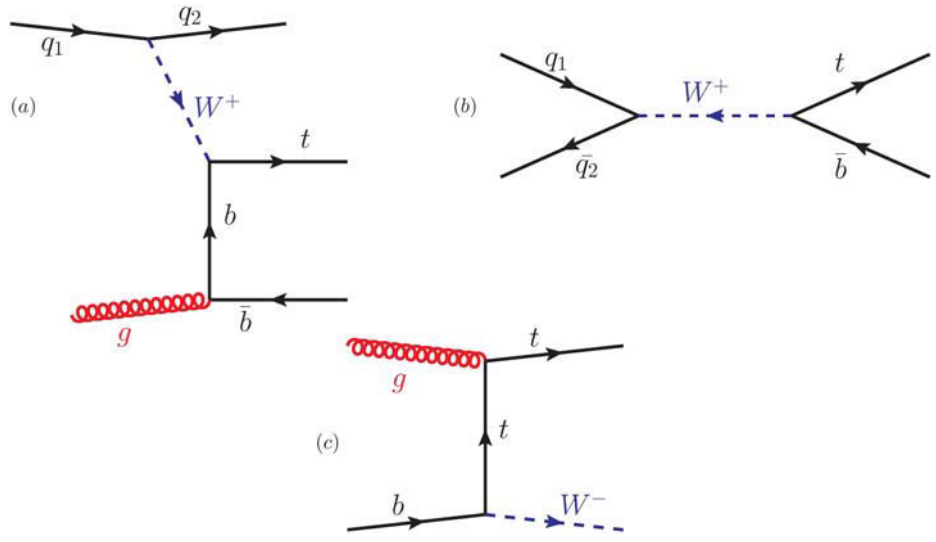

Figure 2.5: Single top quark production diagrams: (a) t-channel, (b) s-channel and (c) Wt production.

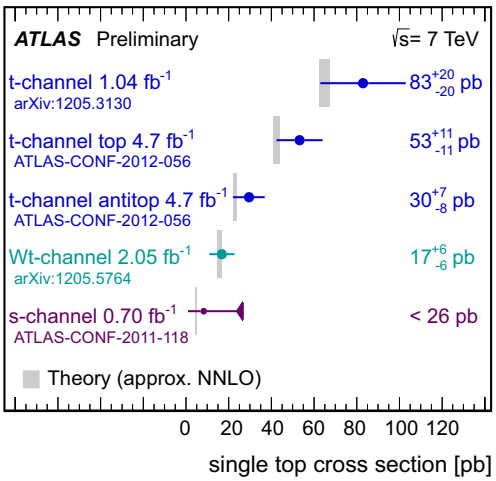

Figure 2.6: Illustration of all single top quark cross section results by the ATLAS collaboration, including combined statistical and systematic uncertainties (horizontal bars) [62]. All measurements agree with the theoretical prediction (vertical grey band).

2.3 Top quark decay

As mentioned at the beginning of the section, top quarks decay almost exclusively into a W boson and a b quark, which is predicted by the CKM matrix. Experimentally, this property is being measured via the branching ratio:

$$R_b = \frac{B(t \to Wb)}{B(t \to Wq)} = \frac{|V_{tb}|^2}{|V_{tb}|^2 + |V_{ts}|^2 + |V_{td}|^2} = |V_{tb}|^2 \approx 1$$

The latest result at the Tevatron has been published by CDF [63]:

$$R_b = 0.94 \pm 0.09(\text{stat.+syst.}) \qquad |V_{tb}| = 0.97 \pm 0.05(\text{stat.+syst.})$$

The first LHC measurement has been published by the CMS collaboration [64]:

$$R_b = 1.023^{+0.036}_{-0.034}(\text{stat.+syst.}) \qquad |V_{tb}| = 1.011^{+0.018}_{-0.017}(\text{stat.+syst.})$$

Both measurements agree with the Standard Model prediction, using the assumption that the CKM matrix is unitary.
The top quark decay width is given at next-to-leading order by [65, 66]:

$$\Gamma_{\text{top}} = \frac{G_F m_{\text{top}}^3}{8\pi\sqrt{2}} |V_{tb}|^2 \left(1 - \frac{m_W^2}{m_{\text{top}}^2}\right)^2 \left(1 + 2\frac{m_W^2}{m_{\text{top}}^2}\right) \left[1 - \frac{2\alpha_s}{3\pi}\left(\frac{2\pi^2}{3} - \frac{5}{2}\right)\right]$$

where terms of order m_b^2/m_{top}^2 and $(\alpha_s/\pi)m_W^2/m_{\text{top}}^2$ have been neglected. With the Fermi coupling constant G_F, a W boson mass of 80.399 GeV, the strong coupling constant $\alpha_s(m_Z) = 0.118$ and a top quark mass of 172.5 GeV, the predicted top quark decay width yields [67]

$$\Gamma_{\text{top}} = 1.33\,\text{GeV}.$$

This corresponds to a mean lifetime of

$$\tau_{\text{top}} = \frac{\hbar}{\Gamma_{\text{top}}} = 5 \cdot 10^{-25}\,\text{s}\,,$$

with the reduced Planck constant $\hbar$. Since the width is significantly larger than the strong hadronization scale of $\Lambda_{\text{QCD}} \approx 250\,\text{MeV/c}^2$, the top quark decays before hadronizing and therefore, the only bare quark to be observed. Official experimental results of the decay width and the mean lifetime have been published by the Tevatron experiments D0 and CDF, respectively [67, 68]:

$$\Gamma_{\text{top}} = (2.00^{+0.47}_{-0.43}(\text{stat. + syst.}))\,\text{GeV},\ \tau_{\text{top}} = (3.29^{+0.90}_{-0.63}(\text{stat. + syst.})) \cdot 10^{-25}\,\text{s}$$
$$\Gamma_{\text{top}} = (2.21^{+1.84}_{-1.11}(\text{stat. + syst.}))\,\text{GeV},\ \tau_{\text{top}} = (2.98^{+3.00}_{-1.35}(\text{stat. + syst.})) \cdot 10^{-25}\,\text{s}$$

Top quark pair events are classified by the decay of the W bosons. A W boson can either decay leptonically into a charged lepton and its corresponding neutrino, or hadronically into two light quarks:

$$W^- \to l^- \bar{\nu_l} \qquad W^- \to q_1 \bar{q_2}$$
$$W^+ \to l^+ \nu_l \qquad W^+ \to q_2 \bar{q_1}$$

The leptonic decay can occur with any of the three lepton flavors, i.e. $l = e, \mu, \tau$, while hadronically, the quark pair is formed by either the first or second quark family ($(q_1, q_2) = (u, d), (c, s)$). This quark pair is always color neutral and hence comprises the three color combinations $(R, \bar{R})$, $(G, \bar{G})$, $(B, \bar{B})$, resulting in six possible final states for the hadronic W boson decay. Each decay mode occurs with the same probability, neglecting any quark and lepton masses, and therefore 2/3 of all W bosons decay hadronically.
Three classes of top quark pair events can be defined:

- All hadronic final state ($t\bar{t} \to bW^+\bar{b}W^- \to bq_1\bar{q}_2\bar{b}q_3\bar{q}_4$): Both W bosons decay hadronically, resulting in a final state of six jets. Due to the lack of a charged lepton, these processes do not have a clear signature to be distinguished from the main background of QCD multijet events, which occur at hadron colliders. Hence, measurements in this channel are difficult to perform, although it has the highest production rate. First analyses were performed by the ATLAS collaboration, extracting all hadronic $t\bar{t}$ events with advanced kinematic methods to reconstruct the top quark mass [69, 70].

- Dileptonic final state ($t\bar{t} \to bW^+\bar{b}W^- \to bl_1^+\nu_{l_1}\bar{b}l_2^-\bar{\nu}_{l_2}$): Both W bosons decay leptonically, achieving the best signal-to-background ratio due to its clear signature with two charged leptons. Difficulties occur in analyses which rely on the kinematic reconstruction of $t\bar{t}$ events: The two neutrinos in the final state cannot be detected, but are reconstructed as a single physics object, the missing energy in the transverse plane of the detector. Hence, dileptonic $t\bar{t}$ events are kinematically underconstrained and can only be reconstructed using assumptions. Further, this channel has the lowest branching ratio, but the latest $t\bar{t}$ cross section results in Figure 2.4 show that analyses with dileptonic events are not statistically limited at the LHC anymore.

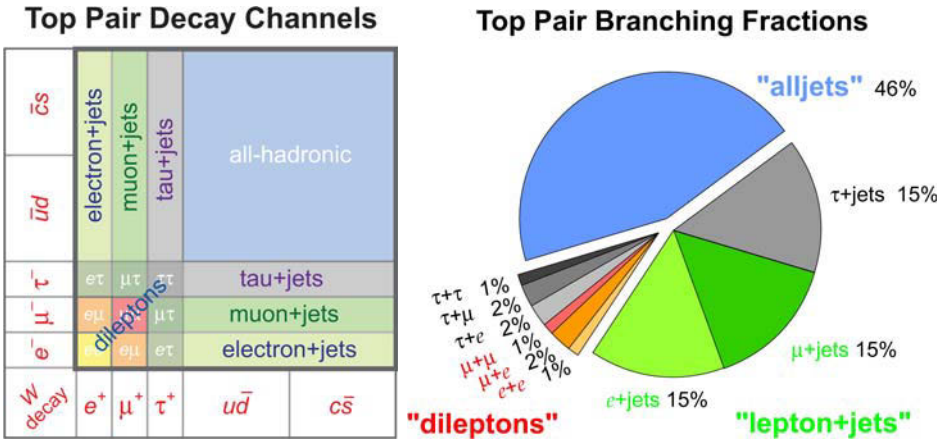

Figure 2.7: Illustration of the top quark pair decay channels (left) and a pie chart representing the top quark decay branching fractions. The $t\bar{t}$ decay is categorized by the decay particles of the W boson, defining three classes: all hadronic ("alljets"), semileptonic ("lepton+jets") and dileptonic ("dileptons ") [71].

- Semileptonic final state ($t\bar{t} \to bW^+\bar{b}W^- \to bq_1\bar{q}_2\bar{b}l^-\bar{\nu}_l$ or $bl^+\nu_l\bar{b}q_1\bar{q}_2$): One W boson decays hadronically and the other one leptonically. This event class is also referred as the "golden channel", as it has a high production rate and a rather clear signature with one high-energetic lepton, which provides a good handle on combinatorial and QCD multijet background. Therefore, most top quark analyses have focused on this decay type. A diagram of a semileptonic $t\bar{t}$ event is shown in Figure 2.8.

The top quark pair branching fractions for all decay modes are shown in Figure 2.7. Experimentally, leptonically decaying W bosons can only be identified if the charged lepton is an electron or muon. Hence, event selections of the semileptonic (and also dileptonic) final state are exclusively optimized for these two leptons, separating the analyses into a single electron and single muon channel, depending on the lepton flavor in the final state. Tau leptons have a special status as they decay further due to their high mass, either leptonically ($\tau \to e\bar{\nu}_e\nu_\tau$ or $\tau \to \mu\bar{\nu}_\mu\nu_\tau$) or into hadrons. Since these leptons from the τ decays are not distiguishable from electrons or muons, which directly decay from a W boson, the leptonic τ decays are included in the electron and the muon channel, respectively. Hadronically decaying τ leptons, which have a branching fraction of 65%, are considered jets in standard top quark analyses, but individual $t\bar{t}$ cross section measurements at the Tevatron and the LHC have focussed on decay channels which include such hadronic τ's [72, 73]: The τ lepton decays preferentially into multiple neutral decay products and one or three charged particles. Hence, the number of tracks provides good separation between signal and background, especially from QCD multijets events, which are dominated by gluon-initiated jets that have a higher track multiplicity than the quark-initiated jets.

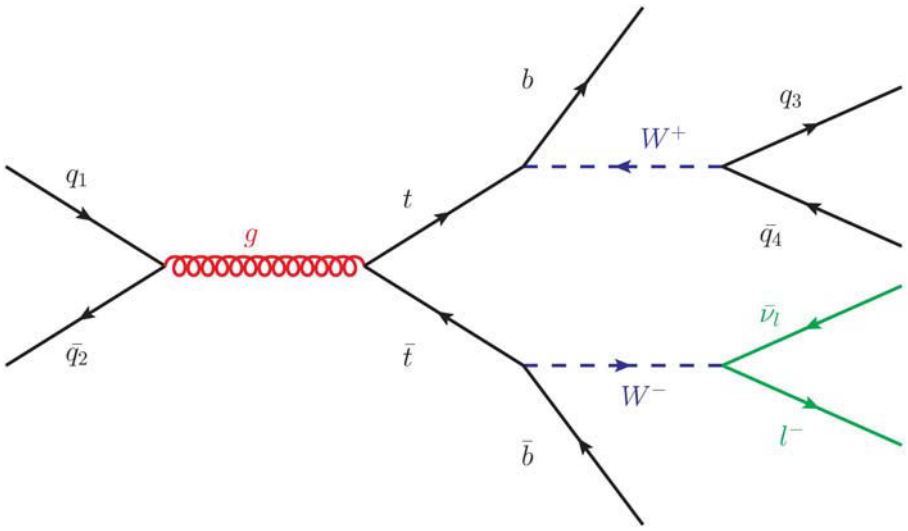

Figure 2.8: Exemplary diagram of a semileptonic $t\bar{t}$ pair event. In this case, the top quark pair is produced via quark-antiquark annihilation, while the W^- boson decays leptonically and the W^+ hadronically.

2.4 Background processes for top quark pair events

The main challenge faced in measurements of specific physics processes are background contributions from processes with the same final state (irreducible background) or processes passing the event selection due to misreconstructed or misidentified objects in the final state (reducible background).
The largest background contribution to semileptonic $t\bar{t}$ events originates from W boson events with additional jets, in which the vector boson decays leptonically. The production rate of W events is around three magnitudes higher than the top quark production rate, as shown in Figure 2.9, but its contribution can be largely reduced when requiring at least four jets. W+jets events are part of the irreducible background, as four jets can emerge from QCD corrections and gluon splitting into a quark-antiquark pair like $b\bar{b}$.
The production of a Z boson with additional jets also add to the $t\bar{t}$ background, when the Z boson decays into two charged leptons ($Z \to l^-l^+$ with $l = e, \mu, \tau$). While its production rate is only slightly lower than the one of the W boson, its contribution can be further reduced by requiring at least four jets and exactly one isolated charged lepton. In this case, one charged lepton has to be misreconstructed, fail the identification criteria or has been produced outside of the detector acceptance. Exemplary diagrams of the W/Z+jets production processes are illustrated in Figure 2.10.
Small contributions are expected from single top or diboson production. Single top quark events can achieve the same final state as $t\bar{t}$ events, when additional jets are produced from QCD corrections. Diboson processes include the production of a WW, WZ and ZZ pair and are part of the irreducible background, when a W boson decays leptonically and the second boson, either a W or Z boson, decays into two quarks. In case of a ZZ event, one boson has to decay leptonically with one charged lepton, which is not reconstructed

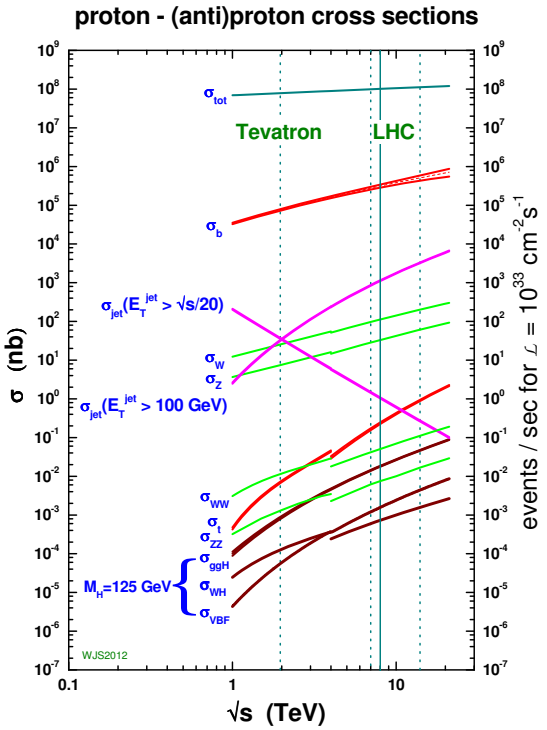

Figure 2.9: QCD predictions for hard scattering cross sections as a function of the center-of-mass energy $\sqrt{s}$. The $t\bar{t}$ production cross section is marked as σ_t. The steps in the curves at $\sqrt{s} = 4\,\text{TeV}$ mark the transition from $p\bar{p}$ scattering to pp scattering. The Tevatron center-of-mass energy of 1.96 TeV is indicated by the first vertical line from left. Further, the LHC energy of 7 TeV (2010-2011), 8 TeV (2012) and 14 TeV (design) are marked [74].

or identified as a lepton. Exemplary diagrams for the diboson production are shown in Figure 2.11.

QCD multijet events do not feature a prompt lepton, but hadrons from jet fragmentation can be misidentified as electrons, and heavy hadrons can decay into electrons or muons within jets ($(b, c) \to l\nu_l X$). This misidentification rate is very small and the number of QCD multijet events can be further suppressed by increasing the lower threshold for the missing transverse energy, but due to the large cross section for QCD multijet events at hadron colliders, the background contribution is non-negligible.

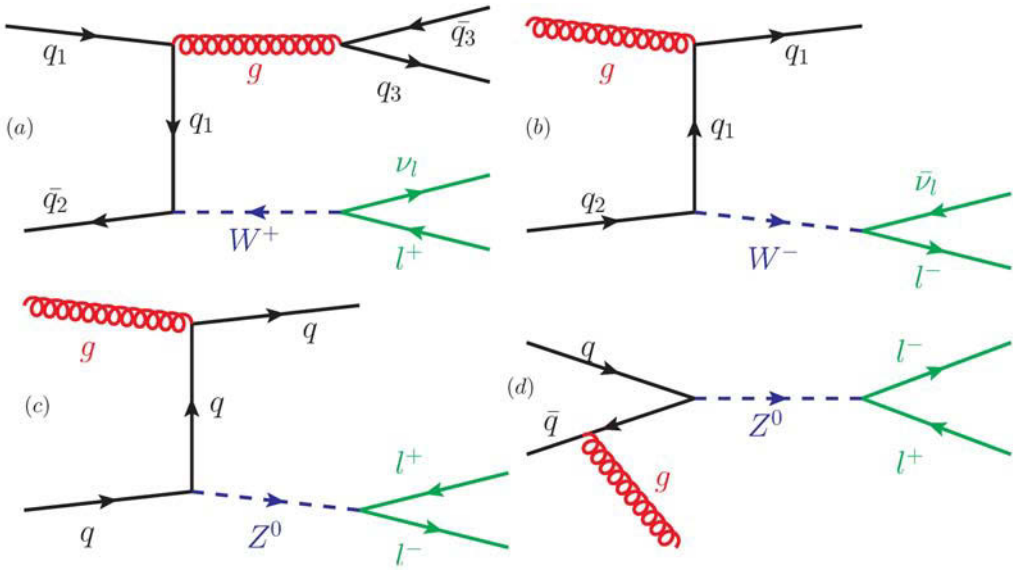

Figure 2.10: Exemplary diagrams for W+jets (a), (b) and Z+jets production processes (c), (d). Events are only considered as background, if the boson decays leptonically. Additional jets can emerge from QCD corrections, like the gluon emitted from the incoming quark in (d), and from gluon splitting into a quark-antiquark pair as indicated in (a).

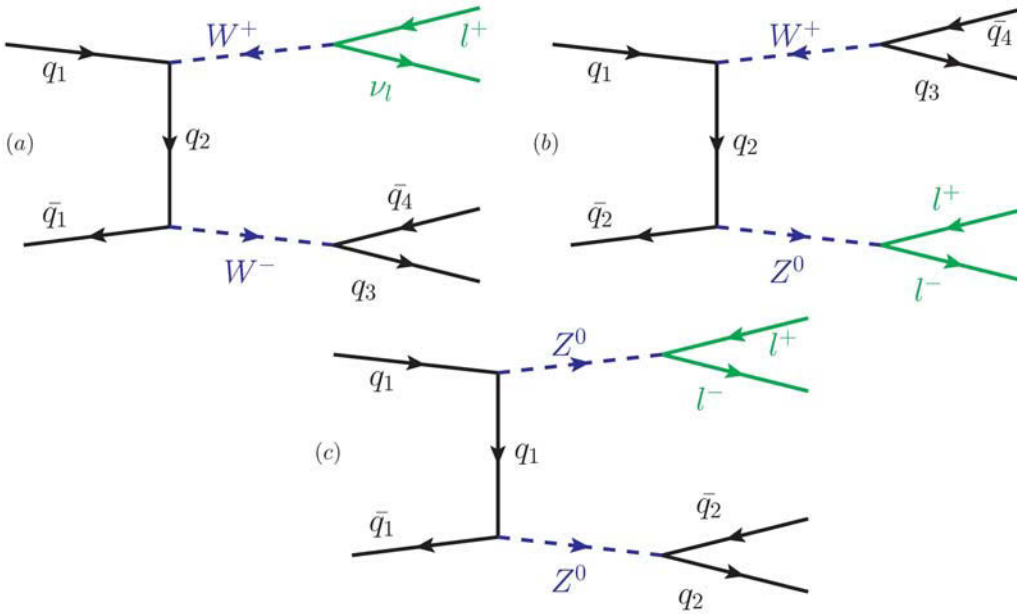

Figure 2.11: Exemplary diagrams for WW (a), WZ (b) and ZZ production (c). Additional jets can emerge from QCD corrections.

2.5 Top quark properties

2.5.1 Mass

A significant difference between the top quark and the other partons of the Standard Model is its enormous mass. Therefore, the top quark mass has become the most precise measured property of any quark with a relative uncertainty of only 0.5% by combining the measurements of the Tevatron experiments D0 and CDF [75]. ATLAS and CMS have also performed various measurements and published a first combined LHC result [76]:

$$m_{\text{top}} = (173.2 \pm 0.6(\text{stat.}) \pm 0.8(\text{syst.}))\,\text{GeV} \qquad \text{Tevatron}$$
$$m_{\text{top}} = (173.3 \pm 0.5(\text{stat.}) \pm 1.3(\text{syst.}))\,\text{GeV} \qquad \text{LHC}$$

The LHC results matches the Tevatron measurements in statistics, but the precision suffers due to higher systematic uncertainties, which are dominated by uncertainites of jet calibration and signal modelling. The individual results used in both combinations are shown in Figure 2.12.

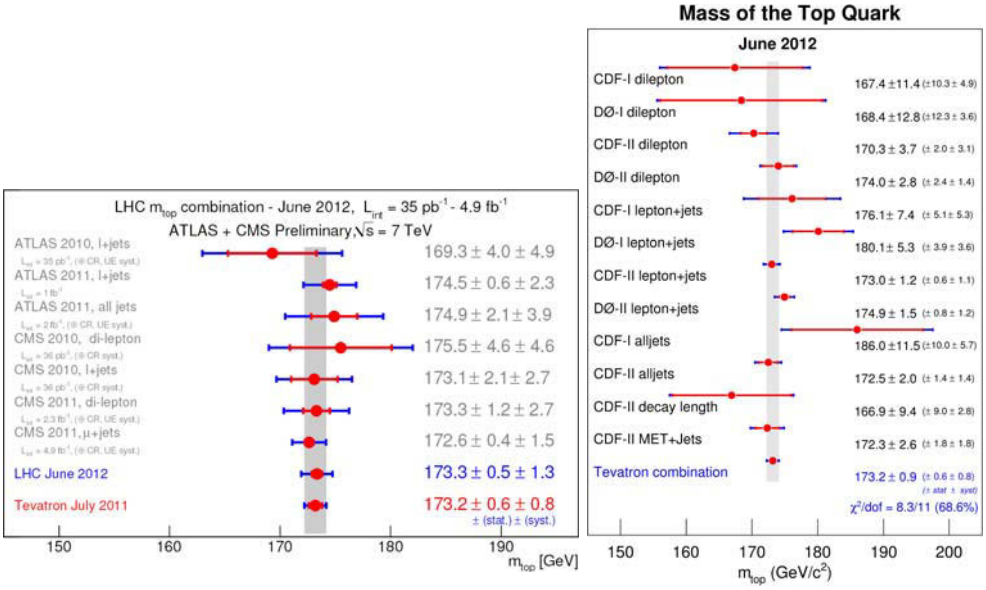

Figure 2.12: Results of top quark mass measurements by the ATLAS and CMS experiments, used for the first LHC combined result (left), as well as the combined Tevatron result including all individual measurements from D0 and CDF (right). Both plots include statistical (red bars), systematic uncertainties (blue bars) and the combined result from the Tevatron experiments (vertical grey band) [75, 76].

2.5.2 Electric charge

According to the Standard Model, the top quark is expected to have an electric charge of $+\frac{2}{3}$e. An alternative option would be an electric charge of $-\frac{4}{3}$e, if the discovered top quark is an exotic quark rather than the isospin partner of the b quark. Since the correlations

of the b quarks and the W bosons in a $t\bar{t}$ event are unknown, it is conceivable that the observed particle actually decays into a W^- boson and a b quark ($\tilde{t} \to W^- b$). Indirect measurements of the electric charge of the top quark were performed by the determination the electric charge of the W boson and the b-jet. The leptonic branch of semileptonic $t\bar{t}$ events were analyzed by measuring the electric charge of the W boson via the charged lepton and the b-jet using two different techniques. In the first method, the electric charge is determined by the sum of all parton charges within the b-jet. The second method uses semileptonic B hadron decays ($B \to c, u + W^- \; rightarrowc, u + l^- \bar{\nu}_l$) to determine the sign of the b quark electric charge. Results from CDF have excluded the exotic model with 99% confidence [77], while it was completely ruled out by the ATLAS collaboration with a significance above 5σ [78].

2.5.3 Polarization of the W boson in top quark decay

The top quark decays via the $V-A$ weak charged-current interaction with the Wtb coupling defined by $\left(-i\frac{g}{\sqrt{2}}V_{tb}\gamma^\mu\frac{1}{2}(1-\gamma_5)\right)$. Due to the $V-A$ structure and the significantly higher masses of the top quark and the W boson, the b quark is almost exclusively left-handed. This limits the W boson to be left-handed or longitudinally polarized, since the angular momentum along the decay axis has to be conserved. The fractions of events containing W bosons with longitudinal, left-handed and right-handed polarization are predicted by next-to-next-to-leading order pQCD calculations to be [79]

$$F_0 = 0.687 \pm 0.005 \qquad F_L = 0.311 \pm 0.005 \qquad F_R = 0.0017 \pm 0.0001\,,$$

assuming a top quark mass of $172.8 \pm 1.3\,\text{GeV}$.
Experimentally, the polarization fractions are obtained from $\cos\Theta^*$ distributions. For leptonically decaying top quarks, Θ^* is defined as the angle between the direction of the charged lepton and the reversed direction of the top quark, both in the rest frame of the W boson. The differential decay rate for top quarks is then given by

$$\frac{1}{\Gamma}\frac{\mathrm{d}\Gamma}{\mathrm{d}\cos\Theta^*} = \frac{3}{8}\left(1+\cos\Theta^*\right)^2 F_R + \frac{3}{8}\left(1-\cos\Theta^*\right)^2 F_L + \frac{3}{4}\left(1-\cos^2\Theta^*\right) F_0\,.$$

The two Tevatron experiments as well as the two LHC collaborations, ATLAS and CMS, each released combined results [80, 81], which are both consistent with the Standard Model prediction, as displayed in Figure 2.13.

2.5.4 Spin correlations in $t\bar{t}$ production

According to the Standard Model, the top quark retains its spin polarization from production till the decay, transferring this information to its decay particles. Hence, the spin information can be measured via angular distributions

$$\frac{1}{N}\frac{\mathrm{d}N}{\mathrm{d}\cos\Theta_i} = \frac{1}{2}[1+\alpha_i\cos\Theta_i]\,,$$

with the angle Θ_i between the direction of decay particle i in the top quark rest frame and the spin quantization direction. The coefficient α_i is the spin analyzing power of particle i.

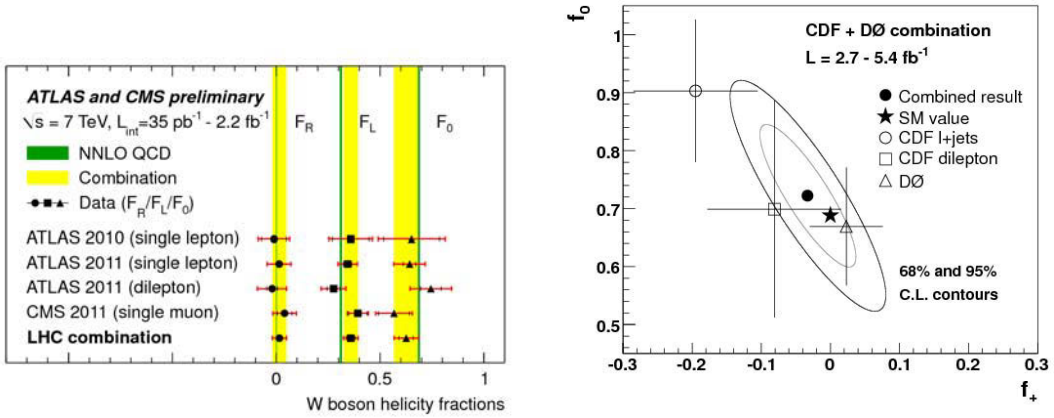

Figure 2.13: Combined results of the W boson polarization fractions in top quark decays by the ATLAS and CMS collaboration (left) as well as the D0 and CDF experiment (right). The left figure is an overview of the four individual measurements as well as the combined result of the two LHC experiments, illustrated by black points and red error bars corresponding to the total uncertainties. The green vertical line indicates the predictions from next-to-next-to-leading order calculations [80]. The right plot is a two-dimensinal presentation of the Tevatron results with the polarization fraction $f_0 = F_0$ on the y-axis and $f_+ = F_R$ on the x-axis. The combined result is marked by a black point, enclosed by two ellipses, indicating the 1σ and 2σ uncertainties. A black star marks the Standard Model prediction [81].

Even though the b quark and W boson are direct decay particles, their analyzing quality is quite low due to the W boson polarization. Charged leptons and down-type quarks are the most effective spin analyzer with an α_i of 1 at leading order.
The top quark polarization is almost negligible in $t\bar{t}$ production process at hadron colliders, but a strong correlation of the two top quark spins is expected according to the Standard Model. This correlation is quantified by the coefficient A, which is defined as the fractional difference in the number of events where the top and antitop quark spins are aligned and those where the top quark spins have opposite alignment:

$$A = \frac{[N(\uparrow\uparrow) + N(\downarrow\downarrow)] - [N(\uparrow\downarrow) + N(\downarrow\uparrow)]}{[N(\uparrow\uparrow) + N(\downarrow\downarrow)] + [N(\uparrow\downarrow) + N(\downarrow\uparrow)]},$$

with the arrows denoting the spins of the top and antitop quarks with respect to a quantization axis. This axis is choosen according to the expected spin correlation. For energies close to the production threshold, the two top quarks produced by gluon fusion tend to have have antiparallel spins (same helicities) while top quarks from quark-antiquark annihilation tend to have parallel spins (opposite helicities). At energies, which are large compared to the top quark mass, opposite spin states dominate for both production mechanisms. At the Tevatron, where the $t\bar{t}$ production is dominated by $q\bar{q}$ annihilation, the beam axis is preferred as quantization axis, yielding a correlation of $A = 0.777^{+0.027}_{-0.042}$ at next-to-leading order [82]. No ideal axis exists for the LHC measurements, the best results

are expected using the direction of the outgoing top quark as quantization axis.
Measurements have been performed at the Tevatron and LHC, all agreeing with the Standard Model [83, 84, 85], with the ATLAS collaboration excluding the zero spin correlation hypothesis with a significance of $5.1\,\sigma$ [86].

2.5.5 Asymmetry in $t\bar{t}$ production

According to higher order calculations in the Standard Model, a significant asymmetry is expected in differential $t\bar{t}$ cross sections. This is caused by interference due to QCD corrections from real or virtual gluon emission. The dominant contribution originates from interference between the leading order diagram for $t\bar{t}$ pairs produced via quark-antiquark annihilation and the corresponding one-loop correction diagrams. Furthermore, interferences between initial state and final state gluon radiation have to be taken into account. No asymmetry arises from gluon fusion at any order.
At the Tevatron, the $t\bar{t}$ production is dominated by quark-antiquark annihilation, i.e. the interaction of a valence quark and a valence antiquark. Hence, the (anti)quark direction can be assumed to coincide with the direction of the incoming (anti)proton, and similarly, the (anti)top quark direction coincide with the incoming (anti)quark direction. A forward backward asymmetry is expected, which can be determined experimentally via the coefficient

$$A_{\mathrm{fb}} = \frac{N(\Delta y > 0) - N(\Delta y < 0)}{N(\Delta y > 0) + N(\Delta y < 0)}\,.$$

Δy is defined as the rapidity difference between the top quark and antitop quark:

$$\Delta y = y_{\mathrm{top}} - y_{\mathrm{antitop}}\,.$$

At the LHC, the top quark pair production is dominated by gluon fusion, which does not contribute to the asymmetry. Further, the directions of the incoming quarks are unknown in proton-proton collisions. However, the incoming quarks are supposed to be mainly valence quarks, while the antiquarks have to be sea quarks, which leads to an excess of top quarks produced in the forward directions of the ATLAS detector. The rapidity distribution of top quarks is therefore broader than the of the more centrally produced top antiquarks, which can be quantified by the charge asymmetry coefficient

$$A_{\mathrm{c}} = \frac{N(\Delta|y| > 0) - N(\Delta|y| < 0)}{N(\Delta|y| > 0) + N(\Delta|y| < 0)}\,.$$

Measurements of the forward backward asymmetry at the Tevatron have resulted in coefficient values, which are more than two standard deviations larger than the next-to-leading order prediction [87, 88]. Two resulting distributions of the CDF measurement are shown in Figure 2.14. First measurements of the charge asymmetry at the LHC are consistent with the Standard Model prediction, but the level of precision is not yet sufficient to explore possible models beyond the Standard Model [89, 90, 91, 92].

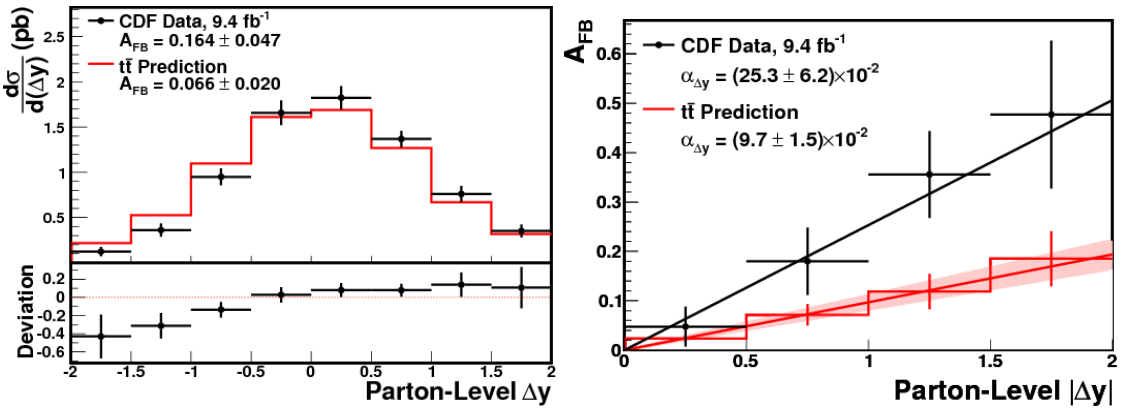

Figure 2.14: Top quark pair forward backward asymmetry results by the CDF collaboration. The left plot shows the differential cross section $d\sigma/d(\Delta y)$ as measured in the data after correction to the parton level compared to the Standard Model prediction. Uncertainties include both statistical and systematic contributions. The data distribution (black) shows a shift towards positive Δy values compared to to the expected distribution (red), resulting in a higher A_{fb} value, which is quoted in the upper left corner. The right plot shows in black the measured forward backward asymmetry coefficient as a function of $|\Delta y|$ with a best-fit line superimposed. Uncertainties are correlated and include both statistical and systematic contributions. The Standard Model expectation is illustrated in red with the shaded region representing the theoretical uncertainty on the slope of the prediction. The data function shows a significantly higher slope than the predicted function, with both values quoted in the upper left corner. A similar behavior has been measured for the dependence of the forward backward coefficient on the invariant mass of the top quark pair [87].

2.6 Top quark pair events associated with an additional photon

The measurement of the top quark coupling to neutral gauge bosons plays an essential role in validity tests of the Standard Model and the possible discovery of new physics. Electroweak couplings of Z bosons and photons to fermions are characterized by the $V-A$ structure, i.e. $\propto \gamma^{\mu}(c_V - c_A\gamma^5)$. The general vertex function describing the interaction of a neutral vector boson V with a top quark pair can be written as [93]

$$\Gamma_{\mu}^{t\bar{t}V}(k^2, q, \bar{q}) = -ie\left\{\gamma_{\mu}\left[F_{1V}^{V}(k^2) + \gamma_5 F_{1A}^{V}(k^2)\right] + \frac{\sigma_{\mu\nu}}{2m_t}(q+\bar{q})^{\nu}\left[iF_{2V}^{V}(k^2) + \gamma_5 F_{2A}^{V}(k^2)\right]\right\},$$

with the elementary charge e, the top quark mass m_t, the outgoing top (antitop) quark four-momentum $q\,(\bar{q})$ and $k^2 = (q+\bar{q})^2$. The vertex includes the terms $F_{1V}^{V}(k^2)$ and $F_{1A}^{V}(k^2)$ with their lower limits at $k^2 = 0$ corresponding to the $t\bar{t}V$ vector and axial vector form factors. Further, possible tensorial coupling terms are considered, which in case of a coupling photon, are related to the magnetic and electric dipole form factors, g_t and d_t^Y

respectively:

$$F_{2V}^{\gamma}(k^2 = 0) = Q_t \frac{g_t - 2}{2}\,, \qquad F_{2A}^{\gamma} = \frac{2m_t}{e} d_t^{\gamma}\,,$$

with the top quark electric charge $Q_t = \frac{2}{3}$. According to the Standard Model at leading order level, no dipole moments exist, i.e. $F_{2V}^{V,\mathrm{SM}} = F_{2A}^{V,\mathrm{SM}} = 0$. The vector and axialvector component of the top quark coupling with a Z boson is described in terms of the Weinberg angle Θ_W, while the coupling to a photon is competely vectorial and depends exclusively on the electric charge of the top quark:

$$F_{1V}^{\gamma,\mathrm{SM}} = -Q_t \qquad\qquad F_{1A}^{\gamma,\mathrm{SM}} = 0$$

$$F_{1V}^{Z,\mathrm{SM}} = -\frac{1}{4\sin\theta_w\cos\theta_w}\left(1 - \frac{8}{3}\sin^2\theta_w\right)\,, \qquad F_{1A}^{Z,\mathrm{SM}} = \frac{1}{4\sin\theta_w\cos\theta_w}\,.$$

At the one-loop level, $F_{2A}^{V,\mathrm{SM}}$ remains zero, while corrections are added to the other coupling components in the order of 10^{-3} to 10^{-2}. Deviations from this prediction would indicate the presence of new physics beyond the Standard Model.

Therefore, the top quark coupling to a photon provides the opportunity to directly measure the electromagnetic charge of the top quark. First theoretical studies have focussed on the discrimination between the Standard Model prediction of $\frac{2}{3}$e and an exotic quark model with an electric charge of $-\frac{4}{3}$e, predicting a precision of 10% with $10\,\mathrm{fb}^{-1}$ of data and a center-of-mass energy of $\sqrt{s} = 14\,\mathrm{TeV}$ [94, 95]. This approach is therefore statistically far more challenging than the indirect measurement via the electric charge of b-jets, and can only be seen as a less attractive alternative measurement, since the exotic top quark model has been already ruled out by the ATLAS collaboration [78].

Experimentally, new physics would manifest in deviations from the predicted cross section or modified kinematic distributions. A first step towards these decisive measurements of the top quark couplings is the observation of the top quark pair process associated with an additional Z boson ($t\bar{t}Z$) or a photon ($t\bar{t}\gamma$) and the experimental determination of their cross sections. A first evidence of the $t\bar{t}Z$ process has been published by the CMS collaboration with a significance of $3.7\,\sigma$ [96]. The measured inclusive cross section of $\sigma_{t\bar{t}Z} = 0.30^{+0.14}_{-0.11}(\mathrm{stat.})^{+0.04}_{-0.02}(\mathrm{syst.})\,\mathrm{pb}$ is larger, but still compatible with the next-to-leading order prediction of 0.1387 pb [97]. The CDF experiment has presented the first evidence of the $t\bar{t}\gamma$ process with a significance of $3.0\,\sigma$ [98]. The cross section ratio of the $t\bar{t}\gamma$ process to the $t\bar{t}$ processs was measured with a required photon transverse momentum above 10 GeV, resulting in a ratio $R = 0.024 \pm 0.009$, which was in perfect agreement with the theoretical prediction of $R = 0.024 \pm 0.005$.

Photons can be emitted from any electrically charged particle in a top quark pair event. Experimentally, it is impossible to determine the origin of the photon and also theoretically, the separation of individual subprocesses is not well-defined, since interference terms between different diagrams occur with non-negligible contributions to the matrix element calculation. Top quark pair processes can be separated into the top quark production and the top quark decay processes via the narrow width approximation. Due to the top decay width, which is much smaller compared to its mass, it can be assumed that the two

top quarks are produced as stable particles, which then decay via weak interaction into b quarks and W bosons. In the matrix element calculation, the Breit-Wigner function within the top quark propagator is reduced to a δ-function, resulting in a factorization of the total cross section into the $t\bar{t}$ production cross section times the branching ratios of the top quarks. With this approximation, $t\bar{t}\gamma$ processes can be divided into:

the radiative top production	$gg \to t\bar{t}\gamma$, $q\bar{q} \to t\bar{t}\gamma$,
the radiative top decay	$t \to bl^+\nu_l\gamma$, $t \to bq_1\bar{q}_2\gamma$.

Figures 2.15 and 2.16 illustrate these two process types including all possibilities of photon radiation within a $t\bar{t}$ event. Since the measurement of the $t\bar{t}\gamma$ cross section has to rely on the most accurate simulation of $t\bar{t}\gamma$ events, the complete 7-particle final state has to be taken into account for the matrix element calculation:

dileptonic $t\bar{t}\gamma$ processes:	$pp \to bl_1^+\nu_{l_1}\bar{b}l_2^-\bar{\nu}_{l_2}\gamma$,
semileptonic $t\bar{t}\gamma$ processes:	$pp \to bq_1\bar{q}_2\bar{b}l^-\bar{\nu}_l\gamma$, $pp \to bl^+\nu_l\bar{b}q_1\bar{q}_2\gamma$.

All possible diagrams have to be considered, which are characterized by two incoming gluons or a quark-antiquark pair, as well as the final state signature of a semileptonic or dileptonic $t\bar{t}$ event with an additional photon. Hence, the measurement of the $t\bar{t}\gamma$ cross section does not only include events with photons coupling to a top quark, but also to all other fermions and the W bosons in top quark pair processes.

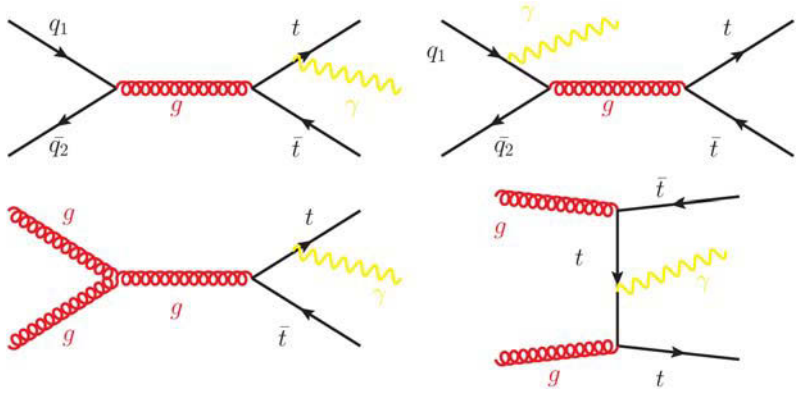

Figure 2.15: Feynman diagrams representing radiative top quark pair production processes. In quark-antiquark annihilation processes, the photon can either be radiated from one of the top quarks (upper left) or one of the incoming quarks (upper right). In gluon fusion events, the photon is emitted by one of the outgoing top quarks (lower left) or by the virtual top quark, which is exchanged between the two incoming gluons (lower right).

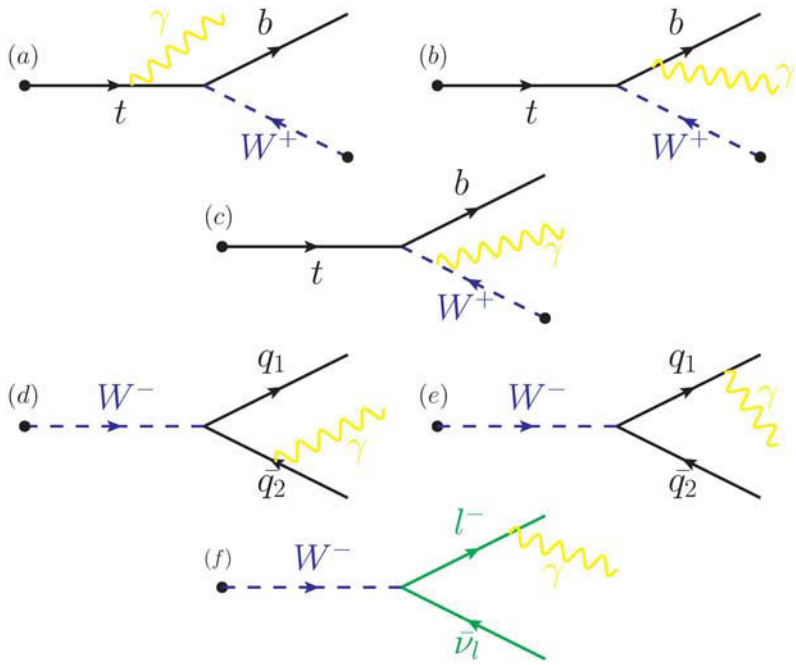

Figure 2.16: Diagrams representing the radiative top quark pair decay. A photon can be emitted from (a) an on-shell top quark or one of its decay particles, (b) the b-quark or (c) the W boson. Further, the daughter particles of the W boson can also be sources for photon radiation: (d,e) Either one of the quarks in a hadronic W decay or (f) the charged lepton from a leptonically decayed W boson.

Chapter 3

The Large Hadron Collider and the ATLAS experiment

3.1 The Large Hadron Collider

The Large Hadron Collider (LHC) [99] is the largest and most powerful particle accelerator worldwide. It is situated close to Geneva on the border between France and Switzerland, at the European Organisation for Nuclear Research CERN. It is built at a depth between 50 m and 175 m inside a 26.7 km long ring tunnel. The LHC uses the infrastructure of its predecessors LEP1 and LEP2, e^+e^--colliders which were operational from 1989 to 2000. Protons are produced from hydrogen atoms, which are stripped off their electrons by a magnetic field. These protons are clustered to bunches and sent through a series of pre-accelerators [100], as illustrated in Figure 3.1. After the bunches are accelerated up to a kinetic energy of 50 MeV in the LINAC (LINear particle ACcelerator), the protons are accelerated up to 1.4 GeV in the Proton Synchrotron Booster (PSB), and then enter the Proton Synchrotron (PS). This is a storage ring with a circumference of 630 m, where the proton energy is increased up to 26 GeV. In the last step of pre-acceleration, the protons are accelerated up to 450 GeV in the Super Proton Synchrotron (SPS), a 6.9 km ring, before entering the two separate beam pipes of the Large Hadron Collider. In the LHC ring, two cavity modules per beam with a super-conducting radio-frequency of 400.8 MHz ensure the final collision energy. Superconducting dipole magnets with a field of up to 8.3 T keep the protons alligned in the two rings. When reaching its nominal operation mode, the LHC will store protons with an energy of 7 TeV per proton and an instantaneous luminosity of $10^{34}\mathrm{cm}^{-2}\mathrm{s}^{-1}$. A total of 2835 bunches, each consisting of 10^{11} protons, with a 25 ns bunch spacing will collide at one of the four interaction points, where the four detectors are located, as shown in Figure 3.2 ATLAS, CMS, LHCb and ALICE. ATLAS (A Toroidal LHC AparatuS) [101] and CMS (Compact Muon Solenoid) [102] are general purpose detectors, designed to cover a broad variety of Standard Model and new physics measurements. The other two experiments focus on specialized physics tasks. LHCb [103] concentrates on b-hadrons in order to investigate charge-parity violation, while ALICE (A Large Ion Collider Experiment) [104] is designed for the investigation of quark-gluon plasma in heavy ion collisions.

The first proton beams were circulated in the LHC ring on September 10th, 2008, but only nine days later, a faulty connection between a dipole and a quadrupole magnet caused a magnet quench in around 100 bending magnets, releasing tons of liquid helium into the tunnel. The escaping vapor expanded explosively and damaged multiple superconducting magnets and their mountings, the vacuum pipe was also contaminated. Repairs and

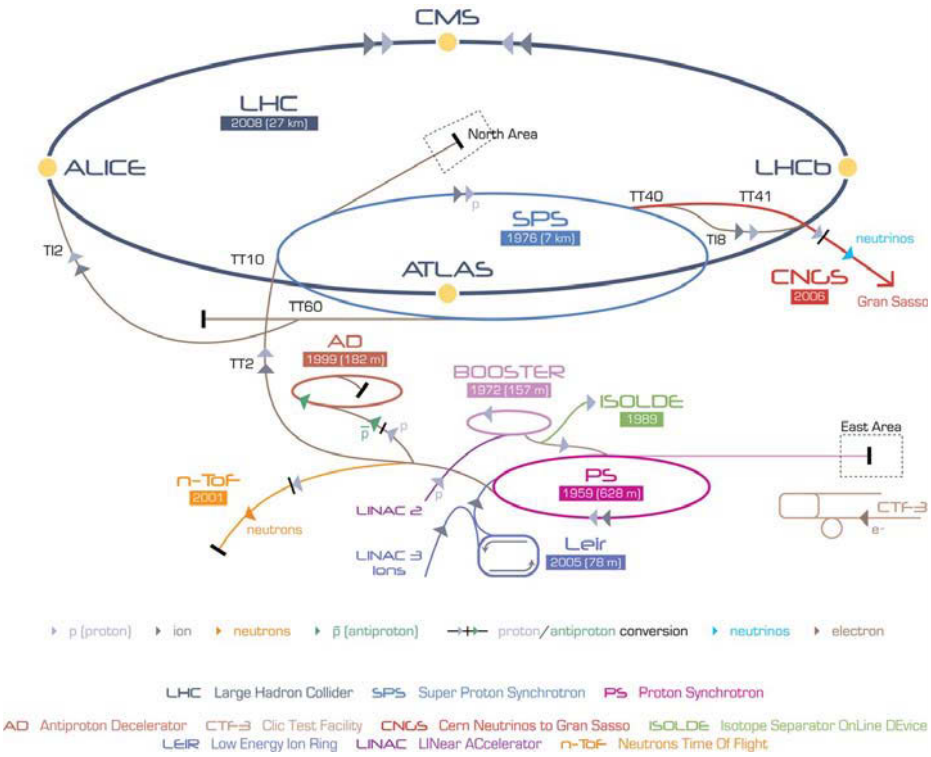

Figure 3.1: Schematic view of the CERN accelerator. Protons are accelerated from the LINAC via the PS and SPS to the LHC, where they are brought to collison at one of the four interaction points, where the four LHC experiments are located. The pre-accelerators also provide protons to other facilities like ISOLDE and CNGS [105].

reviews from the incident took more than a year, till the first proton-proton collisions at the interaction energy of $\sqrt{s} = 900\,\text{GeV}$ took place on November 23rd, 2009. Already on November 30th, 2009, the LHC beat the Tevatron as the highest-energy particle accelerator in the world, when the two beams collided with a center-of-mass energy of $\sqrt{s} = 2.36\,\text{TeV}$. It was decided that the energy could be increased up to $\sqrt{s} = 7\,\text{TeV}$, to minimize the risk of any further incidents and damages with the current accelerator setup. This benchmark was reached on March 30th, 2010, with one colliding bunch per beam, indicating the start of extremely successful periods of data taking over the following two years at this center-of-mass energy. During multiple commissioning phases, beam parameters were varied to continuously increase the instantaneous luminosity delivered by the LHC. For example, the number of bunches was increased steadily up to 368 until November of 2010. The year ended with a four week period of heavy ion collision before the winter shutdown. In total, an integrated luminosity of $48\,\text{pb}^{-1}$ was delivered at the interaction point of the ATLAS experiment in 2010. Operations resumed in March 2011, reaching new peak luminosities in the following months and an integrated luminosity of $5.61\,\text{fb}^{-1}$ of data to the ATLAS experiment until November 2011, when another heavy ion collision period of four weeks ended 2011. In 2012, the center-of-mass energy was increased to $\sqrt{s} = 8\,\text{TeV}$, delivering $23.3\,\text{fb}^{-1}$ of data at the ATLAS interaction point from March to December of

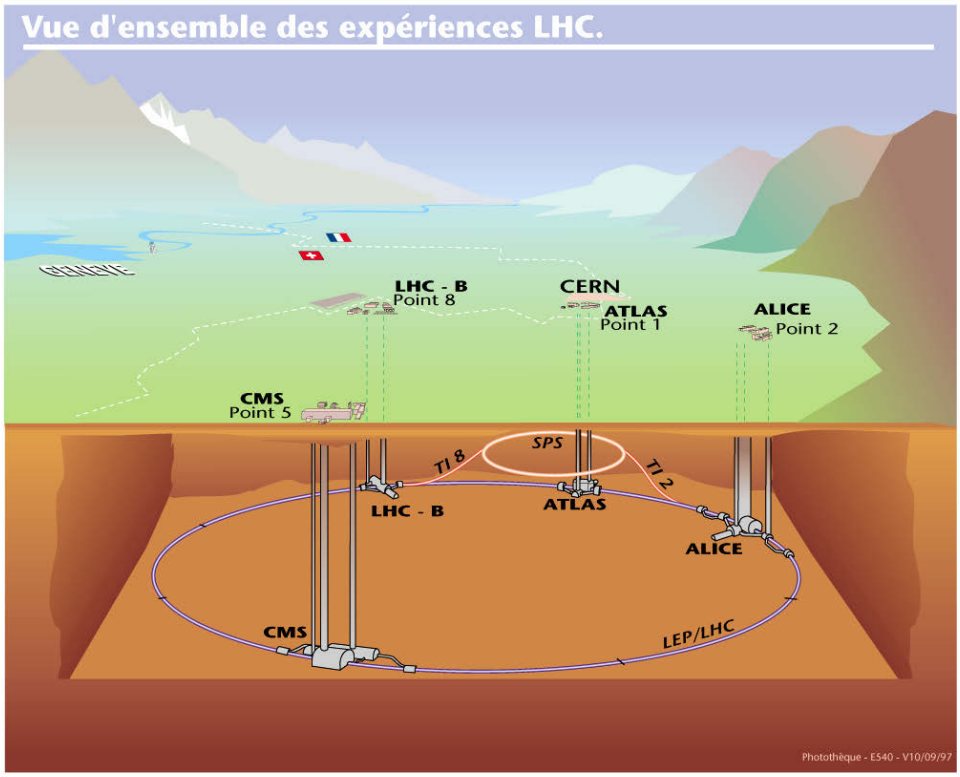

Figure 3.2: Overall view of the LHC and the locations of the four experiments [106].

that year. The LHC ran proton-lead ion collisions till February 2013 and then went into a long shutdown for repairs of the magnet interconnections and detector upgrades to allow operations the LHC at its design center-of-mass energy of $\sqrt{s} = 14\,\text{TeV}$. Current plans aim for the next physics run to start in early 2015. Figure 3.3 shows the the cumulative integrated luminosity and maximum instantaneous luminosity during the first three years of high energy pp-collisions with a center-of-mass energy of $\sqrt{s} = 7\,\text{TeV}$ and $\sqrt{s} = 8\,\text{TeV}$.

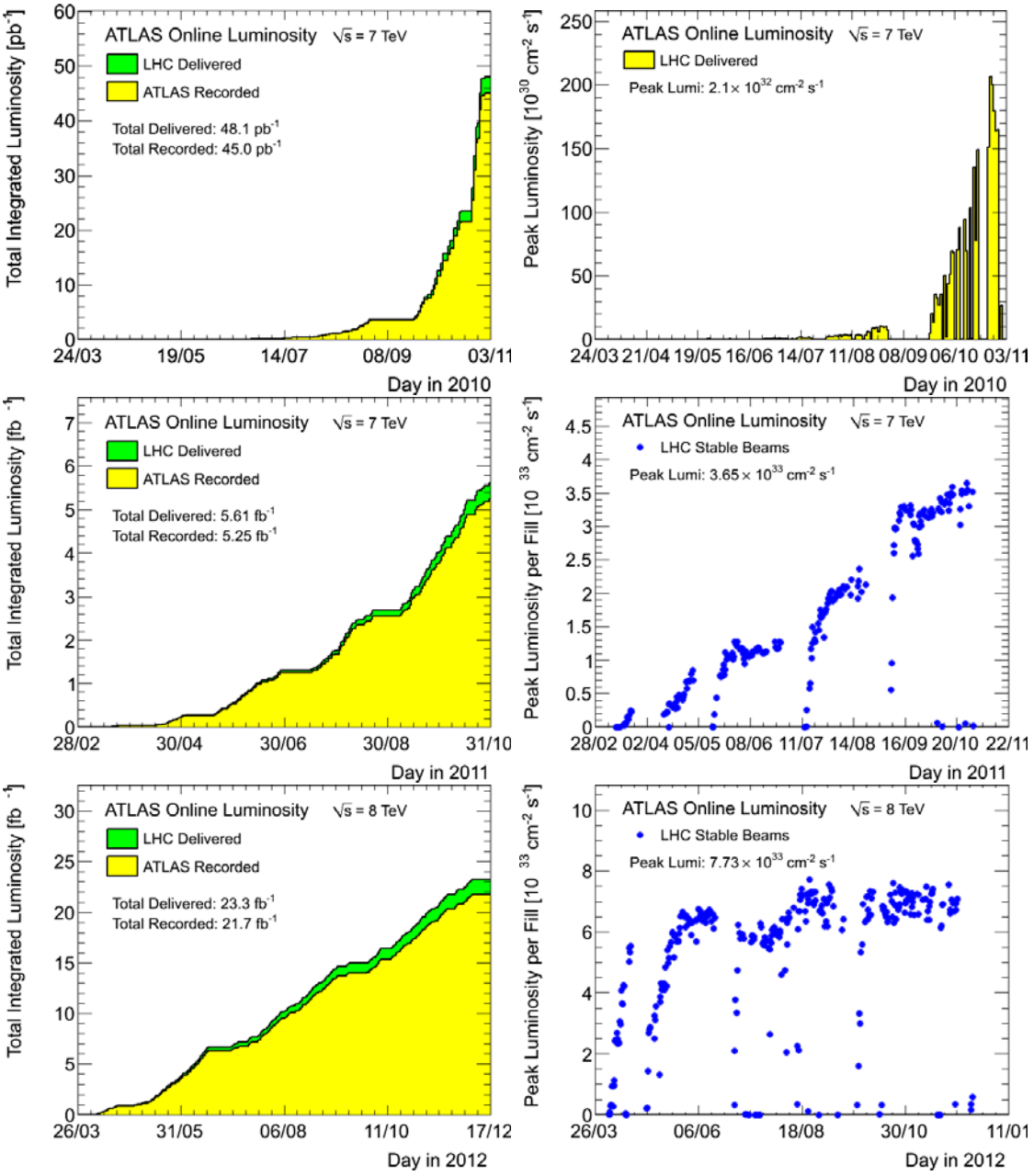

Figure 3.3: Cumulative integrated luminosity (left column) and maximum instantaneous luminosity (right column) versus day delivered at the interaction point of the ATLAS detector during the first three years of data taking at high energies, 2010 (upper row), 2011 (middle row) and 2012 (lower row). The instantaneous luminosity was continouosly increased, reaching a maximum of $> 7 \cdot 10^{33}\,\mathrm{cm}^{-2}\mathrm{s}^{-1}$ in 2012 [107].

3.2 ATLAS Detector Layout

The ATLAS detector is located at injection point 1 of the LHC at a depth of approximately 80 m. It has an overall length of 44 m and a diameter of 25 m with a weight of nearly 7000 t. The ATLAS detector is one of the two multi-purpose detectors at the LHC, covering a wide physics range, from precision measurements of Standard Model processes to the discovery of the BEH boson and the search for physics beyond the Standard Model. Therefore, its layout was optimized to allow for the reconstruction of an event by measuring all possible particles over a wide range of particle momenta and the largest possible geometrical range around the collision point. The detector is built symmetrically around the LHC beam line with the particle interaction point in its center. Radially from the inside to the outside it consists of an inner tracking detector, embedded into a solenoid magnet, a system of electromagnetic and hadronic calorimeters, and finally a muon system inside a large toroidal air magnet. The tracking system is used to reconstruct tracks from charged particles, while the electromagnetic and hadronic calorimeters measure the energy of the electrons/photons and hadronic showers, repectively. Muons, which are minimum ionizing particles, pass the calorimeter system and are detected in the outermost layer, the muon chambers. An overall view of the detector, along with its main components, is illustrated in Figure 3.4. newline

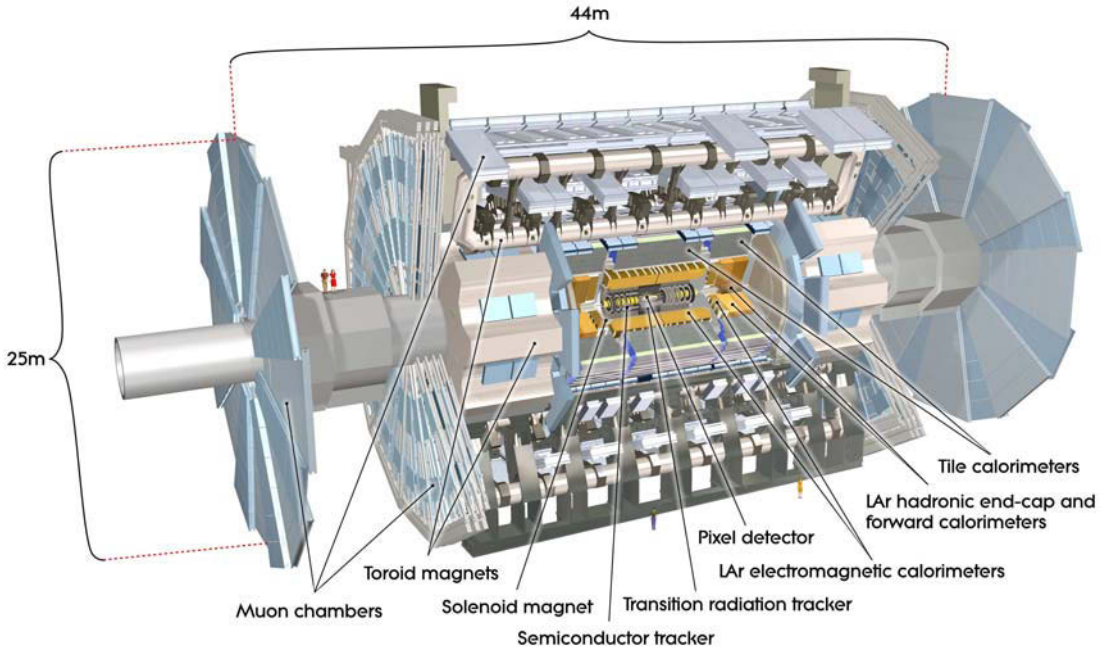

Figure 3.4: Overall layout of the ATLAS detector [101].

3.3 ATLAS Coordinate System

In order to define the geometry, location and orientation of any point or object within the ATLAS detector, a special coordinate system is used [101].
The interaction point in the center of the detector is defined as origin of the coordinate system, while the positive x-axis is oriented from the interaction point to the center of the LHC ring and the positive y-axis points upwards to the surface. The z-axis, which is oriented parallel to the beamline, defines the two sides of the ATLAS detector. Side A for positive values of z, pointing to the LHCb detector, and side C for negative values.
Many observables are defined in the x-y plane as they are then invariant under boosts in beam direction: The transverse momentum p_T, the transverse energy E_T and the missing transverse energy $\not{E}_T$. The azimuthal angle ϕ is measured around the beam axis with ϕ=0 pointing in positive x-axis, while the polar angle θ is the angle measured from the z-axis. It is common to express θ in terms of the pseudorapidity η:

$$\eta = -\ln \tan\left(\frac{\theta}{2}\right) .$$

.

Distances between two objects in the $\eta - \phi$ space are measured by

$$\Delta R = \sqrt{\Delta\eta^2 + \Delta\phi^2} .$$

3.4 The Magnet System

The magnetic field inside the ATLAS detector is provided by a solenoid and three toroid systems [108], shown in Figure 3.5. The solonoid, which is aligned parallel to the beam axis, creates a homogeneous 2 T axial magnetic field for the inner detector operating at a temperature of 4.5 K. In order to not compromise the desired calorimeter performance, the superconducting solenoid magnet shares a vacuum vessel with the barrel electromagnetic calorimeter, while the iron absorber of the hadronic tile calorimeter serves as its return yoke.
Three air-core toroid systems provide the bending field for the muon spectrometer. Each toroid system consists of eight superconducting coils, one barrel system and two end-cap systems. The magnetic field is highly non-uniform with its values varying between 0.2 T and 2.5 T for the barrel toroid and up to 3.5 T for the end-cap magnets.

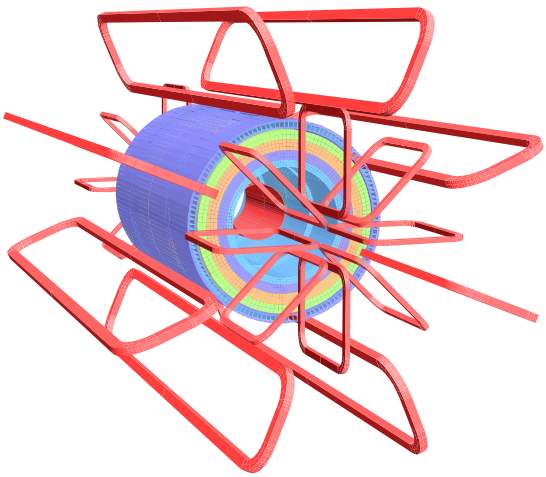

Figure 3.5: Illustration of the ATLAS magnet system, showing the solenoid, the toroids, as well as the tile calorimeter [101].

3.5 The Inner Detector

The inner detector (ID) [109, 110] consists of the two precision tracking detectors, the pixel and the semiconductor tracker (SCT), and the straw tubes of the transition radiation tracker (TRT), offer a fine detector granularity to achive an excellent momentum and vertex resolution in a range of $|\eta| < 2.5$. Within $|\eta| < 2.0$, also electron identification is provided.
With approximately 80.4 million readout channels, the pixel detector [110, 111] provides the highest granuality of the subdetectors in the ID. 1744 segmented sensor modules of $2 \times 6.3\,\text{cm}$ size are arranged in three layers around the beampipe and on three end-cap disks on each side. Each module consists of pixels with a minimum size in $(R-\phi) \times z$ of $(50 \times 400)\,\mu\text{m}^2$. The intrinsic accuracies are $10\,\mu\text{m}$ in the $R-\phi$ direction and $115\,\mu\text{m}$ in the second direction, which is the z-axis in the barrel and R in the disks. These properties are necessary for precise vertex measurements which are essential for heavy flavour and minimum bias tagging, as well as for τ-identification. To minimize multiple scattering of the crossing particles, the support structure is mostly made of carbon, which has a low mass, but also a good mechanical and thermal stability.
The SCT [110, 112] consists of semiconductor strip sensor modules, but has a larger granuality featuring 6.3 million readout channels. In the barrel region, small-angle (40 mrad) stereo strips are installed to enable the measurement of the z-coordinate, and one set of strips in each layer is arranged parallel to the beam axis to measure the $R-\phi$ position. These strips consist of two 6.4 cm long daisy-chained sensors with a strip pitch of $80\,\mu\text{m}$. In the end-cap regions, the detectors have a set of radially arranged strips and a set of stereo strips at an angle of 40 mrad. The intrinsic accuracy is $17\,\mu\text{m}$ in the $R-\phi$ direction and $580\,\mu\text{m}$ in the z-direction of the barrel direction.
The 4 mm diameter straw tubes of the TRT [110, 113] are able to measure particle transitions up to a pseudorapdity $|\eta| = 2.0$. Straw tubes with a length of 144 cm are arranged in

the barrel region parallel to the z-axis, while in the end-cap region, straws with a length of 37 cm are placed radially in wheel segments. The straw tubes are filled with a gas mixture of Xe, CO_2 and O_2 and are read out with an anode of gold plated tungsten. Each tube layer is interlaced with polypropylene fibres in the barrel section and foils in the end-caps. These separating layers are used as transition radiation material to identify electrons. The TRT, with a total of 351,000 readout channels, only provides $R-\phi$ information with an intrinsic accuracy of 130 µm per tube, but contributes significantly to the momentum measurement due to the higher number of track points and longer track length than the silicon detectors.
A longitudinal and transverse section of the inner detector is shown in Figures 3.6 and 3.7.

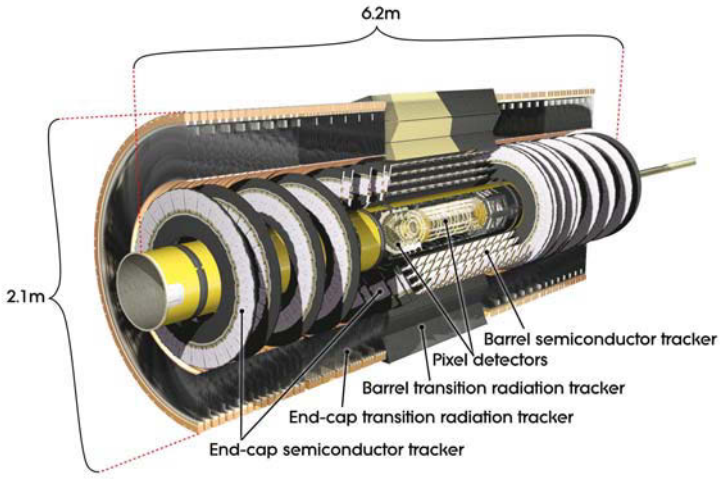

Figure 3.6: Cut-away view of the ATLAS inner detector. It shows a longitudinal section of the inner detector with its different subdetectors: The pixel detector, the semiconductor tracker and the transition radiation tracker [101].

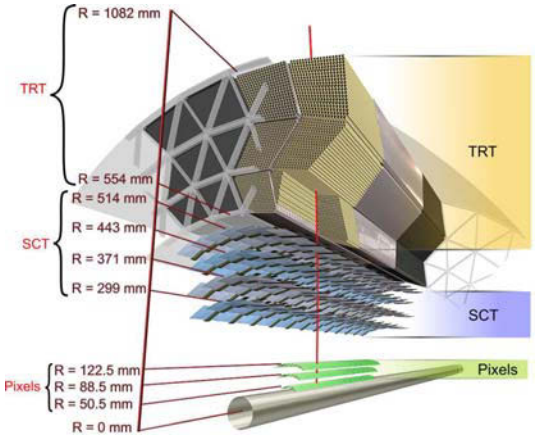

Figure 3.7: Transverse section of the ATLAS inner detector, illustrating the distances of the different detector layers from the beam pipe [101].

3.6 The Calorimeter System

The electromagnetic (EM) and hadronic calorimeters [114, 115, 116] allow the measurement of energy deposits up to an pseudorapidity coverage of $|\eta|=4.9$. In a region of $|\eta| < 2.5$, which is also covered by the inner detector, the EM calorimeter has a fine granularity for precision measurements of electrons, positrons and photons. The other parts of the calorimeter are designated to jet reconstruction and $\not{E}_T$ measurements. In addition, the calorimeter system is designed to provide input for the Level-1 trigger. Figure 3.8 shows a cut-away view of the calorimeter system.

The EM calorimeter is built using sampling technique, utilizing liquid argon (LAr) as the active detector medium and lead plates as the passive absorber material. The lead plates and the polyimide electrodes are built in an accordion geometry providing a complete ϕ symmetry without azimuthal cracks. The calorimeter consists of a barrel part covering up to $|\eta| = 1.475$ and an end-cap part on each side in a range of $1.375 < |\eta| < 3.2$. The barrel calorimeter is devided into two identical halve-shells separated by a 4 mm small gap at z=0, while each of the end-cap calorimeters is divided into two coaxial wheels covering the ranges $1.375 < |\eta| < 2.5$ and $2.5 < |\eta| < 3.2$. For $|\eta| < 2.5$, the EM calorimeter is segmented in three sections in depth, and for $|\eta| > 2.5$, the end-cap wheel is split in two sections in depth with a coarser granularity than the rest. For $|\eta| < 1.8$, a presampler corrects for the energy lost by the electrons and photons upstream of the calorimeter.

The hadronic calorimeter consists of three different subdetectors, a tile, an end-cap and a forward calorimeter. The tile calorimeter is placed directly outside the EM calorimeter shell with its barrel covering a range of $|\eta| < 1.0$, and two extended barrels in a range $0.8 < |\eta| < 1.7$. It is a sampling calorimeter with scintillating tiles as the active material and steel as absorber. The tile calorimeter is radially segmented in three layers extending from an inner radius of 2.28 m to an outer radius of 4.25 m. Two sides of the scintillating tiles are read out by wavelength shifting fibres which are routed into two seperate photomultiplier tubes in η, the readout cells are built by grouping fibres into the photo-

multipliers.
The hadronic end-cap calorimeter (HEC) consists of four wheels, two per end-cap, directly behind the end-cap electromagnetic calorimeter sharing the same liquid argon cryostats. The HEC overlaps with the forward calorimeter in the range of $3.1 < |\eta| < 3.2$ and also slightly with the tile calorimeter for $1.5 < |\eta| < 1.7$ to reduce the drop in material density. Each of the four wheels consists of 32 wedge-shaped modules, assembled with fixtures at the periphery and at the central bore, and is divided into two segments in depth. The wheels are built from parallel copper plates with 8.5 mm LAr gaps, providing the active medium for the sampling calorimeter.
In the calorimeter region near the beam pipe ($3.1 < |\eta| < 4.9$) the forward calorimeter (FCal) is installed. Due to its limits in depth, the FCal has a high-density design. It consists of three modules in each end-cap. The copper module is designed for electromagnetic measurements, the other two are made of tungsten and measure predominantly the energy of hadronic interactions. Each module consists of a metal matrix with regulary spaced longitudinal channels filled with concentric rods and tubes parallel to the beam line. The gaps between the rod and the tube are filled with liquid argon used as the active medium. Like in the EM and the end-cap calorimeter, LAr was chosen due to its good linearity in a wide energy range, its radiation hardness and long term stability. The signal is generated by the incoming particles ionising the argon. The electrons, freed by the ionization process, drift in an electric field towards a readout electrode, where the induced current is measured.

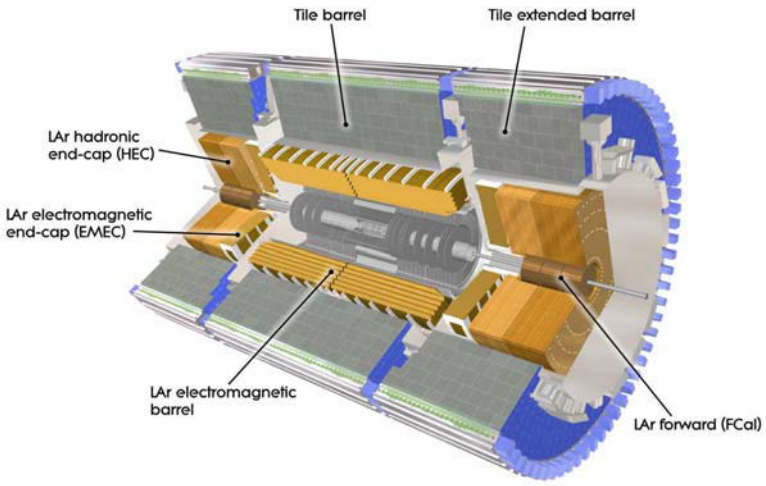

Figure 3.8: Cut-away view of the ATLAS calorimeter system with the EM calorimeter highlighted in brown and the hadronic calorimeter in green and blue [101].

3.7 The Muon System

The muon system [117] provides precise momentum measurement in a range of $|\eta| < 2.7$ and a muon trigger signal up to $|\eta| < 2.4$. A momentum resolution of below 4% is achieved

for muons with a transverse momentum up to $p_T = 200\,\text{GeV}$, rising to 10% for muons with a $p_T = 1\,\text{TeV}$. The toroidal magnet system generates a bending field which is mostly orthogonal to the muon trajectories. The muon spectrometer consists of two types of precision tracking chambers and two types of trigger chambers with a timing resolution in the order of a few nanoseconds. In the barrel region, the chambers are arranged in three cylindrical layers around the beam pipe. In the region of the end-caps, they are placed in three layers perpendicular to the beam axis.
The monitored drift tube chambers consist of two multilayers of three or four tubes with a total of 354,000 tubes installed on 1,150 chambers. The drift tubes are made out of aluminium and filled with a gas mixture of 93% argon and 7% CO_2 at a pressure of about three bar, and tungsten-rhenium alloy wires are used as anodes.
The cathode strip chambers are multi-wire proportional chambers with strip-segmented cathodes and a higher granularity than in the other parts of the muon system to cope with the high interaction rates in the innermost layer of the very forward region.
The resistive plate chambers consist of two parallel electrode plates at a 2 mm distance and filled with a gas mixture of $C_2H_2F_4$/Iso-C_4H_{10}/SF_6. These trigger chambers are read out by metallic strips on the outer faces via capacitive coupling.
The thin gap chambers are multi-wire proportional chambers. They are called thin gap, because the wire-to-cathode distance of 1.4 mm is smaller than the wire-to-wire distance of 1.8 mm. Used as trigger chambers in the forward region $1.5 < |\eta| < 2.4$, these chambers have to deal with a high muon rate, and therefore combine a high granularity with a highly quenching gas mixture of CO_2 and N-C_5H_{12}.
A total of 606 resistive plate chambers and 3,588 thin gap chambers perform the bunch-crossing identification, a fast muon trigger signal and measure track coordinates orthogonal to the coordinates provided by the monitored drift tube and cathode strip chambers.

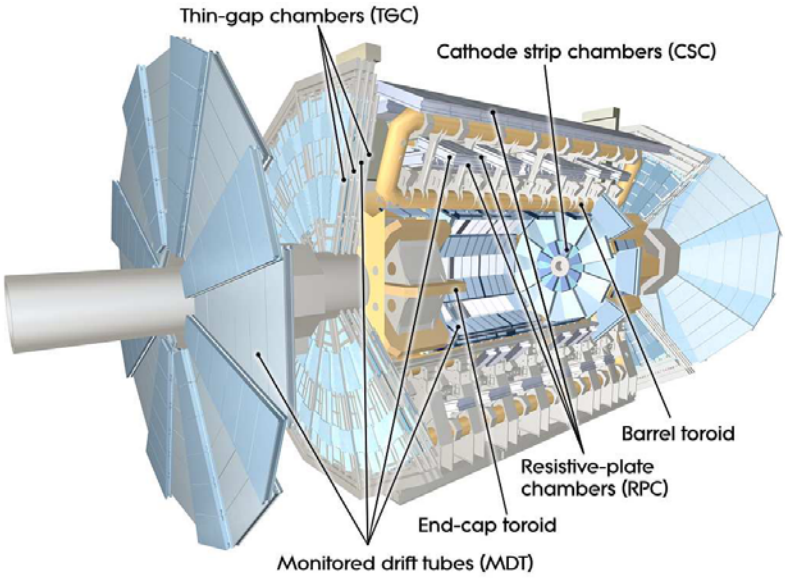

Figure 3.9: Overview of the muon system of the ATLAS detector, the different tracking and trigger chambers as highlighted [101].

3.8 The ATLAS Trigger System

A collision rate of about 40 MHz is expected at the LHC design luminosity of $10^{34}\,\mathrm{cm}^{-2}\mathrm{s}^{-1}$ and a bunch spacing of 25 ns. This large amount of data cannot be stored not only due to limited storage capacities, but also since most of the events are of no interest for further physics analysis. In order to filter events which are considered for data analysis, a trigger system has been installed reducing the data taking rate to roughly 200 Hz. A schematical description of the three-level trigger system [118, 119, 120] is shown in Figure 3.10.
The level-1 trigger is a hardware based trigger using the information from the entire calorimeter system with reduced granularity and data from the muon system trigger chambers. It reduces the rate to about 75 kHz by selecting events which contain leptons or jets with high p_T, as well as events with large E_T or $\not{E}_T$. These selected events define Regions-of-Interest, which are η-ϕ coordinates of detector regions where the events have been triggered. The decision, whether an event will pass the trigger or not, is made with a latency of 2 µs.
The level-2 trigger uses all available detector information within the Regions-of-Interest at full granularity and precision. This trigger reduces the rate to around 1 kHz with a latency of up to 10 ms.
The event filter uses offline analysis procedures to reduce the final rate down to around 200 Hz. The full event is reconstructed with algorithms similar to those used for the final reconstruction. Each event has a size of approximately 1.3 MB, so that several hundreds of MB per second are written to permanent storage.

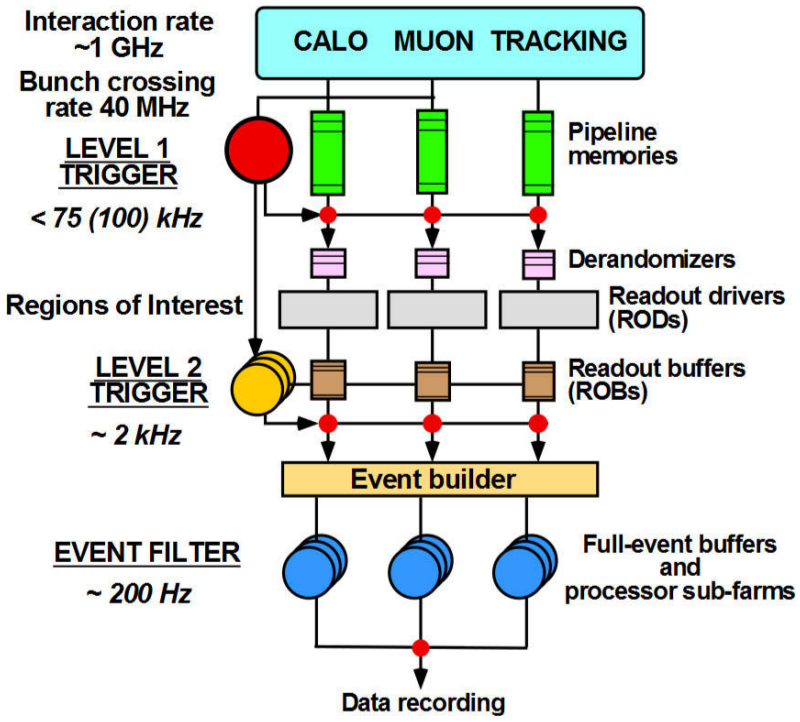

Figure 3.10: Schematical representation of the ATLAS trigger system [121].

Chapter 4

Physics objects

In order to identify specific physics processes in the bulk of collision data, it is necessary to translate the signals recorded in the subsystems of the ATLAS detector into reconstructed physics objects: Photons, charged leptons (electrons and muons), neutrinos which cannot be detected and hence resulting in missing transverse energy and jets originating from single quarks and gluons.
This section presents the reconstruction and identification of physics objects as well as the final object definitions provided by the ATLAS top working group. The definitions include further selections criteria, e.g. lower or upper thresholds on kinematic variables like the transverse momentum and the pseudorapidity, to achieve a high purity for the identification of particles combined with a considerably high selection effiency [122, 123].

4.1 Jet

4.1.1 Reconstruction

Jets are reconstructed using the anti-k_T algorithm [124, 125], which forms clusters of nearby objects, considering the distance between objects d_{ij} and the distance of an object to the beam d_{iB} defined by

$$d_{ij} = \min\left(p_{t,i}^{-2}, p_{t,j}^{-2}\right) \frac{\Delta_{ij}^2}{R^2},$$

$$d_{iB} = p_{t,i}^{-2},$$

with $\Delta_{ij}^2 = (y_i - y_j)^2 + (\phi_i - \phi_j)^2$, $p_{t,i}, y_i$ and ϕ_i are respectively the transverse momentum, rapidity and azimuth of particle i.
Both distances are calculated for two entities i and j and the smallest value is identified. If the lowest distance is between an entity and the beam rather than two entries, it is called a jet and is removed from the list of entities. If the lowest distance is between two entities, they are merged to a pseudojet and the procedure is repeated until no entities are left.
Due to this definition, a high-energetic particle accumulates all particles with a lower transverse momentum in its surroundings, resulting in a perfectly conical jet with the radius R. In rare cases, two high-p_T entities i and j are separated by $R < \Delta_{ij} < 2R$. If entity j has the lower transverse momentum, its jet will be only partly conical, missing the part overlapping with jet i.
The anti-k_T algorithm is implemented with a distance parameter $R = 0.4$ and uses topological calorimeter clusters as input (entity) [126]. Such clusters are groups of cells in

the electromagnetic or hadronic calorimeter that are designed to follow the shower development. The algorithm starts with a seed cell, whose signal-to-noise ratio is above a threshold of 4. The ratio is estimated as the absolute value of the deposited energy in the calorimeter cell divided by the RMS of the energy distribution measured in events triggered at random bunch crossings. Starting from the seed, all neighbouring cells are added to the cluster iteratively, if they have signal-to-noise ratio of 2. After this step, all cells neighbouring that formed topological cluster are added to the cluster.
An additional splitting step is included in the topological cluster algorithm in order to optimize the separation of close-by showers. All cells in a cluster are searched for local maxima with an energy content above 500 MeV, these are used for a new iteration of topological clustering, which splits the original cluster into multiple ones.
The jet energy corresponds to the energy depositions in all cluster cells, measured at the electromagnetic energy scale, which correctly measures the energy deposited by an electromagnetic shower in the calorimeters. This scale has been established using test-beam measurements for electrons in the electromagnetic and hadronic calorimeters, with a small correction it can be derived from in-situ calibration using $Z \to ee$ events.

4.1.2 Energy calibration

The jet energies are corrected in the EM+JES calibration scheme, applying corrections as a function of the jet energy and pseudorapidity at the electromagnetic scale.
The average additional energy due to the effect of both in-time and out-of-time pile-up is subtracted from the measured jet energy. This correction has been taken from Monte Carlo simulation and is parameterized in bins of jet-η according to the number of primary vertices in an event and the number of average interactions in a luminosity block [127].
Jets are then calibrated to the hadronic scale using p_T and η dependent correction factors from Monte Carlo simulations, derived from studies comparing the reconstructed jet energy and the energy of its corresponding truth level jet. Figure 4.1 shows the average energy of jets calibrated at EM scale with respect to the truth jet energy as a function of the jet pseudorapidity for various jet energies, which is the inverse to the average jet energy scale correction.

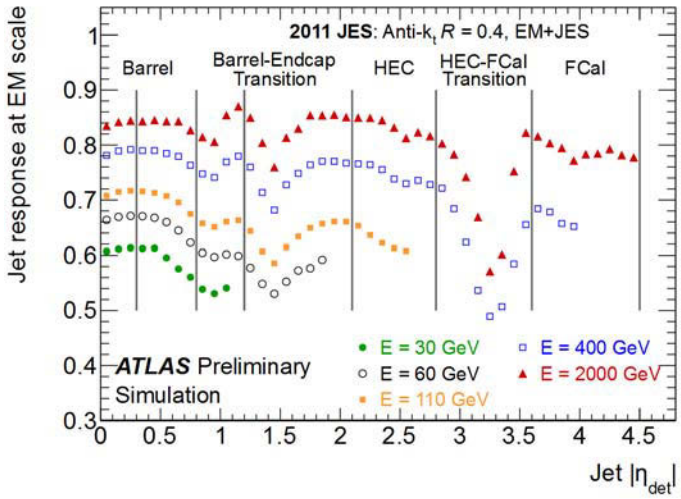

Figure 4.1: Average energy of jets calibrated at EM scale with respect to the truth jet energy as a function of the jet pseudorapidity for various jet energies. The transition regions show a large drop in response and are thus excluded from the reconstruction process. The inverse of the response shown in each bin is equal to the average jet energy scale correction [128].

4.1.3 Quality criteria

Jet quality criteria are applied to identify so-called bad jets. These are jets which are not caused by real energy deposits, but by hardware problems, faulty LHC beam conditions and cosmic-ray showers.
Two types of calorimeter noise are addressed, sporadic noise bursts in the hadronic endcap calorimeter and rare coherent noise in the electromagnetic calorimeter. In the endcap, a single noisy calorimeter cell contributes almost all of the jet energy, resulting in reconstructed jets characterized by a large energy fraction in the endcap calorimeter as well as a large fraction of the energy in calorimeter cells with poor signal shape quality. Due to the capacitive coupling between channels, the neighbouring calorimeter cells will have an apparent negative energy. Similarly, fake jets can arise in the electromagnetic calorimeter, characterized by a large electromagnetic energy fraction, and a large fraction of calorimeter cells with poor signal shape quality.
Cosmic rays or non-collision backgrounds can result in jet candidates, which are not in-time with the beam collision. A cut on the jet time, which is the energy squared weighted cell time defined with respect to the collision time, is applied to reject these backgrounds. In addition, a cut on the electromagnetic energy fraction is applied to make sure that the jet has some energy deposited closest to the interaction region. A cut on the maximum energy fraction in any single calorimeter layer further reduces the non-collision background. A cut on the jet vertex fraction is applied to reduce the effect of in-time pile-up [129]. It requires that at least 75% of all tracks are associated to the jet are originating from the primary vertex, providing a discriminant for jets in form of a probability of the jet to

not being generated by pile-up interactions. This optimized cut is based on the data and Monte Carlo simulation comparison of $Z \to \mu\mu$ and $Z \to ee$ events with specific selections to obtain a sample of hard-scattering jets and pile-up jets.

4.1.4 b-tagging

The unique properties of the b quark provide the opportunity to identify jets originating from these quarks with high efficiency. B mesons which originate from single b quarks have a mean lifetime of $\tau_{B^0} \approx 1.5\,\text{ps}$, significantly longer than quarks with lighter masses. This allows the mesons to travel away from the primary vertex of the event before the decay, resulting in a displaced, secondary vertex.
A variety of algorithms has been developed to identify b quarks with high efficiency, so-called b-tagger. This analysis follows the recommendation of the ATLAS top working group and uses the MV1 tagging algorithm which combines the results of three different b-taggers: IP3D, SV1 and JetFitterCombNN [130].
The IP3D algorithm uses the longitudinal impact parameter z_0 and transverse impact parameter d_0 to determine the position of the secondary vertex. The distance of closest approach of the track to the primary vertex in the r-ϕ plane is defined as d_0, while z_0 is the z-coordinate of the track at the point of closest approach in the r-ϕ plane. The impact parameters of B mesons tend to have a positive sign, which means that the angle between the jet direction and the line joining the primary vertex to the point of closest approach is less than 90°, while the distributions are much more symmetric around zero for other originating jets. The correlation between these two variables is also taken into consideration in this approach.
The SV1 tagger is a secondary vertex-based algorithm. It forms two-track pairs far away from the primary vertex. These pairs are then combined into a single vertex by an iterative χ^2 method. The algorithm relies on a 2D-distribution of two discriminating variables, the invariant mass of all tracks associated to the vertex and the sum of the track energies in the vertex divided by the sum of the all track energies in the jet. In addition, a 1D-distribution of the number of two-track vertices and the distance ΔR between the jet axis and the line joining the primary vertex to the secondary one is used.
JetFitterCombNN is an advanced b-tagger based on the IP3D and the JetFitter algorithm, which are combined by a neural network. The JetFitter tagger exploits the topology of weak b and c hadron decays inside the jet. A Kalman filter approximates a line on which the primary vertex and the b and c vertices lie, as well as their position on this line, defined by the b meson flight path. Figure 4.2 shows that the MV1 tagger has the highest rejection power of light jets compared to other algorithms.

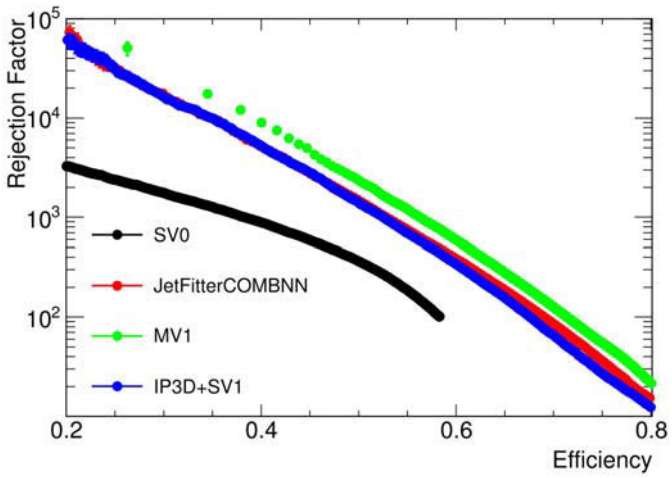

Figure 4.2: The rejection factors as a function of the tagging efficiency for the SV0 (black), IP3D+SV1 (blue), JetFitterCOMBNN (red) and MV1 algorithm (green). The MV1 tagger used in this analysis shows the highest rejection power of light jets [123].

4.1.5 Object defintion

As mentioned previously, jets are reconstructed with the anti-k_t algorithm using a cone size of $\Delta R = \sqrt{(\Delta\eta)^2 + (\Delta\phi)^2} = 0.4$. The algorithm uses topological calorimeter clusters as input with EM+JES calibration. A jet is required to have a transverse momentum above 25 GeV and has to lie within an $|\eta|$ acceptance range of 2.5. Candidates failing these requirements are not considered. Furthermore, the jet vertex fraction has to be above 0.75 and every reconstructed jet has to pass the quality criteria, otherwise the whole event is removed.
The jet algorithm is based entirely on energy deposits in the calorimeters, hence, not only real hadronic jets, but also electrons and photons are considered as a jet candidate. Hence, a jet is rejected, if its distance to a selected electron is $\Delta R < 0.2$. Additionally to the selection criteria in the ATLAS $t\bar{t}$ analyses, jets with a distance to a selected photon of $\Delta R < 0.1$ are removed in this analysis.
A jet candidate is identified as a b-jet, if it fulfills the object definition and in addition passes the requirements of the MV1 tagging algorithm. The used working point requires a tag weight output of more than 0.601713, which corresponds to a b-tag efficiency of $\approx 70\,\%$, optimized in multiple $\eta \times p_T$ regions.
A b-tagging scale factor is applied to all jets in Monte Carlo simulated events, in order to match the tagging efficiencies in simulations $\varepsilon_{\text{b-tag, MC}}$ with the efficiencies measured in data $\varepsilon_{\text{b-tag, data}}$:

$$SF_{\text{b-tag}} = \frac{\varepsilon_{\text{b-tag, data}}}{\varepsilon_{\text{b-tag, MC}}} \tag{4.1}$$

This scale factor is used, if a jet is b-tagged and has originated from a true b quark. In case, the jet has evolved from a light quark (u, d, s) or c quark, a misidentification rate

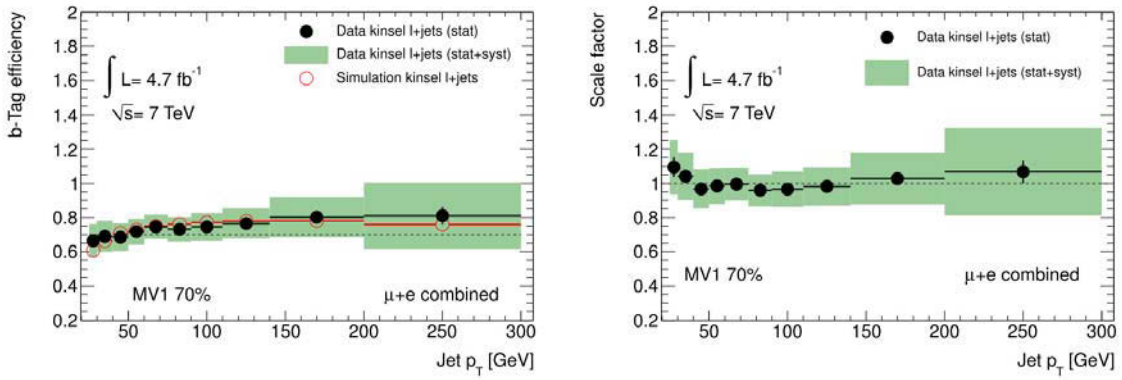

Figure 4.3: The b-jet tagging efficiency estimated from data compared with the efficiency estimated from Monte Carlo simulation (left) and the resulting scale factors $SF_{\text{b-tag}}$ (right) including statistical and systematic uncertainties for the MV1 algorithm as a function of p_T. All scale factors are close to 1 and agree within their uncertainties [123].

scale factor is applied, depending on the true jet flavor:

$$SF_{\text{mistag}} = \frac{\varepsilon_{\text{mistag, data}}}{\varepsilon_{\text{mistag, MC}}} \tag{4.2}$$

The tagging and misidentification rates have been estimated in 10 regions of p_T from 25 GeV to 300 GeV [131]. Figure 4.3 shows the b-tagging efficiencies for data and Monte Carlo simulations in these p_T regions as well as the calculated scale factors $SF_{\text{b-tag}}$. All efficiencies are around 70%, as indicated by the working point and the scale factors are close to unity. The weights of all b-tagged jets in a event are multiplied to form one overall event b-tag weight.

4.2 Electron

4.2.1 Reconstruction

An electron candidate is reconstructed by associating energy deposits in the electromagnetic calorimeter to reconstructed tracks of charged particles in the inner detector [132, 133].
Seed clusters of longitudinal towers with total transverse energy above 2.5 GeV are formed by a sliding window algorithm. The window size is 3×5 in units of 0.025×0.025 in $\eta \times \phi$ space, corresponding to the granularity of the calorimeter middle layer. In the inner detector η-region of $|\eta| < 2.5$, one or more reconstructed tracks are extrapolated to the middle layer of the electromagnetic calorimeter and matched to a seed cluster. The distance between the track impact point and the cluster position is required to pass $\Delta\eta$ <0.05. The $\Delta\phi$-distance between the track and the cluster has to be less than 0.1 on the side where the extrapolated track bends as it traverses the solenoidal magnetic field and is 0.05 on the other side.
In the case where several tracks are matched to the same cluster, the tracks are ordered

according to the quality of their match. Tracks with silicon hits are preferred, and the one with the smallest distance ΔR to the seed cluster is selected. Tracks without silicon hits are considered as more likely to belong to electrons originating from photon conversions. The electron cluster is then recalculated using 3×7 longitudinal towers of cells in the barrel and 5×5 towers in the endcaps.
The cluster energy is corrected by taking several additional contributions into account. The estimated energy deposits in the material in front of the electromagnetic calorimeter, outside the cluster (lateral leakage), and beyond the electromagnetic calorimeter (longitudinal leakage).
The four-momentum of an electron candidate is computed with the information from the final cluster and the best track matched to the original seed cluster. The ϕ and η directions are taken from the corresponding track parameters at the vertex, unless the track contains no silicon hits, in which case η is provided by the cluster position.
The forward region, $2.5 < |\eta| < 4.9$, is not covered by the inner detector, therefore the electron candidates are reconstructed only from energy deposits in the calorimeters by grouping neighbouring cells in three dimensions. The direction of forward electrons is defined by the barycenter of the cells belonging to the cluster. The energy of a candidate is determined by summing the energies in the cluster cells and then corrected for energy loss in the passive material before the calorimeter.

4.2.2 Energy scale and energy resolution

Two methods are used to calibrate the electron energy measured in the electromagnetic calorimeter.
A clean electron sample can be obtained from $Z \to ee$ events due to the well-known value of the Z boson mass. After an event selection with two oppositely charged electrons with a transverse energy above 25 GeV and a dielectron invariant mass in the range 80-100 GeV, the residual miscalibration for a given region i is measured by

$$E_{\text{meas}} = E_{\text{true}}(1 + \alpha_i)\,,$$

with the measured cluster energy E_{meas} and the true electron energy E_{true}. The energy-scale correction factor α is determined in 26 η regions, using a negative unbinned log-likelihood with a probability density function template obtained from Monte Carlo simulation to quantify the compatibility of an event with the Z lineshape. The high number of η-bins was chosen due to possible variations at the transitions between the different calorimeter systems. Variations within a given system can occur to several effects related to electronic calibration, high-voltage corrections, additional material in front of the calorimeter and differences in the calorimeter and presampler energy scales. The determined energy corrections α applied to the electrons are within 0.5% in the barrel region ($|\eta| < 2.47$) and within 1% in the endcaps ($|\eta| < 4.9$) [134]. The calibrated Z mass distribution, measured with full statistics from 2011, is compared to Monte Carlo expectation in Figure 4.4. The same prodedure can also be applied to $J/\Psi \to e^+e^-$ events in order to measure the correction factors for electrons in the low E_T-region down to 5 GeV.
An alternative calibration strategy is the measurement of the ratio of the cluster energy E

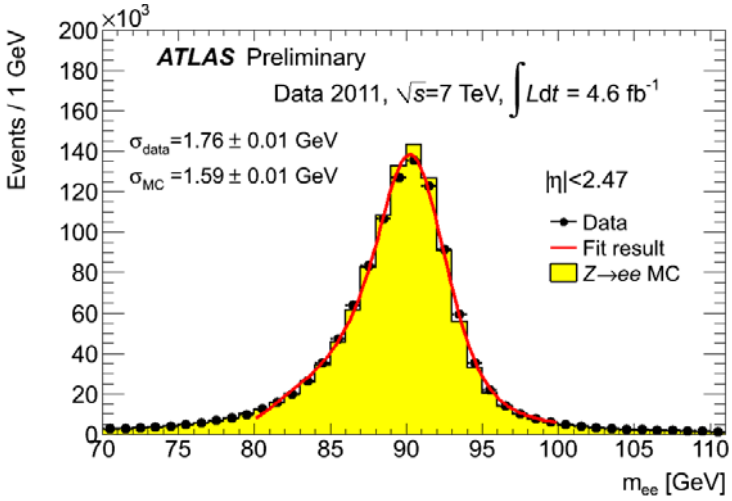

Figure 4.4: $Z \to e^+e^-$ invariant mass with the full 2011 dataset after calibration of the electron energy. The simulated distribution is shown in yellow and data as black points, which are now in good agreement after the calibration [134].

in the electromagnetic calorimeter and the momentum p measured by the inner detector, using $W \to e\nu_e$ events. Due to the very small electron mass compared to its energy, the ratio is expected to be close to unity with a significant tail at large values due to Bremsstrahlung occurring in the inner detector. Results agree within uncertainties with the results of the baseline method using Z boson events.
The fractional energy resolution in the calorimeter is parametrized as

$$\frac{\sigma(E)}{E} = \frac{a}{\sqrt{E}} \oplus \frac{b}{E} \oplus c\,, \tag{4.3}$$

with the sampling term a, the noise term b and the constant term c. The dielectron invariant mass distribution from $Z \to ee$ decays is used to measure the constant term c in data and determine a resolution correction to simulated electrons. The resolutions are derived from fits to the invariant mass distributions after calibration using a Breit-Wigner convoluted with a Crystal Ball function in the mass range $80 - 100\,\text{GeV}$ for central-central events and in the mass range $75 - 105\,\text{GeV}$ for central-forward events.

4.2.3 Identification

The electron identification in the central region ($|\eta| < 2.47$) relies on cuts on variables using calorimeter, tracking and combined calorimeter/tracking variables. This cut-based selection provides a good separation between isolated or non-isolated signal electrons, background electrons, which primarily originate from photon conversions and Dalitz decays, and jets faking electrons. The cuts can be applied independently. Three reference sets of cuts have been defined, which have been optimized for increasing background rejection power: loose, medium and tight with an expected jet rejection of about 500, 5000 and 50000, respectively, based on Monte Carlo simulation.

In the loose selection, shower shape variables of the electromagnetic calorimeter middle layer and hadronic leakage variables are used. The medium selection adds variables from the strip layer, track quality requirements and track-cluster matching. The tight selection introduces cuts on E/p, particle identification using the TRT, and discrimination against photon conversions via a b-layer hit requirement and information about reconstructed conversion vertices. All variables used in the loose, medium and tight selections are listed in Tab. 4.1. The cuts are optimized in 10 bins of η and 11 bins of E_T from 5 GeV to above 80 GeV. The binning in η is chosen by calorimeter geometry, detector acceptances and regions of increasing material in the inner detector.
The shower variables are optimized by performing a multi-variate analysis. This procedure achives the highest possible electron efficiency for a given jet rejection while properly handling correlations between variables.

4.2.4 Isolation

Isolation variables are used as a discriminant to separate prompt electrons from non-prompt electrons as well as misidentified hadrons from jet fragmentation, like $\pi^{\pm}$ mesons. Electron isolation based on calorimeter or track information has been studied and optimized.
The calorimetric isolation discriminator is defined as the sum of all energy deposits in the electromagnetic and hadronic calorimeter within a cone of a radius R_0 around the electron candidate direction, without applying any noise suppression. The energy of the electron itself is excluded by removing the central 5×7 window in the $\eta - \phi$ plane. This simple exclusion of the center removes roughly 95% of the electron energy. The remaining lateral leakage leads to a slow growth in the isolation energy as a function of E_T, which has been studied in simulation and data in order to derive corrections for this effect. Further, pileup corrections are derived from data studies of the calorimeter isolation distribution as a function of the number of reconstructed primary vertices in an event (in-time pileup) or the average number of interactions per bunch crossing (out-of-time pileup) [135].
The tracking based discriminator is the summed scalar p_T of tracks in a cone with radius R_0 around the electron, excluding the one which has been associated with the lepton. Tracks have to pass different criteria to be considered. The transverse momentum has to be above 1 GeV, while one hit in the pixel detector layer and at least 7 hits in silicon detectors have to be observed. In addition, the transverse and longitudinal impact parameter should be less than 1 mm. This variable is quite pileup robust for electrons due the impact parameter cuts constraining the tracks to come from the same vertex as the electron. Hence, no signal leakage or pileup corrections have been applied.

Type	Description	Name
	Loose selection	
Acceptance	$\|\eta\| < 2.47$	
Hadronic leakage	Ratio of E_T in the first layer of the hadronic calorimeter to E_T of the EM cluster, used in the range of $\|\eta\| < 0.8$ and $\|\eta\| > 1.37$	R_{had1}
	Ratio of E_T in the hadronic calorimeter to E_T of the EM cluster, used in the range of $\|\eta\| > 0.8$ and $\|\eta\| < 1.37$	R_{had}
Middle layer of EM calorimeter	Ratio of the energy in 3×7 cells over the energy 7×7 cells centred at the electron cluster position	R_η
	Lateral shower width, $\sqrt{(\sum E_i \eta_i^2)/(\sum E_i) - ((\sum E_i \eta_i)/(\sum E_i))^2}$ of cell i. The sum is calculated within a window of 3×5 cells	$w_{\eta 2}$
	Medium selection (includes loose)	
Strip layer of EM calorimeter	Shower width, $\sqrt{(\sum E_i (i - i_{max})^2)(\sum E_i)}$, where i runs over all strips in a window of $\Delta\eta \times \Delta\phi \approx 0.0625 \times 0.2$, corresponding typically to 20 strips in η, and i_{max} is the index of the highest-energy strip	w_{stot}
	Ratio of the energy difference between the largest and second largest energy deposits in the cluster over the sum of these energies	E_{ratio}
Track quality	Number of hits in the pixel detector	η_{pixel}
	Number of total hits in the pixel and SCT detector	η_{Si}
	Transverse impact parameter	d_0
Track-cluster matching	$\Delta\eta$ between the cluster position in the strip layer and the extrapolated track	$\Delta\eta$
	Tight selection (includes medium)	
Track-cluster matching	$\Delta\phi$ between the cluster position in the middle layer and the extrapolated track	$\Delta\phi$
	Ratio of the cluster energy to the track momentum	E/p
	Tighter $\Delta\eta$ requirement	$\Delta\eta$
Track quality	Tighter transverse impact parameter requirement	d_0
TRT	Total number of hits in the TRT	n_{TRT}
	Ratio of the number of high-threshold hits to the total number of hits in the TRT	f_{HT}
Conversions	Number of hits in the b-layer	n_{BL}
	Veto electron candidates matched to reconstructed photon conversions	

Table 4.1: Short description of electron shower variables used for electron identification [133].

4.2.5 Trigger

In order to decrease the amount of stored collision data, various trigger chains were defined for a first preselection right after data taking, as described in Section 3.8.
The level-1 (L1) electromagnetic (EM) trigger identifies the position of Regions-of-Interest using $\Delta\eta \times \Delta\phi \approx 0.1 \times 0.1$ trigger towers and compute the transverse energy with a precision of 1 GeV [136]. For each trigger tower, the cells of the EM or hadronic calorimeter are summed, forming clusters by identifying local maxima using a sliding window algorithm based on a 4×4 group of trigger towers. A trigger is satisfied if the central 2×2 trigger towers contain one pair of neighbouring towers with a combined energy that passes the defined threshold.
At level-2 (L2), cell clusters are build within the Regions-of-Interest using only the second layer of the EM calorimeter to find the cell with the largest deposited transverse energy (pre-seed). The final cluster position is obtained by calculating the energy weighted average cell positions on a 3×7 grid centred on the pre-seed. In order to accumulate the energy, the same cluster sizes are used as in the offline electron reconstruction and in addition, several corrections are included to improve the resolution of the cluster position and energy. First tracking information is also available, using a fast pattern recognition and track reconstruction.
The event filter (EF) trigger uses offline-like algorithms for the reconstruction of calorimeter quantities in a region slightly larger than the Region-of-Interest, in order to build the EM cluster including all offline based corrections. An event filter track reconstruction makes use of an adapted version of the offline reconstruction software, constrained to the data available in the Region-of-Interest.
Further, the high-level triggers (L2+EF) deploy first electron identification algorithms using similar variables and cuts as the offline identification. At L2, requirements are applied on the deposit of energy in the hadronic calorimeter within the Region-of-Interest, as well as on the R_η and E_{ratio} shower shape variables. At the EF, the identification of electrons is performed using the offline-identification variables.
The unprescaled single electron trigger with the lowest E_T-threshold is chosen in ATLAS top quark analyses involving a prompt electron in the final state. This trigger had to be adjusted two times during the course of 2011 due to changes of the beam conditions and consequantially, the steady increase of the instantaneuous luminosity. At the beginning of 2011, the level-1 EM trigger with a transverse energy threshold of 14 GeV was used (EM14), followed by the high-level triggers e20_medium, which include an E_T-cut of 20 GeV as well as the medium identification criteria. In run period J, the instantaneuous luminosity had reached $2 \cdot 10^{33}\,\text{cm}^{-2}\text{s}^{-1}$, corresponding to an event filter rate of 100 Hz. Hence, the E_T-thresholds were raised by 2 GeV (EM16, e22_medium). In the last two run periods of the years, two new optimizations were added to L1. Threshold settings were modified following the coarse granularity of $\Delta\eta = 0.4$, by increasing the EM threshold in the η regions where the L1 cluster energy response with respect to the offline reconstructed cluster energy was sufficiently good to cause minimal additional efficiency losses. Further, a hadronic leakage requirement was introduced, consisting of a veto on energies above 1 GeV deposited in the hadronic calorimeter within a region of $\eta \times \phi = 0.2 \times 0.2$ behind

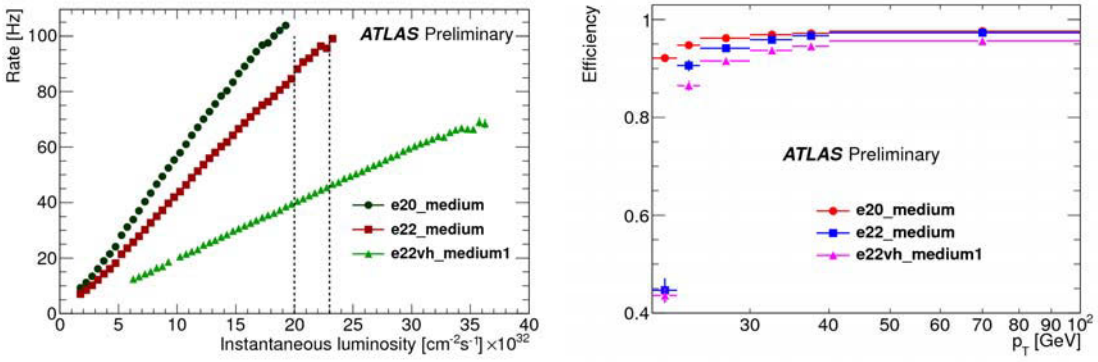

Figure 4.5: The left plot shows the EF trigger rates as function of the instantaneous luminosity for the e20_medium, e22_medium and e22vh_medium1 triggers. The vertical dashed lines mark instantaneous luminosity ranges of validity, when the trigger had to be changed during data taking in 2011. The right plot shows the efficiencies of the single electron triggers measured in data relative to medium offline electrons as a function of the electron-p_T [136].

the EM cluster. These new requirements are indicated by the letters "VH" in the signature names (EM16VH, e22vh_medium1). The medium identification was reoptimized and renamed medium1, which includes tighter cuts on shower variables and additional track requirements. An overview of all single electron triggers are listed with the corresponding run periods of 2011. Figure 4.5 shows EF trigger rates as function of the instantaneous luminosity and the efficiencies of the three single electron triggers. The new L1 requirements significantly reduce the trigger rate by a factor of > 2, while loosing less than 5% in efficiency.

Run period	L1	HLT
B-J	EM14	e20_medium
K	EM16	e22_medium
L-M	EM16VH	e22vh_medium1

Table 4.2: Single electron trigger chains used during data taking in 2011, which had to be reoptimized two times due to changing luminosity conditions. A trigger chain consists of the level-1 (L1) and subsequently the two high-level triggers (HLT), the level-2 and event filter trigger [136].

4.2.6 Object defintion

A reconstructed electron candidate must be in the region $|\eta| < 2.47$, except the transition region between the barrel and endcap part of the electromagnetic calorimeter ($1.37 < |\eta| < 1.52$), and must have a minimum transverse energy of 25 GeV. The transverse energy E_T is defined as the cluster energy divided by the the hyperbolic cosine of the track pseudorapidity:

$$E_T = \frac{E_{\text{cluster}}}{\cosh(\eta_{\text{track}})} .$$

The longitudinal impact parameter of the electron track has to be smaller than 2 mm with respect to the primary vertex. All cluster cells of an electron candidate are analyzed for hardware problems during data taking, such as dead high voltage channels and non-nominal optical transmitters.
In the single electron channel, it is required that the selected lepton is also the particle, which was detected by the trigger system. The electron is tagged as trigger-matched, if its distance to a trigger object, which has passed the event filter trigger criteria, is smaller than $\Delta R = 0.15$.
In order to achieve a high purity of real prompt electrons, the candidates have to pass the tight selection criteria as well as calorimetric and track based isolation requirements. Cuts have been deployed for the calorimetric isolation with $\Delta R = 0.2$ and the track isolation with $\Delta R = 0.3$ in eight regions of $|\eta|$ and seven regions of E_T, which have been optimized for an efficiency of 90%.
Four types of electron scale factors are applied for each simulated single electron event to correct the data-to-Monte Carlo differences in trigger, reconstruction, identification and isolation efficiency. All effciencies are measured in multiple regions of $|\eta|$ and E_T using the tag&probe method with $Z \to ee$ events. This method is based on selecting dielectron events, of which one is required to pass all selection requirements (tag), while a very loose selection chooses the other electron (probe), having an opposite electric charge and an invariant mass with the tag electron close to the Z boson mass. The probe electron is then used for the efficiency measurements. The results of the tight identification efficiency measurements, which in addition also use $W \to e\nu$ events, are shown in Figure 4.6, deviating from unity within 2% over the total η-range as well as for transverse energies above 25 GeV. Overall, one electron weight is defined for each single electron event:

$$\begin{aligned} SF_e &= SF_{\text{trigger}} \cdot SF_{\text{reco}} \cdot SF_{\text{ID}} \cdot SF_{\text{iso}} \\ &= \frac{\varepsilon_{\text{trigger, data}}}{\varepsilon_{\text{trigger, MC}}} \cdot \frac{\varepsilon_{\text{reco, data}}}{\varepsilon_{\text{reco, MC}}} \cdot \frac{\varepsilon_{\text{ID, data}}}{\varepsilon_{\text{ID, MC}}} \cdot \frac{\varepsilon_{\text{iso, data}}}{\varepsilon_{\text{iso, MC}}} \end{aligned} \tag{4.4}$$

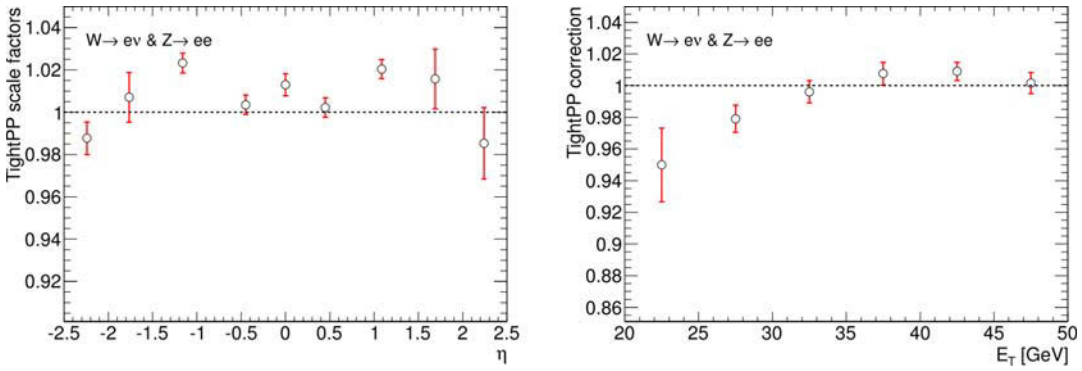

Figure 4.6: Electron tight identification scale factors as a function of η (left) and E_T (right) [123].

4.3 Muon

4.3.1 Reconstruction

Two different sets of algorithms are used in the ATLAS collaboration to reconstruct muons, called Muid and Staco, with the Muid muons recommended by the ATLAS top working group [137, 138]. Four different types of muons are reconstructed, depending on the available detector information. The muon trajectory of standalone muons is only constructed in the muon spectrometer. The direction of flight and the impact parameter of the muon at the interaction point are determined by extrapolating the track back to the point of origin taking the energy depositions in the calorimeters into account. Combined muons also includes information of the inner detector. The algorithm searches for inner detector tracks, which are associated to tracks in the muon system, and performs a global fit in order to calculate the final muon track. This fit is used to determine the transverse momentum of the muon, including corrections due to energy deposition in the calorimeter system. The algorithm of segment-tagged muons starts with a track in the inner detector and searches for associated track segments in the precision muon chamber. Such muons rely on the measurement of the transverse momentum in the inner detector. A fourth algorithm reconstructs calorimeter-tagged muons without information from the muon system, by analyzing the energy deposition along an extrapolated track in the calorimeters.

4.3.2 Momentum resolution

The relative resolution on the momentum measurement is dictated by different effects related to the amount of material that the muon traverses, the spatial resolution of the individual track points and the degree of internal alignment of the two subsystems [138, 139]. For a given value of η, the resolution can be parameterized as a function of p_T:

$$\frac{\sigma(p)}{p} = \frac{p_0^{\mathrm{MS}}}{p_T} \oplus p_1^{\mathrm{MS}} \oplus p_2^{\mathrm{MS}} \cdot p_T \,. \tag{4.5}$$

p_0^{MS}, p_1^{MS} and p_2^{MS} are coefficients related to the energy loss in the calorimeters material, multiple scattering and intrinsic resolution terms, respectively. The approximate parameterization of the inner detector resolution is

$$\frac{\sigma(p)}{p} = p_1^{\mathrm{ID}} \oplus p_2^{\mathrm{ID}} \cdot p_T \qquad \text{for } |\eta| < 1.9$$
$$\frac{\sigma(p)}{p} = p_1^{\mathrm{ID}} \oplus p_2^{\mathrm{ID}} \cdot p_T \frac{1}{\tan^2 \Theta} \qquad \text{for } |\eta| > 1.9$$

where p_1^{ID} and p_2^{ID} are the multiple scattering and the intrinsic resolution terms.
$Z \to \mu\mu$ events are used to determine the resolution corrections needed for simulated events in order to match data distributions. This correction has been identified using the width of the reconstructed di-muon invariant mass peak at the Z pole, which is a convolution of the natural width of the Z boson and the muon momentum resolution. A second quantity is the difference between the independent momentum measurements of the inner detector and muon system for combined muons, which is sensitive to the quadratic sum of two momentum resolutions. This difference is weighted by the muon electric charge $(q/p_T^{\mathrm{ID}} - q/p_T^{\mathrm{MS}})$. The corrections factors are obtained with a combined fit using a Monte Carlo template fit technique of the two quantities. Figure 4.7 shows an example for the Z lineshape for data and simulated events before and after resolution correction.

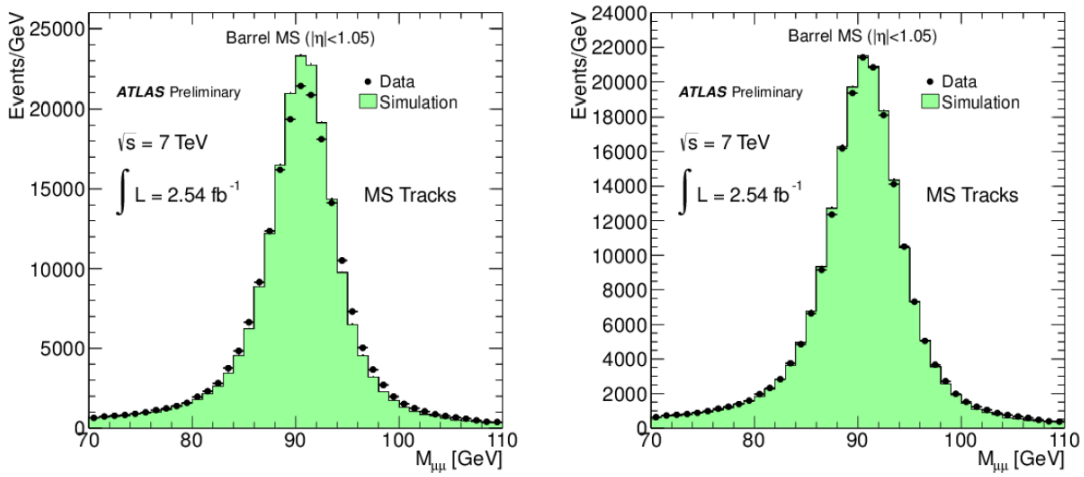

Figure 4.7: Example of data-to-Monte Carlo comparison of $Z \to \mu\mu$ mass distribution before (left) and after resolution correction (right). The data distribution shows a slightly worse resolution than the simulated events, resulting in a slightly broader Z mass peak [139].

4.3.3 Trigger

Three layers of resistive plate chambers in the barrel region ($|\eta| < 1.05$) and three layers of thin gap chambers in the endcap regions ($1.05 < |\eta| < 2.40$) provide the level-1 (L1) muon trigger [140, 141]. Muon candidates are identified by coincidence measurements of hits in layers of the trigger chambers. The hit pattern along the muon track is used to estimate the transverse momentum of the muon.
At level-2 (L2), the candidate is refined by using the precision data from the muon drift tubes. The muon standalone algorithm constructs a track within the Region-of-Interest, while the momentum and track parameters of the candidate are measured by fast fitting algorithms and look-up tables.
Full event data is available at the event filter (EF). Segments and tracks are reconstructed in the Region-of-Interest using information from the trigger and precision chambers. The track is then extrapolated back to the beam line to determine the track parameters at the interaction point. A muon combined trigger is formed by associating the muon candidate with a track in the inner detector. This "outside-in" strategy is complemented by another algorithm which extrapolates an inner detector track to the muon detectors, thus forming muon "inside-out" triggers. This strategy of two algorithms proved to be useful to minimize the risk of loosing events at the online selection.
Similar to the single electron analyses, the ATLAS top working group chose the unprescaled single muon trigger with the lowest p_T-threshold for events with a prompt muon in the final state. The transverse momentum threshold of the high level triggers (L2+EF) was kept at 18 GeV during data taking in 2011, while L1 trigger was changed from 10 GeV (L1_MU10) to 11 GeV (L1_MU11), when the luminosity reached $1.9 \cdot 10^{33}\,\mathrm{cm}^{-2}\mathrm{s}^{-1}$ at the beginning of August. Further, the L1_MU10 trigger was composed of coincidences of hits from a two station trigger in the barrel region and three hits in the endcap ragion, the L1_MU11 trigger used three stations in both regions. The seeding high level triggers are called mu18 and mu18_medium, respectively. Medium does not indicate any identification criteria, but the changed L1 requirements. The trigger chains and their corresponding run periods in 2011 are listed in Table 4.3.

Run period	L1	HLT
B-I	MU10	mu18
J-M	MU11	mu18_medium

Table 4.3: Single muon trigger chains used during data taking in 2011, which had to be reoptimized due to changing luminosity conditions. A trigger chain consists of the level-1 (L1) and subsequently the two high-level triggers (HLT), the level-2 and event filter trigger [141].

4.3.4 Object definition

A muon candidate is only considered if it is reconstructed as a combined muon by the Muid algorithm. Further, the muon is required to have a minimum transverse momentum of 20 GeV and lie within the detector range of $|\eta| < 2.5$. The reconstructed muon track is expected to have a longitudinal impact parameter smaller than 2 mm with respect to the primary vertex.
Additional requirements are applied on the associated inner detector tracks:

- At least one pixel b-layer hit on the muon, except the extrapolated muon track passed an uninstrumented or dead area of the b-layer.
- Number of pixel hits + number of crossed dead pixel sensors > 1.
- Number of silicon microstrip tracker hits + number of crossed dead silicon microstrip tracker sensors > 5.
- Number of pixel holes + number of silicon microstrip tracker holes < 3.
- An extended track is expected to have hits in the transition radiation tracker and a low fraction of outliers. Let $nTRThits$ denote the number of transition radiation tracker hits on the muon track, $nTRToutliers$ the number of transition radiation tracker outliers on the muon track, and $n = nTRThits + nTRToutliers$:
  - $|\eta| < 1.9$: Require $n > 5$ and $nTRToutliers < 0.9\,n$.
  - $|\eta| \geq 1.9$: If $n > 5$, require $nTRToutliers < 0.9\,n$.

In the single muon channel, the selected lepton has also to be the triggered particle. This is verified by matching the muon to a trigger object within a distance of $\Delta R = 0.15$. In order to select real prompt muons with high probability and reject muons inside of jets, e.g. muons from b-meson decays, cuts on the calorimetric and track-based isolation are required. The definitions on both variables are very similar to the isolation of electrons, with slight modifications concerning the good quality of tracks. Considered tracks must have at least four hits in the pixel and silicon strip detectors and a transverse momentum above 1 GeV. Selected muons are expected to have a calorimetric isolation below 2.5 GeV within a cone of ΔR=0.3, and a track-based isolation below 4 GeV for a $\Delta R = 0.2$. In addition, muons are rejected, if the distance between a muon and a jet is smaller than $\mathrm{d}R = 0.4$.
Scale factors are applied to each simulated single muon event to correct the data-to-Monte Carlo differences in trigger, reconstruction and isolation efficiency. Similar to the electron measurements, all effciencies are measured using the tag&probe method with $Z \to \mu\mu$ events. The results of the reconstruction efficiency measurements are shown in Figure 4.8 with scale factors very close to unity for the total η-range. Overall, one muon weight is defined for each single muon event:

$$SF_\mu = SF_{\text{trigger}} \cdot SF_{\text{reco}} \cdot SF_{\text{iso}} = \frac{\varepsilon_{\text{trigger, data}}}{\varepsilon_{\text{trigger, MC}}} \cdot \frac{\varepsilon_{\text{reco, data}}}{\varepsilon_{\text{reco, MC}}} \cdot \frac{\varepsilon_{\text{iso, data}}}{\varepsilon_{\text{iso, MC}}} \,. \tag{4.6}$$

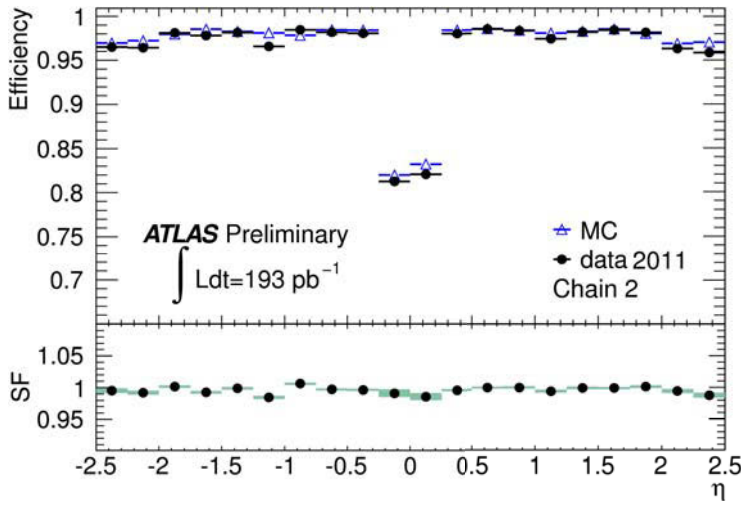

Figure 4.8: Combined muon reconstruction efficiency with respect to the inner tracking efficiency as a function of the pseudorapidity. Only Muid muons with $p_T > 20\,\text{GeV}$ are considered. The panel at the bottom shows the ratio between the measured and predicted efficiencies, i.e. the scale factors, which have been applied to the simulated events [142].

4.4 Missing transverse energy

Neutrinos cannot be detected by any subsystem of the ATLAS detector, but their energies can be estimated from the energy imbalance of an event in the transverse plane [143, 123, 144]. The missing transverse energy $\not{E}_T$ is reconstructed with the assumption that the initial energy in the transverse direction is zero, since protons are colliding in the z-direction. The calculation takes into account contributions from energy deposits in the calorimeters and muon tracks, which are reconstructed either in the muon spectrometer or in the inner detector. Tracks are added to recover the contribution from low-p_T particles which are missed in the electromagnetic or hadronic calorimeter. The $\not{E}_T$ reconstruction uses calorimeter cells calibrated according to the reconstructed physics object to which they are associated. Cell energies, which are not associated with any objects, are included as a cell out term calibrated to the elecromagnetic scale. The missing transverse energy is then calculated as:

$$\not{E}_T = \sqrt{(\not{E}_x)^2 + (\not{E}_y)^2}$$

$$-\not{E}_{x,y} = E_{x,y}^{\text{electron}} + E_{x,y}^{\text{photon}} + E_{x,y}^{\text{muon}} + E_{x,y}^{\text{jets}} + E_{x,y}^{\text{soft jet}} + E_{x,y}^{\text{cell out}}$$

The individual terms take into account following object definitions:

- The electron and photon term are calculated from electron and photon candidates with a transverse energy above 10 GeV, which pass the tight identification criteria.
- Jets with a $p_T > 20\,\text{GeV}$ are used, which have been calibrated to the EM+JES energy scale.
- Soft jets with a p_T between 7 GeV and 20 GeV are also taken into account, calculated at the electromagnetic scale.

- Considered muons are reconstructed as Muid muon candidates with $|\eta| < 2.7$. Combined muons within $|\eta| < 2.5$ are included in the $\not{E}_T$ calculation, while only standalone muons are available in the region $2.5 < |\eta| < 2.7$, which is not covered by the inner detector. Is a muon isolated, i.e. the minimum distance to any jet is $\Delta R = 0.3$, its energy loss in the calorimeters is included in the cell out term. The calorimeter energy deposits of non-isolated muons is included in the jet term.

4.5 Photon

4.5.1 Reconstruction

Photon candidates are reconstructed with the same algorithm as electrons, which is based on seed clusters in the electromagnetic calorimeter [145, 146]. Two types of photons have to be considered: unconverted photons and photons, which have converted into an electron-positron pair. If no track is associated to the energy deposit, the cluster is considered to be an unconverted photon candidate. Photons reconstructed as converted are characterized by at least one track matching energy deposit originating from a conversion vertex detected in the inner detector, which results in a certain amount of ambiguity between electrons and photons. The conversion vertices are classified depending on the number of electron tracks assigned to them. Typically, two tracks are assigned to the vertex, which is reconstructed by performing a constrained vertex fit using the track parameters of the two participating electrons. There are possibilities, where one track can fail to be reconstructed, In case of asymmetric conversions a track can have a transverse momentum below the reconstruction threshold of 500 MeV, other than that, both electrons can be very high energetic resulting in two tracks which are too close to each other to be adequately separated. In case of these single-track conversion vertex candidates, a vertex fit cannot be performed. The conversion vertex is then placed at the location of the first measurement of the participating track, but the original photon momentum vector cannot be determined. If any of these single- or double-track conversion vertex candidates matches an electromagnetic energy cluster, it is considered a converted photon candidate. This matching procedure varies according to the characteristics of the conversion vertex candidate: In case of a single-track conversion, the track is extrapolated to the second calorimeter sampling from its last measurement. For double-track conversion vertex candidates, where one track momentum is more than four times smaller than the other track momentum, the original converted photon direction is extrapolated to the second sampling of the electromagnetic calorimeter. If the ratio between the two track momenta is less than four, each track is extrapolated individually to the calorimeter second sampling, as in the case of the single-track conversion vertex candidates. If both then are matched to the same cluster, the conversion vertex candidate is considered as matched to that cluster, too. In all three cases, a converted photon candidate is found, if the impact point in the calorimeter is within a 0.05×0.05 window in η-ϕ-space from the cluster center in that sampling.
After the initial reconstruction steps, almost all converted photons are treated as electron candidates, as well as a few unconverted photon candidates that have erroneously

matched tracks from other sources than an electron or conversion track. Recovery procedures have been established to identify these candidates and hence eliminate possible double counting between photon and electron candidates. For electron candidates with assigned conversion vertex candidates, the best matched track is evaluated against the tracks originating from the best conversion vertex candidate matched to the same cluster. If the track coincides with a track coming from the conversion vertex, then this electron is treated as a converted photon. The only exception is the case of a double-track conversion vertex candidate where one track lacks a b-layer hit. If the track does not coincide with any of the tracks assigned to the conversion vertex candidate, then it is kept as an electron, unless the transverse momentum of the track is smaller than the one of the converted photon candidate. Converted photons can also be recovered without an assigned conversion vertex candidate: If the originally reconstructed electron has a best matched track that is made of only hits in the transition radiation tracker with $p_T > 2\,\text{GeV}$ and a ratio of the cluster energy and track momentum smaller than 10, it is also considered a converted photon. All the electrons matched with a track, which was only reconstructed in the transition radiation tracker and with $p_T < 2\,\text{GeV}$, are automatically considered to be unconverted photon candidates. In addition, electrons that failed to be considered as converted photon candidates, and for which their best matched track has $p_T > 2\,\text{GeV}$ or a ratio of the cluster energy and track momentum smaller than 10, will also be treated as unconverted photon candidates.

4.5.2 Identification

The photon identification is based on rectangular cuts using calorimetric variables which deliver good separation between prompt photons and photons from meson decays, in particular $\pi^0 \to \gamma\gamma$ which originate in jet fragmentations. Two reference sets of cuts have been defined, loose and tight, which include cuts on hadronic leakage, variables using the second longitudinal compartment of the electromagnetic calorimeter and variables using the first longitudinal compartment, the so-called strip layer. A very brief description of these variables is listed in Table 4.4. The cuts are optimized by performing a multivariate analysis in various $|\eta|$ regions. Tight cuts are separately optimized for unconverted and converted photon candidates.

For trigger purposes, electrons and photons share a common set of loose cuts and cut thresholds. This subset of discriminating variables shows relatively small differences for unconverted and converted photons, so using only these variables in the loose selection keeps the two efficiencies for the two types of photons as similar as possible. The values of the cuts are optimized for nine different $|\eta|$ regions.

The tight photon requirements comprise tighter cuts on the variables used for the loose cut selection, an additional cut on one middle layer quantity, and especially cuts on quantities computed from the energy deposit in the strip layer, which provides a good separation between prompt photons and π^0 due to its fine granularity. Therefore, photon candidates have to be within the pseudorapidity region covered by the finely segmented part of the first layer of the electromagnetic calorimeter: $|\eta| < 2.37$, except the crack region between 1.37 and 1.52. The tight cuts are separately optimized for unconverted and converted

photon candidates, in each of the seven pseudorapidity regions covered by the strip layer. The cut thresholds are chosen in order to provide an identification efficiency around 85% with respect to the collection of reconstructed candidates for both unconverted and converted photons with $E_T > 20\,\text{GeV}$.
Discrepancies have been observed between the discriminating variables (DV) recorded in data and Monte Carlo simulation [147, 148]. These discrepancies are particularly pronounced for variables accounting for the lateral electromagnetic shower profile, e.g. R_η, $w_{\eta 2}$ and F_{side}, with increasing disagreement at lower transverse energies. Representative examples for distributions of R_η and $w_{\eta 2}$ are shown in Figure 4.9. These discrepancies can be at first order approximated by a small shift, that can be evaluated as the difference between the means of the DV distributions in data and simulation:

$$\Delta\mu_{\text{DV}} = \langle \text{DV}_{\text{data}} \rangle - \langle \text{DV}_{\text{MC}} \rangle \,.$$

These corrections have been evaluated in multiple regions of η and E_T and then applied to each photon candidate in Monte Carlo simulation, before checking its compatibility with the tight identification criteria:

$$\text{DV}_{\text{MC}}^{\text{corr}} = \text{DV}_{\text{MC}} + \Delta\mu_{\text{DV}}(E_T, \eta) \,.$$

Figure 4.10 show the data-driven identification efficiencies, compared to Monte Carlo predictions with and without corrections. The uncorrected Monte Carlo efficiencies tend to be overestimated with respect to the corrected Monte Carlo and the data-driven values, both of which are in reasonable agreement within their uncertainties. This is the consequence of electromagnetic showers from photons typically being narrower in the simulation compared to those in data. The different results converge at high transverse energies. For unconverted and converted photons, the corrected Monte Carlo overestimates the efficiency in the high η region at low E_T by up to 9%. This feature is associated to the tight thresholds applied to the R_ϕ and F_{side} variables, where even small differences between data and Monte Carlo can lead to large discrepancies. Otherwise, the difference is always within $\pm 5\%$.

Type	Description	Name
	Loose selection	
Acceptance	$\|\eta\| < 2.47$	
Hadronic leakage	Ratio of E_T in the first layer of the hadronic calorimeter to E_T of the EM cluster, used in the range of $\|\eta\| < 0.8$ and $\|\eta\| > 1.37$	R_{had1}
	Ratio of E_T in the hadronic calorimeter to E_T of the EM cluster, used in the range of $\|\eta\| > 0.8$ and $\|\eta\| < 1.37$	R_{had}
Middle layer of EM calorimeter	Ratio in η of the energy in 3×7 cells over the energy 7×7 cells centered at the electron cluster position	R_η
	Lateral shower width, $\sqrt{(\sum E_i \eta_i^2)/(\sum E_i) - ((\sum E_i \eta_i)/(\sum E_i))^2}$, where E_i is the energy and η_i is the pseudorapidity of cell i. The sum is calculated within a window of 3×5 cells	$w_{\eta 2}$
	Tight selection (includes loose)	
Acceptance	$\|\eta\| < 2.37$, excluding $1.37 < \|\eta\| < 1.52$	
Middle layer of EM calorimeter	Ratio in ϕ of the energy in 3×3 cells over the energy 3×7 cells centered at the electron cluster position	R_ϕ
Strip layer of EM calorimeter	Shower width, $\sqrt{(\sum E_i (i - i_{max})^2)(\sum E_i)}$, where i runs over all strips in a window of $\Delta\eta \times \Delta\phi \approx 0.0625 \times 0.2$, corresponding typically to 20 strips in η, and i_{max} is the index of the highest-energy strip	w_{stot}
	Shower width for three strips around maximum strip	w_{s3}
	Fraction of energy outside core of three central strips, but within seven strips	F_{side}
	Difference between the energy associated with the second maximum in the strip layer, and the energy reconstructed in the strip with the minimal value found between the first and second maxima	ΔE
	Ratio of the energy difference between the largest and second largest energy deposits in the cluster over the sum of these energies	E_{ratio}

Table 4.4: Short description of photon shower variables used for photon identification [146].

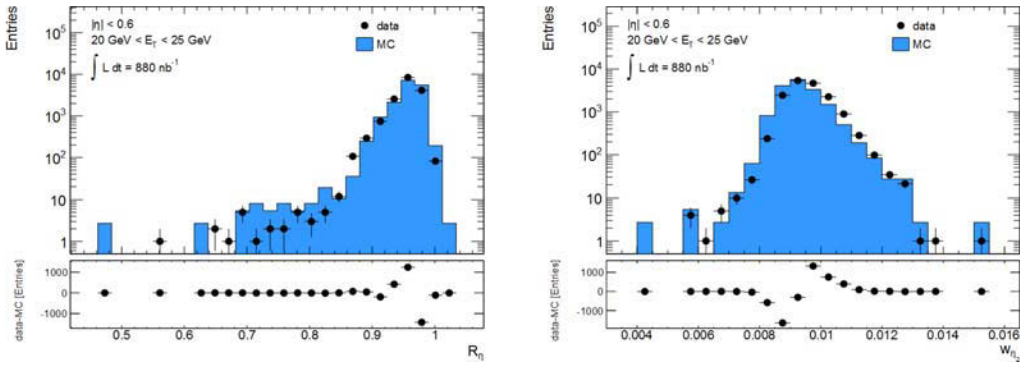

Figure 4.9: R_η and $w_{\eta 2}$ distributions in data (black points) and Monte Carlo simulation (blue distributions) for photon candidates with $|\eta| < 0.6$ and $20\,\text{GeV} < E_T < 20\,\text{GeV}$. The data-to-Monte Carlo difference subfigures indicate, that a simple shift of the simulated distribution is sufficient to match data [147].

4.5.3 Object defintion

A photon candidate is considered, if it has been reconstructed as an unconverted or converted photon with a minimum transverse energy of 20 GeV. The energy is defined as the cluster energy divided by the hyperbolic cosine of the track pseudorapidity, both measured in the second sampling of the electromagnetic calorimeter:

$$E_T = \frac{E_{\text{cluster, s2}}}{\cosh(\eta_{\text{track, s2}})}\,.$$

The energy was calibrated as described in Section 4.2.2. Since no pure photon sample could be obtained with high enough statistics, the energy scale factors of electrons were corrected using Monte Carlo simulation to include small differences between the shower shapes of unconverted photons, converted photons and electrons. The pseudorapidity range is limited to the first calorimeter layer ($|\eta| < 2.37$), excluding the transition region between the barrel and endcap part of the electromagnetic calorimeter ($1.37 < |\eta| < 1.52$). Further, all cluster cells of a photon candidate have to be checked for possible hardware problems during data taking. This also includes the photon cleaning procedure, which disentangles the signal of real energy deposits in the calorimeter and electronic noises by classifying the quality of the photon cluster [149]. Finally, a photon candidate has to pass the tight identification criteria, in order to select real prompt photons with high probability.

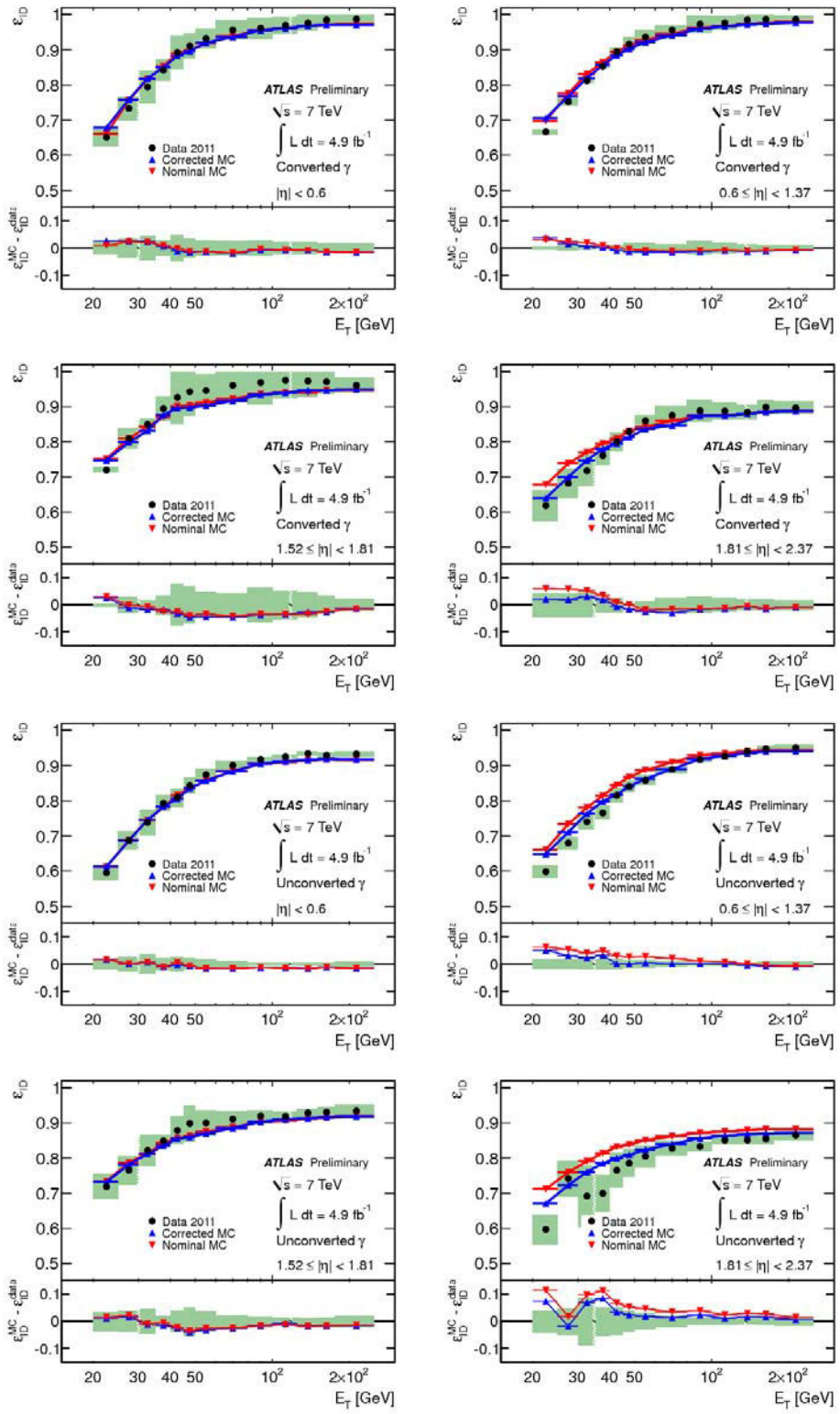

Figure 4.10: Photon identification efficiencies of converted (upper two rows) and unconverted photons (lower two rows) in a transverse energy range $15\,\text{GeV} < E_T < 300\,\text{GeV}$ and four different η regions. Data measurements are shown as black points, including green uncertainty banda corresponding to the combined statistical and systematic uncertainties. Effiencies from Monte Carlo simulation are shown before (red) and after shower shape corrections (blue), including statistical uncertainties. The lower part of each figure shows the difference between the data-driven curve and nominal and corrected Monte Carlo predictions [148].

Chapter 5

Data sample and Monte Carlo modeling

5.1 Dataset

2011 was a highly successful year for the LHC and its experiments. After the first year of high energy collisions at $\sqrt{s} = 7\,\text{TeV}$ delivering around $48\,\text{pb}^{-1}$ of data in 2010 [107], the instantaneous luminosity of the LHC was steadily increased throughout the year 2011, reaching a total integrated luminosity of $5.61\,\text{fb}^{-1}$. The ATLAS experiment achieved a high data taking efficiency of around 93.5 % and $5.25\,\text{fb}^{-1}$ of data, recorded from March 13th to October 30th.
The instantaneous luminosity was increased by focussing the proton beams more tightly at the interaction points, increasing the numbers of proton bunches filled in the LHC up to a maximum of 1380 and reducing the bunch spacing time from 75 ns to 50 ns.
A big challenge for analyses with 2011 data is the increasing amount of pile-up, i.e. additional interactions per bunch crossing. The increased number of protons and the improved focusing of both beams enhanced the contribution of additional proton-proton interactions in the same bunch crossing (in-time pile-up). The reduced bunch spacing adds interactions from more than one bunch crossing (out-of-time pile-up), which is recorded due to the finite integration time of subdetector components. This leads to a wrong assignment of detector signals to bunch crossings. Figure 5.1 shows the distribution of the average number of intersections per bunch crossing in the 2011 dataset.
Each LHC fill contains at least one ATLAS run, which is defined by the time period during which the expriment takes data. Ideally, one run is corresponding to one LHC fill, if data taking is not interrupted due to problems with the subdetector systems. Each run is subdivided into time intervalls of approximately one minute, called luminosity blocks. Runs with similar beam and detector conditions are grouped in periods. In 2011, a total of twelve periods were defined, from B to M.
Online and offline data quality monitoring systems [150, 151] are operated by ATLAS to ensure that data were taken under well defined and stable conditions. The online monitoring checks data right after recording to quickly respond to possible problems with detector systems or the LHC beam conditions. The offline monitoring is performed after the first event reconstruction to identify problems in the detector systems or data acquisition and processing. All this information is combined to obtain a list of luminosity blocks in each run of data taking, which have passed the data quality criteria and hence are usable for analyses. In 2011, $4.66\,\text{fb}^{-1}$ of the total recorded data passed these quality checks and are used in this analysis. Table 5.1 shows an overview of all data periods and the correspond-

ing integrated luminosities, considering only luminosity blocks passing the quality criteria.

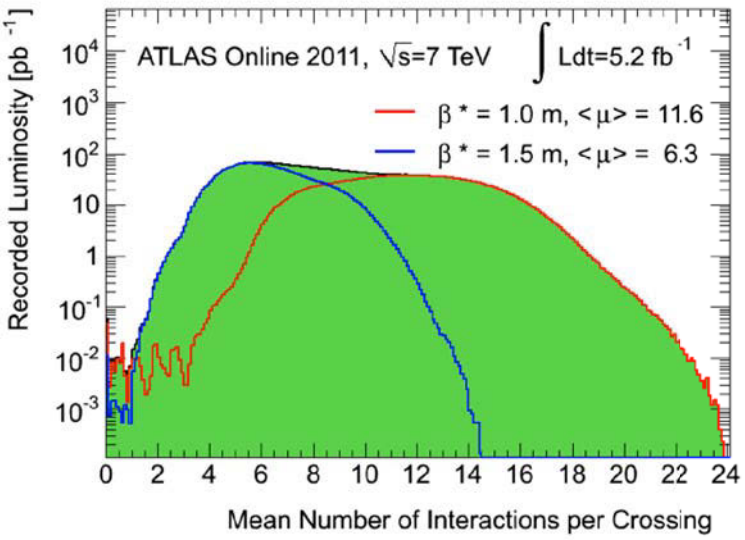

Figure 5.1: The luminosity-weighted distribution of the mean number of interactions per bunch crossing for 2011 data. The amplitude function β^*, which describes the beam size at the interaction point, was reduced in the September technical stop from 1.5 m to 1.0 m. The plot shows the distribtutions before the stop (blue) and after the parameter change (red) [107].

period	run range	int. luminosity [pb^{-1}]
B-D	177986 - 180481	176.25
E-H	180614 - 184169	937.71
I	185353 - 186493	333.24
J	186516 - 186755	223.49
K	186873 - 187815	583.27
L-M	188902 - 191933	2401.77

Table 5.1: Overview of all data periods and the corresponding run number ranges, subdividing all data recorded by ATLAS in 2011. The listed integrated luminosities only take into account luminosity blocks passing the data quality checks.

5.2 Data streams

Three different types of event filter are applied to data, which are specificied for the ATLAS top working group. These filters are used to reduce the number of data events before analysis. Two of these data streams preselect events with a lepton above a certain p_T-threshold and are used for the corresponding channel in the single lepton analysis. The third event filter selects events with four or five jets above specific p_T-thresholds. This stream was defined for $t\bar{t}$ analyses in the all-hadronic channel, but is also used in this analysis for the control region of background events with hadrons misidentified as photons.
At least of the conditions listed below has to be fulfilled in each data stream.

Electron event

1. At least one electron with $p_T > 20$ GeV.
2. At least one electron with $p_T > 13$ GeV, and
   - $\not{E}_T$ above 20 GeV or
   - two leptons (electron or muon) with $p_T > 13$ GeV.

Muon event

1. At least one muon with $p_T > 18$ GeV.
2. At least one muon with $p_T > 13$ GeV, and
   - $\not{E}_T$ above 20 GeV or
   - two leptons (electron or muon) with $p_T > 13$ GeV.

Jet event

1. At least four jets with $p_T > 20$ GeV and at least two jets with $p_T > 40$ GeV.
2. At least five jets with $p_T > 20$ GeV.

5.3 Event simulation

The simulation of Monte Carlo processes is performed in several steps:

1. A leading-order or next-to-leading-order Monte Carlo generator is used to calculate the matrix element of a particular hard scattering process and generate events, consisting of the four-momenta of incoming and final state particles and in most cases also the intermediate state particles.
2. The hard process events are interfaced to a second Monte Carlo generator which provides models for the non-perturbative evolution of the final state including parton showering and hadronization. Two main generators are used in ATLAS, providing two different hadronization models. The PYTHIA generator is based on the Lund

string model [152], while the HERWIG generator uses a cluster model [153]. These generators also provide simulations of initial state and final state radiation, multiple parton interactions and pile-up. In case of HERWIG, a library of routines called JIMMY is linked to simulate underlying events [154]. In addition, the PHOTOS package is linked to both showering programs providing improved predictions for QED corrections [155].

3. In the next step, the events are passed to the detector simulation with Geant4 [156, 157]. Using the latest, detailed descripton of the ATLAS detector, the interactions of the particles with matter and their behavior within the magnetic field of the detector are simulated [158].

4. The detector response is translated into digital signals simulating the response of the ATLAS readout system.

5. The digitized events are passed to the reconstruction algorithm, which are the same ones used for the event reconstruction in data.

5.4 $t\bar{t}\gamma$ simulation

The $t\bar{t}\gamma$ signal sample was generated with the Monte Carlo generator WHIZARD, taking into account all possible processes leading to the seven particle final states

$$pp \to bl_1^+\nu_{l_1}\bar{b}l_2^-\bar{\nu}_{l_2}\gamma\,,\;\; pp \to bq_1\bar{q}_2\bar{b}l^-\bar{\nu}_l\gamma\,,\;\; pp \to bl^+\nu_l\bar{b}q_1\bar{q}_2\gamma\,.$$

WHIZARD considers the CKM matrix to be unitary, hence the two incoming partons of the colliding protons are either two gluons or a quark-anti-quark pair ($u\bar{u}$, $d\bar{d}$, $c\bar{c}$, $s\bar{s}$, $b\bar{b}$). The two quarks $q_1\bar{q}_2$ in the final state are an up-type light quark paired with the anti-particle of its down-type partner ($u\bar{d}$, $d\bar{u}$, $c\bar{s}$, $s\bar{c}$). All three lepton flavors are considered in the final state: $l^\pm = e^\pm$, $\mu^\pm$, $\tau^\pm$.
Light quarks (u, d, s, c) and electrons are assumed to be massless. The masses of muons and tau leptons are set to $m_\mu = 105\,\text{MeV}$ and $m_\tau = 1776\,\text{MeV}$, respectively. Bottom quarks have a mass of $m_b = 4.2\,\text{GeV}$, while the top quark mass was set to $m_t = 172.5\,\text{GeV}$. The Standard Model Higgs boson is also considered in the calculations with a mass of $m_H = 115\,\text{GeV}$.
In order to avoid collinear and infrared divergences, a lower bound of the photon energy and a minimum distance between various incoming and final state partons had to be defined for the phase space calculation. Therefore, the transverse momentum of the photon had to be above 8 GeV and the invariant masses of the following parton pairs were required to be above 5 GeV:

- $m_{\text{inv}}(q_1, q_2)$: Both light quarks in the final state,
- $m_{\text{inv}}(q_i, \gamma)$: Each of the light quarks in the final state and the photon,
- $m_{\text{inv}}(l, \gamma)$: The charged lepton and the photon,

- $m_{\text{inv}}(Q_i, \gamma)$: Each of the incoming light quarks and the photon,
- $m_{\text{inv}}(g_i, q_j)$: Each of the incoming gluons and each of the light quarks in the final state,
- $m_{\text{inv}}(Q_i, q_j)$: Each incoming light quark and the same parton in the final state,
- $m_{\text{inv}}(l_1, l_2)$: The two charged leptons in the final state.

Further, a lower p_T-threshold of all final state particles, except the photon, was set to 10 GeV. The signal sample has an absolute cross section of 0.84 pb. Theoretical calculations of the $t\bar{t}\gamma$ cross section provided a 2.55 times larger result with next-to-leading order precision [159, 160], compared to the leading order expectation. This k-factor was applied to the WHIZARD sample, including an uncertainty of 0.50 estimated by the comparison of the k-factors renormalization scales of m_t and $2m_t$, the latter being the scale used for the event generation.
These events were interfaced to the parton showering program HERWIG, which also calculated photon radiation from quarks. QED corrections from leptons were perfomed by PHOTOS. The CTEQ6L1 PDF set [47] was applied during the matrix element calculation and event generation with WHIZARD as well for the parton showering.

5.4.1 WHIZARD

WHIZARD is a multi-purpose, leading-order Monte Carlo event generator with automatic matrix element generation [161]. In contrast to many other Monte Carlo programs, WHIZARD is not limited by a fixed library of physics processes. Any process can be considered that is possible on tree level for two incoming partons and up to eight partons in the final state. All possible Feynman diagrams are included in the calculation for a defined final state, which is a necessary feature for the $t\bar{t}\gamma$ generation, as the calculation also takes into account any possible interference terms.
The matrix element is calculated by the O'MEGA generator [162]. The evaluation of a tree level matrix element can be very time consuming and demanding on computer hardware, hence O'MEGA uses numerical approaches to reduce the growth in calculational effort from a factorial of the number of particles to an exponential. The tree-level scattering amplitude is expressed in terms of sub-amplitudes with one external off-shell particle that can be constructed recursively. Feynman diagrams are therefore not generated separately and sub-amplitudes appearing more than once in the amplitude are factorized by construction, avoiding redundant code [163].
WHIZARD is linked to the VAMP algorithm for phase space integration which is a multichannel modification of the VEGAS algorithm [164].

5.5 Background simulation

Several different Monte Carlo generators are used to generate top quark pair events as well as various background processes [165, 166]. All Monte Carlo samples, that are used in this analysis, are listed in Appendix A with their respective cross sections and k-factors.

5.5.1 Top quark pair production

MC@NLO [167, 168] is used as the default generator for the $t\bar{t}$ production in ATLAS, producing top quark pair events without explicit photon radiation within the hard scattering process. MC@NLO is a next-to-leading order Monte Carlo generator, i.e. it produces $pp \to t\bar{t}$ events at next-to-leading order accuracy. The events are then passed to the HERWIG Monte Carlo generator, which handles the decay of the top quarks as well as the subsequent parton showering. Events are generated with the PDF set CT10 [169], while HERWIG parameters for parton showering and the underlying event simulation were set to the ATLAS AUET1 tune [170].
The total cross section is calculated by the HATHOR tool with an approximate next-to-next-to-leading order calculation precision [171], resulting in a cross section of $\sigma_{t\bar{t}} = 165^{+11}_{-16}\,\mathrm{pb}^{-1}$.
Additional $t\bar{t}$ samples are produced with various Monte Carlo generators in order to study systematic uncertainties related to the choice of the generator. POWHEG [172] is used as an alternative next-to-leading-order generator to MC@NLO. Two different POWHEG samples were produced. One sample is interfaced with HERWIG, the other one with PYTHIA, to study possible differences between the two parton showering programs. The amount of initial state and final state radiation is studied using ACERMC samples [173] interfaced to PYTHIA with modified radiation parameters [174].

5.5.2 W boson production with additional partons

W boson production processes with up to five additional partons in the final state (W+jets events) were generated with ALPGEN [175] using the PDF set CTEQ6L1. The W boson is decaying leptonically into one of the three charged leptons and their corresponding anti-neutrino ($W \to e\bar{\nu}_e$, $\mu\bar{\nu}_\mu$, $\tau\bar{\nu}_\tau$). Parton showering is run with HERWIG using the ATLAS AUET1 tune. Samples are produced separately for zero to five partons and a specific jet-parton matching scheme is applied. Jets produced by the showering program HERWIG are matched to the final state from the matrix element calculation. The event is kept if each parton can be matched to a jet within a defined η-ϕ distance, otherwise it is rejected. For parton multiplicities up to four, each simulated jet has to match to one parton (exclusive sample), while the sample with the highest jet multiplicity, extra jets are allowed to be present after the parton showering (inclusive sample).
W+jets processes are the main background source for $t\bar{t}$ analyses, with a significant fraction originating from events with b- and c-quark in the final state passing the b-tagging requirements. Hence, statistics were enhanced by generating additional samples for $W+b\bar{b}$+jets, $W+c\bar{c}$+jets and $W+c$+jets events with up to a total of five partons in

the final state. Overlapping events within the heavy flavor and nominal W+jets samples were removed to avoid double-counting [166].
The total cross sections of the individual samples are calculated with next-to-next-to-leading-order accuracy using the FEWZ and ZWPROD programs [176, 177, 178].

5.5.3 W boson production associated with a photon and additional partons

Two different types of Monte Carlo samples are used in this analysis which include W boson production processes with up to five additional partons and a photon in the final state (W+jets+γ events):
First, events were simulated with up to five partons using ALPGEN and HERWIG with exactly the same settings as the nominal W+jets samples. To avoid collinear and infrared divergencies, the photon has a transverse momentum above 10 GeV and a minimum distance in η-ϕ-space to other final state particles of $\Delta R = 0.1$. The total cross sections calculated by ALPGEN are corrected with a k-factor of 1.37 obtained from the ATLAS $W + \gamma$ cross section measurement [179].
The leading-order Monte Carlo generator SHERPA [180] was used for another set of W+jets+γ samples. The generator not only simulates the hard scattering processes, but also the parton showering of the final state quarks. The matrix element calculation considered all processes of a leptonically decaying W boson, a photon and up to three partons, including light and heavy quarks (u, d, s and c, b). Like for the ALPGEN samples, the photon-p_T was required to be above 10 GeV and the minimum distance between the photon and the other final state particles is $\Delta R = 0.1$.

5.5.4 Z boson production with additional partons

Z boson production processes with up to five additional partons in the final state (Z+jets events) were generated in analogy to the W+jets simulation, using ALPGEN interfaced to HERWIG with the AUET1 tune and the CTEQ6L1 PDF set. The Z boson is decaying leptonically into a lepton-anti-lepton pair ($Z \to e^+e^-$, $\mu^+\mu^-$, $\tau^+\tau^-$). Parton-jet-matching was perfomed for these samples as well, exclusively for events up to four partons and inclusively for five partons. Samples containing Z+$b\bar{b}$+jets events are produced with up to three additional partons in the final state and the overlapping events with the nominal samples are removed.
The total Alpgen cross sections are corrected by next-to-next-to-leading-order calculations with FEWZ and ZWPROD.
The cross section uncertainties are evaluated using Berends-Giele scaling [181, 182], depending on the number of jets in the final state. The uncertainty is estimated to 24% for each jet, which are treated uncorrelated and hence added quadratically to 48% for events with at least four jets.

5.5.5 Single Top Quark Production

Single top quark processes in the Wt- and s-channel are simulated with MC@NLO interfaced to HERWIG. ACERMC+PYTHIA is used for the simulation of t-channel processes. Due to an ambiguity of diagrams from the top quark pair production and the Wt-channel, overlapping diagrams are removed from the single top sample [183].
The cross sections are calculated with approximate next-to-next-to leading order accuracy: $64.6^{+2.7}_{-2.0}\,\mathrm{pb}^{-1}$ for the t-channel, $4.6 \pm 0.2\,\mathrm{pb}^{-1}$ for the s-channel and $15.7 \pm 1.1\,\mathrm{pb}^{-1}$ for Wt-channel [56, 57, 58].

5.5.6 Diboson production

HERWIG is used for parton showering and the simulation of the hard scattering processes of the diboson samples, separately for WW, WZ and ZZ events. The samples are filtered for events with at least one lepton in the final state with $p_T > 10\,\mathrm{GeV}$ to ensure that not both bosons have decayed hadronically.
k-factors are calculated with the MCFM code [184] to correct the total cross sections obtained from HERWIG.

5.6 Signal phase space overlap

The $t\bar{t}$ Monte Carlo simulation, which is generated with MC@NLO and HERWIG, does include photon radiation within the top quark pair event. Such photons are not considered in the matrix element calculation, but are added as corrections in the parton showering process, either emitted from single quarks by HERWIG or from charged leptons by the PHOTOS package. Hence, the $t\bar{t}$ sample has to be checked for $t\bar{t}\gamma$ events within the phase space, already covered by the WHIZARD simulation.
First, the MC@NLO sample is checked on Monte Carlo generator level (before detector simulation), if a photon is emitted in the top quark pair event from either the initial quarks, the top quarks or their decay particles. If this is the case, the event is investigated with regard to the phase space cuts, which have been applied to the WHIZARD sample, i.e. the invariant mass requirements as well as the lower p_T-thresholds of the final state partons, as listed in Section 5.4. The event is removed from the event selection, if all cuts are fulfilled, in order to avoid an overlap with the WHIZARD sample. Top quark events with an associated photon in the MC@NLO sample, which fail at least one requirement, are kept and considered to be background contribution. Overall, 0.5% of all MC@NLO events are removed due to the signal phase space overlap.

5.7 Monte Carlo event weights

Deviations have been observed between Monte Carlo prediction and measured data due to various sources of detector and physics mismodeling. Such descrepancies are adjusted by applying combined event weights to simulated events.
First, event weights w_{MC} are generated by the Monte Carlo generator, which are equal to

one, except for MC@NLO, where around 10% of the events are applied a weight of -1.
As described in Chapter 4, various event weights are assigned on object level to correct efficiency discrepancies in Monte Carlo and data. For each electron and muon, which passes the object selection, scale factors are applied to correct trigger, reconstruction, identification and isolation efficiencies (see equations 4.4 and 4.6). Further, b-tag efficiencies are corrected in simulated events by applying scale factors for each jet, which passes the object definition and b-tagging criteria, with different weights depending, if the jet has originated from a real b quark or not (see equations 4.1 and 4.2).
The pileup conditions during 2011 data-taking could not be perfectly simulated in Monte Carlo samples. In order to deal with these deviations, an event reweighting is applied to Monte Carlo simulation using the number of interactions per bunch crossing, averaged over all crossings within one luminosity block, $\langle\mu\rangle$. An event weight is assigned to each simulated event by comparing the $\langle\mu\rangle$-distributions in Monte Carlo and data in a range of 3.7 to 7.9 with an equal size of each bin i of 0.1:

$$w_{\text{pileup}} = \frac{\langle\mu\rangle_{i,\text{ Data}}}{\sum_i \langle\mu\rangle_{i,\text{ Data}}} \Bigg/ \frac{\langle\mu\rangle_{i,\text{ MC}}}{\sum_i \langle\mu\rangle_{i,\text{ MC}}} \ .$$

All weights are multiplied to one overall event weight:

$$\begin{aligned} w_{\text{event}} = & \prod_{\text{electrons}} (\text{SF}^{e}_{\text{trigger}}\text{SF}^{e}_{\text{reco}}\text{SF}^{e}_{\text{ID}}\text{SF}^{e}_{\text{iso}}) \prod_{\text{muons}} (\text{SF}^{\mu}_{\text{trigger}}\text{SF}^{\mu}_{\text{reco}}\text{SF}^{\mu}_{\text{iso}}) \\ & \times \prod_{\text{true } b-\text{jets}} \text{SF}_{\text{b-tag}} \prod_{\text{misid. } b-\text{jets}} \text{SF}_{\text{mistag}} \\ & \times w_{\text{MC}}\, w_{\text{pileup}} \, . \end{aligned}$$

The final event weight is applied to any event, regardless whether it has passed a certain step in the event selection (see Chapter 6) or not.

Chapter 6

Event selection and event yield

6.1 Event selection

An event selection is chosen according to the $t\bar{t}\gamma$ event signature in the single lepton decay channel: Exactly one electron or muon, high missing transverse energy $\not{E}_T$, four jets and one photon in the final state. The selection follows closely that of the single lepton $t\bar{t}$ analyses [185, 186], with the addition of photon selection cuts. It is applied in twelve subsequential steps:

1. A lepton trigger has fired. The specific trigger is chosen according to the data period and the single lepton channel. Further, events with large noise in the LAr calorimeter are discarded.

2. At least five tracks have to be associated to the primary vertex.

3. Electron channel: At least one selected electron is found in the event.

   Muon channel: At least one selected muon is found in the event.

4. Electron channel: Exactly one selected electron and no selected muon are required in the event.

   Muon channel: Exactly one selected muon and no selected electron are required in the event.

5. The only selected lepton has to match the trigger object within $\Delta R = 0.15$.

6. At least four jets have been selected. Further, events with one or more bad jets are discarded.

7. Electron channel: The missing transverse energy is required to be $\not{E}_T > 30\,\text{GeV}$.

   Muon channel: The missing transverse energy is required to be $\not{E}_T > 20\,\text{GeV}$.

8. Electron channel: The transverse mass of the leptonically decayed W boson is above 30 GeV. The transverse mass is defined as $m_{\text{T}}^{\text{W}} = \sqrt{2(p_{T,l}\,\not{E}_T - p_{x,l}\,\not{E}_x - p_{y,l}\,\not{E}_y)}$.

   Muon channel: The sum of $\not{E}_T$ and the transverse mass of the leptonically decayed W boson must be larger then 60 GeV, $\not{E}_T + m_{\text{T}}^{\text{W}} > 60\,\text{GeV}$

9. At least one of the selected jets has to be identified as a b-jet passing the MV1 tagging requirements.

10. At least one selected photon is required.

11. In case of the electron channel, the invariant mass of the selected electron and selected photons must not be within ±5 GeV of the Z boson mass window (86 GeV < $M_{\text{inv}} < 96$ GeV).

12. The minimum distance between the selected photons and each of the selected jets has to be $\Delta R = 0.5$.

The event selection is optimized to find $t\bar{t}\gamma$ events, while rejecting a large fraction from background processes. It is required that at least five tracks are coming from the primary vertex (at least one track per jet and one track of the charged lepton), which was introduced to reject non-collision background. The high threshold on the missing transverse energy as well as the requirements on the transverse mass of the leptonically decaying W boson reject a significant fraction of the QCD multijet background. Further, the requirement of at least one b-tagged jet largely reduces background contributions, e.g. from W+jets and

		e+jets channel	μ+jets channel
cuts	brief description	event yield	event yield
0	no cut	219386466	209422144
1	lepton trigger & LAr noise	164644802	170000278
2	prim. vertex with ≥ 5 tracks	163927865	169107111
3	≥ 1 lepton	19578304	34479705
4	exactly one lepton	18882270	32654364
5	trigger matching	18861076	32581314
6	≥ 4 jets, no bad jet	78138	101933
7	$\not{E}_{\text{T}}$ cut	48972	82733
8	$\not{E}_{\text{T}} + M_{\text{T}}(W)$ / $M_{\text{T}}(W)$ cut	40918	71767
9	≥ 1 b-tagged jet	21902	37963
10	≥ 1 photon	208	285
11	$m_{\text{inv}}(\gamma, e)$ window cut	184	285
12	$\Delta R(\gamma, \text{jet}) > 0.5$	165	249

Table 6.1: Data event yields after each cut of the $t\bar{t}\gamma$ event selection, shown separately for the e+jets and the μ+jets channel

Z+jets events, as these feature a small amount of b- and c-jets.
Top quark pair events are obtained by the first nine selection steps, which are optimized for the ATLAS top quark pair cross section measurements [187, 188]. Signal $t\bar{t}\gamma$ events are identified by requiring an additional photon. The p_T-threshold is set to a rather low value due to the steep slope of the photon p_T-spectrum in $t\bar{t}\gamma$ events. The invariant mass cut of the selected electron and photon is introduced to suppress the background contribution of Z+jets events, where an electron is misidentified as a photon. The minimum distance between the selected photon and all selected jets in $\eta - \phi-$space is included due to a decreasing photon identification efficiency for $\Delta R < 0.5$. This indicates that the photon shower shape variables used for the identification criteria are affected by energy deposits of close-by jets and therefore introduced a bias in the photon object selection.
Table 6.1 shows the number of data events after each selection step, separately for the e+jets and μ+jets channel. Accordingly to the single lepton channel, the electron and muon data stream are used, which introduce a preselection of the whole dataset of $4.7\,\text{fb}^{-1}$. After the signal selection, 165 $t\bar{t}\gamma$ event candidates were found in the e+jets channel and 249 $t\bar{t}\gamma$ event candidates in the μ+jets channel.
Table 6.2 lists the expected $t\bar{t}\gamma$ signal yield and selection efficiency after each selection cut for $4.7\,\text{fb}^{-1}$. The numbers are estimated with the WHIZARD Monte Carlo sample and include statistical uncertainties and k-factor uncertainties ($k = 2.55 \pm 0.5$). After the full selection, 58.1 ± 11.5 signal events are expected in the e+jets channel and 88.9 ± 17.5 events in the μ+jets channel, predicting that around 35% of the data candidates are indeed $t\bar{t}\gamma$ events. The drop in efficiency between cut 9 and 10 is due to the fact that the photon-p_T threshold in the Monte Carlo sample is 8 GeV, while a transverse momentum above 20 GeV is required for the reconstructed photon.
Figures 6.1 and 6.2 show various kinematic distributions measured in data, which are in good agreement with the expectation from Monte Carlo simulation using Monte Carlo samples described in Chapter 5. Further control plots are shown in Appendix B.1.

	e+jets channel		μ+jets channel	
cuts	event yield	efficiency	event yield	efficiency
0	9971 ± 1955	100 %	9971 ± 1955	100 %
1	2825 ± 554	28.3 %	2832 ± 555	28.4 %
2	2822 ± 553	28.3 %	2829 ± 555	28.4 %
3	1602 ± 314	16.1 %	1841 ± 361	18.5 %
4	1434 ± 281	14.4 %	1659 ± 325	16.6 %
5	1432 ± 281	14.4 %	1626 ± 319	16.3 %
6	599 ± 117	6.0 %	681 ± 134	6.8 %
7	483 ± 95	4.8 %	625 ± 123	6.3 %
8	402 ± 79	4.0 %	588 ± 115	5.9 %
9	346 ± 68	3.5 %	508 ± 100	5.1 %
10	72.4 ± 14.2	0.7 %	104.3 ± 20.5	1.0 %
11	68.4 ± 13.5	0.7 %	104.3 ± 20.5	1.0 %
12	58.1 ± 11.5	0.6 %	88.9 ± 17.5	0.9 %

Table 6.2: Signal event yields estimated with $t\bar{t}\gamma$ Monte Carlo sample. The number of events and corresponding selection efficiencies are listed after each cut of the $t\bar{t}\gamma$ event selection, shown separately for the e+jets and the μ+jets channel. The event yields are scaled to $4.7\,\mathrm{fb}^{-1}$ and include statistical uncertainties as well as uncertainties of the next-to-leading-order cross section prediction.

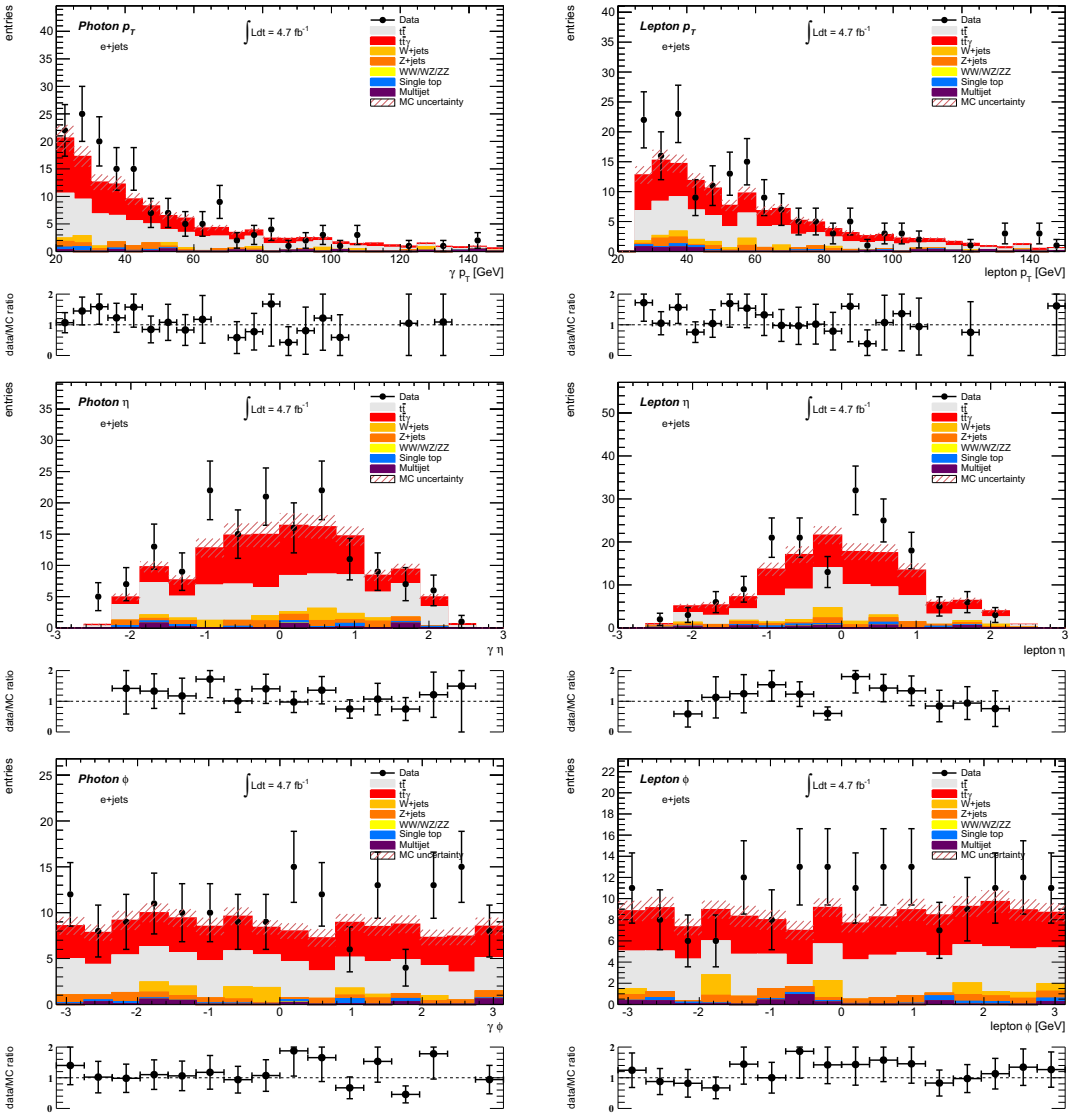

Figure 6.1: Comparison between data and the expectation from Monte Carlo simulation for events passing the $t\bar{t}\gamma$ event selection in the electron channel. p_T (upper row), η (middle row) and ϕ distributions are shown for selected photons (left column) and electrons (right column). Data points are shown in black with statistical uncertainties, while the stacked histogram includes the Monte Carlo expectation of the signal process and all background contributions. Each plot also illustrates systematic uncertainties on the Monte Carlo prediction. Further, a data to Monta Carlo ratio plot is included in each figure with statistical uncertainties.

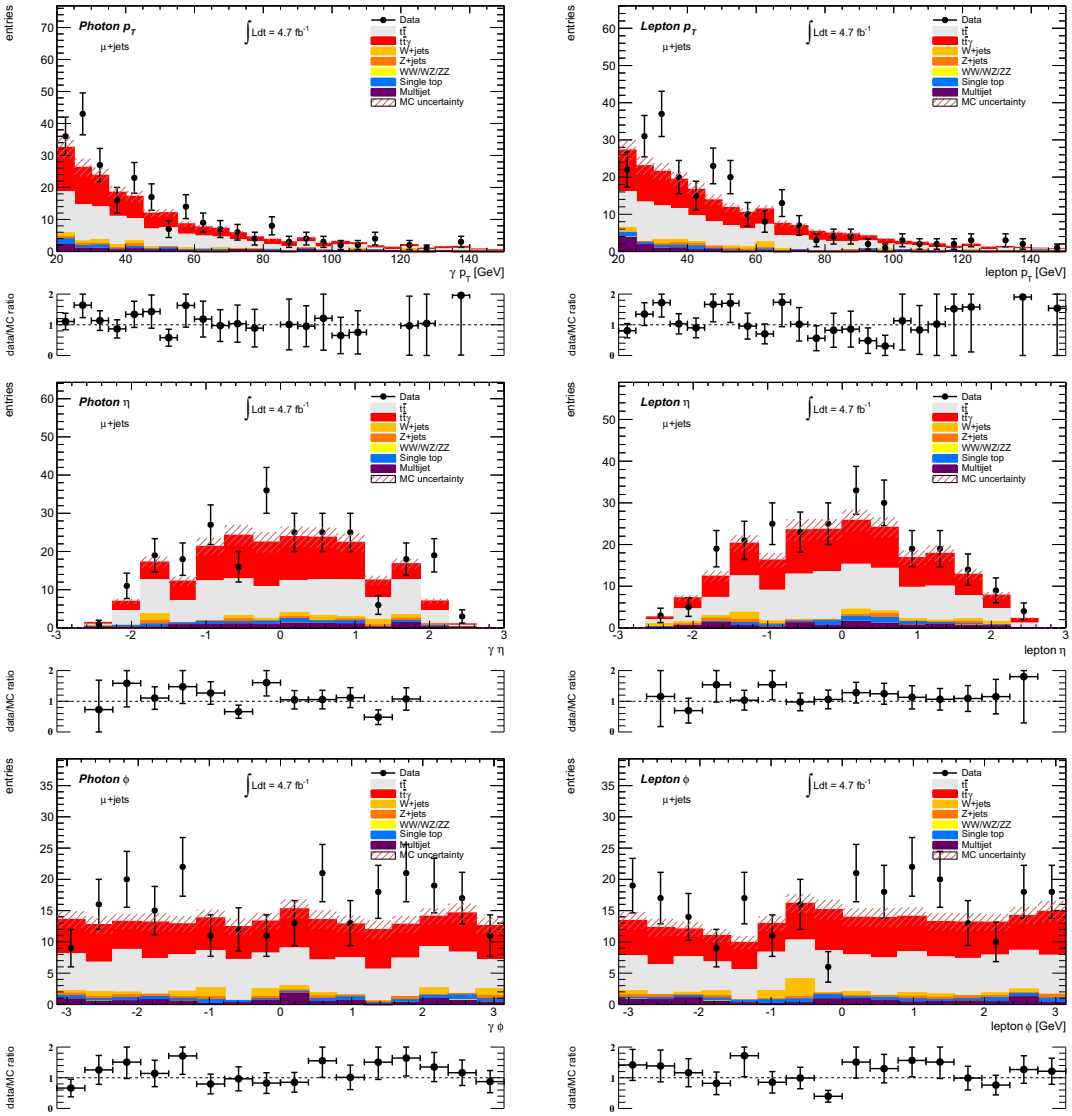

Figure 6.2: Comparison between data and the expectation from Monte Carlo simulation for events passing the $t\bar{t}\gamma$ event selection in the muon channel. p_T (upper row), η (middle row) and ϕ distributions are shown for selected photons (left column) and muons (right column). Data points are shown in black with statistical uncertainties, while the stacked histogram includes the Monte Carlo expectation of the signal process and all background contributions. Each plot also illustrates systematic uncertainties on the Monte Carlo prediction. Further, a data to Monta Carlo ratio plot is included in each figure with statistical uncertainties.

Chapter 7

Analysis strategy to estimate the $t\bar{t}\gamma$ cross section

In order to measure the $t\bar{t}\gamma$ cross section, it is essential to find methods to distinguish between signal and background processes. Initially, events can be categorized in three classes, depending on the photon, which has passed the selection criteria:

- Prompt photons: Photons are emitted from any electrically charged particle within the hard scattering process, before the hadronization process of the final state quarks starts. This definition includes the signal photons of the $t\bar{t}\gamma$ process, as described in Section 2.6.
- Electrons misidentified as photons: Electron and photon candidates are reconstructed with the same algorithms from energy deposits in the electromagnetic calorimeter. A physical object is only categorized as an electron, when a track is associated to the energy cluster. When this track is poorly reconstructed and does not pass all quality criteria, this electron can be mistaken for a photon.
- Hadrons misidentified as photons: Mesons and baryons are created inside of jets during the hadronization process, which can include photons in their decay products. The majority of these photons originate from the $\pi^0 \to \gamma\gamma$ decay. The $t\bar{t}$ Monte Carlo sample predicts that 94.3% of all misidentified hadrons passing the full event selection are π^0 mesons, while 3.4% of such photons are produced in the $\eta \to \gamma\gamma$ decay. The remaining photons stem from other hadron processes. This large percentage of π^0 remains even after the π^0 suppression from the calorimeter strips in the photon identification procedure.

Prompt photons tend to be well isolated, while misidentified hadrons are surrounded by other particles created in the hadronization process. Hence, isolation observables are expected to achieve a high separation power to distinguish between prompt photons and misidentified hadrons. Prompt photons or electrons misidentified as photons from background processes cannot be distinguished from signal photons using isolation. Their contributions have to be estimated separately.

7.1 Discriminating variable

Isolation variables are studied to distinguish between prompt photons and hadrons misidentified as photons. The photon isolation variables follow the same definitions as the electron isolation, as described in Section 4.2.4. The calorimetric and track-based isolation variables has been studied with different cone sizes around the selected photon to find the variable with the highest discrimination power between prompt photons and misidentified hadrons. Since $t\bar{t}$ events with misidentified hadrons compose the main background in this analysis, photons from the WHIZARD $t\bar{t}\gamma$ Monte Carlo sample are compared to misidentified hadrons from the MC@NLO $t\bar{t}$ sample. Reconstructed photons are selected in both samples, which have passed the object definition, and in addition for the $t\bar{t}$ events, only photons are considered, which do not stem from any particle within the hard scattering process or any bremsstrahlung process.

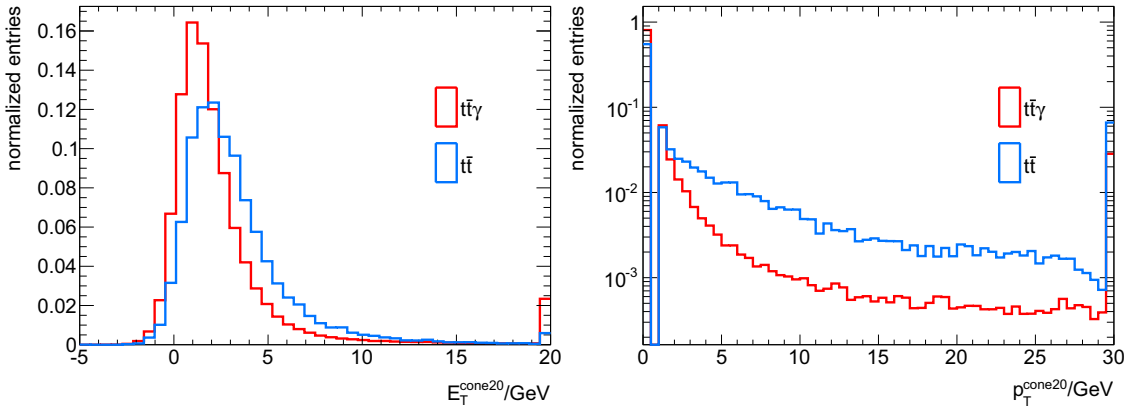

Figure 7.1: Comparison of the E_T^{cone20} (left) and p_T^{cone20} isolation distributions of the signal photons from $t\bar{t}\gamma$ Monte Carlo simulation and misidentified hadrons from the $t\bar{t}$ Monte Carlo sample. Both isolation variables show distinct differences with more entries at higher energy values for background photon distributions.

Figure 7.1 shows calorimetric and track-based isolation for both samples for a ΔR of 0.2, called E_T^{cone20} and p_T^{cone20} respectively. Both variables show distinct differences between prompt photons and misidentified hadrons. The $t\bar{t}$ sample shows a broader E_T^{cone20} distribution, which is also shifted to higher values compared to the signal photons of the $t\bar{t}\gamma$ sample. The p_T^{cone20} distribution has distinctively more entries at values above 1 GeV for the $t\bar{t}$ events, since only 55% of the misidentified hadrons are not surrounded by any track, i.e. $p_T^{\text{cone20}} = 0\,\text{GeV}$, compared to around 85% of the prompt photons in the $t\bar{t}\gamma$ sample. The isolation efficiency is calculated as the number of selected photons with an isolation below a defined upper threshold, divided by the total number of selected photons. Figure 7.2 compares the isolation efficiency of the signal photons to the background rejection, which is defined as 1 minus the isolation efficiency of the misidentified hadrons in the $t\bar{t}$ sample. First, both types of isolation show a better background rejection for $\Delta R = 0.2$, compared to a larger cone size of $\Delta R = 0.3$. This is expected, as the signal photons do not have a clean environment, but are surrounded by at least four jets and a lepton from the

top quark pair event. The track-based isolation variable p_T^{cone20} shows by far the highest discriminating power at a high signal efficiency above 80% and is therefore chosen as the discriminating variable in this analysis.

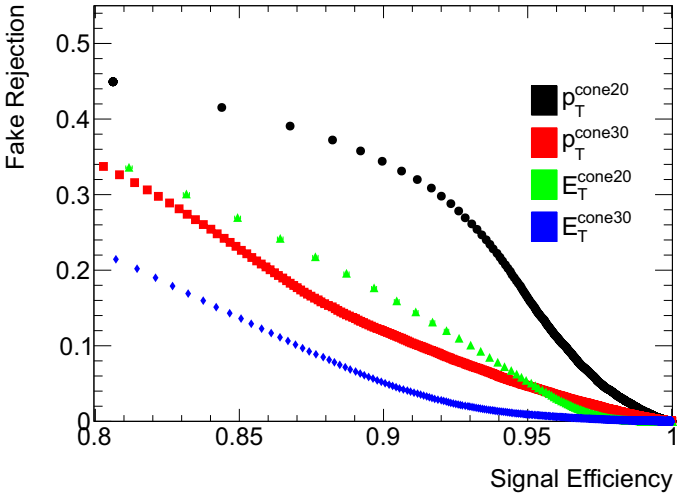

Figure 7.2: Signal efficiency vs. background rejection for different isolation variables. For a signal efficiency range from 0.8 to 1, the track-based isolation variable p_T^{cone20} shows the the highest discriminating power and is therefore chosen as the discriminating variable in this analysis.

7.2 Template fitting

Events passing the full $t\bar{t}\gamma$ event selection contain either prompt photons, or electrons and hadrons misidentified as photons. In order to measure the number of signal events s and consequently the $t\bar{t}\gamma$ cross section, the difference between the distribution shapes of the p_T^{cone20} isolation variable of prompt photons and photons from hadronic decays is exploited. This is achieved by fitting the p_T^{cone20} distribution of the $t\bar{t}\gamma$ event candidates to two template distributions describing the shape of prompt photons only (signal) and hadrons misidentified as photons only (background). The expected difference between the two templates is described in the previous section and shown in the right plot of Figure 7.1. The final templates used in this analysis are derived using data-driven methods given in Chapter 8.

The template fit is performed in the following way: First, the two templates are both normalized to unity. In this analysis $N_{\text{bins}} = 5$ bins are chosen: [0 GeV, 1 GeV), [1 GeV, 3 GeV), [3 GeV, 5 GeV), [5 GeV, 10 GeV) and [10 GeV, ∞). The first bin corresponds to no track around the photon, showing the most distinct difference between the signal and background template. The other bin sizes were chosen to reach similar statistics in the background template bins. Further information concerning the derivation of the templates can be found in Chapter 8. Each bin i is filled with N_i observed events, while the expected

number of events λ_i is given by the sum of the expected signal yield $\varepsilon_i s$ and all N_{bkg} background contributions:

$$\lambda_i = \varepsilon_i s + \sum_{j=1}^{N_{\text{bkg}}} b_{i,j} \,.$$

The expected number of signal events $\varepsilon_i s$ include the acceptance and selection efficiency estimated from the $t\bar{t}\gamma$ Monte Carlo sample, as well as the probability to end up in bin i. A binned likelihood is then defined, which assumes that the fluctuations in each bin are of Poisson nature and independent of each other:

$$L = \prod_{i=1}^{N_{\text{bins}}} \frac{\lambda_i}{N_i!} e^{-\lambda_i} \prod_{j=1}^{N_{\text{bkg}}} P(b_j) \cdot P(s)$$

where the first term describes the Poissonian probability to observe N_i events in the i-th bin for a given expectation λ_i. $P(b_j)$ and $P(s)$ are the prior probabilities for the j-th background contribution and for the signal process respectively. Signal events and background events with a misidentified hadron are treated as free parameters and hence have constant probabilities. Background processes with a prompt photon or misidentified electron cannot be distinguished from signal events due to similar isolation properties of electrons and photons. Due to this fact, these background contributions are described by the same signal template as the $t\bar{t}\gamma$ events. Therefore, background events with a prompt photon or misidentified electron are determined seperately and are then included in the fit as fixed parameters. Gaussian prior probabilities are assigned to these contributions with the Gaussian width defined by the statistical uncertainty of the respective background yield. These background contributions and the data distributions are estimated in the single electron and single muon channel separately, but the signal expectation s is estimated in one combined template fit:

$$\begin{aligned} L = &\prod_{i=1}^{N_{\text{bins}}} \frac{\lambda_i^{e+\text{jets}}}{N_i^{e+\text{jets}}!} e^{-\lambda_i^{e+\text{jets}}} \prod_{j=1}^{N_{\text{bkg}}} P(b_j^{e+\text{jets}}) \cdot \\ &\prod_{i=1}^{N_{\text{bins}}} \frac{\lambda_i^{\mu+\text{jets}}}{N_i^{\mu+\text{jets}}!} e^{-\lambda_i^{\mu+\text{jets}}} \prod_{j=1}^{N_{\text{bkg}}} P(b_j^{\mu+\text{jets}}) \cdot P(s) \end{aligned}$$

The likelihood is maximized in the fit using Markov Chain Monte Carlo to determine the final number of signal events s. The template fit is performed with the Bayesian Analysis Toolkit [189].

7.3 Cross section calculation

The result of the template fit s represents the total number of $t\bar{t}\gamma$ events extrapolated to the phase space of the Whizard Monte Carlo sample, as described in Section 5.4. Therefore, the result can be written as:

$$s = \frac{N - N_b}{C} \,,$$

with the observed number of events N and the number of background events N_b. The total selection efficiency of the $t\bar{t}\gamma$ Monte Carlo sample is denoted as C, which include kinematic and geometric acceptance cuts, as well as efficiency corrections like trigger and identification scale factors. The event selection, which is described in Chapter 6, is only optimized for single lepton events, but since the Monte Carlo sample also includes dileptonic events, the final result will be the $t\bar{t}\gamma$ cross section times the branching ratio into the semileptonic and dileptonic decay channel:

$$\sigma \times \mathrm{BR} = \frac{s}{\mathcal{L}} \,,$$

with the integrated luminosity $\mathcal{L} = 4.7\,\mathrm{fb}^{-1}$.

Chapter 8

Derivation of signal and background templates

8.1 Signal template

The template distribution of prompt photons is derived with a data-driven approach. A data sample containing prompt photons predominantly cannot be selected with sufficient statistics. Hence, it has been exploited that electrons and photons have very similar isolation properties due to their similar signature in the electromagnetic calorimeter. Therefore, the p_T^{cone20} isolation distribution is first derived from data using electrons from $Z \to e^+e^-$ events. Differences between such electrons and photons from $t\bar{t}\gamma$ events are then taken into account by introducing corrections derived from Monte Carlo simulation.
$Z \to e^+e^-$ events are selected with the following selection:

1. The electron trigger has fired, which is chosen according to the specific data period.
2. At least five tracks are associated to the primary vertex.
3. The calorimeter object, which has fired the trigger, is matched to the highest-p_T electron

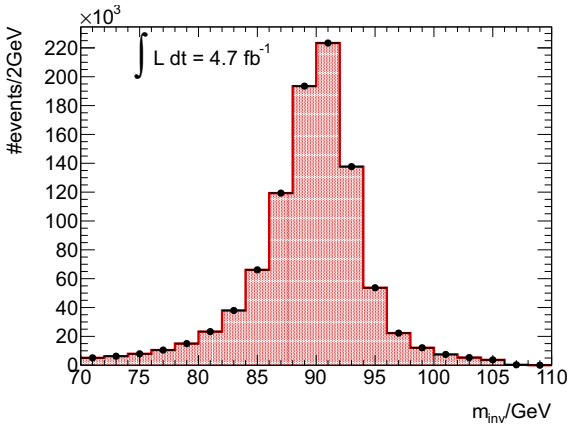

Figure 8.1: Invariant mass distribution of the two electrons from data. The mass peak of the Z boson is very well described by the distribution ($m(Z^0) = 91.2\,\text{GeV}$) with a small root mean square of 4.88 GeV, verifying that the events passing the data selection are vastly dominated by $Z \to e^+e^-$ decays.

4. The two highest-p_T electrons have to pass the tight identification criteria, which are described in Section 4.2.3. Furthermore, the minimum p_T value of the first electron is 25 GeV, while the second electron is required to have a p_T above 20 GeV to match the threshold of the photon in the $t\bar{t}\gamma$ selection.

5. The two selected electrons have opposite electric charge.

6. The invariant mass of both electrons has to be within 25 GeV of the Z boson mass, i.e. in a range from 66 GeV to 116 GeV.

960,000 events are selected from the whole dataset of $4.7\,\mathrm{fb}^{-1}$, resulting in an invariant mass distribution of the two selected electrons shown in Figure 8.1. The distribution shows a distinct peak at the Z boson mass, indicating that events passing the chosen selection are real $Z \to e^+e^-$ data events and that the background from QCD multijet events is negligibly small.
The highest-p_T electron triggers the event, while the electron with the second highest-p_T is utilized for these isolation studies. Hence, only the second object is used for all isolation distributions. The p_T^{cone20} variable is investigated for possible dependencies in p_T and $|\eta|$ by comparing distributions in different p_T and $|\eta|$ regions. Four pseudorapidity regions are chosen:

$$[0, 0.60), \qquad [0.60, 1.37), \qquad [1.52, 1.81), \qquad [1.81, 2.37)\,.$$

The intervals are driven by the detector geometry. The first region is the central part of the electromagnetic calorimeter (ECAL) barrel, with relatively little material in front. The second region is the side barrel, where the material increases rapidly. The third interval

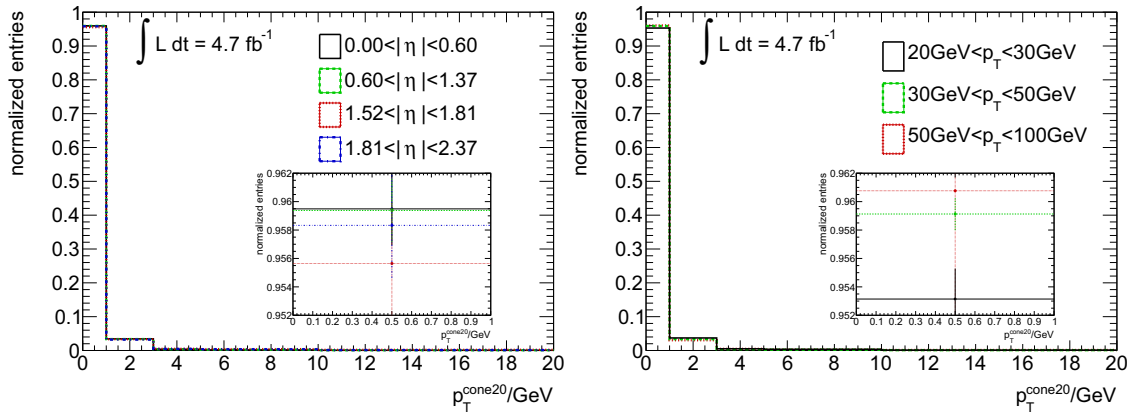

Figure 8.2: p_T^{cone20} distributions from $Z \to e^+e^-$ data in different regions of $|\eta|$ (left) and p_T (right), normalized to 1. Both figures show the total isolation distributions from 0 to 20 GeV, with the last bin including overflow events as well as a display window of the entries in the first bin. Overflow events have a track isolation value of $p_T^{\mathrm{cone20}} > 20$ GeV. The statistical uncertainties for each histogram are smaller than 1% in each bin and are not displayed in the main plots. In both figures, no differences are visible between the different histograms, which is verified by a display windows of the first bin, showing that all histograms agree within statistical uncertainties.

is the outer part of the ECAL endcap, equipped with a presampler. The last region is the remaining portion of the large ECAL endcap wheel [190]. Three p_T regions are chosen with increasing interval width at higher p_T values, which is motivated by lower statistics:

$$[20\,\text{GeV}, 30\,\text{GeV}), \qquad [30\,\text{GeV}, 50\,\text{GeV}), \qquad [50\,\text{GeV}, 100\,\text{GeV})\,.$$

The distributions are shown in Figure 8.2, indicating no dependencies within their small statistical uncertainties of below 1% in each bin.
Differences between electrons and photons are studied in Monte Carlo simulated events. Electron events are selected from a $Z \to e^+e^-$ sample with the same selection as the data events, while photons from the simulated $t\bar{t}\gamma$ sample are used for the comparison, after passing the $t\bar{t}\gamma$ signal selection. Isolation distributions are derived for both samples in 12 different $p_T \times |\eta|$ regions, the same bins as defined before. As expected, the electrons from Monte Carlo simulation show exactly the same behavior as in data, with around 96% of all entries in the first bin and no dependence in $|\eta|$ and p_T. However, the photon isolation distributions illustrate such a dependency. Exemplary, Figure 8.3 shows the p_T^{cone20} distributions for an $|\eta|$ range from 0 to 0.6 and different regions of p_T, indicating a shift to higher isolation values with increasing transverse momentum. All remaining histograms are displayed in Appendix B.2. Overall, photons from $t\bar{t}\gamma$ events are less isolated than the electrons from $Z \to e^+e^-$ events, which can be explained due to the different topology of both types of processes. While the photons are surrounded by large hadronic activity with at least four jets in the final state, no jets are produced in most events of the Z boson decay (see $Z \to e^+e^-$ cross sections listed in Appendix A). This assumption is verified by Figure 8.4, which shows the electron isolation distributions for $Z \to e^+e^-$ events with additional selected jets. The electrons are less isolated and hence more similar to the photon distribution shape with increasing number of jets.
The differences between the electron and photon distributions in Monte Carlo simulation are used as correction factors to derive the final prompt photon templates $t^{\text{sig}}_{\text{data},\gamma}$ from the electron templates $t^{\text{sig}}_{\text{data,e}}$ measured in data:

$$t^{\text{sig}}_{\text{data},\gamma} = t^{\text{sig}}_{\text{data,e}} + \sum_i w_i (t^{\text{sig}}_{\text{MC},\gamma,i} - t^{\text{sig}}_{\text{MC},e,i})$$

The calculation of the correction factors w_i is performed in the described 12 different regions in $p_T \times |\eta|$. In each of the twelve regions i, the simulated electron distribution $t^{\text{sig}}_{\text{MC},e,i}$ is subtracted from the simulated photon template $t^{\text{sig}}_{\text{MC},\gamma,i}$, after both being normalized to one. The resulting distributions are then summed, using relative weights w_i according to the number of $t\bar{t}\gamma$ events in interval i:

$$w_i = \frac{N_i}{\sum_i N_i}\,.$$

These weights are listed for all photons as well as unconverted and converted photons in table 8.1. The final signal template is shown in Figure 8.5. Also shown are the signal templates separately for converted and unconverted photons. Both templates are derived in the same way as given above and using only converted or unconverted photons.

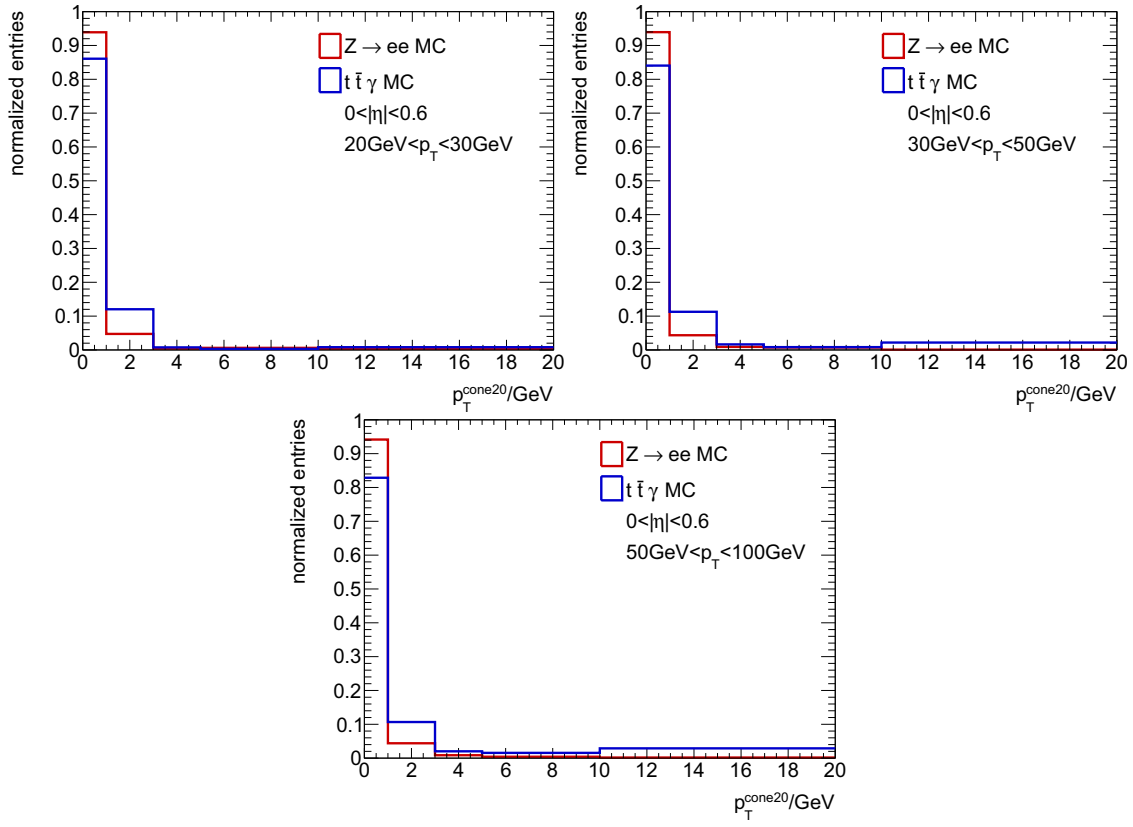

Figure 8.3: p_T^{cone20} distributions of electrons from $Z \to e^+e^-$ Monte Carlo simulation (red) and photons from the $t\bar{t}\gamma$ Monte Carlo simulation (blue). All histograms are normalized to 1 and show the total isolation distributions from 0 to 20 GeV, with the last bin including overflow events. The statistical uncertainties for each histogram are smaller than 0.5% for electrons and smaller than 2% for photons in each bin and are not displayed. The histograms show distributions of electrons and photons with an $|\eta|$ between 0 and 0.6 in different regions of p_T: [20 GeV, 30 GeV) (upper left), [30 GeV, 50 GeV) (upper right), [50 GeV, 100 GeV) (lower row). The electron distributions are constant with η, while the photon distributions shift to higher p_T^{cone20} values with increasing p_T.

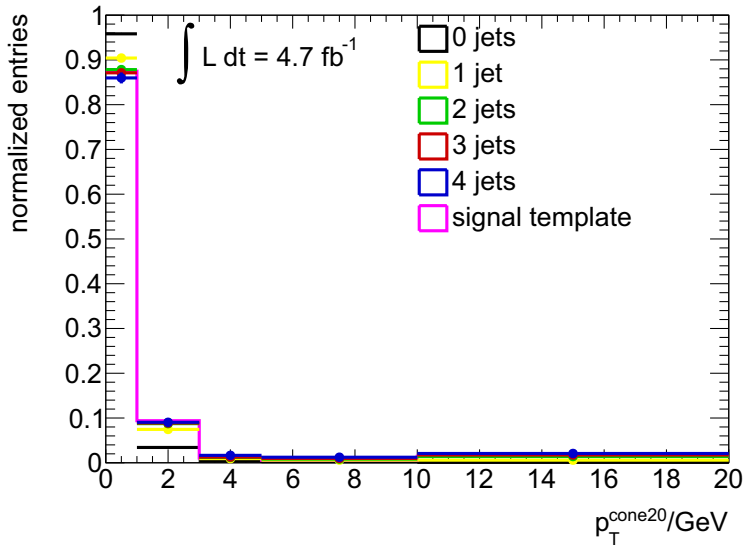

Figure 8.4: Electron p_T^{cone20} distributions from $Z \to e^+e^-$ data with the selection of additional jets, normalized to 1. The total isolation distributions is shown from 0 to 20 GeV, with the last bin including overflow events. The $Z \to e^+e^-$ selection is varied from none to up to four additional jets, indicating that electrons are less isolated with increasing jet multiplicities. As a comparison, the final signal template is also displayed in this figure.

p_T/GeV	$\lvert\eta\rvert$			
	[0,0.60)	[0.60,1.37)	[1.52,1.81)	[1.81,2.37)
$[20, 30)$	0.13 | 0.15 | 0.08	0.12 | 0.11 | 0.15	0.03 | 0.02 | 0.04	0.03 | 0.03 | 0.03
$[30, 50)$	0.14 | 0.16 | 0.11	0.14 | 0.12 | 0.16	0.03 | 0.02 | 0.04	0.03 | 0.04 | 0.03
$[50, 100)$	0.15 | 0.18 | 0.11	0.15 | 0.14 | 0.16	0.03 | 0.02 | 0.04	0.03 | 0.03 | 0.03

Table 8.1: Relative weights w_i of correction factors used to derive the final prompt photon templates. Weights for 12 $p_T \times |\eta|$ regions are calculated according to the number of $t\bar{t}\gamma$ events in each region. The first number in each cell refers to all photons, the second number to unconverted photons and the third number is calculated for converted photons.

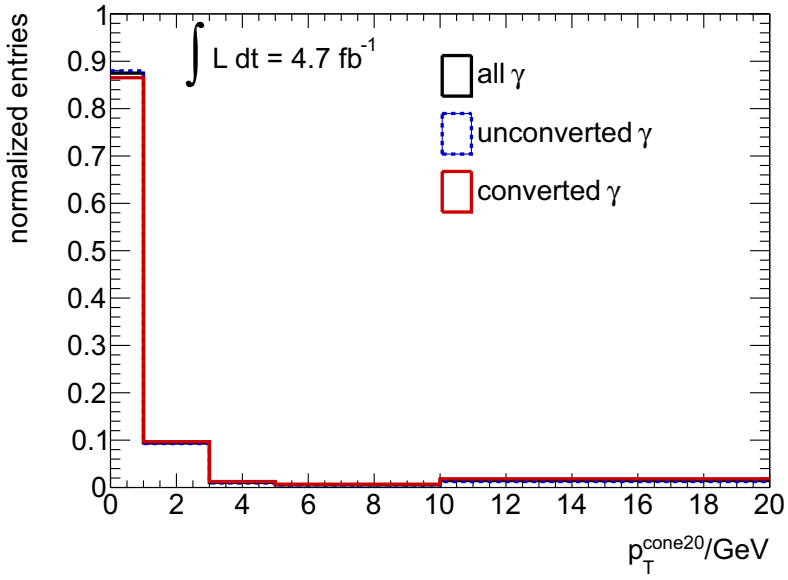

Figure 8.5: Final signal templates used for the $t\bar{t}\gamma$ cross-section extraction, for all photons (black) as well as separated into unconverted (blue) and converted photons (red). All histograms are normalized to 1 and show the total isolation distributions from 0 to 20 GeV, with the last bin including overflow events.

8.2 Background template

A data-driven method is used to extract the background templates. This ensures that there is no influence of Monte Carlo modeling uncertainties of the energy flow inside jets and the fragmentation to neutral mesons. The p_T^{cone20} distributions of misidentified hadrons are derived from a background-enhanced control region, which is defined by selecting events with a photon passing the background identification criteria. In this definition, at least one out of the following four shower shape variables failed the cut from the tight photon identification menu, while all other criteria coincide with the good photon definition: ΔE, F_{side}, w_{s3} and E_{ratio}. These variables rely on information from the first layer of the electromagnetic calorimeter and are chosen for two reasons: Firstly, the calorimeter layer is very finely granulated in $|\eta|$ and is usually used to suppress the photon background. Neutral mesons decaying into two photons result into two maxima in the cluster energy distribution and a broader electromagnetic shower profile than prompt photons. Secondly, the shower shape variables are fairly correlated to the photon isolation variables, since they are extracted within the core of the photon cluster, which is excluded in the calculation of the p_T^{cone20} isolation, as described in Section 4.2.4.
Data events from the skim of the jet stream are used for the derivation of the p_T^{cone20} distributions. This stream is chosen in order to avoid the preselection of a high energetic lepton, as done in the other two available streams described in Section 5.2, which can be the source of prompt photons or electrons misidentified as photons.
The distributions are studied for possible dependencies in p_T and $|\eta|$, in analogy to the signal template. Fig. 8.6 shows the distributions of the background photon candidates for

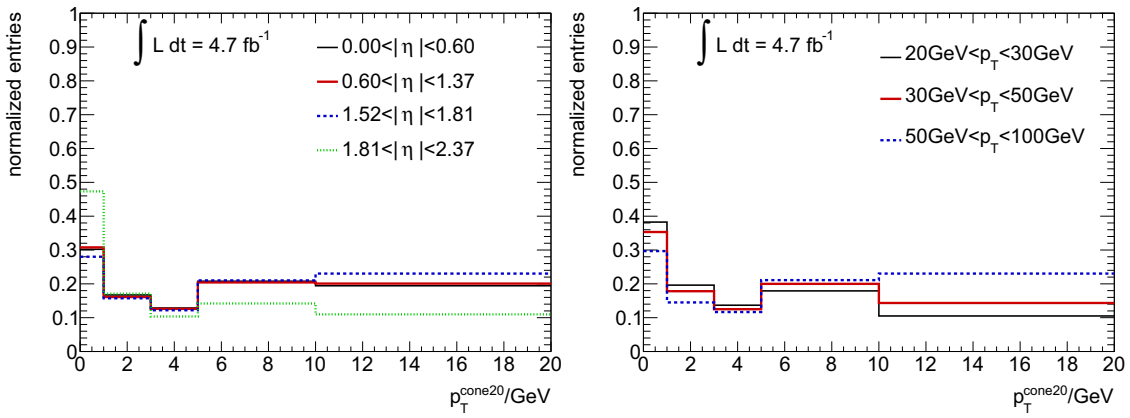

Figure 8.6: p_T^{cone20} distributions from background photon candidates in different regions of $|\eta|$ (left) and p_T (right), normalized to 1. Both figures show the total isolation distributions from 0 to 20 GeV, with the last bin including overflow events. The statistical uncertainties for each histogram are smaller than 0.5% in each bin and are not displayed. In both figures, no differences are visible between the different histograms

different values of p_T and $|\eta|$, indicating a clear dependence on p_T and η. The histograms show that misidentified hadrons are less isolated with increasing p_T, which is expected, as high-p_T hadrons are likely to originate more collinear to high-energetic jets. Further, the first two $|\eta|$ regions up $|\eta| < 1.37$ show the same behavior, but deviations to the other two distributions for $1.52 < |\eta| < 1.81$ and $1.81 \leq |\eta| < 2.37$. Dependencies have been identified in all three studied p_T regions, [20 GeV, 30 GeV), [30 GeV, 50 GeV) and [50 GeV, 100 GeV), as well as three $|\eta|$ regions, [0, 1.37), [1.52, 1.81) and [1.81, 2.37). The final background template has therefore be constructed as the weighted sum of the individual distributions in the 9 $p_T \times |\eta|$ bins. The weights are calculated according to the p_T and $|\eta|$ spectra of $t\bar{t}\gamma$ event candidates with a misidentified hadron passing the photon selection criteria.

These spectra are obtained by a control region using an altered $t\bar{t}\gamma$ event selection, where the good photon definition is replaced by the background photon definition described before in this section. A total of 229 events are selected in this control region, with 148 of these events having identified a converted photon. This approach is validated using the $t\bar{t}$ Monte Carlo sample, as shown in Figure 8.7. First, the transverse momentum distributions of simulated events passing the background photon event selection are in very good agreement to the distributions of true misidentified hadrons, i.e. it has been checked on generator level that the selected photon has indeed originated from hadron decay. Furthermore, all p_T distributions obtained in the three different $|\eta|$ regions agree within statistical uncertainties, so that consequently, the reweighting of the background templates can be performed independently in p_T and $|\eta|$. In addition, the p_T and $|\eta|$ spectra from Monte Carlo simulation agree very well with the data distributions, verifying that events passing the altered $t\bar{t}\gamma$ event selection are dominantly $t\bar{t}$ events with a misidentified hadron. The isolation templates $t_i^{\text{bkg}}(\eta)$ in the three $|\eta|$ regions are weighted according to the

fraction of events N_i selected in each bin i:

$$w_{\eta,i} = \frac{N_i}{\sum\limits_i N_i} \,.$$

The distribution of the transverse momentum is modelled by an exponential function f_{exp}. A fit is performed to this spectrum and each background template $t_j^{\text{bkg}}(p_T)$ in p_T region j is weighted by

$$w_{p_T,j} = \frac{\int_{b^j_{p_T,\text{low}}}^{b^j_{p_T,\text{up}}} f_{\text{exp}}(p_T)\mathrm{d}p_T}{\int_0^\infty f_{\text{exp}}(p_T)\mathrm{d}p_T} \,,$$

where $b^j_{p_T,\text{low}}$ and $b^j_{p_T,\text{up}}$ are the lower and upper limits of bin j, respectively. Figure 8.8 displays the $|\eta|$ distributions for all selected photons and separately for unconverted and converted photons, as well as the p_T spectra including the fit results. Furter, Table 8.2 lists all values of $w_{\eta,i}$ and $w_{p_T,j}$. The final background template is then calculated by

$$t^{\text{bkg}} = \sum_i \sum_j w_{\eta,i} w_{p_T,j} t_j^{\text{bkg}}(p_T, |\eta|)$$

The final background templates are shown in Figure 8.9.

$w_{\eta,i}$	[0,1.37)	[1.52,1.81)	[1.81,2.37)
	0.71 | 0.79 | 0.66	0.18 | 0.10 | 0.22	0.11 | 0.11 | 0.11
$w_{p_T,i}$	[20 GeV, 30 GeV)	[30 GeV, 50 GeV)	[50 GeV, 100 GeV)
	0.37 | 0.45 | 0.37	0.39 | 0.39 | 0.39	0.24 | 0.16 | 0.25

Table 8.2: Calculated weights used to derive the final background template as the weighted sum of the isolation distributions in three p_T and $|\eta|$ regions. The first number in each cell refers to all photons, the second number to unconverted photons and the third number is calculated for converted photons.

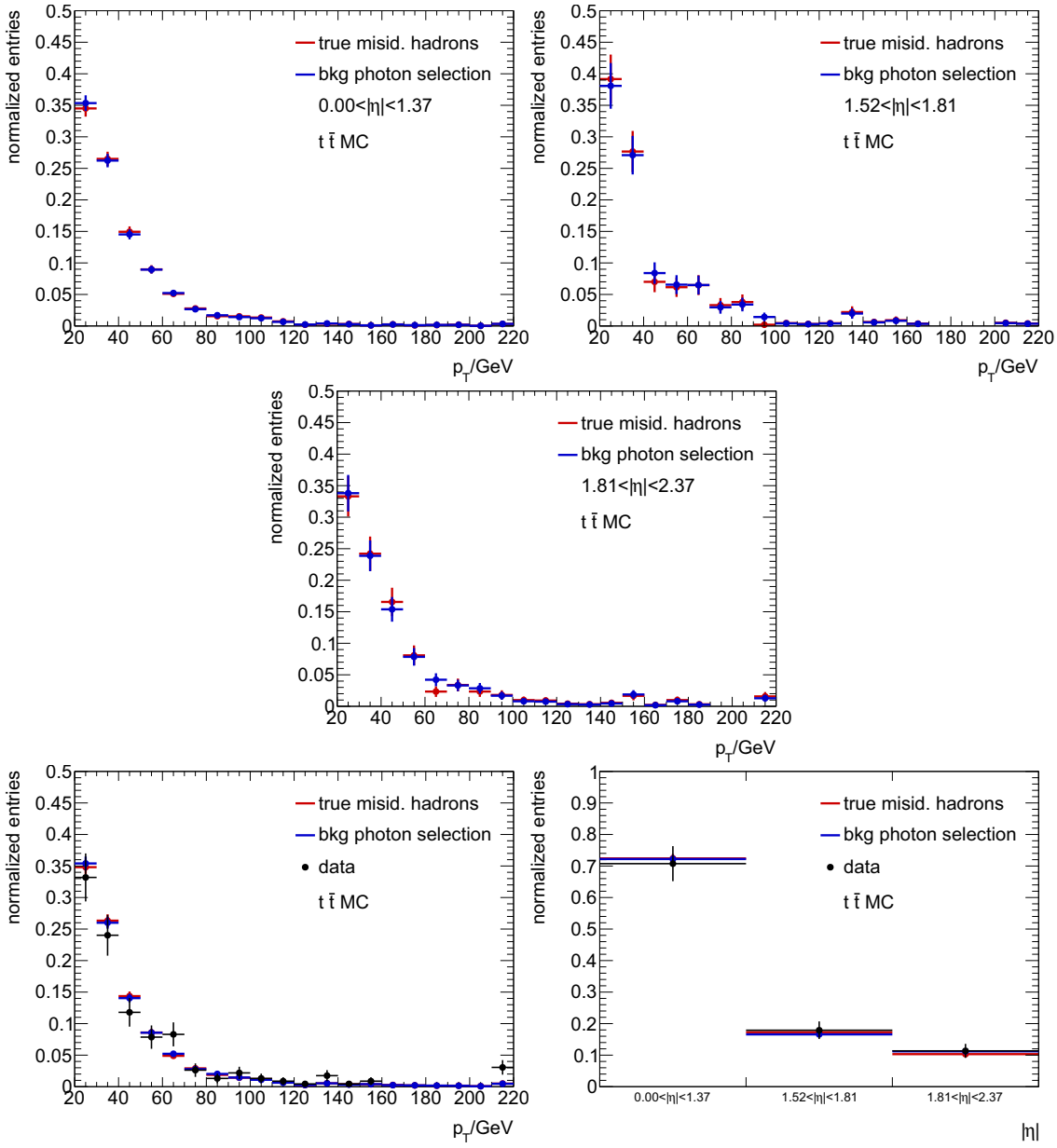

Figure 8.7: p_T distributions from background photon candidates in simulated $t\bar{t}$ events, for $0 < |\eta| < 0.60$ (upper left), $0.60 < |\eta| < 1.81$ (upper right) and $1.81 < |\eta| < 2.37$ (middle row). All figures show the distributions of true misidentified hadrons (red) as well as reconstructed photons (blue) passing the background identification. The two histograms in each plot and all six displayed histograms agree within statistical uncertainties. Further, the figures in the lower row show, that the simulated p_T and $|\eta|$ distributions also agree with the data expectation of event candidates passing the $t\bar{t}\gamma$ -selection with the background photon identification.

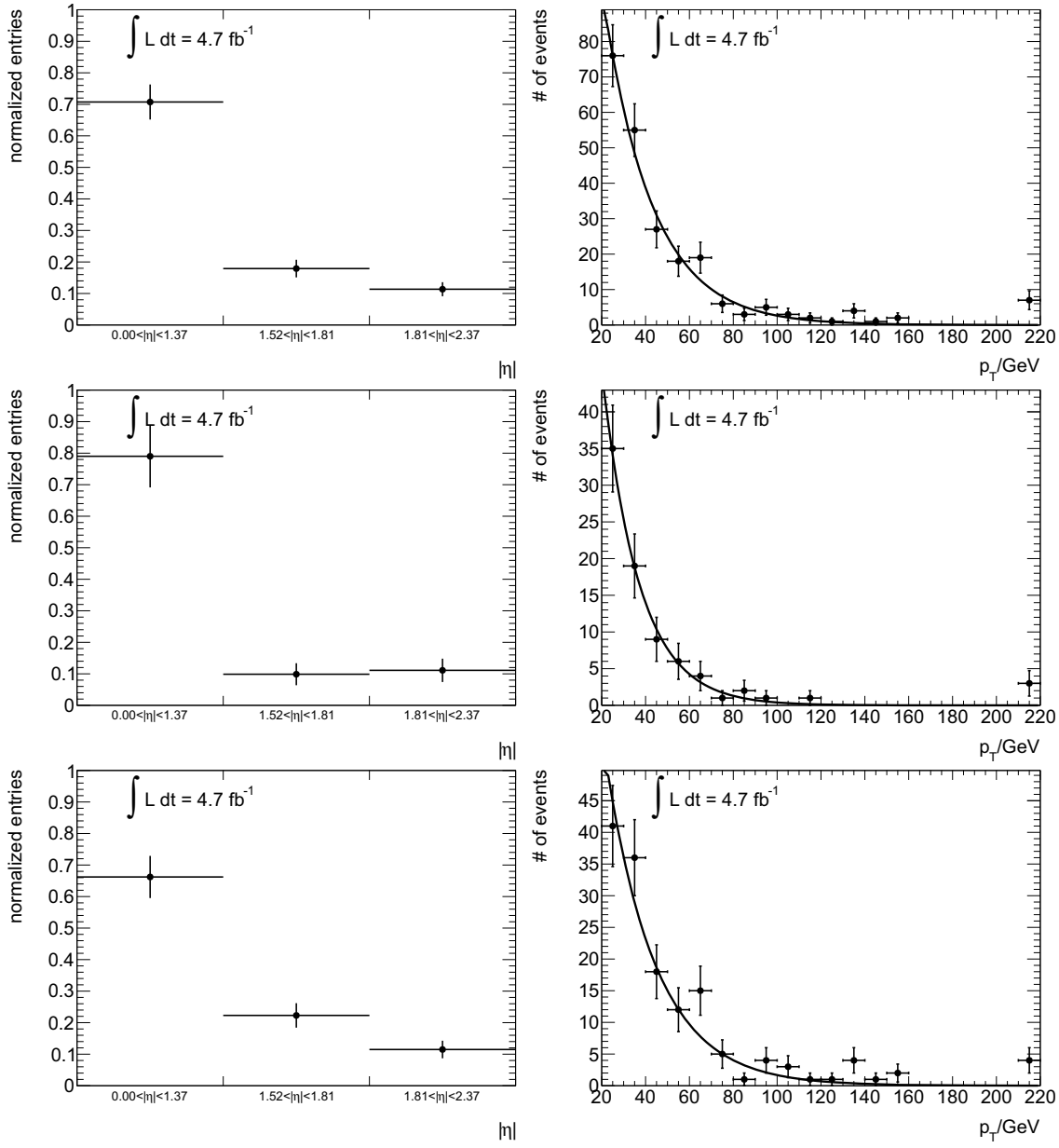

Figure 8.8: $|\eta|$ (left column) and p_T distributions (right column) from background photon candidates in data after passing the $t\bar{t}\gamma$ event selection using the background photon definition. Spectra are shown for all photons (upper row), unconverted photons (middle row) and converted photons (lower row), including statistical uncertainties. Further, the p_T plots include the resulting functions of the exponential fit. Overall, the unconverted photons show a larger fraction of events in the first $|\eta|$ bin and a steeper p_T distribution than converted photons.

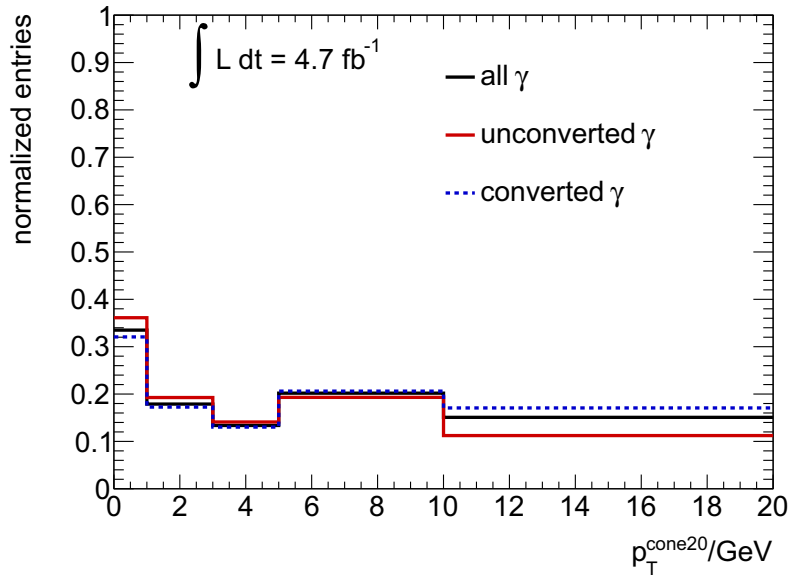

Figure 8.9: Final background templates used for the $t\bar{t}\gamma$ cross-section extraction, for all photons (black) as well as separated into unconverted (blue) and converted photons (red). All histograms are normalized to 1 and show the total isolation distributions from 0 to 20 GeV, with the last bin including overflow events.

Chapter 9

Estimation of the $e \to \gamma$ misidentification rate

One large contribution to the $t\bar{t}\gamma$ background are events with an electron in the final state, which is misidentified as a photon, as mentioned in Chapter 7. The probability that a real electron is misidentified as a photon is given by the electron-to-photon misidentification rate $f(e \to \gamma)$. It is derived from data and Monte Carlo simulation using $Z \to ee$ events, as this process provides a clean environment and high statistics to measure electron properties. Scale factors are then calculated in twelve different regions of photon p_T and $|\eta|$, which is the ratio of $f(e \to \gamma)$ measured in data and $f(e \to \gamma)$ measured in Monte Carlo. These scale factors are used in this analysis to correct the misidentification rate in Monte Carlo samples to the data expectation.

9.1 Estimation of the $e \to \gamma$ misidentification rate

The $e \to \gamma$ misidentification rate is determined by the number of $Z \to e\gamma_{\text{misId}}$ events, where an electron is misidentified as a photon, compared to the number of $Z \to ee$ events in data. Events are selected after passing following criteria:

1. The electron trigger has fired. The specific trigger menu is chosen corresponding to the data period.

2. At least five tracks are associated to the primary vertex.

3. The calorimeter object, which has fired the trigger, is matched to the highest-p_T electron.

4. $Z \to ee$: The two highest-p_T electrons have to pass the tight identification criteria. Furthermore, the minimum p_T value of the first electron is 25 GeV, while the second electron is required to have a p_T above 20 GeV to match the value of the photon in the $t\bar{t}\gamma$ selection.

   $Z \to e\gamma_{\text{misId}}$: An electron with a p_T above 25 GeV has to pass the tight identification criteria, while one good photon with $p_T > 20$ GeV has to be found. Furthermore, the electron is required to have a higher transverse momentum than the photon.

5. Since decay particles from the Z boson are expected to be emitted back-to-back, the angle between both selected particles in the x-y plane is required to be at least $\Delta\phi = 150°$.

6. The invariant mass of the selected electron pair or the selected electron and photon has to be within 20 GeV to the Z boson mass to ensure that the two objects are almost exclusively decay particles of a Z boson.

Therefore, the highest-p_T electron triggers the event, while the second electron of the Z boson is used to measure the $e \to \gamma$ misidentification rate. The number of $Z \to ee$ events ($N(ee)$) and $Z \to e\gamma_{\text{misId}}$ events ($N(e\gamma)$) is given by:

$$N(ee) = \varepsilon_1 \cdot \varepsilon_2 \cdot N,$$

$$N(e\gamma) = \varepsilon_1 \cdot f(e \to \gamma) \cdot N,$$

where ε_1 is the combined trigger, reconstruction and identification efficiency of the highest-p_T electron, ε_2 the combined reconstruction and identification efficiency of the second electron and N the total number of true $Z \to ee$ events. The $e \to \gamma$ misidentification rate $f(e \to \gamma)$ is therefore

$$f(e \to \gamma) = \varepsilon_2 \cdot \frac{N(e\gamma)}{N(ee)} = \varepsilon_2 \cdot \rho(e \to \gamma)\,.$$

The ratio of the number of $Z \to e\gamma_{\text{misId}}$ and $Z \to ee$ events, $\rho(e \to \gamma)$, is estimated in data and simulation using different methods.
The number of events $N(ee)$ and $N(e\gamma)$ is measured in data from fits to the invariant mass distributions of the selected electron pair or the selected electron and photon. The fit functions are combined models, which take into account the expected $Z \to ee$ signal distribution as well as small background contributions from other processes passing the event selection. The signal distribution f_{signal} is modelled with a convolution of a Breit-Wigner and Crystal-Ball distribution, describing the Z boson mass peak as well as the mass resolution. The background distribution f_{bkg} is described by an exponential function, which is expected to consist mainly of QCD multijet events with mesons from jet fragmentation, which are misidentified as electrons or photons. The combined fit has a total of nine free parameters. This includes two parameters each from the Breit-Wigner and exponential function, four from the Crystal-Ball function and one normalization factor for the convoluted signal function. The overall fit function is

$$f_{\text{fit}} = f_{\text{signal}} + f_{\text{bkg}} = \text{norm.} \cdot (f_{\text{CB}} \otimes f_{\text{BW}}) + f_{\text{bkg}}$$

with the individual components

$$f_{\text{CB}}(m; \alpha, n, \bar{m}, \sigma) = \begin{cases} \exp\left(-\frac{(m-\bar{m})^2}{2\sigma^2}\right) & , \frac{m-\bar{m}}{\sigma} > -\alpha \\ \left(\frac{n}{|\alpha|}\right)^n \cdot \left(\frac{|\alpha|^2}{2}\right) \cdot \left(\frac{n}{|\alpha|} - |\alpha| - \frac{m-\bar{m}}{\sigma}\right)^{-n} & , \text{else} \end{cases},$$

$$f_{\text{BW}}(m; \bar{m}, \Gamma) = \frac{\Gamma}{2\pi\left((m-\bar{m})^2 + \left(\frac{1}{2}\cdot\Gamma\right)^2\right)},$$

$$f_{\text{bkg}}(m; a, b) = a \cdot \exp\left(-m \cdot b\right).$$

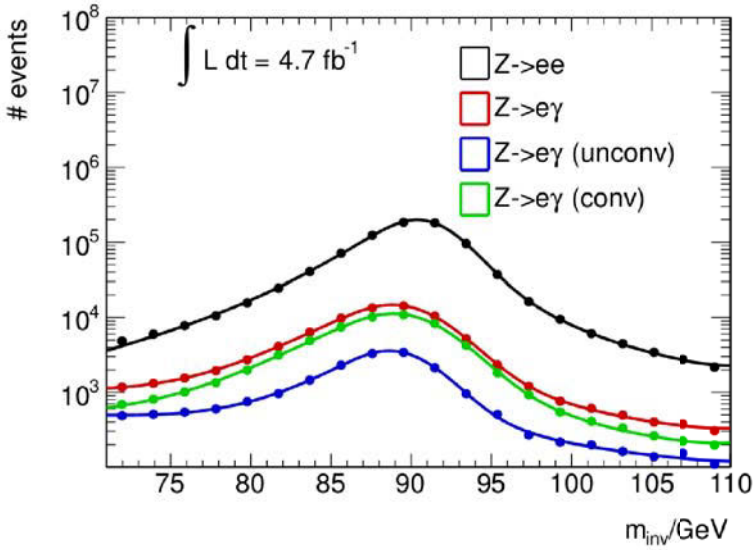

Figure 9.1: Invariant mass distributions of $Z \to ee$ data events (black) and $Z \to e\gamma_{\text{misId}}$ events (red), which are in addition shown for unconverted (blue) and converted photons (green) separately. Further, the combined signal+background fit is shown for each distribution, which is used to calculate the number of signal Z events.

The fit is performed in an invariant mass range from 71 GeV to 110 GeV and the number of events N_{data} is estimated by

$$N_{\text{data}} = \int_{71\,\text{GeV}}^{110\,\text{GeV}} f_{\text{signal}}(m_{\text{inv}}) \mathrm{d}m_{\text{inv}} \,.$$

Figure 9.1 shows the invariant mass distributions for all events passing the $Z \to ee$ and the $Z \to e\gamma_{\text{misId}}$ selection in data. In addition, events with a misidentified photon are separated into converted and unconverted photons. The fit function are also shown in the plot and describe the measured distribution very well. Furthermore, Figure 9.2 compares the p_T spectrum of electrons with the second highest p_T from $Z \to ee$ events to the distribution of selected photons from $Z \to e\gamma_{\text{misId}}$ events.
Monte Carlo $Z \to ee$ events, which have been simulated with up to five additional jets by the Monte Carlo generator ALPGEN, are also investigated to determine $\rho(e \to \gamma)$. Since only signal events are included in the simulated sample, the fit procedure is not necessary to measure the number of events N_{MC} within the defined invariant mass range:

$$N_{\text{MC}} = \sum_i N_i(m_{\text{inv}}), \text{ if } m_{\text{inv}} \in [71\,\text{GeV}, 110\,\text{GeV}] \,.$$

Due to the strict event selection criteria, the probability of selecting events with an electron, which has not originated from the Z boson, is negligibly small.
The number of events $N(ee)$ and $N(e\gamma)$ are estimated in twelve $p_T \times |\eta|$ regions, in order to improve the precision of the misidentification rate correction in Monte Carlo samples

to the data expectation. The same $|\eta|$ regions are chosen as in Chapter 8, which are

$$[0, 0.60), \qquad [0.60, 1.37), \qquad [1.52, 1.81), \qquad [1.81, 2.37)\,.$$

The three p_T regions are

$$[20\,\text{GeV}, 25\,\text{GeV}), \qquad [25\,\text{GeV}, 30\,\text{GeV}), \qquad [30\,\text{GeV}, 40\,\text{GeV})\,.$$

The invariant mass distributions for a p_T above 40 GeV cannot be described by f_{signal} anymore and are therefore neglected. Further, the distributions for a $p_T > 45$ GeV suffer due to low statistics, which is expected, as events with a Z boson decaying into two leptons are very rare where both decay particles have a high transverse momentum above 45 GeV. The different invariant mass distributions from data in each $p_T \times |\eta|$ region are shown in Appendix B.3, including the combined fit functions.

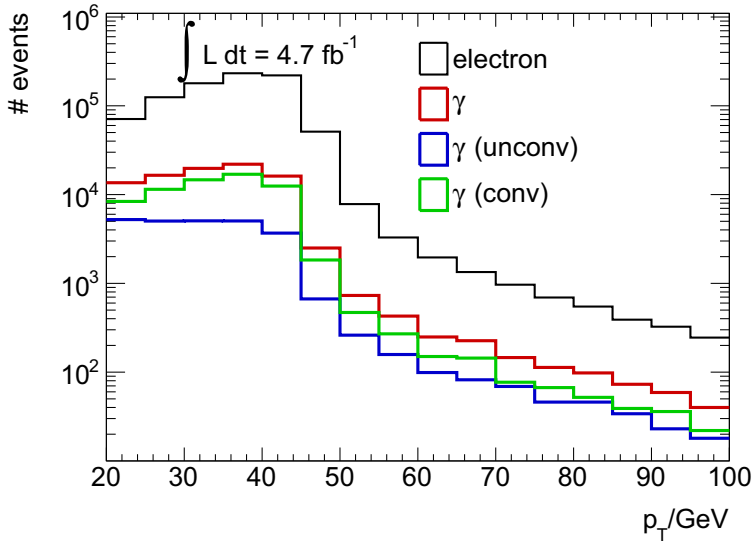

Figure 9.2: Transverse momentum spectra of electrons from $Z \to ee$ data events (black) with the second highest p_T and selected photons from $Z \to e\gamma_{\text{misId}}$ events (red). Additionally, the distributions of unconverted (blue) and converted photons (green) are shown separately.

9.2 Derivation of the $e \to \gamma$ misidentification scale factors

The $e \to \gamma$ scale factor is defined as the misidentification rate measured in data $f(e \to \gamma)_{\text{data}}$ divided by the misidentification rate in Monte Carlo simulation $f(e \to \gamma)_{\text{MC}}$:

$$\begin{aligned} \text{SF}_{e\to\gamma} &= \frac{f(e \to \gamma)_{\text{data}}}{f(e \to \gamma)_{\text{MC}}} = \frac{\varepsilon_2 \rho(e \to \gamma)_{\text{data}}}{\varepsilon_2 \rho(e \to \gamma)_{\text{MC}}} \\ &= \frac{\rho(e \to \gamma)_{\text{data}}}{\rho(e \to \gamma)_{\text{MC}}} = \frac{\left(\frac{N(e\gamma)}{N(ee)}\right)_{\text{data}}}{\left(\frac{N(e\gamma)}{N(ee)}\right)_{\text{MC}}} \end{aligned}$$

Scale factors for the electron reconstruction and identification efficiencies are applied to Monte Carlo simulation in order to match the data efficiencies. Hence, it is assumed that ε_2 is the same in data and simulation and therefore cancels out in the calculation of $\text{SF}_{e\to\gamma}$. The measured ratios of $Z \to e\gamma_{\text{misId}}$ and $Z \to ee$ events in data, $\rho(e \to \gamma)_{\text{data}}$, are shown in Figure 9.3. The highest ratio is measured in the third $|\eta|$ region between 1.52 and 1.81. Furthermore, slightly higher ratios are measured in the lowest p_T bin below 25 GeV, compared to the other two p_T regions. Since approximately 80% of the misidentified electrons are categorized as a converted photon, $\rho(e \to \gamma)_{\text{data}}$ is similar for all photons and converted photons.

The resulting scale factors $\text{SF}_{e\to\gamma}$ are given in Figure 9.4. They lie in a range of 20% around 1 for all and converted photons and show higher deviations from unity for unconverted photons, but also include larger uncertainties. Since the measurement is limited to a transverse momentum of 40 GeV, no scale factors are derived above this threshold. However, it is well-motivated to use the scale factors in the p_T region from 30 GeV to 40 GeV also for higher transverse energies with an additional uncertainty of 15%, in order to make these scale factors compatible with the results in the lower p_T regions.

Multiple sources of uncertainties are taken into account. A fit uncertainty is estimated by increasing the invariant mass window from [71 GeV,110 GeV] to [61 GeV,120 GeV]. Further, uncertainties concerning electron and photon modelling are considered, as described in Section 12.4.2. Dependencies on the pile-up conditions are studied by comparing scale factors for events with up to seven primary vertices and events with more than seven primary vertices. The results agree within statistical uncertainties with the nominal scale factors. This is expected, since the Monte Carlo events are reweighted to the same pile-up conditions present during data taking. Hence, an additional uncertainty due to pile-up effects is not considered. Tables 9.1, 9.2 and 9.3 list all uncertainties as well as the quadric sum of all uncertainties.

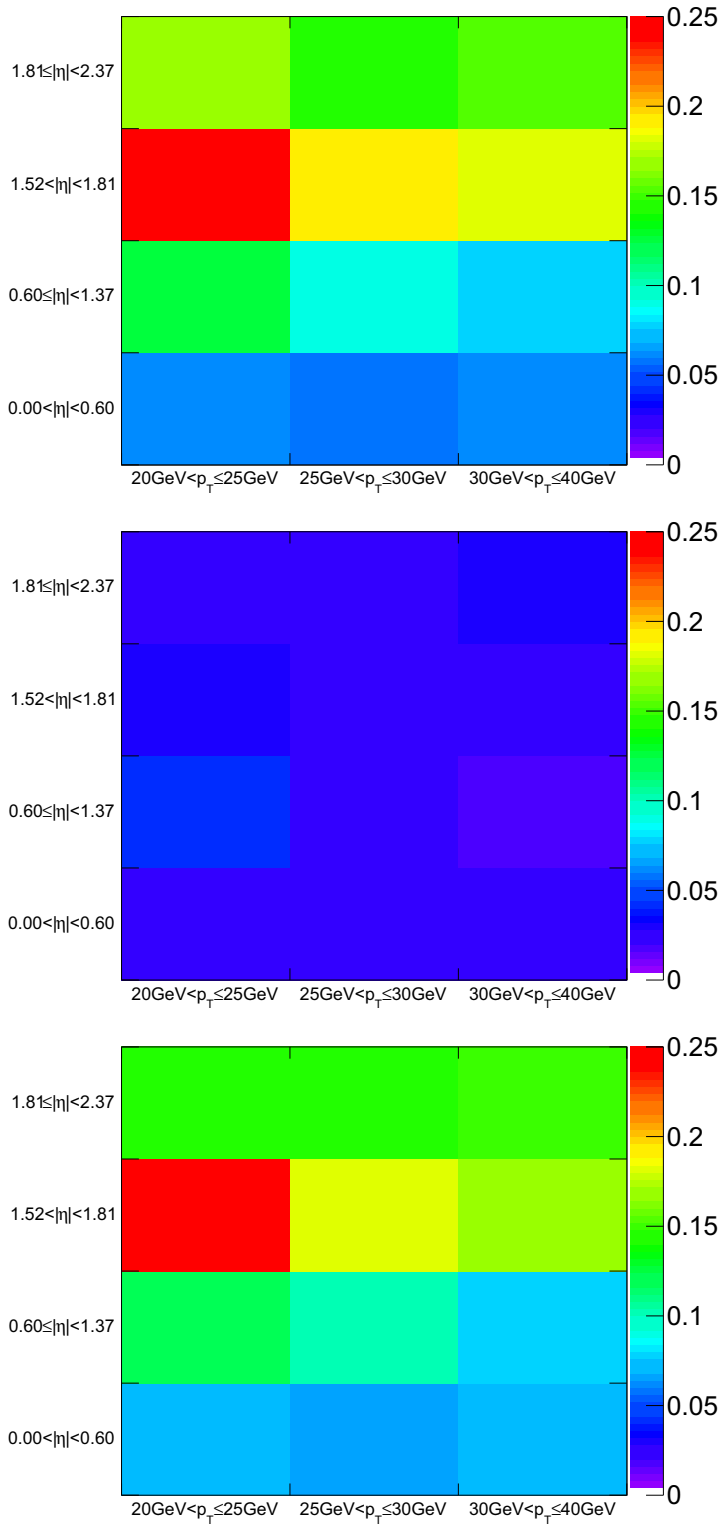

Figure 9.3: Ratio of $Z \to e\gamma_{\text{misId}}$ and $Z \to ee$ events in twelve different $p_T \times |\eta|$ regions for all identified photons (upper row), unconverted photons (middle row), and converted photons (lower row). The highest ratio is measured in the $|\eta|$ region $(1.52, 1.81)$. Slightly higher ratios are measured in the lowest p_T region than the other two p_T bins.

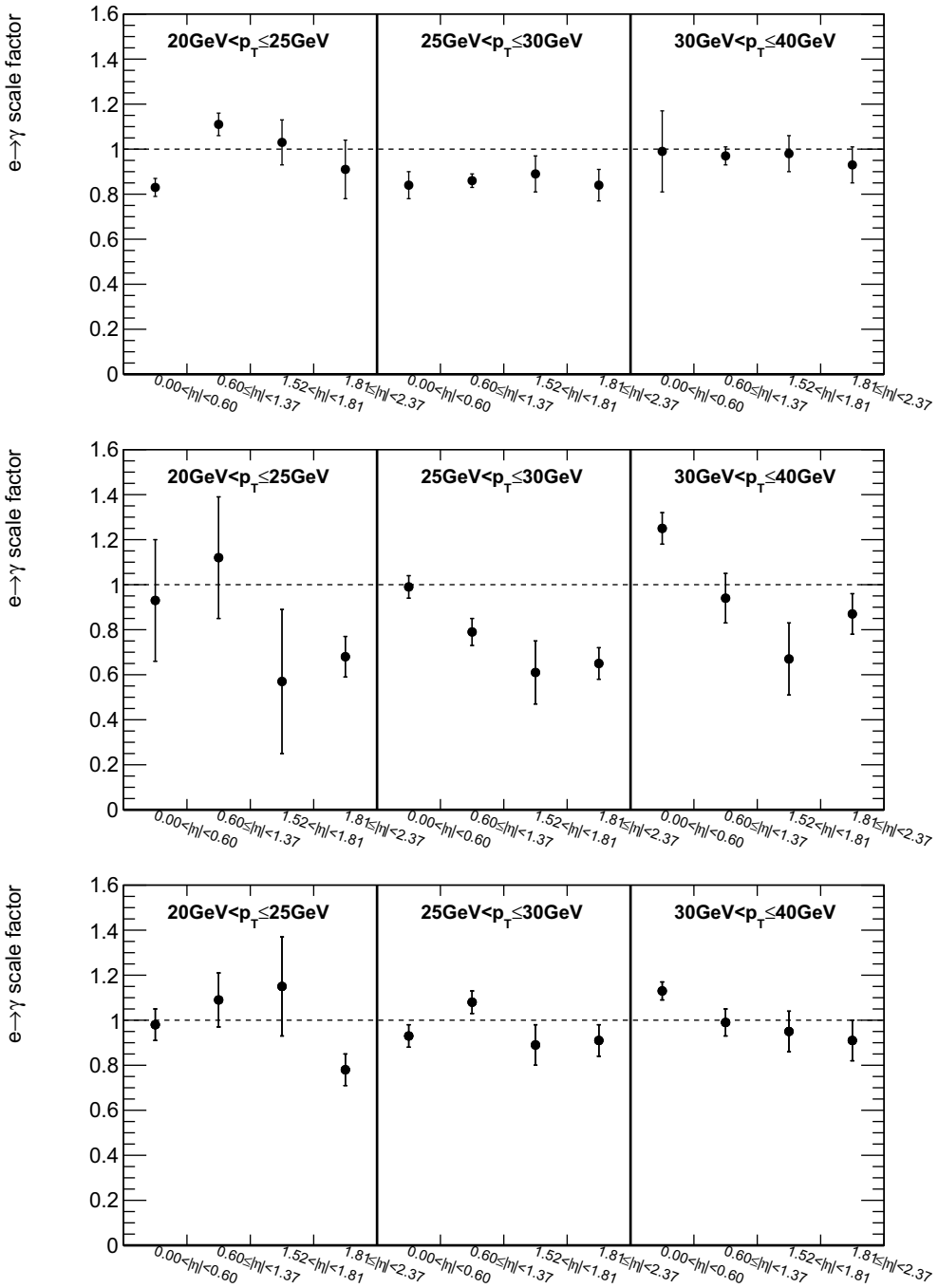

Figure 9.4: Resulting $e \to \gamma$ misidentification scale factors for all photons as wells unconverted and converted photons, derived from $e \to \gamma$ misidentification rate measurement in twelve different $p_T \times |\eta|$ regions. The error bars include statistical and systematic uncertainties. The dashed horizontal line marks a scale factor of one, i.e. the same misidentification rate in data and simulation.

uncertainty	$0 \leq \lvert\eta\rvert < 0.60$			$0.60 \leq \lvert\eta\rvert < 1.37$		
	p_T/GeV					
	[20,25)	[25,30)	[30,40]	[20,25)	[25,30)	[30,40]
statistical	0.03	0.02	0.15	0.03	0.02	0.02
fit	0.10	0.05	0.01	0.16	0.04	<0.01
e energy scale	0.02	0.06	0.09	0.03	<0.01	<0.01
e resolution	0.01	<0.01	0.01	0.01	<0.01	0.01
e reco. and ID efficiency	<0.01	0.01	0.02	<0.01	0.02	0.03
e trigger efficiency	<0.01	0.01	0.01	<0.01	0.01	0.01
γ energy scale	<0.01	<0.01	<0.01	0.02	<0.01	<0.01
γ resolution	<0.01	0.01	<0.01	0.01	0.01	0.01
γ ID efficiency	0.01	0.01	0.01	0.01	<0.01	0.01
total	0.10	0.08	0.17	0.17	0.05	0.04
uncertainty	$1.52 < \lvert\eta\rvert < 1.81$			$1.81 \leq \lvert\eta\rvert < 2.37$		
	p_T/GeV					
	[20,25)	[25,30)	[30,40]	[20,25)	[25,30)	[30,40]
statistical	0.04	0.03	0.02	0.03	0.03	0.02
fit	0.06	0.03	<0.01	0.14	0.02	<0.01
e energy scale	0.01	<0.01	<0.01	0.11	<0.01	<0.01
e resolution	0.03	0.01	<0.01	<0.01	0.01	0.01
e reco. and ID efficiency	<0.01	0.04	0.04	<0.01	0.02	0.01
e trigger efficiency	<0.01	0.02	0.02	<0.01	<0.01	<0.01
γ energy scale	0.03	<0.01	<0.01	0.01	0.03	<0.01
γ resolution	0.01	0.02	<0.01	0.01	0.01	0.01
γ ID efficiency	0.09	0.06	0.07	0.06	0.06	0.08
total	0.12	0.08	0.08	0.20	0.07	0.08

Table 9.1: Overview of all uncertainties, which have been taken into account for the measurement of the $e \to \gamma$ misidentification scale factors for all photons. These include fit uncertainties as well as uncertainties on corrections applied on data (e/γ energy scale) and Monte Carlo simulation.

uncertainty	$0 \leq \lvert\eta\rvert < 0.60$			$0.60 \leq \lvert\eta\rvert < 1.37$		
	p_T/GeV					
	[20,25)	[25,30)	[30,40]	[20,25)	[25,30)	[30,40]
statistical	0.13	0.03	0.03	0.05	0.05	0.10
fit	0.20	0.08	0.01	0.26	0.05	0.05
e energy scale	0.05	<0.01	0.03	0.07	<0.01	<0.01
e resolution	0.01	<0.01	0.01	0.01	<0.01	0.01
e reco. and ID efficiency	<0.01	0.02	0.02	0.01	0.02	0.02
e trigger efficiency	<0.01	0.01	0.01	0.01	0.01	0.01
γ energy scale	0.22	<0.01	<0.01	0.25	<0.01	<0.01
γ resolution	0.02	<0.01	0.01	<0.01	<0.01	0.01
γ ID efficiency	0.02	0.03	0.05	0.02	0.01	0.01
total	0.34	0.10	0.08	0.37	0.08	0.11
uncertainty	$1.52 < \lvert\eta\rvert < 1.81$			$1.81 \leq \lvert\eta\rvert < 2.37$		
	p_T/GeV					
	[20,25)	[25,30)	[30,40]	[20,25)	[25,30)	[30,40]
statistical	0.01	0.13	0.15	0.03	0.02	0.05
fit	0.01	0.07	0.04	<0.01	0.06	0.01
e energy scale	<0.01	<0.01	<0.01	0.01	<0.01	<0.01
e resolution	0.03	0.01	<0.01	<0.01	0.01	0.01
e reco. and ID efficiency	<0.01	0.02	0.03	<0.01	0.01	0.02
e trigger efficiency	<0.01	0.01	0.02	<0.01	<0.01	<0.01
γ energy scale	0.30	0.02	0.01	0.03	<0.01	<0.01
γ resolution	0.04	0.03	<0.01	<0.01	0.02	0.02
γ ID efficiency	0.09	0.03	0.06	0.07	0.06	0.07
total	0.32	0.15	0.16	0.11	0.09	0.09

Table 9.2: Overview of all uncertainties, which have been taken into account for the measurement of the $e \to \gamma$ misidentification scale factors. These include fit uncertainties as well as uncertainties on corrections applied on data (e/γ energy scale) and Monte Carlo simulation. The scale factors only considers electrons, which have been identified as unconverted photons.

uncertainty	$0 \leq \lvert\eta\rvert < 0.60$			$0.60 \leq \lvert\eta\rvert < 1.37$		
	p_T/GeV					
	[20,25)	[25,30)	[30,40]	[20,25)	[25,30)	[30,40]
statistical	0.04	0.04	0.02	0.03	0.03	0.04
fit	0.09	0.02	0.01	0.02	0.03	<0.01
e energy scale	0.05	<0.01	0.02	0.10	<0.01	<0.01
e resolution	0.01	0.01	0.01	<0.01	0.01	<0.01
e reco. and ID efficiency	<0.01	0.02	0.02	<0.01	0.03	0.03
e trigger efficiency	<0.01	<0.01	0.01	<0.01	0.01	0.01
γ energy scale	0.02	<0.01	<0.01	0.04	<0.01	0.02
γ resolution	0.01	0.01	<0.01	0.01	0.01	<0.01
γ ID efficiency	0.01	0.01	<0.01	0.02	0.01	0.01
total	0.12	0.05	0.04	0.12	0.06	0.06
uncertainty	$1.52 < \lvert\eta\rvert < 1.81$			$1.81 \leq \lvert\eta\rvert < 2.37$		
	p_T/GeV					
	[20,25)	[25,30)	[30,40]	[20,25)	[25,30)	[30,40]
statistical	0.01	0.04	0.05	0.02	0.02	0.04
fit	0.05	0.02	<0.01	0.07	0.06	0.01
e energy scale	0.01	<0.01	<0.01	0.01	<0.01	<0.01
e resolution	0.03	0.01	<0.01	<0.01	<0.01	<0.01
e reco. and ID efficiency	<0.01	0.04	0.04	<0.01	0.02	0.01
e trigger efficiency	<0.01	0.02	0.02	<0.01	<0.01	<0.01
γ energy scale	0.20	<0.01	<0.01	0.02	<0.01	0.03
γ resolution	<0.01	0.01	<0.01	0.01	0.01	0.01
γ ID efficiency	0.08	0.07	0.06	0.05	0.06	0.08
total	0.22	0.09	0.09	0.07	0.07	0.09

Table 9.3: Overview of all uncertainties, which have been taken into account for the measurement of the $e \to \gamma$ misidentification scale factors. These include fit uncertainties as well as uncertainties on corrections applied on data (e/γ energy scale) and Monte Carlo simulation. The scale factors only consider electrons, which have been identified as converted photons.

Chapter 10

Background contributions with a prompt photon and misidentified electron in the final state

Due to the similar isolation properties of electrons and photons, it is not possible to distinguish prompt photons and electrons misidentified as photons using the p_T^{cone20} variable. Furthermore, signal $t\bar{t}\gamma$ events cannot be discriminated from background processes with a prompt photon in the final state. Hence, the photon p_T^{cone20} isolation distributions of these signal and background processes follow the shape of the prompt photon template and only the sum of all contributions from processes with a prompt photon and misidentified electron in the final state are estimated from the template fit. Therefore, background contributions with a prompt photon or misidentified electron in the final state have to be estimated separately, either via a data-driven approach (QCD multijet+γ and W+jets+γ production) or using Monte Carlo simulation (Z+jets+γ, diboson+γ and single top+γ production).
The main contribution arises from top quark pair events, where an electron is misidentified as a photon, or real $t\bar{t}\gamma$ events, which are not included in the definition of the signal phase space or fiducial region, where the final $t\bar{t}\gamma$ cross section is measured. These yields are also estimated from Monte Carlo simulation. In the following, prompt photons will not only include bremsstrahlung photons from quarks or radiation from charged leptons, but also electrons misidentified as photons, if not explicitly mentioned.

10.1 QCD multijet+γ contribution

QCD multijet processes feature jets in the final state as well as fake leptons. Such electrons or muons are not produced in the hard process, but in the decay of heavy flavor mesons, especially $\pi^{\pm}$ particles, or hadrons from jet fragmentation, which are misidentified as leptons. These QCD multijet events can include prompt photons, which are produced in the hard process (γ+jet production) or are emitted from leptons and quarks in the jet fragmentation. The estimation of the QCD multijet background contribution with a prompt photon in the final state is performed in three steps:

1. The matrix method [191, 123] is used to estimate the contribution and also the differential distributions of the QCD multijet background after the $t\bar{t}$ event seletion (signal event selection up to cut 9).

2. The photon-related cuts are added to complete the final event selection (cut 10-12), yielding a sample of events with a fake lepton and a photon candidate.

3. A template fit, as described in Section 7.2, is performed to the p_T^{cone20} distribution of these candidate photons to estimate the fraction of events with a prompt photon in the final state.

These three steps are described in detail in the next subsections.

10.1.1 QCD multijet estimation with the matrix method

The matrix method is a data-driven technique to estimate the amount of events containing a fake lepton. The method is based on a selection which differs from the standard $t\bar{t}$ selection using a loose lepton definition for the selection of the good muon or electron, instead of the tight lepton definition. For the loose electron definition, the tight electron identification is replaced by the medium menu, which is defined by less strict shower shape requirements. In addition, no isolation cut is used. For the loose muon definition, the track and calorimeter isolation cuts are dropped, compared to the standard tight selection.
The number of events with a selected loose lepton N_{loose} consists of events with either a real lepton $N_{\text{real}}^{\text{loose}}$ or a fake lepton $N_{\text{fake}}^{\text{loose}}$ passing the loose selection:

$$N^{\text{loose}} = N_{\text{real}}^{\text{loose}} + N_{\text{fake}}^{\text{loose}} .$$

This equation can also be derived for the number of events with a tight lepton:

$$N^{\text{tight}} = N_{\text{real}}^{\text{tight}} + N_{\text{fake}}^{\text{tight}} = \varepsilon_{\text{real}} \cdot N_{\text{real}}^{\text{loose}} + \varepsilon_{\text{fake}} \cdot N_{\text{fake}}^{\text{loose}} ,$$

where $\varepsilon_{\text{real}}$ and $\varepsilon_{\text{fake}}$ are the probabilities of real and fake loose leptons to also be selected as tight leptons. The number of events with a fake lepton fulfilling the tight selection can be expressed as

$$N_{\text{fake}}^{\text{tight}} = w^{\text{loose}} \cdot N^{\text{loose}} \cdot \varepsilon_{\text{real}} + w^{\text{tight}} \cdot N^{\text{tight}}$$

$$\text{with:} \quad w^{\text{loose}} = \frac{\varepsilon_{\text{real}} \cdot \varepsilon_{\text{fake}}}{\varepsilon_{\text{real}} - \varepsilon_{\text{fake}}} > 0 \quad \text{and} \quad w^{\text{tight}} = -\frac{\varepsilon_{\text{fake}}}{\varepsilon_{\text{real}} - \varepsilon_{\text{fake}}} < 0 .$$

In addition to the total yield, kinematic distributions of the QCD multijet background can be extracted by weighting events which pass the loose selection. The weight w^{tight} is applied to events passing both event selections, the weight w^{loose} is applied only to events which pass the loose selection, but not the tight selection.
The efficiencies for real leptons $\varepsilon_{\text{real}}$ are measured using $Z \to l^+l^-$ data events which are selected with the tag & probe method for electrons and muons [191, 123]. The efficiencies of selecting fake leptons $\varepsilon_{\text{fake}}$ are estimated in a control region dominated by QCD multijet events:

$$\text{Electron channel} : 5\,\text{GeV} < \not{E}_T < 20\,\text{GeV} ,$$
$$\text{Muon channel} : m_T^W < 20\,\text{GeV} \text{ and } \not{E}_T + m_T^W < 60\,\text{GeV} .$$

Events are selected with at least one good jet and exactly one loose lepton. The efficiency $\varepsilon_{\text{fake}}$ is equivalent to the fraction of loose candidates passing also the tight selection. The

main background contributions in these control regions, W+jets and Z+jets events, are estimated from Monte Carlo simulation and subtracted from the yields in the control region.
The real and fake efficiencies in the muon channel are parameterized as a function of the muon-η and and as a function of the highest p_T of the selected jets. In the electron channel, the efficiencies are parameterized as a function of the electron-η.
In agreement with the recommendation of the ATLAS top working group, a systematic uncertainty of 50% was assigned to the QCD multijet estimate in the electron channel and 20% in the muon channel [191, 123].

10.1.2 QCD multijet estimation with a prompt photon in the final state

The photon-related selection cuts are added to the loose and tight selection to determine the number of QCD multijet events $N_{\text{QCD+}\gamma}$ using the matrix method. Since loose electrons can also be identified as photons, a minimal distance of $\Delta R = 0.1$ is required between the selected loose electrons and photons. In order to estimate only the contribution featuring prompt photons and not hadrons which have been misidentified as photons, a template fit is performed to the p_T^{cone20} distributions in data as described in Section 7.2. Template fits cannot be executed for data distributions featuring events with Poissonian probability density functions which are not well-defined, i.e. events with negative weights w^{tight}. Since the estimated yield is dominated by events passing only the loose selection which have the positive weight w^{loose}, the fraction of prompt photon events is only estimated from events with a positive weight. This approach is valid, as the photon isolation and the electron identification criteria are uncorrelated.
The derivation methods of the signal and background templates have been discussed in Chapter 8. The same signal templates can be used for the purity estimation of prompt photons within the QCD+γ multijet candidates, while the background templates need to be reweighted according to the p_T and $|\eta|$ spectra of QCD multijet events with a misidentified hadron. However, the control region does not provide enough statistics in both channels, so that the $t\bar{t}\gamma$ background templates are used for the estimation. The template fits are performed to the p_T^{cone20} distribution of $N^{\text{loose}}_{\text{QCD+}\gamma}$ loose lepton events without applying the QCD event weight w^{loose}. Figure 10.1 shows the results of the template fits in both channels for all photons, as well as separately for unconverted and converted photons. The resulting fraction of prompt photon events f_γ^{prompt} is calculated by the estimated yield of the signal template, divided by the total yield of both signal and background template. The final number of QCD multijet events with a prompt photon $N^{\text{prompt}}_{\text{QCD+}\gamma}$ is then

$$N^{\text{prompt}}_{\text{QCD+}\gamma} = f_\gamma^{\text{prompt}} \cdot N_{\text{QCD+}\gamma}\,.$$

The results for $N_{\text{QCD+}\gamma}$, f_γ^{prompt} and $N^{\text{prompt}}_{\text{QCD+}\gamma}$ in the single electron and muon channel, separately for unconverted and converted photons, are listed in Table 10.1. The templates in the different p_T and $|\eta|$ region, which are shown in Figure 8.6, are used for fits to the p_T^{cone20} distributions of the QCD+γ candidates and the largest deviations to the nominal result are applied as systematic uncertainties. Table 10.2 lists all uncertainties to the

Electron channel			
	unconverted	converted	all
$N^{\text{loose}}_{\text{QCD}+\gamma}$	33 ± 5.7	44 ± 6.6	77 ± 8.8
$f^{\text{prompt}}_{\gamma}$	0.66± 0.33	0.57± 0.27	0.60± 0.21
$N_{\text{QCD}+\gamma}$	0.6 ± 1.3	2.4 ± 1.5	3.0 ± 2.0
$N^{\text{prompt}}_{\text{QCD}+\gamma}$	0.4± 0.9	1.4± 1.1	1.8± 1.4
Muon channel			
	unconverted	converted	all
$N^{\text{loose}}_{\text{QCD}+\gamma}$	30 ± 5.5	27 ± 5.2	57 ± 7.5
$f^{\text{prompt}}_{\gamma}$	0.70± 0.35	0.06± 0.20	0.42± 0.20
$N_{\text{QCD}+\gamma}$	3.2 ± 0.7	2.2 ± 0.6	5.3 ± 1.0
$N^{\text{prompt}}_{\text{QCD}+\gamma}$	2.2± 1.2	0.1± 0.4	2.2± 1.2

Table 10.1: Results for QCD multijet events with a prompt photon, separately for unconverted, converted and all photons in the electron and muon channel, including statistical uncertainties. The table include the number of QCD multijet+γ candidates with a loose lepton $N^{\text{loose}}_{\text{QCD}+\gamma}$ without applying the QCD event weight w^{loose}. These events are used for the template fits to estimate the fraction of prompt photon events $f^{\text{prompt}}_{\gamma}$. Further, the table lists the number of QCD multijet+γ candidates $N_{\text{QCD}+\gamma}$ estimated with the matrix method and the final QCD multijet yields with a prompt photon $N^{\text{prompt}}_{\text{QCD}+\gamma}$, which is calculated by $N_{\text{QCD}+\gamma}$ multiplied by the fraction of prompt photon events $f^{\text{prompt}}_{\gamma}$.

background contribution of QCD multijet events with a prompt photon.

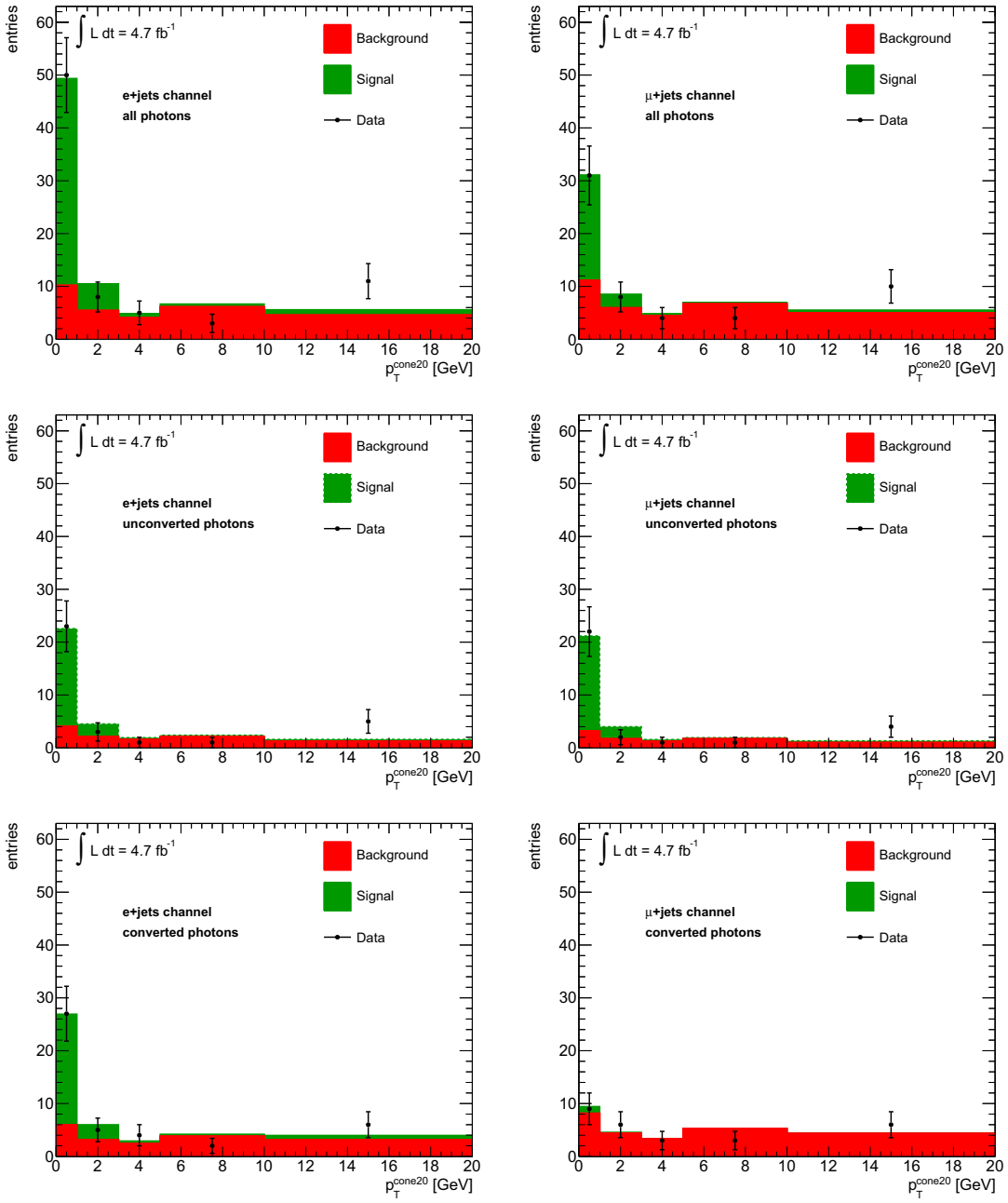

Figure 10.1: Template fit results for QCD multijet events with a selected photon candidate in the electron (left column) and muon channel (right column). Data p_T^{cone20} distributions are shown as black points, together with the fit results of the signal templates (green) and background templates (red), for all photons (top) as well as unconverted (middle) and converted photons (bottom). The fraction of prompt events is calculated by the expected event yield of the signal template, divided by the total expected event yield of the signal template and the background template.

Electron channel			
uncertainty	unconverted	converted	all
statistical	± 0.9	± 1.1	± 1.4
QCD multijet yield	± 0.2	± 0.7	± 0.9
p_t-reweighting of bkg. template	± 0.04	± 0.03	± 0.02
η-reweighting of bkg. template	± 0.2	± 0.2	± 0.2
total	± 0.9	± 1.3	± 1.6
Muon channel			
uncertainty	unconverted	converted	all
statistical	± 1.2	± 0.4	± 1.2
QCD multijet yield	± 0.4	± 0.3	± 0.4
p_t-reweighting of bkg. template	± 0.03	± 0.03	± 0.02
η-reweighting of bkg. template	± 0.2	± 0.1	± 0.2
total	± 1.3	± 0.4	± 1.3

Table 10.2: Overview of all uncertainties, which have been considered for the measurement of QCD multijet events with a prompt photon in the final state, separately for unconverted and converted photons in the electron and muon channel.

10.2 W+jets+γ contribution

The contribution from W+jets processes with a prompt photon in the final state is also estimated with a data-driven approach. The final event selection is modified to define a control region, which is dominated by W+jets+γ events:

1. A minimum of one and up to three jets are required instead of at least four jets (selection cut 6).
2. None of the selected jets have to be identified as a b-jets (selection cut 9).
3. The invariant mass cut of the selected electron and the selected photon is extended to $\pm 15\,\text{GeV}$ around the Z-boson mass, in order to further decrease the Z+jets background contribution (selection cut 11).

The event yields in the control region are estimated in both channels, which include events with prompt photons as well as hadrons misidentified as photons. Figures 10.2 and 10.3

show various kinematic distributions, measured in the control region, compared to the Monte Carlo expectation. Additional figures are included in Appendix B.4. The number of prompt photon events in the control region are calculated using the same approach as for the QCD multijet+γ background, estimating the fraction of events with a prompt photon with template fits to the data p_T^{cone20} distribution. The background templates are reweighted in p_T and η using events which have passed the control region selection with the background photon identification, as described in Section 8.2. It is assumed that the fraction of prompt photon events does not depend on the jet multiplicity and is therefore constant in the control and signal region. This assumption has been studied by splitting the control region into three bins of different jet multiplicities and perform separate template fits to the data p_T^{cone20} distributions with results listed in Table 10.3. No dependence on the jet multiplicity is observed within statistical uncertainties. This behavior has been also investigated in Monte Carlo with Alpgen W+jets events using truth information, showing also a constant fraction of prompt photon events for different jet multplicities. The template fit results for the control region are shown in Figure 10.4 and the expected prompt photon data yield in Table 10.4.

Contributions from $t\bar{t}$, Z+jets, single top, and diboson events with a prompt photon in the final state have to be subtracted from the number of events with a prompt photon $N_{\text{data, CR}}^{\text{prompt}}$. They are estimated from Monte Carlo simulation. Events are considered, when they have passed the event selection of the W+jets+γ control region. In addition, the selected reconstructed photon has to be matched to a true photon on generator level within a cone size of $\Delta\eta \times \Delta\phi = 0.025 \times 0.050$ or a true electron within a cone of $\mathrm{d}R = 0.15$. In case of a misidentified electron, this truth matching procedure tends to mismatch the reconstructed photon to a very low-energetic truth photon, which has been emitted from the final state electron. Events with a matched truth photon-p_T below 5 GeV are therefore additionally checked, whether a truth parton around the reconstructed photon has a transverse momentum closer to the reconstructed value, in order to categorize such events correctly.

All Monte Carlo samples are explained in Chapter 5, with the $t\bar{t}$ expectation calculated

	Electron channel	Muon channel
1 jet	0.69 ± 0.04	0.76 ± 0.03
2 jets	0.73 ± 0.06	0.75 ± 0.05
3 jets	0.72 ± 0.09	0.73 ± 0.08
CR	0.71 ± 0.03	0.75 ± 0.02

Table 10.3: Results of the template fits for different jet multiplicities of the W+jets+γ control region and the entire region (1-3 jets, CR) to determine the fraction of events with a prompt photon, including statistical uncertainties.

Electron channel			
	unconverted	converted	all
$N_{\text{data, CR}}$	2320 ± 48	2029 ± 45	4349 ± 66
f_γ^{prompt}	0.82± 0.04	0.62± 0.04	0.71± 0.03
$N_{\text{data, CR}}^{\text{prompt}}$	1902± 111	1248± 77	3076± 132
Muon channel			
	unconverted	converted	all
$N_{\text{data, CR}}$	4868 ± 70	3526 ± 59	8394 ± 92
f_γ^{prompt}	0.83± 0.03	0.64± 0.03	0.75± 0.02
$N_{\text{data, CR}}^{\text{prompt}}$	4050± 169	2267± 119	6311± 205

Table 10.4: Estimated total data yields in the W+jets+γ control region $N_{\text{data, CR}}$, prompt photon fraction f_γ^{prompt}, which is estimated with template fits, and data yield in control region for events with a prompt photon or misidentified electron in the final state $N_{\text{data, CR}}^{\text{prompt}}$. All numbers are listed seperately for unconverted and converted photons in the electron and muon channel.

as a combination of the WHIZARD $t\bar{t}\gamma$ sample and MC@NLO $t\bar{t}$ events after overlap removal. Uncertainties on each expected cross section are taken into account for the simulated events, which read ±20% for WHIZARD $t\bar{t}\gamma$, ±10% for MC@NLO $t\bar{t}$ and ±5% for diboson production. The uncertainties for the s-, t- and Wt-channel of the single top quark samples are $^{+4\%}_{-3\%}$, ±4% and ±7%, respectively. The Berends-Giele scaling [192, 181] is considered for the Z+jets Monte Carlo sample, which assumes an uncertainty of 24% for each simulated jet in the final state. This results in $\sigma_z = \sqrt{i} \cdot 24\%$ with $i = 1, 2, 3$ jets. Further, the Z+jets, single top, diboson and MC@NLO $t\bar{t}$ Monte Carlo samples do not include photon radiation at matrix element level, but only photon radiation as QED corrections simulated by the PHOTOS package or radiation from quarks provided by PYTHIA or HERWIG. A systematic uncertainty has been estimated by comparing the W+jets and W+jets+γ Monte Carlo samples, generated with ALPGEN+HERWIG. Events with a good photon are selected in each sample, if the photon is emitted from a parton of the hard process. The difference between the two calculated yields is 23.8%, which is used as a symmetric uncertainty.

In case of an electron misidentified as a photon, scale factors are applied, which are calculated using the electron misidentification fake rates in data and Monte Carlo simulation, as described in Chapter 9. Uncertainties on these scale factors are included in the systematic uncertainties of the Monte Carlo yields.

Electron channel			
	unconverted	converted	all
$N^{\text{prompt}}_{\text{data, CR}}$	1902± 111	1248± 77	3076± 132
$t\bar{t}\gamma$	84.7 ± 14.3	57.7 ± 9.1	142.3 ± 22.9
$t\bar{t}$ (misid. $e^{\pm}$)	32.4 ± 3.4	132.9 ± 14.0	165.3 ± 16.6
Z+jets+γ	218.5 ± 93.4	146.5 ± 62.3	364.9 ± 154.1
Z+jets (misid. $e^{\pm}$)	59.6 ± 30.3	261.0 ± 130.4	320.6 ± 155.6
diboson+γ	11.1 ± 2.9	7.1 ± 2.0	18.2 ± 4.7
diboson (misid. $e^{\pm}$)	3.4 ± 0.7	14.6 ± 1.6	18.0 ± 1.7
single top+γ	7.1 ± 2.0	4.8 ± 1.4	12.0 ± 3.2
single top (misid. $e^{\pm}$)	0.1 ± 0.1	0.2 ± 0.2	0.2 ± 0.3
QCD	30.7 ± 16.3	43.6 ± 22.5	77.6 ± 39.5
$N^{\text{prompt}}_{W+\gamma,\text{CR}}$	1454± 150	580± 82	1957± 261
Muon channel			
	unconverted	converted	all
$N^{\text{prompt}}_{\text{data, CR}}$	4050± 169	2267± 119	6311± 205
$t\bar{t}\gamma$	150.3 ± 25.4	98.9 ± 15.6	249.3 ± 40.1
$t\bar{t}$ (misid. $e^{\pm}$)	58.3 ± 6.0	233.4 ± 23.2	281.7 ± 28.0
Z+jets+γ	572.6 ± 240.1	329.0 ± 138.9	901.7 ± 376.7
Z+jets (misid. $e^{\pm}$)	3.8 ± 2.5	14.8 ± 8.1	18.5 ± 9.9
diboson+γ	20.5 ± 5.2	13.9 ± 3.6	34.4 ± 8.6
diboson (misid. $e^{\pm}$)	5.8 ± 0.8	19.5 ± 1.7	25.3 ± 1.9
single top+γ	15.4 ± 4.0	7.7 ± 2.1	23.0 ± 5.9
single top (misid. $e^{\pm}$)	0.3 ± 0.2	1.1 ± 0.4	1.4 ± 0.5
QCD	277.0 ± 58.4	130.0 ± 28.6	404.0 ± 83.6
$N^{\text{prompt}}_{W+\gamma,\text{CR}}$	2946± 301	1419± 188	4372± 440

Table 10.5: Estimated data and background yields in the W+jets+γ control region. The table lists the number of data events in the control region $N^{\text{prompt}}_{\text{data, CR}}$, the estimated background yields and the number of W+jets+γ candidates $N^{\text{prompt}}_{W+\gamma,\text{CR}}$. The different background yields are estimated from Monte Carlo simulation, except for the QCD yield, and include only events with a prompt photon or a misidentified electron. $N^{\text{prompt}}_{W+\gamma,\text{CR}}$ is calculated from the data yield after subtracting all background contributions. All numbers are listed separately for unconverted and converted photons in the electron and muon channel, including combined statistical and systematic uncertainties.

The contribution from QCD multijet events with a prompt photon is estimated with the same approach as described in Section 10.1, using the matrix method and template fits to the p_T^{cone20} distribution.
The results for the individual contributions in the control region are subtracted from the number of events in the control region $N^{\text{prompt}}_{W+\gamma,\text{data, CR}}$ to yield the number of W+jets+γ events $N^{\text{prompt}}_{W+\gamma,\text{CR}}$. The individual numbers and their corresponding uncertainties are given in Table 10.5.
The final yield in the signal region $N^{\text{prompt}}_{W+\gamma,\text{SR}}$ is calculated by extrapolating the estimated number of events in the control region $N^{\text{prompt}}_{W+\gamma,\text{CR}}$ to the signal region by using W+jets+γ events from Monte Carlo simulation:

$$N^{\text{prompt}}_{W+\gamma,\text{SR}} = N^{\text{prompt}}_{W+\gamma,\text{CR}} \cdot \frac{N_{\text{MC, SR}}}{N_{\text{MC, CR}}} \,.$$

The extrapolation factor is calculated using the SHERPA Monte Carlo sample, which include jets from light quarks as well as heavy flavor quarks in the final state. Two corrections are applied to this sample. First, the total yield is rescaled using data-driven estimations from the W boson charge asymmetry method [193, 123]. This approach uses the overall charge asymmetry in the W boson production at the LHC due to differences in the quark and antiquark parton distribution functions. Processes are therefore favored which involve u valence quarks ($u\bar{d} \to W^+$). The ratio of cross sections, $r = \frac{\sigma(pp\to W^+)}{\sigma(pp\to W^+)}$ is theoretically well understood and hence used to extract the number of W+jets background events:

$$N_W = N_{W^+} + N_{W^-} = \left(\frac{r+1}{r-1}\right)(D^+ - D^-)\,,$$

where D^+ and D^- are the number of events with a positively and negatively charged lepton, respectively. The formula is valid since the processes $t\bar{t}$, QCD multijet and Z+jets are charge symmetric.
Further, the extrapolation factor is using b-tagging information in the signal region and is therefore sensitive to the heavy flavor content of the Monte Carlo sample. These flavor fractions (W+$c(\bar{c})$, W+$b\bar{b}$, W+light quarks) have been measured in data using events with a W boson and two jets and are applied as scale factors to the simulated events [193, 123]. Multiple systematic variations have been considered for both corrections, resulting in combined systematic uncertainties up to 27% on the extrapolation factors. The final results of the W+jets+γ yields with a prompt photon are listed in Table 10.6.

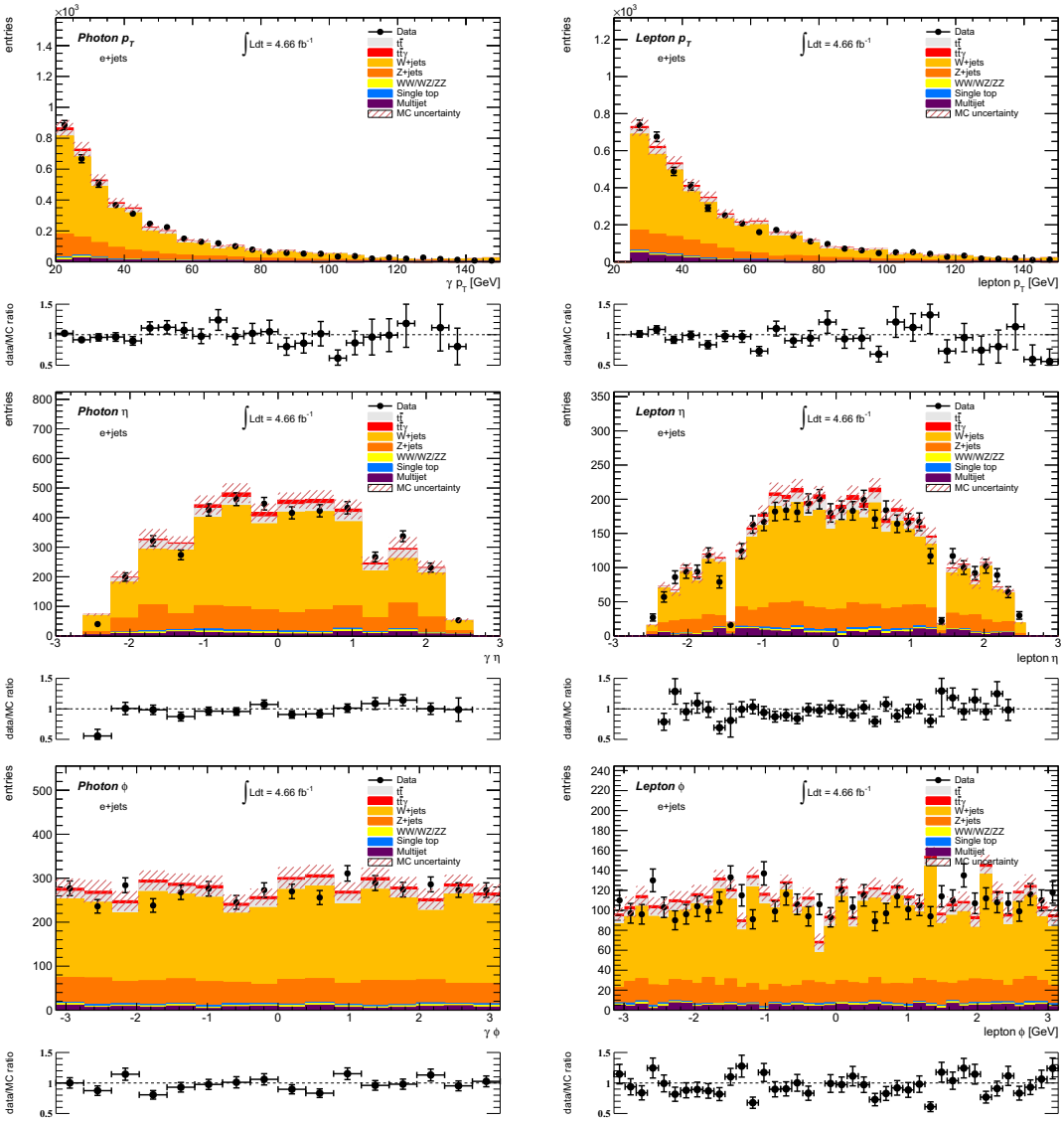

Figure 10.2: Comparison between data and the expectation from Monte Carlo simulation for events passing the event selection of the W+jets+γ control region in the electron channel. p_T (upper row), η (middle row) and ϕ (lower row) distributions are shown for selected photons (left column) and electrons (right column). Data points are shown in black with statistical uncertainties, while the stacked histogram includes the Monte Carlo expectation of the signal process and all background contributions. Each plot also illustrates systematic uncertainties on the Monte Carlo prediction. Further, a data to Monte Carlo ratio plot is included in each figure with statistical uncertainties.

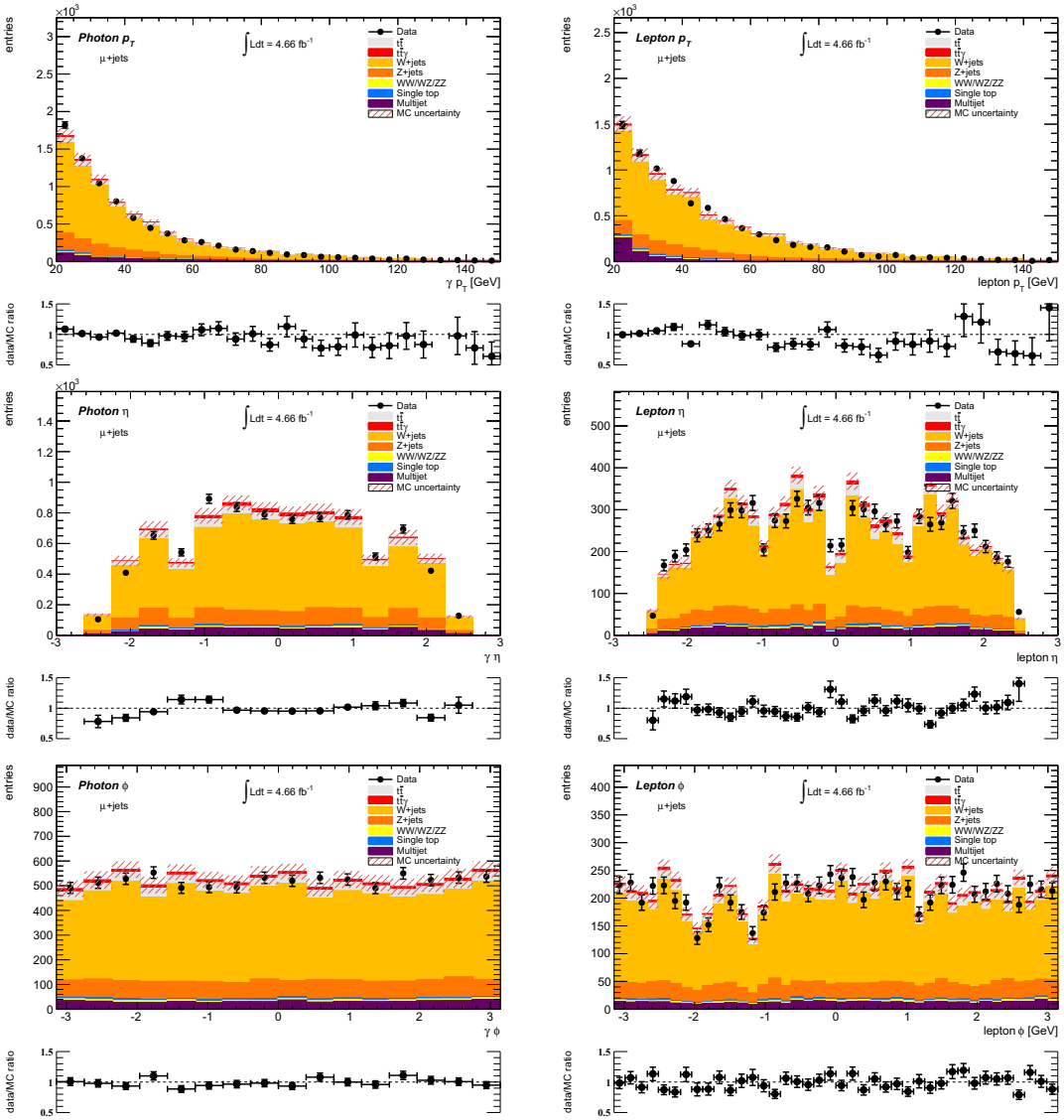

Figure 10.3: Comparison between data and the expectation from Monte Carlo simulation for events passing the event selection of the W+jets+γ control region in the muon channel. p_T (upper row), η (middle row) and ϕ (lower row) distributions are shown for selected photons (left column) and muons (right column). Data points are shown in black with statistical uncertainties, while the stacked histogram includes the Monte Carlo expectation of the signal process and all background contributions. Each plot also illustrates systematic uncertainties on the Monte Carlo prediction. Further, a data to Monte Carlo ratio plot is included in each figure with statistical uncertainties.

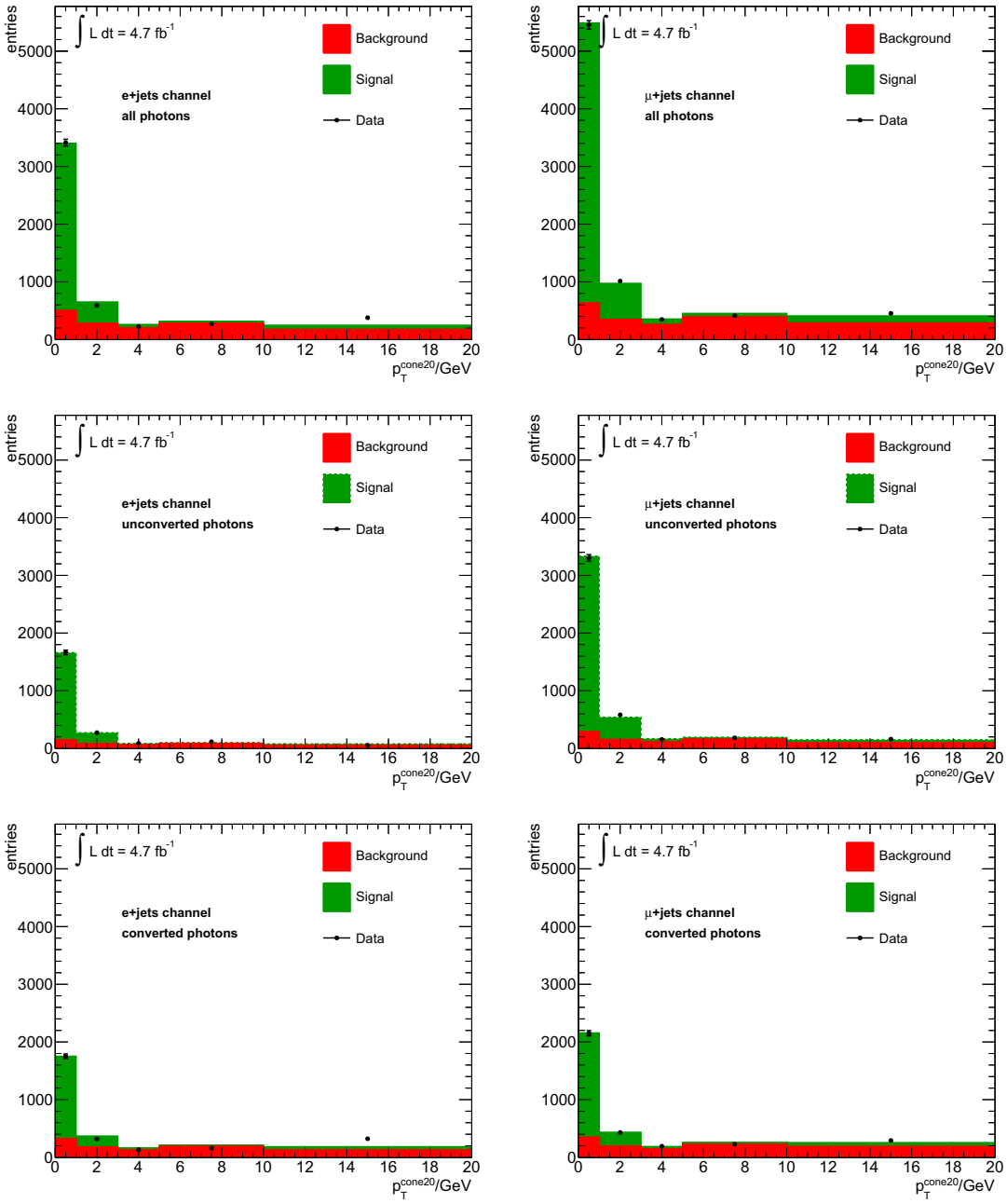

Figure 10.4: Template fit results for W+jets events with a selected photon candidate in the electron (left column) and muon channel (right column). Data p_T^{cone20} distributions are shown as black points, together with the fit results of the signal templates (green) and background templates (red), for all photons (top) as well as unconverted (middle) and converted photons (bottom). The fraction of prompt events is calculated by the expected event yield of the signal template, divided by the total expected event yield of the signal template and the background template.

Electron channel			
	unconverted	converted	all
$\frac{N_{\text{MC, SR}}}{N_{\text{MC, CR}}}[\times 10^{-3}]$	3.3 ± 1.0	3.3 ± 1.2	3.3 ± 0.9
$N^{\text{prompt}}_{W+\gamma,\text{SR}}$	4.8±1.5	1.9±0.8	6.5±2.0
Muon channel			
	unconverted	converted	all
$\frac{N_{\text{MC, SR}}}{N_{\text{MC, CR}}}[\times 10^{-3}]$	4.1 ± 1.0	4.3 ± 1.2	4.2 ± 1.0
$N^{\text{prompt}}_{W+\gamma,\text{SR}}$	12.1±3.3	6.0±1.9	18.2±4.5

Table 10.6: Extrapolation factors $\frac{N_{\text{MC, SR}}}{N_{\text{MC, CR}}}$ and final W+jets+γ background yields with a prompt photon in the final state $N^{\text{prompt}}_{W+\gamma,\text{SR}}$. All numbers include combined statistical and systematic uncertainties.

10.3 Top quark pair background

The main $t\bar{t}\gamma$ background arises from top quark pair production. The contribution of $t\bar{t}$ events with a misidentified hadron is included in the misidentified hadron background yield estimated from the template fit. Other contributions are estimated separately and described in the following section.

10.3.1 $t\bar{t}$ events with a misidentified electron in the final state

The main prompt photon background is composed from $t\bar{t}$ events with a misidentified electron in the final state. The contributions in the single electron and single muon channel are estimated using the MC@NLO $t\bar{t}$ sample, considering events which have passed the $t\bar{t}\gamma$ event selection. In addition, the selected photon has to be matched to a true electron. The $e \to \gamma$ misidentification scale factors are applied to these events for the yield estimations. The systematic uncertainties of these scale factors are considered as well as an uncertainty of ±10% on the expected $t\bar{t}$ cross section.
The largest fraction of events are dileptonic $t\bar{t}$ events, where no photon is emitted within the hard scattering process, but an electron in the final state is misidentified and passes the standard photon selection. Table 10.7 lists the total yields as well as the results divided into the true final state of the respective $t\bar{t}$ event, indicating that around 90% of the total yields result from such dileptonic events. Small contributions are added by single electron events, where the electron in the final state is misidentified as a photon and a fake lepton from hadron decay passes the lepton selection.

Furthermore, $t\bar{t}\gamma$ events contribute to this category of background. A high-energetic photon is emitted from the final state electron with a very small distance in $\eta - \phi$ space of $\Delta R < 0.02$. In this case, the e/γ reconstruction algorithm fails to discriminate both partons, but reconstructs the electron as a photon, while omitting the true photon. Due to the very small ΔR values, the truth matching procedure tends to mismatch the reconstructed photon to the true photon, rather than the true electron. Hence, it is additionally checked, which of the two true partons has a transverse momentum closer to the reconstructed p_T. Overall, such misidentified $t\bar{t}\gamma$ events do not occur in the WHIZARD sample due to the minimum invariant mass requirements between the photon and the lepton, disregarding events with photons collinear to any other final state parton.

10.3.2 $t\bar{t}\gamma$ events outside of signal phase space

The signal phase space is defined by the phase space cuts used for the generation of the WHIZARD Monte Carlo events, as decribed in Section 5.4. This results in possible $t\bar{t}\gamma$ events outside of the signal phase space, which pass the final event selection and therefore are to be treated as a background source. Top quark pair events generated with MC@NLO are used to estimate this contribution. This sample contains $t\bar{t}\gamma$ events due to photons from lepton emission, provided by the PHOTOS package, or from quarks, which were simulated from HERWIG. In order to avoid double counting of signal events in Monte Carlo simulation, events in the MC@NLO sample which overlap with the WHIZARD sample were removed, as discussed in Section 5.6. The yields are estimated using the true $t\bar{t}\gamma$ events after the overlap removal, with the results listed in Table 10.8. The number of expected events are shown separately according to the respective origin of the identified photon. These photon sources, which are determined on generator level, are either charged leptons from the $t\bar{t}$ final state or quarks before hadronization. Systematic uncertainties include $\pm 10\%$ on the expected $t\bar{t}$ cross section and 23.8%, since photons have not been included in the MC@NLO matrix element calculation (see Section 10.2).

10.3.3 $t\bar{t}\gamma$ events outside of fiducial region

The $t\bar{t}\gamma$ cross section is measured in a fiducial region, selecting only photons with $p_T > 20\,\text{GeV}$ and $|\eta| < 2.37$ on generator level. The fiducial measurement will be discussed in detail in Chapter 11. Since the geometrical and kinematic limits of the photon match on generator and reconstruction level, migration effects can occur, when a reconstructed final state photon passes the object selection, even though the true photon has been generated outside of the defined fiducial region. These events have to be assigned to the $t\bar{t}\gamma$ background and hence, their contributions are estimated separately using the WHIZARD $t\bar{t}\gamma$ sample.
Events are selected after passing the $t\bar{t}\gamma$ signal selection with photons matched to a true photon from the hard scattering process. Contributions are negligibly small from events, where the photon fails the object selection, but an electron is misidentified as a photon. Figure 10.5 shows histograms of the reconstructed photon p_T and $|\eta|$ versus the corresponding truth values of the WHIZARD photon. As expected, the reconstructed and

Electron channel			
true final state	unconverted	converted	all
no final state photon			
$e + e$	3.3±0.5	13.0±1.6	16.3±1.9
$e + \mu/\tau$	0.1±0.1	1.7±0.3	1.7±0.3
other dilep.	<0.1	<0.1	<0.1
semilep.	0.4±0.1	0.4±0.3	0.8±0.3
collinear final state photon			
$e + \mu/\tau$	0.5±0.2	1.2±0.4	1.7±0.5
other	<0.1	-0.1±0.1	-0.1±0.1
total	4.0±0.6	16.0±2.1	20.0±2.2
Muon channel			
true final state	unconverted	converted	all
no final state photon			
$e + e$	<0.1	<0.1	<0.1
$e + \mu/\tau$	4.5±0.6	19.2±2.1	23.7±2.4
other dilep.	0.4±0.2	0.9±0.2	1.3±0.3
semilep.	0.2±0.2	1.1±0.4	1.3±0.4
collinear final state photon			
$e + e$	0.2±0.1	0.9±0.4	1.1±0.4
other	<0.1	<0.1	<0.1
total	5.6±0.8	22.3±2.8	27.9±2.9

Table 10.7: Estimated $t\bar{t}$ background yields with a misidentified electron in the final state. The table lists the number of events divided into the respective true final state of the $t\bar{t}$ event, which are mostly dileptonic events where one electron is misidentified as a photon. Furthermore, it is differentiated, whether a true photon exist in the final state, which is radiated collinear to a final state electron and is thus lost in the reconstructed process, or if it is a true $t\bar{t}$ event. All yields are listed separately for unconverted and converted photons in the electron and muon channel, including combined statistical and systematic uncertainties.

Electron channel			
photon source	unconverted	converted	all
radiation from e	0.18±0.15	-0.03±0.03	0.15±0.15
radiation from μ	0.17±0.14	0.15±0.08	0.31±0.17
radiation from τ	<0.01	0.08±0.08	0.08±0.08
bremsstrahlung	0.56±0.21	0.35±0.15	0.92±0.31
total	0.9±0.3	0.6±0.3	1.5±0.4
Muon channel			
photon source	unconverted	converted	all
radiation from e	0.52±0.21	0.37±0.16	0.89±0.31
radiation from μ	0.39±0.18	0.39±0.17	0.77±0.29
radiation from τ	0.20±0.11	0.09±0.06	0.29±0.13
bremsstrahlung	1.06±0.35	0.28±0.16	1.34±0.43
total	2.2±0.5	1.1±0.3	3.3±0.6

Table 10.8: Estimated number of $t\bar{t}\gamma$ events, which are not included in the WHIZARD $t\bar{t}\gamma$ sample. The photon can be emitted from a charged lepton (e, μ, τ) or as a bremsstrahlung photon from a quark before the hadronization process. All yields are listed separately for unconverted and converted photons in the electron and muon channel, including combined statistical and systematic uncertainties. Negative yields can arise from Monte Carlo weights used by MC@NLO of -1 and 1.

truth values are highly correlated with almost all entries surrounding the identity line. Single events are visible in these histograms, where the reconstructed values show large deviations from the truth p_T or $|\eta|$. In around 0.2% of all selected events, the WHIZARD photon does not pass the object selection, but a second high-energetic photon is emitted within the hard scattering process and fulfills the selection requirements. These photons are simulated during the parton showering step by either HERWIG or PHOTOS and therefore do not match the truth values of the WHIZARD photons. Nevertheless, these are true $t\bar{t}\gamma$ events, which have to be included in the estimation. The final yields are listed in Table 10.9 and include the 20% uncertainty from the $t\bar{t}\gamma$ k-factor.

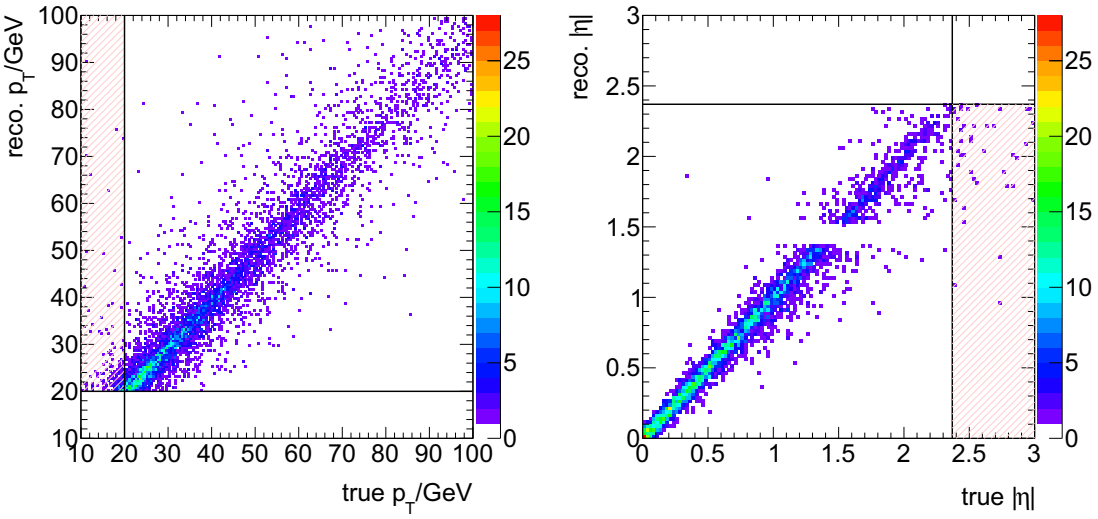

Figure 10.5: Reconstructed photon p_T (left) and $|\eta|$ (right) versus corresponding truth values, which include only events passing the $t\bar{t}\gamma$ signal selection. The black vertical and horizontal lines indicate the thresholds of the fiducial region. The hatched red areas illustrate the regions, where photons outside of the fiducial definition pass the object selection and have to be considered as a background source. As expected, the reconstructed and truth values are highly correlated with almost all entries surrounding the identity line.

Electron channel			Muon channel		
unconverted	converted	all	unconverted	converted	all
1.6±0.4	0.6±0.2	2.3±0.5	2.3±0.5	1.4±0.3	3.8±0.8

Table 10.9: Estimated number of $t\bar{t}\gamma$ events, which are included in the WHIZARD $t\bar{t}\gamma$ sample, but not in the defined fiducial region of the photon. All yields are listed separately for unconverted and converted photons in the electron and muon channel, including combined statistical and systematic uncertainties.

10.4 Other contributions

The remaining background contributions from Z+jets, single top and diboson processes with a prompt photon in the final state are estimated using Monte Carlo simulation. Events are selected, which pass the $t\bar{t}\gamma$ selection with a photon matched to a true prompt photon or a true electron. As described in Section 10.2, uncertainties on each expected cross section are taken into account, which are $^{+4\%}_{-3\%}$, ±4% and ±7% for the s-, t- and Wt-channel of the single top quark samples, and ±5% for the diboson sample. According to the Berends-Giele scaling, an uncertainty of 48% is considered for the Z+jets Monte Carlo sample, since at least 4 jets are required in the final state. Further, an uncertainty

of 23.8% is applied for all samples, as none of the processes include a prompt photon on matrix event level. The $e \to \gamma$ misidentification scale factors, which have been derived in Chapter 9 including systematic uncertainties, are applied to events with a misidentified electron. The results are listed in Table 10.10.

Electron channel			
	unconverted	converted	all
Z+jets+γ	1.9 ± 1.6	1.2 ± 1.0	3.0 ± 2.3
Z+jets (misid. $e^{\pm}$)	1.0 ± 0.8	3.1 ± 1.4	4.0 ± 2.5
single top+γ	1.4 ± 0.5	1.0 ± 0.4	2.4 ± 0.9
single top (misid. $e^{\pm}$)	0.1 ± 0.1	0.5 ± 0.2	0.6 ± 0.2
dibosons+γ	<0.1	<0.1	<0.1
dibosons (misid. $e^{\pm}$)	<0.1	0.1 ± 0.1	0.1 ± 0.1
Muon channel			
	unconverted	converted	all
Z+jets+γ	2.9 ± 2.1	1.8 ± 1.5	4.7 ± 3.2
Z+jets (misid. $e^{\pm}$)	<0.1	0.1 ± 0.1	0.1 ± 0.1
single top+γ	2.6 ± 0.9	1.1 ± 0.6	3.7 ± 1.2
single top (misid. $e^{\pm}$)	0.4 ± 0.2	0.8 ± 0.3	1.1 ± 0.4
dibosons+γ	0.3 ± 0.2	0.1 ± 0.1	0.3 ± 0.2
dibosons (misid. $e^{\pm}$)	<0.1	<0.1	<0.1

Table 10.10: Estimates for the background contributions from Z+jets+γ, single top+γ and dibosons+γ, separately for unconverted and converted photons in the electron and muon channel, including statistical and systematic uncertainties. Furthermore, the contributions are separated prompt photon events and events with electrons misidentified as photons.

Chapter 11

Measurement of the $t\bar{t}\gamma$ cross section

The $t\bar{t}\gamma$ cross section is obtained by a combined template fit to the p_T^{cone20} data distributions in the single electron and single muon channel, as described in Section 7.2. The signal and background templates for this final fit have been derived in Chapter 8. No differentiation between unconverted and converted photons is made at this point, but will be included as systematic uncertainties discussed in Sections 12.1.1 and 12.1.2. Table 11.1 lists the different yields used as input to the template fit. Gaussian prior probabilities are assigned to the prompt photon background contributions according to their expectation values, which have been estimated in Chapter 10, with the Gaussian width defined by the respective statistical uncertainty. These background sources are grouped into five categories. The highest yields emerge from top quark pair events with an electron misidentified as a photon, while true $t\bar{t}\gamma$ events are defined as a background source, when the generated event is not included in the defined signal phase space or fiducial region. Furthermore, the two data-driven estimations for QCD multijet+γ and W+jets+γ production are included separately. All remaining contributions from di-boson, single top and Z+jets events are combined to one yield. The $t\bar{t}\gamma$ signal yield as well as the number of background events with a hadron misidentified as a photon are free parameters, which are solely estimated by the final yields of the signal and background template, respectively.
The number of signal events has to be estimated before any selection cuts, in order to calculate the $t\bar{t}\gamma$ cross section. This involves an extrapolation from the detector phase space, defined by the geometrical acceptance of the detector and the kinematic cuts applied in the event selection, to the total phase space of the WHIZARD $t\bar{t}\gamma$ sample. Since this can lead to large theoretical uncertainties, a fiducial region is defined on generator level, taking into account only final state photons which have been generated by WHIZARD with a $p_T > 20\,\text{GeV}$ and $|\eta| < 2.37$. The kinematic cut matches the thresholds of the reconstructed photon, with the exception of the calorimeter crack-region $1.37 < |\eta| < 1.52$, restricting the fiducial phase space to a region that can be well measured. Overall, the extrapolation can be largely reduced, especially due to the minimum transverse momentum raised from 8 GeV to 20 GeV, resulting in 45% of the simulated $t\bar{t}\gamma$ events passing the new photon criteria. Consequently, the WHIZARD cross section in this phase space is $0.45 \cdot 0.84\,\text{pb} = 0.38\,\text{pb}$. The $t\bar{t}\gamma$ selection efficiencies are recalculated in both channels, considering only generated events inside the new fiducial phase space. These efficiencies, which read 1.2% in the single electron channel and 1.8% in the single muon channel, are included as the final input parameters in the template fit to estimate the total number of $t\bar{t}\gamma$ events before any selection cuts.
Figure 11.1 shows the result for the single electron channel and single muon channel after the final combined template fit. The distribution of expected events is shown without

the application of the $t\bar{t}\gamma$ event selection efficiencies. After performing the template fit to the p_T^{cone20} distribution of 414 data events, 155.8 ± 21.3 $t\bar{t}\gamma$ signal events and a combined background yield of 256.9 ± 41.5 are estimated. The background is comprised of 107.7 ± 4.0 events with a prompt photon or a misidentified electron in the final state and 149.1 ± 17.2 events with a hadron misidentified as a photon. After marginalization and the application of the event selection efficiencies, the expectation value of signal events $N_{\text{exp}}(t\bar{t}\gamma)$ is

$$N_{\text{exp}}(t\bar{t}\gamma) = 5161 \pm 709\,.$$

	processes	Electron channel	Muon channel
$t\bar{t}\gamma$ signal		free parameter	free parameter
$t\bar{t}\gamma$ background	outside signal phase space	1.5±0.3	3.3±0.4
	outside fiducial region	2.3±0.2	3.8±0.3
	total	3.8±0.4	7.2±0.5
$t\bar{t}$ (misid. $e^{\pm}$)	no final state photon	18.9±1.0	26.3±1.2
	collinear final state photon	1.1±0.2	1.6±0.3
	total	20.0±1.0	27.9±1.2
W+jets+γ		6.5±0.5	18.2±0.9
QCD+γ		1.8±1.4	2.2±1.2
other background	Z+jets+γ	3.0±1.6	4.7±1.9
	Z+jets (misid. $e^{\pm}$)	4.0±1.5	0.1±0.1
	single top+γ	2.4±0.6	3.7±0.8
	single top (misid. $e^{\pm}$)	0.6±0.2	1.1±0.3
	diboson+γ	<0.1	0.3±0.2
	diboson (misid. $e^{\pm}$)	0.1±0.1	<0.1
	total	10.2±2.3	10.0±2.1
misid. hadrons		free parameter	free parameter

Table 11.1: Estimated process yields included in the template fit. The $t\bar{t}\gamma$ signal expectation and the number of background events with a misidentified hadron are free parameters, while Gaussian prior probabilities are assigned to the prompt photon background contributions according to their estimated contributions. The Gaussian width is defined by the respective statistical uncertainty, which is also stated in the table.

The cross section is then defined by $N_{\text{exp}}(t\bar{t}\gamma)$ divided by the integrated luminosity of $\mathcal{L} = 4.7\,\text{fb}^{-1}$, as described in Section 7.3. The $t\bar{t}\gamma$ cross section times the branching ratio into the semileptonic and dileptonic decay channels, determined in a fiducial region with a photon-p_T above 20 GeV and a pseudorapidity $|\eta| < 2.37$ as well as the cuts used in the signal generation (see Section 5.4), is measured to be

$$\sigma_{t\bar{t}\gamma} \times \text{BR} = [1.11 \pm 0.15(\text{stat.})]\ \text{pb}\,.$$

The theoretical prediction is defined by the leading order cross section of the WHIZARD sample multiplied by the k-factor of the $t\bar{t}\gamma$ process. The k-factor corrects the cross section of the Monte Carlo sample to next-to-leading order precision and is given as $k = 2.55 \pm 0.50$, while the WHIZARD cross section in the defined fiducial phase space is 0.38 pb. The theoretical expectation is therefore

$$\left(\sigma_{t\bar{t}\gamma} \times \text{BR}\right)_{\text{theo.}} = [1.0 \pm 0.2(\text{syst.})]\ \text{pb}\,,$$

which is in very good agreement with the experimental result.

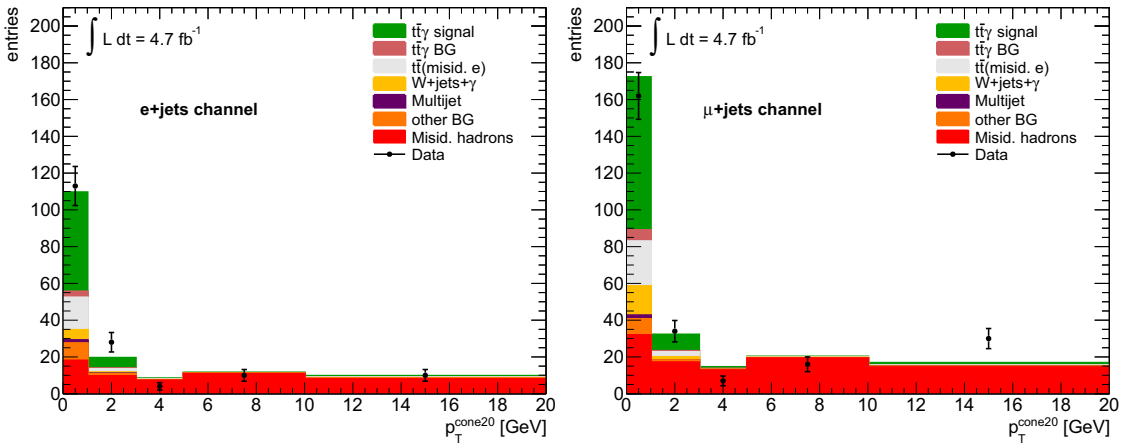

Figure 11.1: Result of the final template fit for the single electron (left) and the single muon channel (right), which is performed simultaneously in both channels. Both histograms show the total p_T^{cone20} isolation distributions from 0 to 20 GeV, with the last bin including the overflow bin. The data distributions are displayed as black points, including statistical uncertainties. The stacked histograms show the results of the templates, including the the background template in red, measuring events with a misidentified hadron in the final state. The signal template includes the final number of $t\bar{t}\gamma$ signal events after applying the $t\bar{t}\gamma$ event selection (green) and the prompt photon background expectations (various colors).

Chapter 12

Systematic uncertainties

Various systematic uncertainties can effect the measurement of the $t\bar{t}\gamma$ cross section:

- Systematic biases can influence the shapes of the signal and background template.
- Contributions from prompt photon background, which have been estimated in Chapter 10, also include systematic uncertainties.
- Uncertainties can arise due to the usage of certain Monte Carlo generators and settings used for the generation of the $t\bar{t}\gamma$ signal sample.
- The detector modeling can affect the kinematic properties of the measured physics objects, which may change the selection efficiency of the $t\bar{t}\gamma$ sample.
- The measurement of the integrated luminosity introduces a systematic uncertainty.

The impact of each systematic uncertainty on the $t\bar{t}\gamma$ cross section is estimated separately. The systematics influence is then determined by shifting the corresponding variables or smearing factors in positive and negative direction, while the size of the shift is determined by the corresponding systematic error. Uncertainties on the template shapes are estimated from fit results using templates derived from different compositions than the nominal ones, e.g. using only unconverted or converted photons. This results in a modified event selection efficiency, background estimation or template shape and consequently in a $t\bar{t}\gamma$ cross section deviating from the nominal result presented in Chapter 11. The evaluation of the systematic uncertainty can be strongly biased by statistical fluctuations, due to the statistical limitation of the 414 measured $t\bar{t}\gamma$ event candidates. Therefore, 5000 ensembles of pseudo data are created by fluctuating each bin of the measured p_T^{cone20} distribution according to the Poissonian uncertainty around the expectation. A new template fit is performed for each ensemble yielding a distribution of expected number of signal events $\bar{N}_{\text{exp}}$ with its mean being the most likely result of the considered systematic effect. The difference of mean values with respect to the nominal result $\bar{N}_0$ is considered as the systematic uncertainty:

$$\sigma_{\text{syst.}} = \frac{\bar{N}_{\text{exp}} - \bar{N}_0}{\bar{N}_0} \,.$$

The statistical uncertainty of the mean value for a distribution of 5000 ensembles is estimated to be less than 0.2%, and therefore negligible. Figure 12.1 shows examplarily the resulting distributions for the largest systematic uncertainty, originating from the jet energy scale. All other plots of the considered systematic uncertainties can be found in Appendix B.5. The result for each systematic uncertainty is given in Table 12.2.

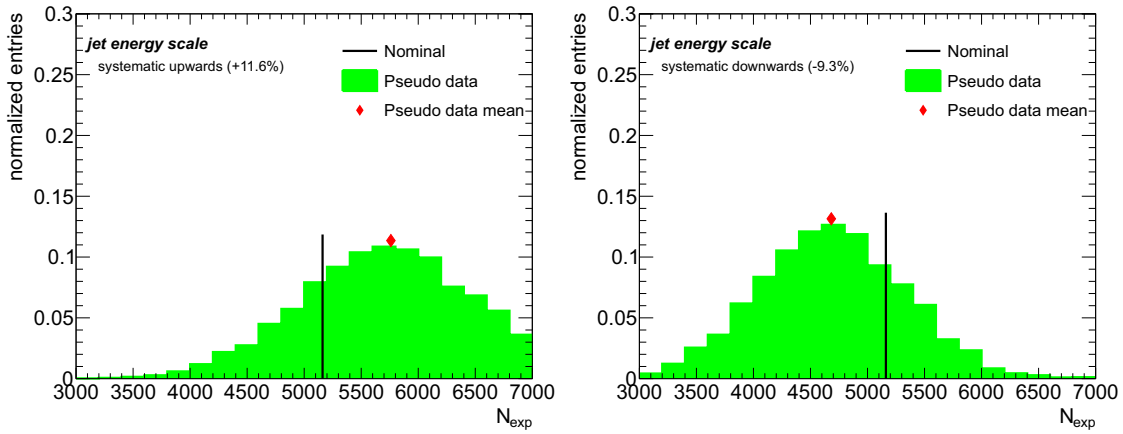

Figure 12.1: Distribution of the expected number of signal events N_{exp} for 5000 pseudo experiments, shown for the largest systematic uncertainty originating from the jet energy scale. The mean of the distribution is marked in red, while the vertical black line shows the nominal result. The difference between the two markers is considered as systematic uncertainty.

12.1 Template Modeling

12.1.1 Signal template

The shapes of the signal templates separately for unconverted and converted photons have been derived in Section 8.1. Since only the template of all photons has been used for the cross section measurement, the nominal fit result is compared to the template fits using the signal templates of the different photon types. While unconverted photons tend to be more isolated then converted photons, the template fit using the unconverted photons only template yields a higher cross section than the nominal result and is therefore assigned as the upwards systematic uncertainty. The opposite is the case for the fit result using the converted photons only template and is therefore assigned as the downwards systematic uncertainty.

As explained in Section 8.1, the signal template is derived from data using the electron isolation distribution of $Z \to ee$ decay particles. A Monte Carlo correction is then introduced for the electron-to-photon extrapolation. The differences between the electron and the photon distributions, which are shown in Appendix B.2, can be mostly explained by the different event topologies. While electrons from Z boson decay are mostly surrounded by no additional jets, the environment of the photon in $t\bar{t}\gamma$ events is crowded by one lepton and at least four jets from the top quark pair decay. Figure 8.4 shows that electrons in $Z \to ee$ become less isolated, if additional jets are present, and hence show a distribution shape more similar to the final signal template. In order to match the more crowded surrounding of the photon from $t\bar{t}\gamma$ events, electrons are selected in data from $Z \to ee$ events with four jets passing the object definition and their p_T^{cone20} isolation distribution is used as the signal template. A template fit is then performed with the difference to the

nominal cross section result defined as a symmetric systematic uncertainty.

12.1.2 Background template

Similar to the signal template, a systematic uncertainty is assigned to the different isolation distribution shapes of unconverted and converted photons. The background templates of the two different photon types, which have been derived in Section 8.2, are used for template fits to estimate new $t\bar{t}\gamma$ cross sections. The difference to the nominal result is defined as a systematic uncertainty.

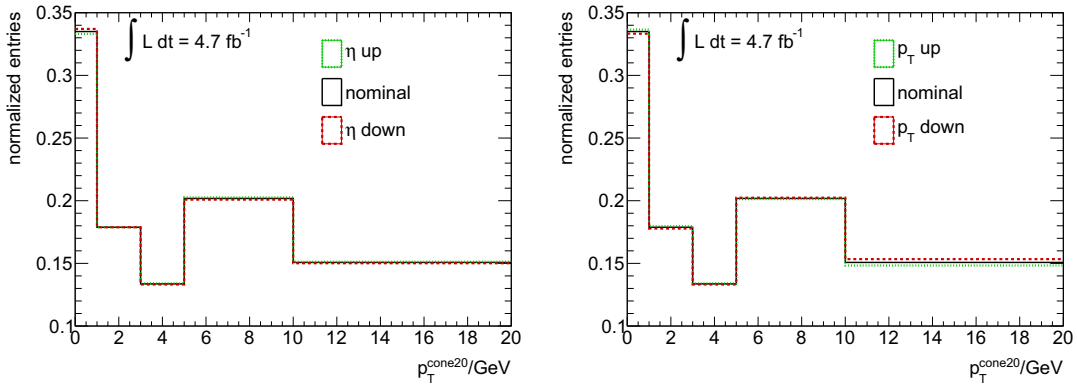

Figure 12.2: Systematic background templates considering uncertainties due to p_T and $|\eta|$ reweighting, normalized to 1. The total p_T^{cone20} isolation distributions is shown from 0 to 20 GeV, with the last bin including overflow events. The reweighting factors are shifted up and down according to their uncertainties with the results shown on the left for the $|\eta|$ variations and on the right for the p_T variations. As a comparison, the final background template is also displayed in both histograms.

For the derivation of the final background template, the p_T^{cone20} distribution of background photon candidates are reweighted according to the p_T and $|\eta|$ spectra of the $t\bar{t}\gamma$ photons passing the background photon definition. An exponential fit has been performed to the p_T spectrum, which has two free fit parameters, one for the normalization and one for the slope of the exponential function. In order to consider the fit uncertainties, both parameters are shifted simultaneously upwards and downwards by their uncertainties for the estimation of new p_T reweighting factors. The resulting background templates, which are shown in figure 12.2, are used to perform template fits and the difference to the nominal cross section value is defined as a systematic uncertainty. Similarly, each of the three bins of the $|\eta|$ distribution is varied within its statistical uncertainty. The background templates, which result in the highest upwards and downwards deviation from the nominal cross section result, is taken as a systematic uncertainty.
Even though the background photon definition selects hadrons misidentified as photons with high purity, a contamination of real prompt photons has to be taken into account. This is investigated in Monte Carlo simulated dijet samples generated with PYTHIA, which include jet-jet and also γ-jet processes. Events are selected according to the preselection of the jet data stream, described in Section 5.2. In addition, at least one object has

to pass the background photon definition. A subset of these events is created by selecting only events, where no selected photon is matched to a true photon on generator level within a cone size of $\Delta\eta \times \Delta\phi = 0.025 \times 0.050$. Further, this true photon must not be originated from bremsstrahlung or from the hard scattering processes. Two background templates are derived from the two sets, one including real prompt photons and hence resembling the composition of the nominal background template, and one which only includes misidentified hadrons. The two distributions are shown in Figure 12.3. As expected, prompt photons cause more entries in the first two bins, since they tend to be much more isolated than misidentified hadrons. Both templates are used to perform template fits and the difference between the fit results is assigned as a systematic uncertainty. It is introduced as a positively contributing uncertainty, since the subtraction of the prompt photon contamination in the background template yields a higher cross section result.

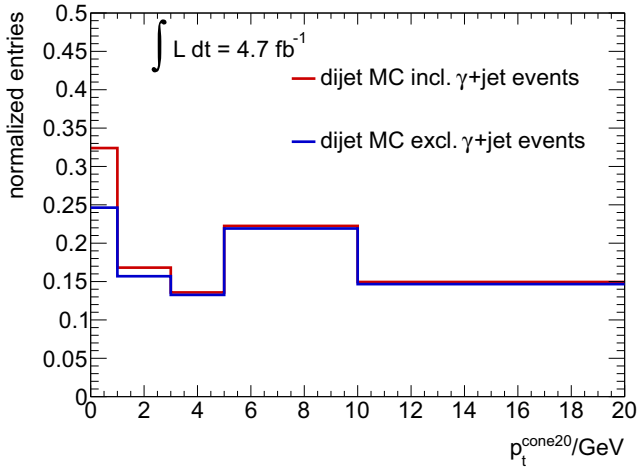

Figure 12.3: Systematic background templates to evaluate prompt photon contamination, derived from dijet Monte Carlo simulation. The total p_T^{cone20} isolation distributions is shown from 0 to 20 GeV, with the last bin including overflow events. One distribution includes all photons, while prompt photons are neglected for the other distribution using truth information. Both distributions are scaled by the inverse of the number of photons in the background photon only template in order to highlight the size ot the prompt photon fraction.

12.2 Prompt photon background

The systematic uncertainties of the prompt photon background contributions have been estimated separately in Chapter 10. The QCD multijet+γ and W+jets+γ background has been estimated using data-driven methods. The QCD multijet+γ uncertainty is dominated by fake lepton estimation, while the main uncertainties of the W+jets+γ yield originates from the extrapolation to the signal region. The extrapolation factors have been derived from Monte Carlo simulation, which include corrections to the yield normalization and the heavy flavor fractions. All other background contributions have been

derived from Monte Carlo simulation only. These estimations include uncertainties on the expected cross sections, $e \to \gamma$ misidentification scale factors and uncertainties for Monte Carlo samples, which have not included prompt photons in the matrix calculation.

12.3 Monte Carlo modeling

The choice of the Monte Carlo generator, the parton showering program and the generation settings are evaluated as sources of systematic uncertainties for the modelling of the $t\bar{t}\gamma$ signal sample. The uncertainties are obtained by the relative differences between the event selection efficiencies of two different $t\bar{t}$ Monte Carlo samples as $t\bar{t}\gamma$ Monte Carlo samples with different settings are not available. In order to have the same topology as in $t\bar{t}\gamma$ events, only those events in the $t\bar{t}$ sample are used that have a true prompt photon. When applying the full $t\bar{t}\gamma$ event selection on those samples, the statistical uncertainties become much larger than the systematic ones. Hence, statistics are increased by applying a simplified selection for all samples:

1. At least five tracks are associated to the primary vertex.

2. At least one selected photon is required. In addition, the selected reconstructed photon has to be matched to a true photon on generator level within a cone size of $\Delta\eta \times \Delta\phi = 0.025 \times 0.050$. The true photon has to be emitted during the hard scattering process to select only true $t\bar{t}\gamma$ events.

All samples used for the estimation of the Monte Carlo modeling uncertainties are listed in Appendix A. Following Monte Carlo modeling effects have been estimated, with the calculated systematic uncertainties listed in Table 12.1:

- **Next-to-leading order Monte Carlo generator**: Event selection efficiencies have been compared for samples generated with the two next-to-leading order generators MC@NLO and POWHEG. Both generators are interfaced to HERWIG for parton showering. This uncertainty estimates the dependency on the choice of one Monte Carlo generator.

- **Leading order vs. next-to-leading order calculation**: The difference between a fixed order calculation at the leading order and the next-to-leading order level is estimated using the MC@NLO sample and a leading order sample generated with ACERMC, both showered with HERWIG. This uncertainty addresses the difference in generation between leading and next-to-leading order, since the signal sample is produced with a leading order generator.

- **Parton showering**: The impact of different parton showering programs is obtained by comparing two POWHEG samples. For one sample, POWHEG is interfaced to HERWIG, while PYTHIA is used for the other one.

- **Inital/final state radiation**: The amount of additional gluons radiated within the top quark pair event can influence the event selection efficiency. This can lead

to additional jets passing the jet object definition, but also alters the production energy of the top quark pair and the reconstructed energy of the final state jets. The strength of radiation can be modified in Monte Carlo simulation, resulting in more or less soft jets. Two $t\bar{t}$ samples have been produced with ACERMC and PYTHIA with modified parameters to generate events with simultaneously enhanced or reduced initial or final state radiation. The difference between the enhanced and reduced radiation sample is defined as a systematic uncertainty.

- **Underlying event**: Uncertainties due to non pertubative modeling include the simulation of underlying events. Two POWHEG samples are compared, both interfaced to PYTHIA, but with different underlying event tunes [174].

- **Color reconnection**: Another uncertainty of non pertubative modeling arises from color reconnection. Two Monte Carlo samples have been generated with POWHEG and PYTHIA using different PYTHIA settings [174]. Since the result is much smaller than the uncertainty of the next-to-leading order generator, the color reconnection has not been included in the final systematic uncertainty combination.

- **Renormalization/factorization scale**: The effect of the renormalization and factorization scale used for the event generation is estimated with MC@NLO samples interfaced to HERWIG. Events have been simulated with different settings by simultaneously varying both scales by a factor of 2 and 0.5 with respect to the default setup.

- **Parton distribution function**: As described in Section 2.1, the momenta of the incoming partons are given by the center-of-mass energies of the protons and the parton distribution functions (PDF). Hence, the choice of the PDF as well as the uncertainties of a specific one have an effect on the event selection efficiency [194, 195]. The PDF uncertainty is determined using the nominal $t\bar{t}$ Monte Carlo sample, generated with MC@NLO and interfaced to HERWIG. The impact of three different PDF sets are estimated: CT10 [169], MSTW2008nlo68cl [196] and NNPDF20_100 [197], which are provided by three PDF research groups. For each event from the MC@NLO sample passing the event selection, a new event weight w_{PDF} is calculated from the original momentum fractions of the incoming partons $f_0(x_1, Q^2)$ and $f_0(x_2, Q^2)$ and the according fractions calculated from the new PDF set $f_1(x_1, Q^2)$ and $f_1(x_2, Q^2)$:
$$w_{\mathrm{PDF}} = \frac{f_1(x_1, Q^2) \cdot f_1(x_2, Q^2)}{f_0(x_1, Q^2) \cdot f_0(x_2, Q^2)},$$
yielding a new event selection efficiency. Each of the three PDFs includes a set of error PDFs to estimate the intra-PDF uncertainties, which are calculated according to the the PDF4LHC recommendations [194, 195]. The inter-PDF uncertainty is estimated by combining all uncertainties in a linear way. The minimum and maximum of all variations are taken, called the envelope, and the half of the envelope is defined as the overall uncertainty.

source	systematic uncertainty [%]
next-to-leading order generator	7.2±0.6
leading order vs. next-to-leading order	6.3±0.3
parton showering	5.0±0.6
initial/final state radiation	0.3±0.3
underlying event scale	0.2±0.6
color reconnection	0.6±0.6
renormalization/factorization scale	0.3±0.8
parton distribution function	3.9

Table 12.1: Overview of all uncertainties related to Monte Carlo modeling. All values are listed with statistical uncertainties, except for the parton distribution function due to its specific estimation method.

12.4 Detector Modeling

Since the ATLAS detector is not described perfectly in Monte Carlo simulated events, various corrections are applied to the reconstructed physics objects (see Section 4). These corrections are subject to systematic uncertainties which affect the description of jets, electrons, muons, photons and the missing transverse energy. Uncertainties on the detector modeling do not influence the shape of the photon isolation templates, but the event selection efficiency of the $t\bar{t}\gamma$ signal sample.

12.4.1 Jet

Detector modeling uncertainties affecting jets can be categorized in influences on the jet energy scale and effects on the jet energy resolution. Furthermore, uncertainties are included for the jet reconstruction and the b-jet identification efficiencies.
Multiple sources of systematic uncertainties affect the jet energy scale [198, 123]:

- Deviations of the reconstructed and calibrated jet energy and p_T from the true values on generator level have been studied using simulated dijet samples. Slight discrepancies have been found and taken into account.
- The response and corresponding uncertainties of single particles interacting in the ATLAS calorimeters can be used to derive the jet energy scale uncertainty in the central calorimeter [199]. This has been studied in data and Monte Carlo simulation, measuring the single hadron energy in a cone around an isolated track in the momentum range from $0.5\,\text{GeV} < p < 20\,\text{GeV}$. Further, the initial pion response measurements performed in the 2004 combined ATLAS test-beam are considered,

where a full slice of the ATLAS detector has been exposed to pion beams with momenta between 20 and 350 GeV. The dominating uncertainty to the calorimeter response is related to particles with $p > 400\,\text{GeV}$, which are estimated conservatively to be 10% to take into account calorimeter non linearities and longitudinal leakage.

- Two types of uncertainties are considered due to mismodeling of the detector simulation. Topoclusters are constructed based on the signal-to-noise ratio of calorimeter cells. Discrepancies can occur, because the noise can change over time in data, while it is fixed at the time of the production of the simulated data. Therefore, differences in the cluster shapes and the presence of fake clusters can affect the jet reconstruction. Further, the jet energy scale is affected by possible deviations in the material description. This uncertainty has been estimated using specific Monte Carlo samples with distorted geometries.

- Uncertainties due to generator modeling of the parton fragmentation and underlying events and other parameters of the Monte Carlo event generator are taken into account. They are obtained using Monte Carlo samples with different generator tunes and showering programs.

- The jet energy scale uncertainties determined in the central detector are extrapolated to the forward regions by exploiting the transverse momentum balance of a central and a forward jet in events with dijet topologies. In such events, the responses of the forward jets are measured relatively to those of the central jets [200].

- For the jet energy scale calibration, an average offset correction is applied to account for the average increase of the jet energy due to pileup. This correction is parameterized as a function of the primary vertices [201]. Uncertainties of this correction are considered, like the effect of variations of the trigger selection on the measured tower energy distribution that is input to the offset correction.

- The calibration constants have been obtained from isolated jets using simulated dijet events. A jet is defined as isolated, if the distance to the closest jet with $p_T > 7\,\text{GeV}$ at the electromagnetic energy scale is $R_{\text{min}} > 1.0$ in $\eta - \phi$ space. Since the calibration is also applied to non-isolated jets, the impact of close-by jets has been evaluated [202]. The transverse momenta of isolated and non-isolated jets have been compared in data and Monte Carlo simulation, resulting in systematic uncertainties of up to 2.8%.

- The fragmentation differences between jets initiated by a quark and jets initiated by a gluon lead to a flavor dependence in the jet energy scale [203]. Light-quark-jets have a significantly different response from those identified as gluon-jets, with the response defined as the p_T-ratio of the reconstructed jet and the true jet on generator level. The gluon-jets tend to induce more particles, which also tend to be softer. Additionally, the gluon-jets tend to be wider and have hence a lower energy density in the core before interacting with the detector. The response difference is up to 6% at low-p_T and decreases to several percent for higher transverse momenta.

The gluon-jet and light-quark-jet fractions of multijet events have been extracted in simulation and data, resulting in a jet energy scale systematic uncertainty of below 1%.

- An additional uncertainty is applied to b-jets in simulated events. If a jet is identified to be originating from a bottom quark using truth information, the flavor composition uncertainty is neglected and the b-jet uncertainty is included, which has been derived from various Monte Carlo samples and validated with the comparison of track jets and calorimeter b-jets in data. The b-jet uncertainty is displayed as a function of the jet-p_T in the right plot of Figure 12.4.

The left plot of Figure 12.4 shows the total jet energy scale uncertainty as a function of the jet transverse momentum.
The jet energy resolution is measured with two different methods, the dijet balance and the bisector technique [204, 205]. The resolution agrees in data and Monte Carlo within statistical uncertainties, and therefore, no smearing is applied to the central values of jets in Monte Carlo simulation. The uncertainty on the jet energy resolution is considered by smearing jets according to the systematic uncertainties of the resolution measurements, which vary depending on the in-situ technique from about 8% at a p_T of 30 GeV down to 4% at a p_T of 500 GeV.
Besides the standard jet reconstruction method using calorimeter topological clusters as inputs for the anti-k_T algorithm (calorimeter jet), jets can also be built using tracks reconstructed in the inner detector as inputs to the jet finding algorithm (track jet). The calorimeter jet reconstruction efficiency is measured relatively to track jets, using a tag and probe technique in dijet events [206]. The reconstruction efficiency, which is defined as the fraction of track jets matched to a calorimeter jet, is evaluated in data and Monte Carlo simulation. The observed difference is applied to simulated events by discarding a fraction of jets taken at random within the inefficiency range [123].
As described in Section 4.1.5, scale factors are applied to events with jets identified as b-quarks in simulated events, in order to match the b-jet identification and misidentification rate measured in data. These scale factors are also affected by systematic uncertainties, which have been estimated following closely the $t\bar{t}$ cross section analyses [131, 207].

12.4.2 Leptons & photon

The reconstruction, trigger, identification and isolation efficiencies of selected muons and electrons are corrected in simulated events to the data expectation. This is achieved with scale factors, which have been obtained from $Z \to l^+l^-$ events using the tag&probe method (see Sections 4.2.6 and 4.3.4). Systematic uncertainties of these scale factors have to be taken into account. Various sources of uncertainties have been considered like the background subtraction in data and simulation, the considered invariant mass range of the two leptons around the Z boson mass, possible pileup dependencies and the lepton energy scales.
The photon identification efficiency is corrected in Monte Carlo simulation by shifting the means of the discriminating variable distributions to match the mean values in data.

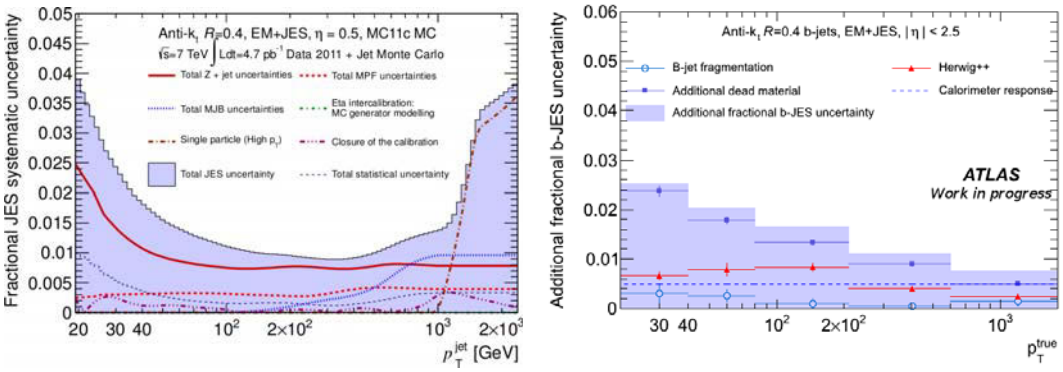

Figure 12.4: Summary plots of the jet energy scale (left) and b-jet energy scale uncertainty (right) as a function of the jet transverse momentum [123]. The total uncertainties are shown as blue histograms, and additionally, various individual uncertainty components are included in the figures.

Comparisons of the efficiency in simulation after applying the corrections with data-driven measurements still have found discrepancies, which are taken into account by a systematic uncertainty. This considered uncertainty is 5%, except for all photons with a transverse energy below 30 GeV and unconverted photons at a high pseudorapidity of $1.81 < |\eta| < 2.37$ over the whole E_T range, for which a 10% uncertainty is applied [208].
The energy scale and resolution of electrons and photons are corrected in data and Monte Carlo samples, respectively, in order to match the object descriptions in simulation and data. Systematic uncertainties on the energy scale include the imperfect knowledge of the material in front of the calorimeter system, pileup effects and background contamination in the selected electron sample [132]. Furthermore, the in-situ calibration only fixes one overall scale and therefore cannot correct for possible differences within the electromagnetic calorimeter. Possible differences are considered for the presampler, which is used to correct for energy lost upstream of the active electromagnetic calorimeter, and cells belonging to different sampling layers in calorimeter, which may have different energy scales due to cross-talk and uncertainties arising from an imperfect electronic calibration. The energy resolution is described by the parameterized Equation 4.3. The uncertainties are dominated by the uncertainties of the parameters, especially the sampling term, but also consider deviations due to the fit procedure.
The muon momentum resolution is adjusted in simulated events to fit data measurements. Similar to electrons and photons, the momentum resolution of muons is parameterized as a function of p_T (see Equation 4.5) with the parameters affected by systematic uncertainties [138]. The combined muon resolution is determined by individual measurements in the inner detector and the muon spectrometer. For the systematic uncertainty, the muon spectrometer and inner detector components are varied with positive and negative contributions separately, resulting in four different event selection efficiencies. Template fits are performed with these efficiencies and the final uncertainty is defined as half the difference between the maximum and minimum cross section value. The systematic uncertainty of the muon momentum scale is determined by the difference of the $t\bar{t}\gamma$ selection efficiencies

with and without the scale correction applied.

12.4.3 Missing transverse energy

The $\not{E}_T$ is calculated from all selected objects as well as any additional energy deposits in the calorimeter which are not associated to any object. This implies that any systematic variations of the jet, lepton and photon energy scales and resolutions are propagated into the calculation of the missing transverse energy.
Additional uncertainties are introduced for the cell out and soft jet terms [123] (see Section 4.4). The cell out term uncertainty is estimated from simulated multijet samples with varied amount of dead material used in detector simulation, alternative shower models and different minimum bias tunes to simulate the underlying soft interactions. The uncertainty on this term is approximately 13%, decreasing slightly as a function of E_T [143]. The systematic uncertainty of soft jets is approximately 10%, evaluated with the same approach as the cell out term. The overall uncertainties on cell out and soft jet terms are fully correlated.
The uncertainty of extra energy deposited due to pile up interactions is treated as a separate scale uncertainty, affecting the jet, soft jet, and cell out components. The value of these components is varied by 6.6%, which has been estimated by the dependence of the $\not{E}_T$ on the number of pile-up interactions.

12.5 Pileup dependence

The $t\bar{t}\gamma$ Monte Carlo sample is investigated for possible effects of in-time and out-of-time pileup on the signal selection efficiency. For this, the $t\bar{t}\gamma$ selection efficiency with respect to the $t\bar{t}$ preselection (cut 1-10, see Chapter 6) is studied for a possible dependence on the number of vertices with at least five associated tracks (in-time) and the average number of interactions per bunch-crossing (out-of-time). The results are shown in Figure 12.5, separately for the electron and muon channel. No clear dependence is observed and hence no systematic uncertainties are assigned due to pileup.

12.6 Luminosity

The integrated luminosity of the LHC has been measured with van der Meer scans [209], with an uncertainty for the 2011 dataset of 1.8% [210, 211]. It is considered as a global systematic uncertainty to all signal and background processes, and is hence quoted separately in the final $t\bar{t}\gamma$ cross section result.

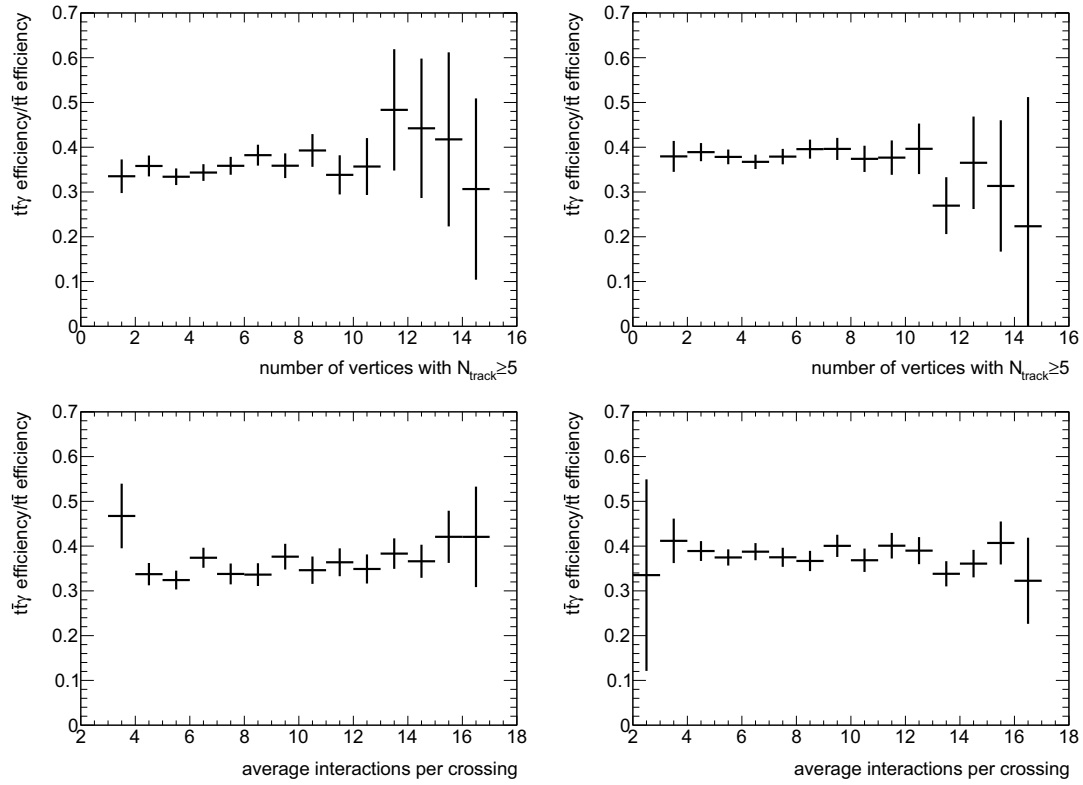

Figure 12.5: $t\bar{t}\gamma$ selection efficiency with respect to the $t\bar{t}$ preselection (cut 1-10), estimated as function of the number of vertices with at least five associated tracks (upper row) and the average number of interactions per bunch-crossing (lower row). The efficiencies are calculated separately for the electron (left column) and muon channel (right column), showing no dependence on the investigated variables.

12.7 Total systematic uncertainty

All systematic uncertainties, which have been discussed in this chapter are considered as uncorrelated and hence are summed up in quadrature. The final systematic uncertainty reads $^{+22.3}_{-18.6}\%$. The positive and negative values of each uncertainty are listed in Table 12.2, which are evaluated separately by performing 5000 pseudo experiments with modified $t\bar{t}\gamma$ selection efficiencies, background estimations or template shapes. As quoted before, the estimated systematic uncertainties have a statistical uncertainty below 0.2%, calculated by the ratio of the root-mean-square and the mean value for an ensemble distribution. Therefore, systematic uncertainties below that value are stated conservatively as 0.2%, since they cannot be resolved.
The largest uncertainty is due to the jet energy scale. Further sizable uncertainties yield from Monte Carlo modeling, explicitly the difference between leading order and next-to-leading order calculation as well as the choice of next-to-leading order generator and parton showering program, the photon identification efficiency and the uncertainties assigned to the template shapes.

systematic source	systematic downwards	systematic upwards
Signal template modeling		
(un)converted photons	−1.5%	+3.4%
$Z \to ee + 4\,\text{jets}$	−5.4%	+5.4%
Background template modeling		
(un)converted photons	−5.4%	+3.2%
p_T-reweighting	−0.3%	+0.5%
$\lvert\eta\rvert$-reweighting	−0.3%	+0.4%
prompt photons	-	+7.7%
Prompt photon background		
QCD multijet $+\gamma$	$< 0.2\%$	$< 0.2\%$
W+jets+γ	−3.9%	+4.1%
Monte Carlo bkg.	−3.3%	+3.5%
$t\bar{t}\gamma$ background	−0.8%	+1.0%
$t\bar{t}$ (misid. $e^{\pm}$)	−2.9%	+3.0%
Monte Carlo modeling		
NLO generators	−6.7%	+7.9%
LO vs. NLO	−5.9%	+6.8%
parton showering	−4.8%	+5.4%
initial/final state radiation	−0.3%	+0.5%
underlying event	−0.5%	+0.7%
ren./fac. scale	−0.8%	+1.0%
PDF	−3.7%	+4.1%
Jet modeling		
energy scale	−9.3%	+11.6%
energy resolution	−0.7%	+0.7%
reconstruction efficiency	$< 0.2\%$	$< 0.2\%$
b-tagging	−3.7%	+4.6%

systematic source	systematic downwards	systematic upwards
Electron modeling		
reconstruction/identification	-0.3%	$+0.4\%$
trigger	$< 0.2\%$	$+0.2\%$
momentum resolution	$< 0.2\%$	$< 0.2\%$
energy scale	$< 0.2\%$	$< 0.2\%$
Muon modeling		
reconstruction	$< 0.2\%$	$< 0.2\%$
isolation	-0.2%	$+0.4\%$
trigger	-0.7%	$+0.9\%$
momentum resolution	-1.1%	$+1.1\%$
momentum scale	-0.6%	$+0.6\%$
Photon modeling		
identification	-4.9%	$+5.6\%$
momentum resolution	$< 0.2\%$	$< 0.2\%$
energy scale	-2.2%	$+0.7\%$
$\not{E}_T$ modeling		
cellout/ soft jets	$< 0.2\%$	$< 0.2\%$
pileup	$< 0.2\%$	$+0.7\%$
total systematics	-18.6%	$+22.3\%$

Table 12.2: Overview of all systematic uncertainties considered for the $t\bar{t}\gamma$ cross section measurement.

Chapter 13

Signal significance

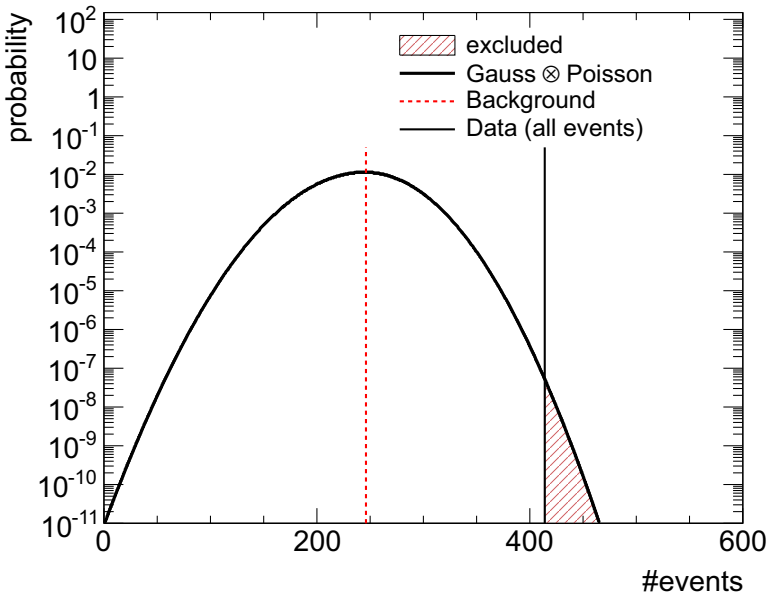

Figure 13.1: Probability distribution of the observed number of events for the background only hypothesis given the combined statistical and systematic uncertainties. The red vertical line marks the estimated number of background events and therefore the mean value of the distribution. The black vertical line shows the number of observed $t\bar{t}\gamma$ event candidates. Its intercept point with the distribution indicates the probability if the background only hypothesis of this measurement.

The significance of the $t\bar{t}\gamma$ signal is calculated using the assumption that the selected events contain no signal events, i.e. estimating the probability of measuring at least 414 background event candidates in data. The calculation is based on the search of any $t\bar{t}\gamma$ signal events and is not restricted by the signal definition of the cross section measurement. Therefore, $t\bar{t}\gamma$ events outside of the signal phase space or fiducial region, which have been determined separately in Sections 10.3.2 and 10.3.3, are not considered as background contributions. The total non-$t\bar{t}\gamma$ background yield has been estimated from the template fit to be $246.1 \pm 17.6(\text{stat.})^{+24.2}_{-30.0}(\text{syst.})$ events. Since the background contributions have been estimated separately (prompt photon, misidentified electrons) or solely from data using the template fit (misidentified hadrons), the total background yield includes systematic uncertainties due to template modeling and the prompt photon background.

The combined statistical and systematic uncertainty is modelled by a Gaussian probability distribution function, convoluted with a Poissonian distribution to account for statistical fluctuations. The distribution is shown in Figure 13.1, indicating a probability of the background only hypothesis for a measured number of 414 events of $p = 3.48483 \cdot 10^{-7}$, which corresponds to a significance of $4.96\,\sigma$ for the existence of a $t\bar{t}\gamma$ signal in data and hence an evidence of the $t\bar{t}\gamma$ process.

Chapter 14

Summary and Outlook

The cross section measurement of top quark pair production with an additional prompt photon in the final state ($t\bar{t}\gamma$) has been presented in this thesis. The total 2011 dataset of $4.7\,\mathrm{fb}^{-1}$ has been analyzed in this analysis, recorded by the ATLAS detector in proton-proton collisions at the LHC with a center-of-mass energy of $\sqrt{s} = 7\,\mathrm{TeV}$.
A event selection has been developed for the single electron and single muon channels, following closely the selection used in $t\bar{t}$ cross section measurements published by the ATLAS collaboration [185, 186], with the addition of photon selection cuts, identifying a total of 414 $t\bar{t}\gamma$ event candidates in the dataset. Various background contributions have been estimated, which can be categorized in three classes according to the true type of the selected photon. Besides true prompt photons, electrons and hadrons from jet fragmentation can be misidentified as photons. A significant difference has been found in the photon distribution shape of the track isolation variable p_T^{cone20} between misidentified hadrons and prompt photons. This has been exploited to distinguish these types of photons using a template fit to the p_T^{cone20} data distribution and consequently extract the final $t\bar{t}\gamma$ cross section. Background processes including a prompt photon or misidentified electron have been estimated separately, which include data-driven methods for contributions from W boson production with additional jets and QCD multijet events. The remaining background yields from Z boson production with additional jets as well as single top, diboson and top quark pair production have been determined from Monte Carlo simulation. These separate estimations have been then included in the template fit.
The final result of the $t\bar{t}\gamma$ cross section in the non full hadronic decay channels with a transverse mometum of the prompt photon above 20 GeV and a pseudorapidity of $|\eta| < 2.37$ and the cuts used in the signal generation (see Section 5.4) reads:

$$\sigma_{t\bar{t}\gamma} \times \mathrm{BR} = \left[1.11 \pm 0.15(\mathrm{stat.})^{+0.25}_{-0.21}(\mathrm{syst.}) \pm 0.02(\mathrm{lumi.})\right]\ \mathrm{pb}\,.$$

This results in an evidence of the $t\bar{t}\gamma$ process with a significance of $4.96\,\sigma$ with respect to the background only hypothesis. Further, this measurement is in very good agreement with the Standard Model expectation of $\left(\sigma_{t\bar{t}\gamma} \times \mathrm{BR}\right)_{\mathrm{theo.}} = [1.0 \pm 0.2(\mathrm{syst.})]$ pb.
The total systematic uncertainty has been determined to be $\sigma_{\mathrm{syst.}} = ^{+22.3\%}_{-18.6\%}$. The estimation includes uncertainties due to the template shapes, prompt photon background contributions, Monte Carlo modeling and detector modeling of the different physics objects. The largest contribution arises from uncertainties due to the jet energy scale.
Proton-proton collision data with an integrated luminosity of $21.7\,\mathrm{fb}^{-1}$ have been recorded by the ATLAS detector in 2012 at a center-of-mass energy of $\sqrt{s} = 8\,\mathrm{TeV}$. Since the $t\bar{t}$ cross section has increased more than 40% with increased energy [53, 212], it can be expected that the number of $t\bar{t}\gamma$ candidates is more than six times larger than in the dataset

collected in 2011. This will provide new opportunities for the analysis of this process. While a significance above $5\,\sigma$ and hence the discovery of the $t\bar{t}\gamma$ process will definitely be reached, enough statistics should be available to also select and analyze dileptonic $t\bar{t}\gamma$ events. Furthermore, a first differential cross section measurement can be performed, which will open up the possibility to extract the momentum spectrum of prompt photons from top quark pair events.

In the long term, $t\bar{t}\gamma$ events can be analyzed for the direct measurement of the electromagnetic coupling of the top quark. Since this process is directly sensitive to the structure and strength of this coupling, it will provide an important validity check of the Standard Model and possibilities for the search of new physics, in case of anomalous results of the $t\gamma$-vertex beyond the Standard Model.

Appendix A

Monte Carlo samples

A.1 $t\bar{t}$ Monte Carlo samples

Process	$\boldsymbol{pp \to b\bar{b}j_1j_2l_1\nu_1\gamma}$ **or** $\boldsymbol{b\bar{b}l_1\nu_1l_2\nu_2\gamma}$ **with** $\boldsymbol{l = e, \mu, \tau}$ **and** $\boldsymbol{j = u, d, c, s}$				
Generators	Whizard+HERWIG/JIMMY				
Information	DSID	# events	σ [pb]	k-factor	PDF
	117402	499796	0.84	2.55	CTEQ6L1

Table A.1: WHIZARD $t\bar{t}\gamma$ Monte Carlo sample

Process	$\boldsymbol{pp \to t\bar{t} \to b\bar{b}j_1j_2l_1\nu_1}$ **or** $\boldsymbol{b\bar{b}l_1\nu_1l_2\nu_2}$ **with** $\boldsymbol{l = e, \mu, \tau}$ **and** $\boldsymbol{j = u, d, c, s}$				
Generators	MC@NLO+HERWIG/JIMMY				
Information	DSID	# events	σ [pb]	k-factor	PDF
	105200	14995000	79.01	1.22	CT10
	110006	9989490	89.47	1.08	CT10
	110007	9982491	68.51	1.41	CT10
Comments	110006: ren./fac. scale variation up, 110007: ren./fac. scale variation down.				

Table A.2: MC@NLO $t\bar{t}$ Monte Carlo sample

Process	$pp \to t\bar{t} \to b\bar{b}j_1j_2l_1\nu_1$ **or** $b\bar{b}l_1\nu_1l_2\nu_2$ **with** $l = e, \mu, \tau$ **and** $j = u, d, c, s$				
Generators	POWHEG+HERWIG/JIMMY or PYTHIA				
Information	DSID	# events	σ [pb]	k-factor	PDF
	105860	499995	80.85	1.12	CT10
	117050	9992492	80.07	1.20	CT10
	117428	9994491	80.07	1.20	CT10
	117429	9992985	80.07	1.20	CT10
	117430	9995991	80.07	1.20	CT10
Comments	Parton showering with HERWIG (105860) or PYTHIA, 117050: Perugia11C tune, 117428: Perugia11 tune, 117429: Perugia11mpiHI tune with modified underlying event activity, 117430: Perugia11NOCR tune with modified color reconnection.				

Table A.3: POWHEG $t\bar{t}$ Monte Carlo samples

Process	$pp \to t\bar{t} \to b\bar{b}j_1j_2l_1\nu_1$ **or** $b\bar{b}l_1\nu_1l_2\nu_2$ **with** $l = e, \mu, \tau$ **and** $j = u, d, c, s$				
Generators	ACERMC+PYTHIA				
Information	DSID	# events	σ [pb]	k-factor	PDF
	105205	1999497	58.23	1.53	CTEQ6L1
	117862	9993485	41.01	2.35	CTEQ6L1
	117863	9975490	41.01	2.35	CTEQ6L1
Comments	117862: ISR/FSR variation up, 117863: ISR/FSR variation down.				

Table A.4: ACERMC $t\bar{t}$ Monte Carlo samples

A.2 W+jets+γ Monte Carlo samples

Process	$\boldsymbol{pp \to W(\to l\nu) + N}$ **partons** $\boldsymbol{+\gamma}$ **with** $\boldsymbol{l = e, \mu, \tau}$					
Generators	ALPGEN+HERWIG/JIMMY					
Information	N	DSID	# events	σ [pb]	k-factor	PDF
	0	117410	2118995	213.06	1.37	CTEQ6L1
	1	117411	529998	52.20	1.37	CTEQ6L1
	2	117412	175000	17.22	1.37	CTEQ6L1
	3	117413	264999	5.34	1.37	CTEQ6L1
	4	117414	64999	1.38	1.37	CTEQ6L1
	5	117415	20000	0.34	1.37	CTEQ6L1

Table A.5: ALPGEN W+jets+γ Monte Carlo samples with up to five partons

Process	$\boldsymbol{pp \to W(\to l\nu)}$ **+ up to 3 partons** $\boldsymbol{+\gamma}$ **with** $\boldsymbol{l = e, \mu, \tau}$					
Generator	SHERPA					
Information	W decay	DSID	# events	σ [pb]	k-factor	PDF
	$e\nu$	126739	399999	139.66	1.20	CT10
	$\mu\nu$	126742	399900	139.52	1.20	CT10
	$\tau\nu$	126856	399599	139.45	1.20	CT10

Table A.6: SHERPA W+jets+γ Monte Carlo samples with up to three partons

A.3 W+jets Monte Carlo samples

Process	$pp \rightarrow W(\rightarrow e\nu) + N$ **partons**					
Generators	ALPGEN+HERWIG/JIMMY					
Information	N	DSID	# events	σ [pb]	k-factor	PDF
	0	107680	6952874	6930.50	1.20	CTEQ6L1
	1	107681	4998487	1305.30	1.20	CTEQ6L1
	2	107682	3768632	378.13	1.20	CTEQ6L1
	3	107683	1008947	101.86	1.20	CTEQ6L1
	4	107684	250000	25.68	1.20	CTEQ6L1
	5	107685	69999	6.99	1.20	CTEQ6L1

Table A.7: $W(\rightarrow e\nu)$+jets Monte Carlo samples with up to five partons

Process	$pp \rightarrow W(\rightarrow \mu\nu) + N$ **partons**					
Generators	ALPGEN+HERWIG/JIMMY					
Information	N	DSID	# events	σ [pb]	k-factor	PDF
	0	107690	6962239	6932.40	1.20	CTEQ6L1
	1	107691	4988236	1305.90	1.20	CTEQ6L1
	2	107692	3768737	378.07	1.20	CTEQ6L1
	3	107693	1008446	101.85	1.20	CTEQ6L1
	4	107694	254950	25.72	1.20	CTEQ6L1
	5	107695	70000	7.00	1.20	CTEQ6L1

Table A.8: $W(\rightarrow \mu\nu)$+jets Monte Carlo samples with up to five partons

Process	$\boldsymbol{pp \to W(\to \tau\nu) + N}$ **partons**					
Generators	ALPGEN+HERWIG/JIMMY					
Information	N	DSID	# events	σ [pb]	k-factor	PDF
	0	107700	3418296	6931.80	1.20	CTEQ6L1
	1	107701	2499194	1304.90	1.20	CTEQ6L1
	2	107702	3750986	377.93	1.20	CTEQ6L1
	3	107703	1009946	101.96	1.20	CTEQ6L1
	4	107704	249998	25.71	1.20	CTEQ6L1
	5	107705	65000	7.00	1.20	CTEQ6L1

Table A.9: $W(\to \tau\nu)$+jets Monte Carlo samples with up to five partons

Process	$\boldsymbol{pp \to W(\to l\nu) + b\bar{b} + N}$ **partons with** l=$\boldsymbol{e, \mu, \tau}$					
Generators	ALPGEN+HERWIG/JIMMY					
Information	N	DSID	# events	σ [pb]	k-factor	PDF
	0	107280	474997	47.35	1.20	CTEQ6L1
	1	107281	205000	35.76	1.20	CTEQ6L1
	2	107282	174499	17.33	1.20	CTEQ6L1
	3	107283	69999	7.61	1.20	CTEQ6L1

Table A.10: $W + b\bar{b}$+jets Monte Carlo samples with up to three partons

Process	$\boldsymbol{pp \to W(\to l\nu) + c\bar{c} + N}$ **partons with l=**$\boldsymbol{e, \mu, \tau}$					
Generators	ALPGEN+HERWIG/JIMMY					
Information	N	DSID	# events	σ [pb]	k-factor	PDF
	0	117284	1274846	127.53	1.20	CTEQ6L1
	1	117285	1049847	104.68	1.20	CTEQ6L1
	2	117286	524947	52.08	1.20	CTEQ6L1
	3	117287	170000	16.96	1.20	CTEQ6L1

Table A.11: $W + c\bar{c}$+jets Monte Carlo samples with up to three partons

Process	$\boldsymbol{pp \to W(\to l\nu) + c + N}$ **partons with l=**$\boldsymbol{e, \mu, \tau}$					
Generators	ALPGEN+HERWIG/JIMMY					
Information	N	DSID	# events	σ [pb]	k-factor	PDF
	0	117293	6497837	644.4	1.20	CTEQ6L1
	1	117294	2069646	205.0	1.20	CTEQ6L1
	2	117295	519998	50.8	1.20	CTEQ6L1
	3	117296	115000	11.4	1.20	CTEQ6L1
	4	117297	30000	2.8	1.20	CTEQ6L1

Table A.12: $W + c$+jets Monte Carlo samples with up to four partons

A.4 Z+jets Monte Carlo samples

Process	$\boldsymbol{pp \to Z(\to ee) + N}$ **partons**					
Generators	ALPGEN+HERWIG/JIMMY					
Information	N	DSID	# events	σ [pb]	k-factor	PDF
	0	107650	6618284	668.32	1.25	CTEQ6L1
	1	107651	1334897	134.36	1.25	CTEQ6L1
	2	107652	2004195	40.54	1.25	CTEQ6L1
	3	107653	549949	11.16	1.25	CTEQ6L1
	4	107654	149948	2.88	1.25	CTEQ6L1
	5	107655	50000	0.83	1.25	CTEQ6L1

Table A.13: $Z(\to ee)$+jets Monte Carlo samples with up to five partons

Process	$\boldsymbol{pp \to Z(\to \mu\mu) + N}$ **partons**					
Generators	ALPGEN+HERWIG/JIMMY					
Information	N	DSID	# events	σ [pb]	k-factor	PDF
	0	107660	6615230	668.68	1.25	CTEQ6L1
	1	107661	1334296	134.14	1.25	CTEQ6L1
	2	107662	1999941	40.33	1.25	CTEQ6L1
	3	107663	549896	11.19	1.25	CTEQ6L1
	4	107664	150000	2.75	1.25	CTEQ6L1
	5	107665	50000	0.77	1.25	CTEQ6L1

Table A.14: $Z(\to \mu\mu)$+jets Monte Carlo samples with up to five partons

Process		$pp \rightarrow Z(\rightarrow \tau\tau) + N$ **partons**				
Generators		ALPGEN+HERWIG/JIMMY				
Information	N	DSID	# events	σ [pb]	k-factor	PDF
	0	107670	10613179	668.40	1.25	CTEQ6L1
	1	107671	3334137	134.81	1.25	CTEQ6L1
	2	107672	1004847	40.36	1.25	CTEQ6L1
	3	107673	509847	11.25	1.25	CTEQ6L1
	4	107674	149999	2.79	1.25	CTEQ6L1
	5	107675	45000	0.77	1.25	CTEQ6L1

Table A.15: $Z(\rightarrow \tau\tau)$+jets Monte Carlo samples with up to five partons

Process	$\boldsymbol{pp \to Z(\to ee) + b\bar{b} + N}$ **partons**					
Generators	ALPGEN+HERWIG/JIMMY					
Information	N	DSID	# events	σ [pb]	k-factor	PDF
	0	109300	409999	6.57	1.25	CTEQ6L1
	1	109301	160000	2.48	1.25	CTEQ6L1
	2	109302	60000	0.89	1.25	CTEQ6L1
	3	109303	30000	0.39	1.25	CTEQ6L1
Process	$\boldsymbol{pp \to Z(\to \mu\mu) + b\bar{b} + N}$ **partons**					
Generators	ALPGEN+HERWIG/JIMMY					
Information	N	DSID	# events	σ [pb]	k-factor	PDF
	0	109305	409949	6.56	1.25	CTEQ6L1
	1	109306	155000	2.47	1.25	CTEQ6L1
	2	109307	60000	0.89	1.25	CTEQ6L1
	3	109308	29999	0.39	1.25	CTEQ6L1
Process	$\boldsymbol{pp \to Z(\to \tau\tau) + b\bar{b} + N}$ **partons**					
Generators	ALPGEN+HERWIG/JIMMY					
Information	N	DSID	# events	σ [pb]	k-factor	PDF
	0	109310	409999	6.57	1.25	CTEQ6L1
	1	109311	160000	2.49	1.25	CTEQ6L1
	2	109312	60000	0.89	1.25	CTEQ6L1
	3	109313	30000	0.39	1.25	CTEQ6L1

Table A.16: $Z + b\bar{b}$+jets Monte Carlo samples with up to three partons

A.5 Diboson Monte Carlo samples

Process	$pp \to WW$				
Generator	HERWIG				
Information	DSID	# events	σ [pb]	k-factor	PDF
	105985	2489244	11.50	1.48	LO**
Process	$pp \to WZ$				
Generator	HERWIG				
Information	DSID	# events	σ [pb]	k-factor	PDF
	105986	999896	3.46	1.60	LO**
Process	$pp \to ZZ$				
Generator	HERWIG				
Information	DSID	# events	σ [pb]	k-factor	PDF
	105987	249999	0.97	1.30	LO**

Table A.17: Diboson Monte Carlo sample

A.6 Single top Monte Carlo samples

Process	**s-channel: $pp \to W(\to l\nu) + b\bar{b}$**					
Generators	MC@NLO+HERWIG/JIMMY					
Information	W decay	DSID	# events	σ [pb]	k-factor	PDF
	$e\nu$	108343	299948	0.47	1.06	CT10
	$\mu\nu$	108344	299998	0.47	1.06	CT10
	$\tau\nu$	108345	299899	0.47	1.06	CT10
Process	**t-channel: $pp \to W(\to l\nu) + bb(\bar{b}\bar{b})$**					
Generators	ACERMC+Pythia					
Information	W decay	DSID	# events	σ [pb]	k-factor	PDF
	$e\nu$	117360	999295	8.06	0.87	LO**
	$\mu\nu$	117361	999948	8.06	0.87	LO**
	$\tau\nu$	117362	998995	8.05	0.87	LO**
Process	**Wt-channel: $pp \to t + W(\to l\nu)$**					
Generators	MC@NLO+HERWIG/JIMMY					
Information	W decay	DSID	# events	σ [pb]	k-factor	PDF
	$l\nu$	108346	899694	14.59	1.08	CT10

Table A.18: Single top production Monte Carlo sample

A.7 Dijet Monte Carlo samples

Process	$pp \to j_1 j_2$ **with** $j = u, d, c, s, b, \gamma$				
Generator	PYTHIA				
Information	DSID	# events	σ [pb]	k-factor	PDF
	105802	9999419	$1.37 \cdot 10^6$	1.00	CTEQ6L1
	105807	4999423	$6.44 \cdot 10^4$	1.00	CTEQ6L1
	105814	999948	$3.67 \cdot 10^3$	1.00	CTEQ6L1
Comments	Generation cut: $p_T(j) > 17\,\text{GeV}$ (105802), 35 GeV (105807), 70 GeV (10814).				

Table A.19: Dijet Monte Carlo sample

Appendix B

Additional plots

B.1 Additional plots of Chapter 6

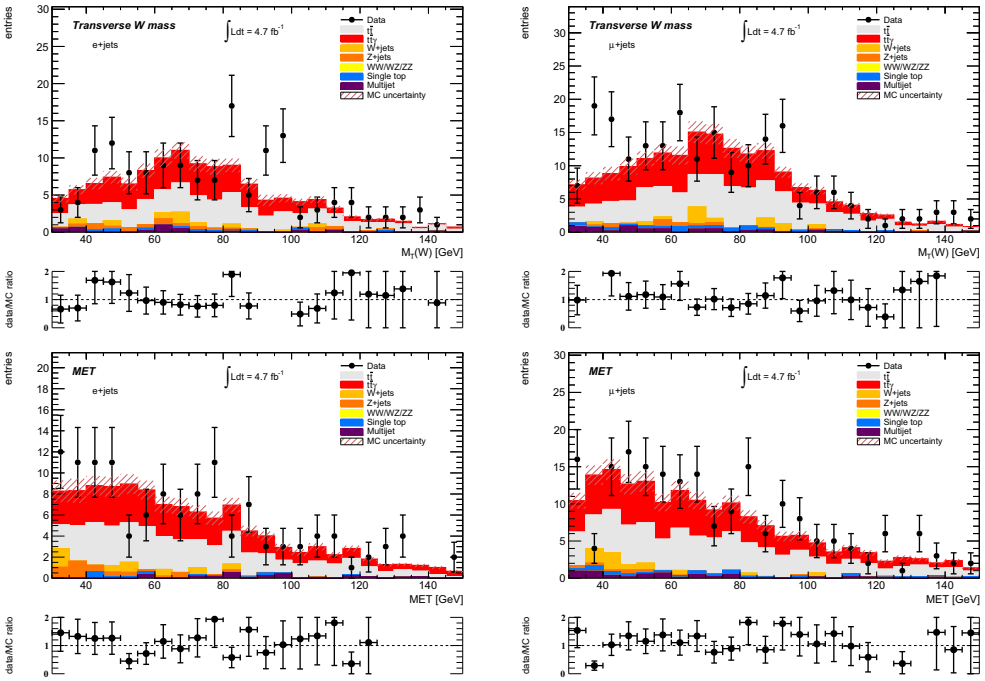

Figure B.1: Comparison between data and the expectation from Monte Carlo simulation for events passing the $t\bar{t}\gamma$ event selection. The transverse W boson mass (upper row) and missing transverse energy (lower row) are shown for the electron channel (left column) and muon channel (right column) of each event. Data points are shown in black with statistical uncertainties, while the stacked histogram includes the Monte Carlo expectation of the signal process and all background contributions. Each plot also illustrates systematic uncertainties on the Monte Carlo prediction. Further, a data to Monte Carlo ratio plot is included in each figure with statistical uncertainties.

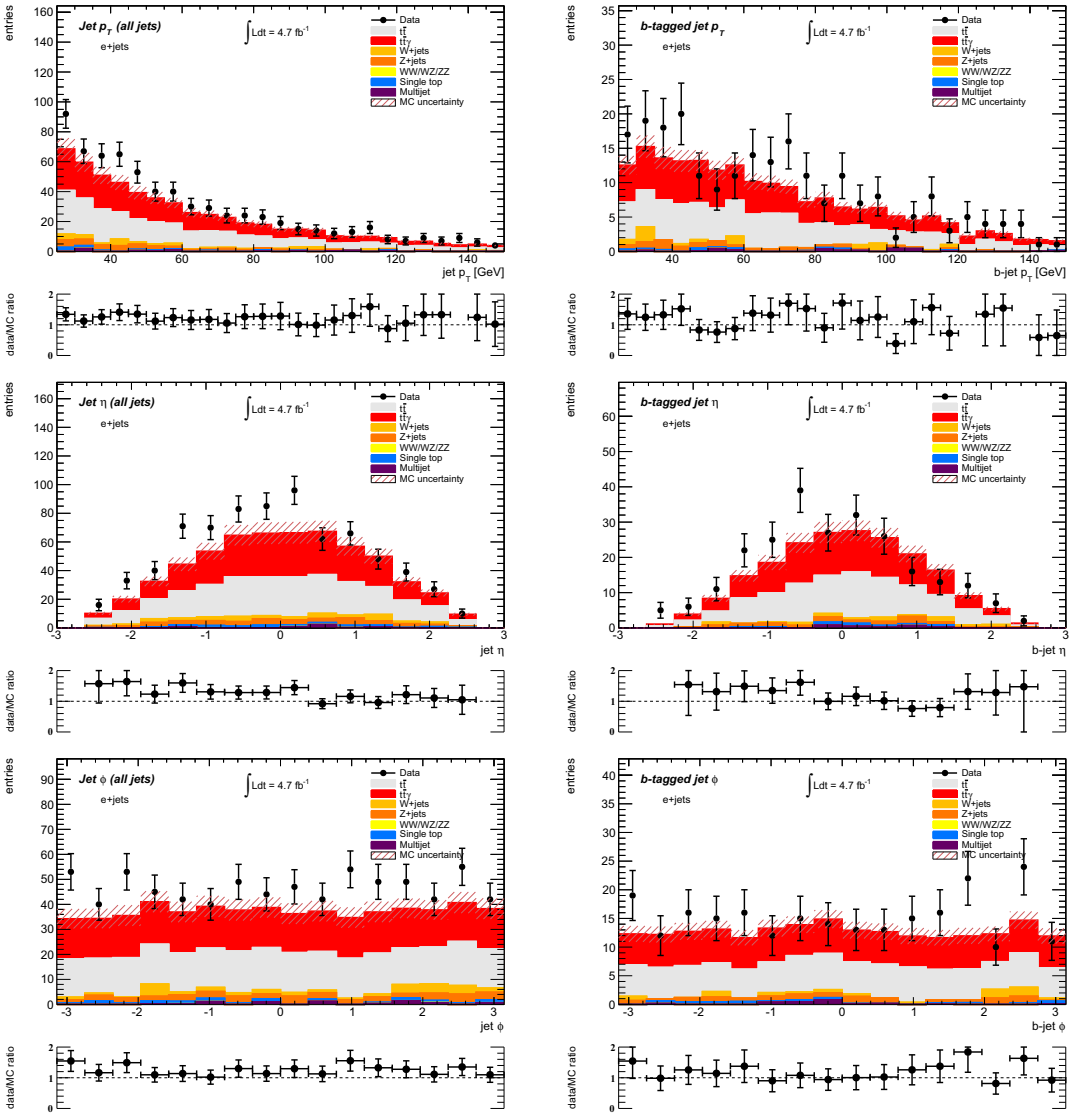

Figure B.2: Comparison between data and the expectation from Monte Carlo simulation for events passing the $t\bar{t}\gamma$ event selection in the electron channel. p_T (upper row), η (middle row) and ϕ distributions are shown for all selected jets (left column) and b-tagged jets (right column). Data points are shown in black with statistical uncertainties, while the stacked histogram includes the Monte Carlo expectation of the signal process and all background contributions. Each plot also illustrates systematic uncertainties on the Monte Carlo prediction. Further, a data to Monte Carlo ratio plot is included in each figure with statistical uncertainties.

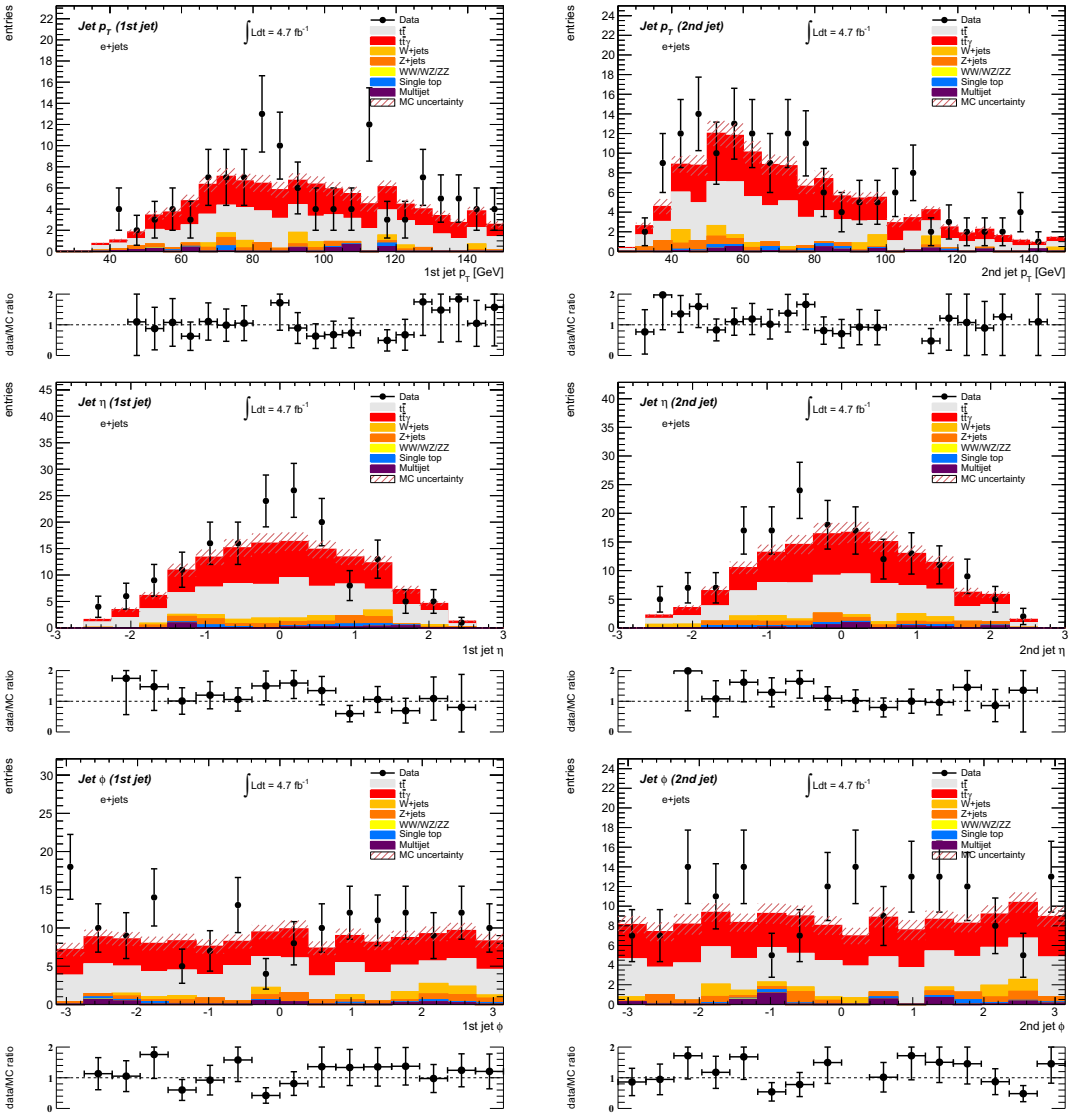

Figure B.3: Comparison between data and the expectation from Monte Carlo simulation for events passing the $t\bar{t}\gamma$ event selection in the electron channel. p_T (upper row), η (middle row) and ϕ distributions are shown for all selected jets with the highest p_T (left column) and second highest p_T (right column) in each event. Data points are shown in black with statistical uncertainties, while the stacked histogram includes the Monte Carlo expectation of the signal process and all background contributions. Each plot also illustrates systematic uncertainties on the Monte Carlo prediction. Further, a data to Monte Carlo ratio plot is included in each figure with statistical uncertainties.

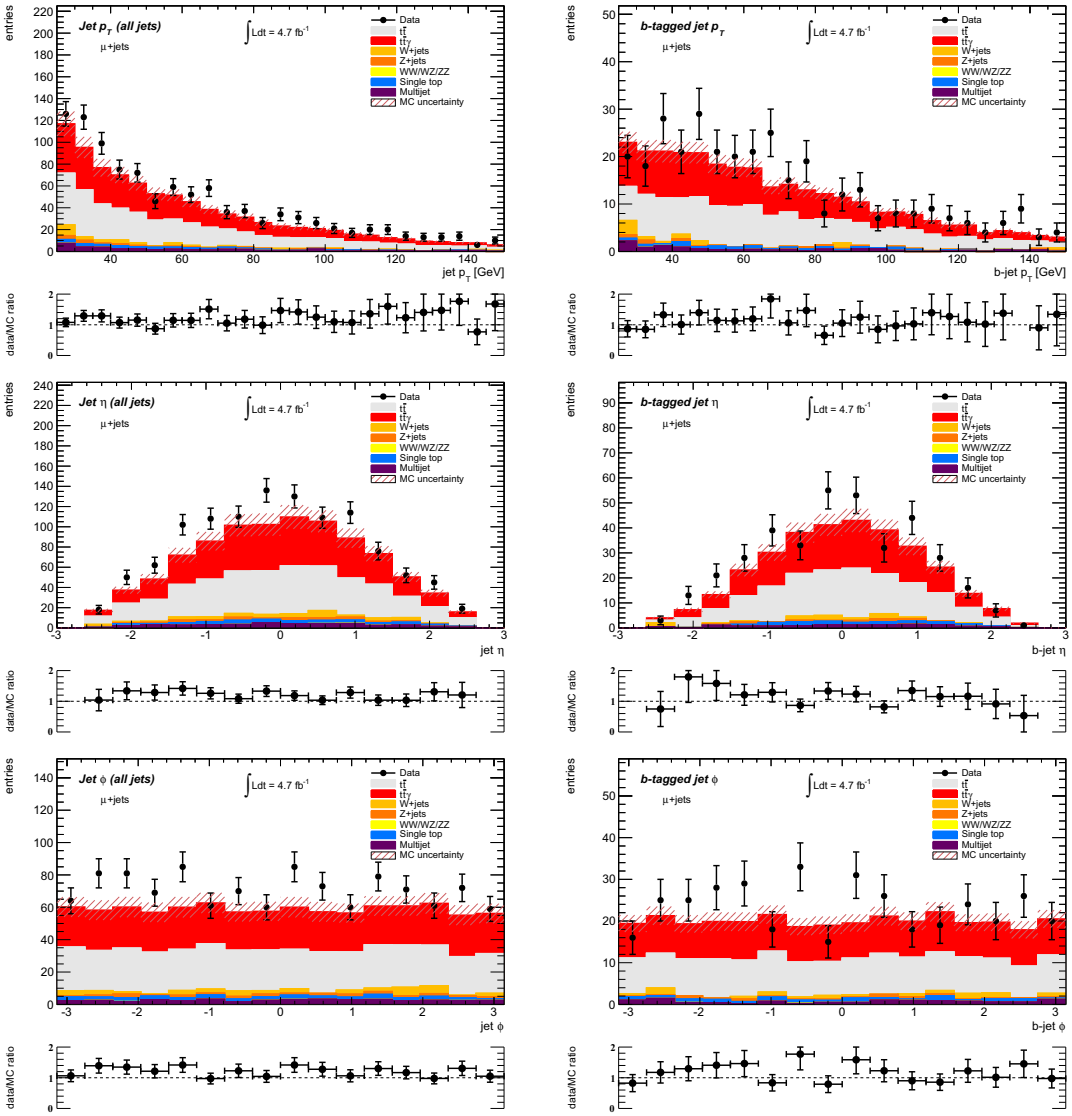

Figure B.4: Comparison between data and the expectation from Monte Carlo simulation for events passing the $t\bar{t}\gamma$ event selection in the muon channel. p_T (upper row), η (middle row) and ϕ distributions are shown for all selected jets (left column) and b-tagged jets (right column). Data points are shown in black with statistical uncertainties, while the stacked histogram includes the Monte Carlo expectation of the signal process and all background contributions. Each plot also illustrates systematic uncertainties on the Monte Carlo prediction. Further, a data to Monte Carlo ratio plot is included in each figure with statistical uncertainties.

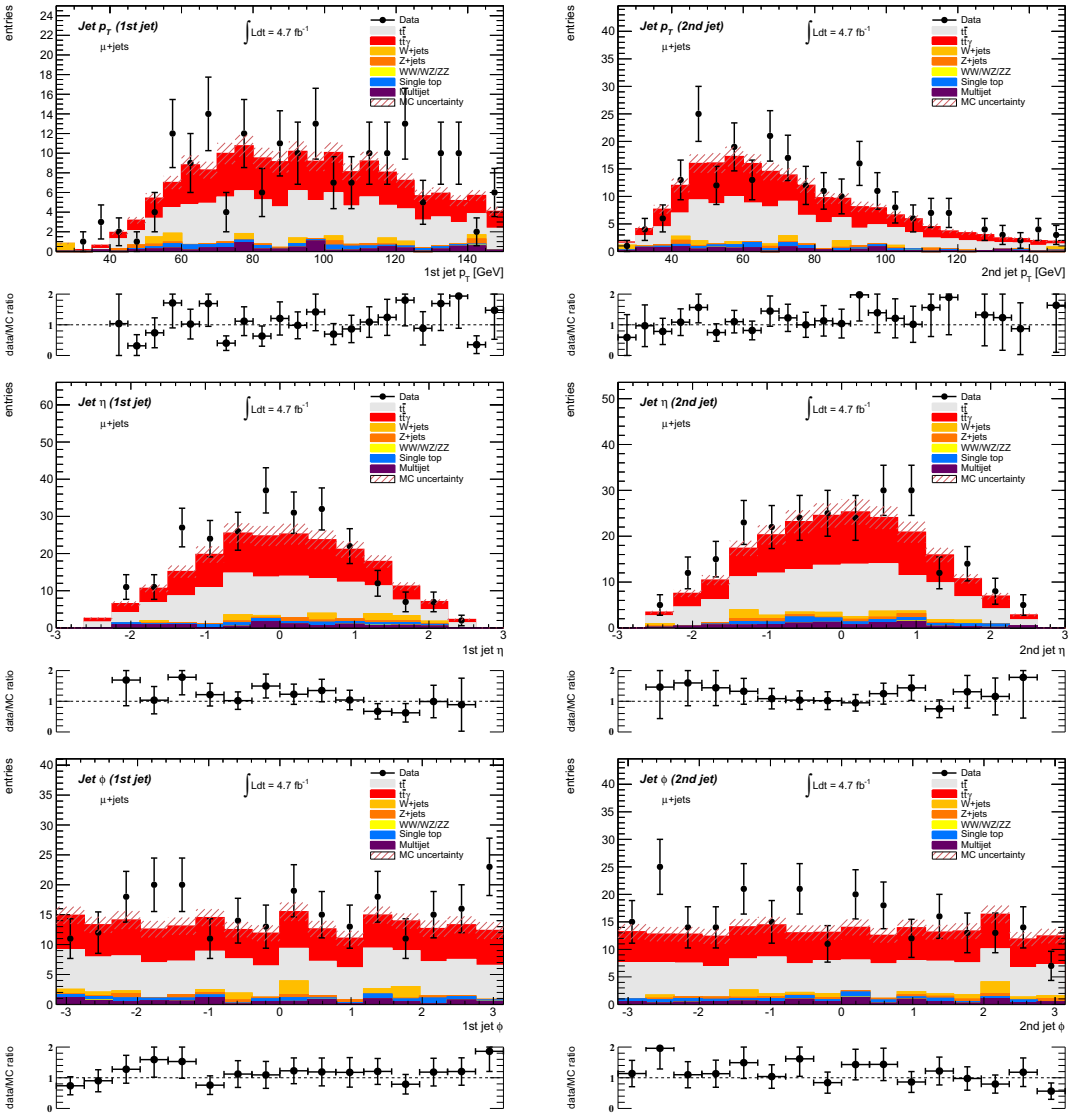

Figure B.5: Comparison between data and the expectation from Monte Carlo simulation for events passing the $t\bar{t}\gamma$ event selection in the muon channel. p_T (upper row), η (middle row) and ϕ distributions are shown for all selected jets with the highest p_T (left column) and second highest p_T (right column) in each event. Data points are shown in black with statistical uncertainties, while the stacked histogram includes the Monte Carlo expectation of the signal process and all background contributions. Each plot also illustrates systematic uncertainties on the Monte Carlo prediction. Further, a data to Monte Carlo ratio plot is included in each figure with statistical uncertainties.

B.2 Additional plots of Chapter 8

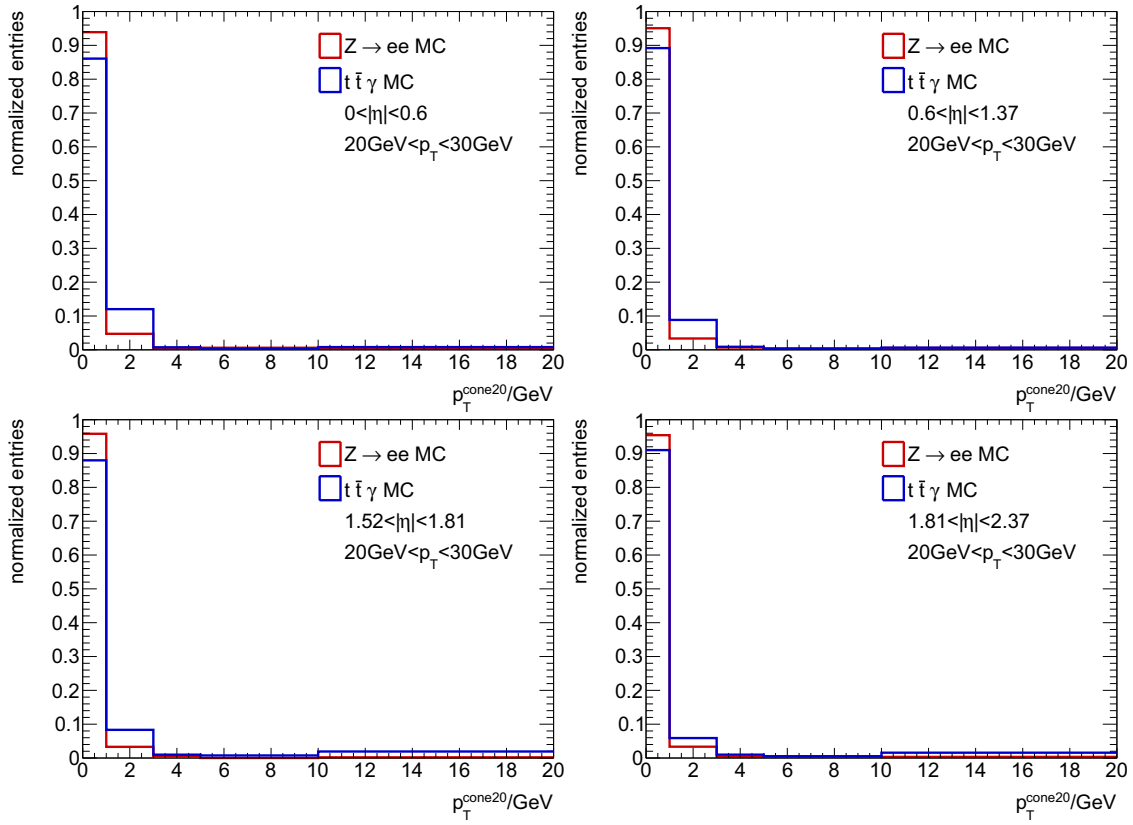

Figure B.6: p_T^{cone20} distributions of electrons from $Z \to e^+e^-$ Monte Carlo simulation (red) and photons from the $t\bar{t}\gamma$ Monte Carlo simulation (blue). All histograms are normalized to 1 and show the total isolation distributions from 0 to 20 GeV, with the last bin including overflow events. The statistical uncertainties for each histogram are smaller than 0.5% for electrons and smaller than 2% for photons in each bin and are not displayed. The histograms show distributions of electrons and photons with a p_T between 20 GeV and 30 GeV in different regions of $|\eta|$: [0, 0.60) (upper left), [0.60, 1.37) (upper right), [1.52, 1.81) (lower left), [1.81, 2.37) (lower right). The electron distributions are constant with η, while the photon distributions shift to lower p_T^{cone20} values with increasing $|\eta|$.

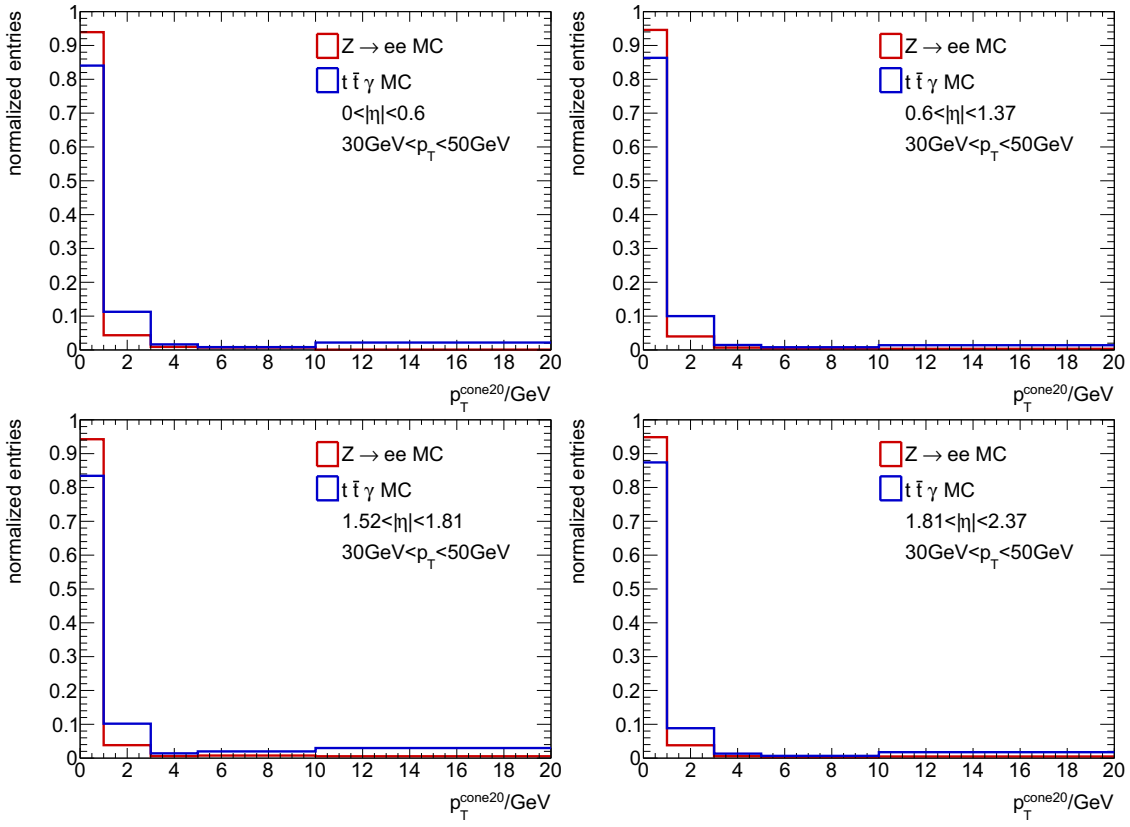

Figure B.7: p_T^{cone20} distributions of electrons from $Z \to e^+e^-$ Monte Carlo simulation (red) and photons from the $t\bar{t}\gamma$ Monte Carlo simulation (blue). All histograms are normalized to 1 and show the total isolation distributions from 0 to 20 GeV, with the last bin including overflow events. The statistical uncertainties for each histogram are smaller than 0.5% for electrons and smaller than 2% for photons in each bin and are not displayed. The histograms show distributions of electrons and photons with a p_T between 30 GeV and 50 GeV in different regions of $|\eta|$: [0, 0.60) (upper left), [0.60, 1.37) (upper right), [1.52, 1.81) (lower left), [1.81, 2.37) (lower right). The electron distributions are constant with η, while the photon distributions shift to lower p_T^{cone20} values with increasing $|\eta|$.

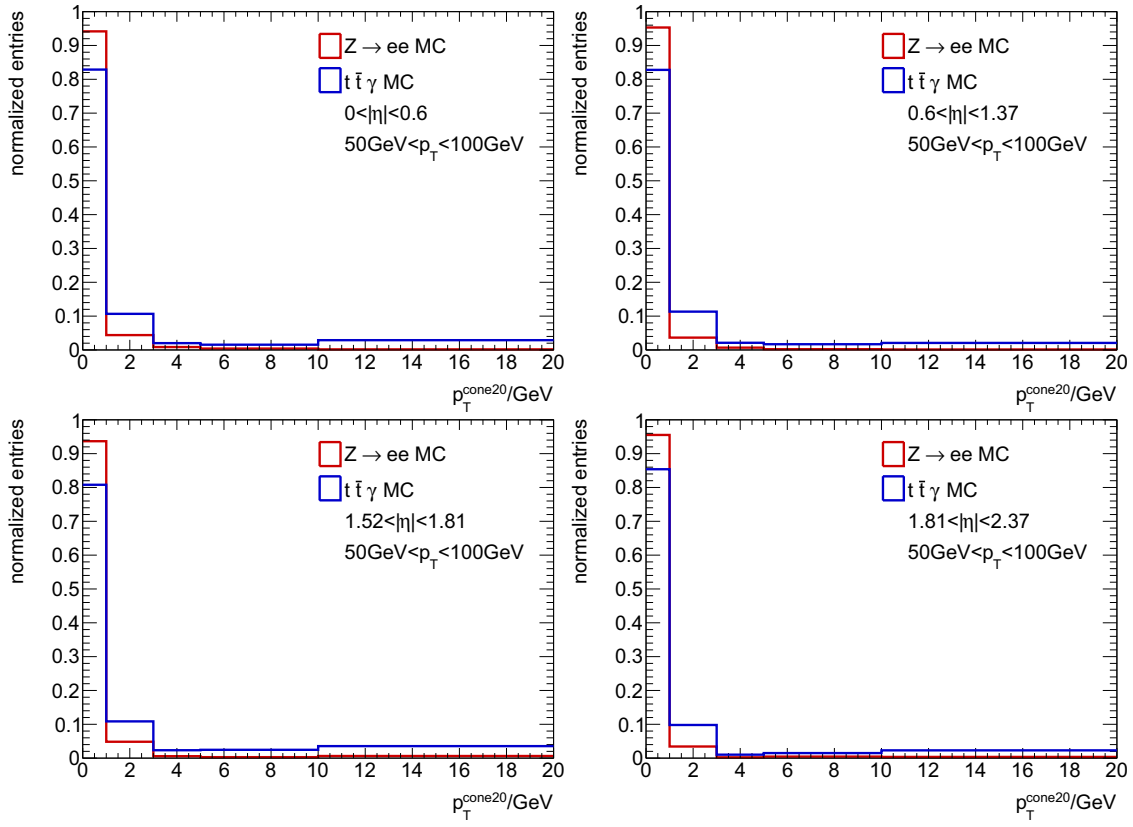

Figure B.8: p_T^{cone20} distributions of electrons from $Z \to e^+e^-$ Monte Carlo simulation (red) and photons from the $t\bar{t}\gamma$ Monte Carlo simulation (blue). All histograms are normalized to 1 and show the total isolation distributions from 0 to 20 GeV, with the last bin including overflow events. The statistical uncertainties for each histogram are smaller than 0.5% for electrons and smaller than 2% for photons in each bin and are not displayed. The histograms show distributions of electrons and photons with a p_T between 50 GeV and 100 GeV in different regions of $|\eta|$: [0, 0.60) (upper left), [0.60, 1.37) (upper right), [1.52, 1.81) (lower left), [1.81, 2.37) (lower right). The electron distributions are constant with η, while the photon distributions shift to lower p_T^{cone20} values with increasing $|\eta|$.

B.3 Additional plots of Chapter 9

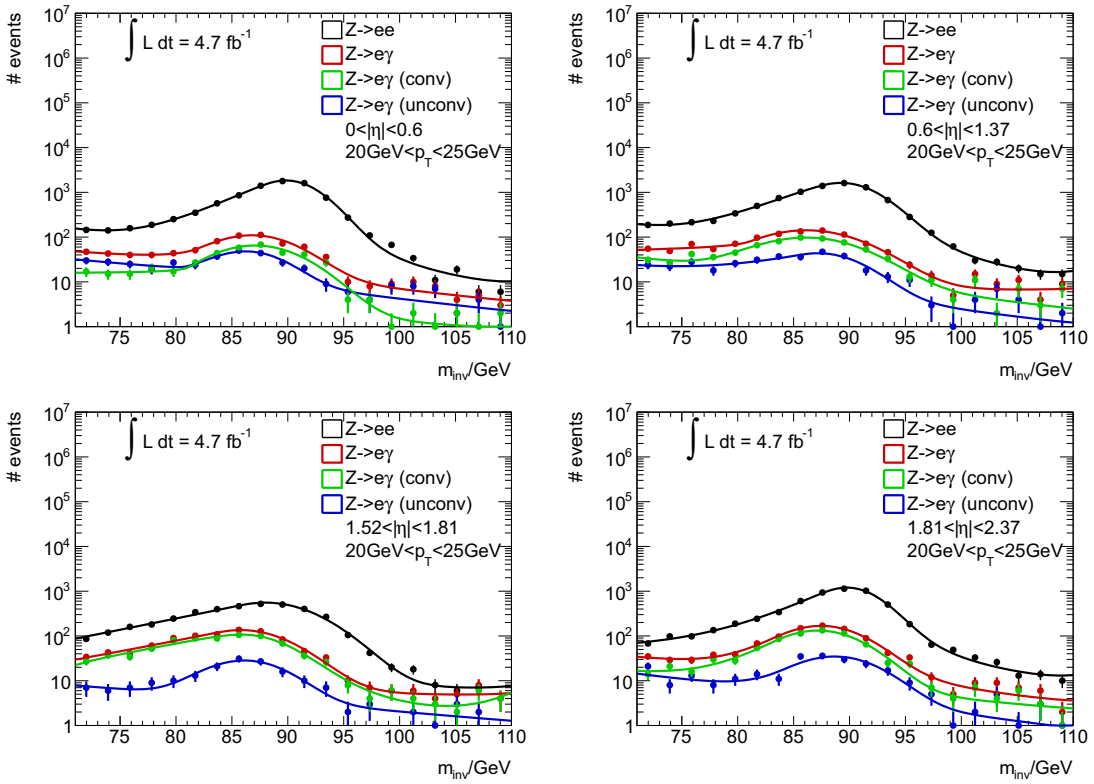

Figure B.9: Invariant mass distributions of $Z \to ee$ data events (black) and $Z \to e\gamma_{\mathrm{misId}}$ events (red), which are in addition shown for unconverted (blue) and converted photons (green) separately. Further, the combined signal+background fit is shown for each distribution, which is used to calculate the number of signal Z events. Electrons with a p_T between 20 GeV and 25 GeV have been investigated in four different $|\eta|$ regions: [0, 0.60), [0.60, 1.37), [1.52, 1.81), [1.81, 2.37).

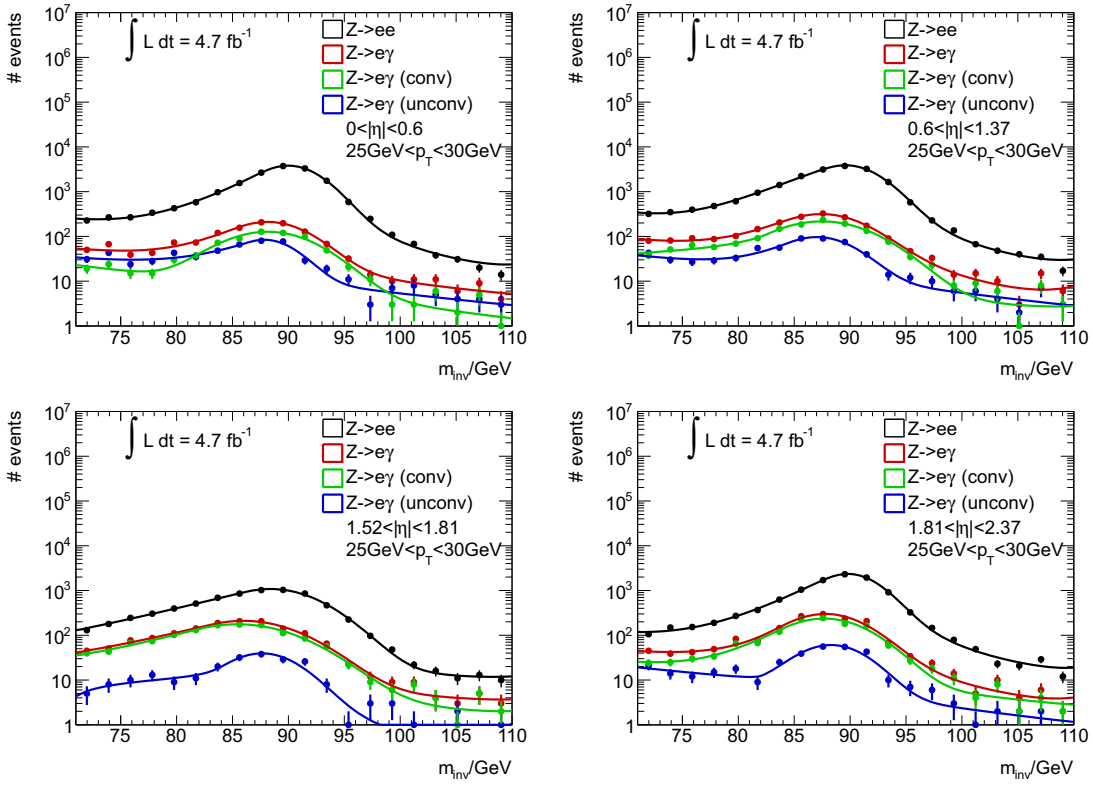

Figure B.10: Invariant mass distributions of $Z \to ee$ data events (black) and $Z \to e\gamma_{\mathrm{misId}}$ events (red), which are in addition shown for unconverted (blue) and converted photons (green) separately. Further, the combined signal+background fit is shown for each distribution, which is used to calculate the number of signal Z events. Electrons with a p_T between 25 GeV and 30 GeV have been investigated in four different $|\eta|$ regions: [0, 0.60), [0.60, 1.37), [1.52, 1.81), [1.81, 2.37).

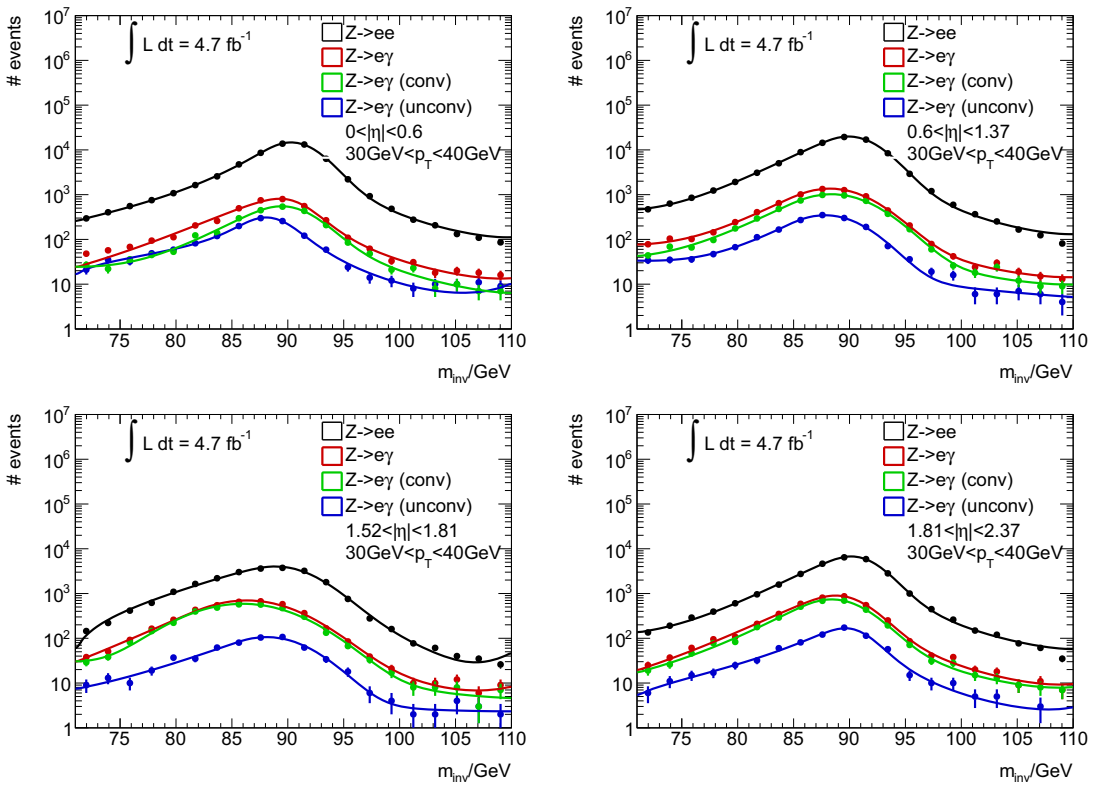

Figure B.11: Invariant mass distributions of $Z \to ee$ data events (black) and $Z \to e\gamma_{\mathrm{misId}}$ events (red), which are in addition shown for unconverted (blue) and converted photons (green) separately. Further, the combined signal+background fit is shown for each distribution, which is used to calculate the number of signal Z events. Electrons with a p_T between 30 GeV and 40 GeV have been investigated in four different $|\eta|$ regions: [0, 0.60), [0.60, 1.37), [1.52, 1.81), [1.81, 2.37).

B.4 Additional plots of Chapter 10

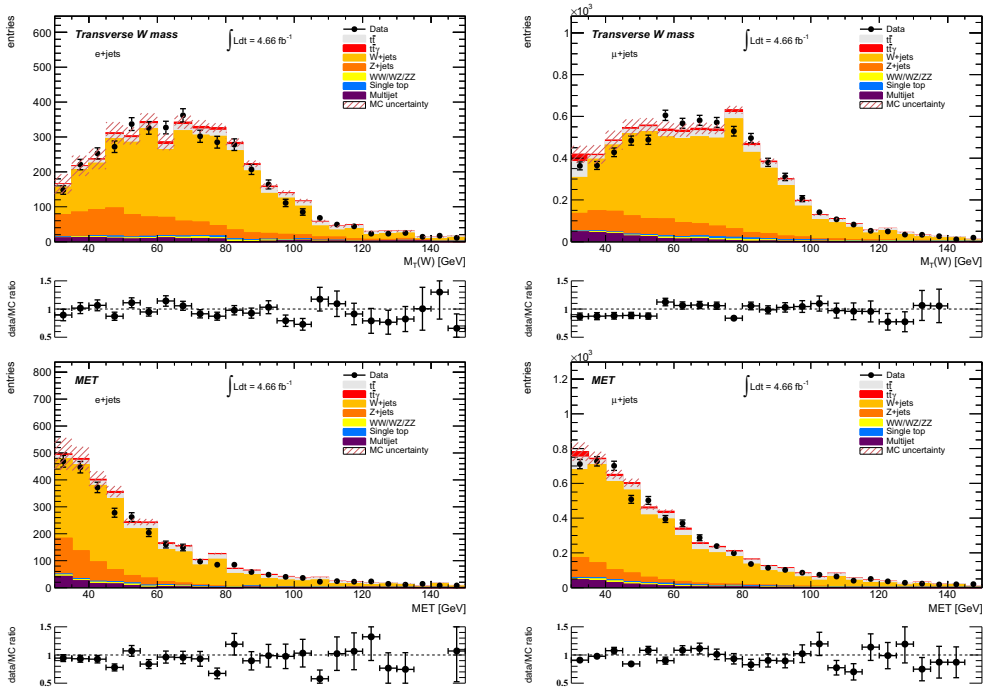

Figure B.12: Comparison between data and the expectation from Monte Carlo simulation for events passing the event selection of the W+jets+γ control region. The transverse W boson mass (upper row) and missing transverse energy (lower row) are shown for the electron channel (left column) and muon channel (right column) of each event. Data points are shown in black with statistical uncertainties, while the stacked histogram includes the Monte Carlo expectation of the signal process and all background contributions. Each plot also illustrates systematic uncertainties on the Monte Carlo prediction. Further, a data to Monte Carlo ratio plot is included in each figure with statistical uncertainties.

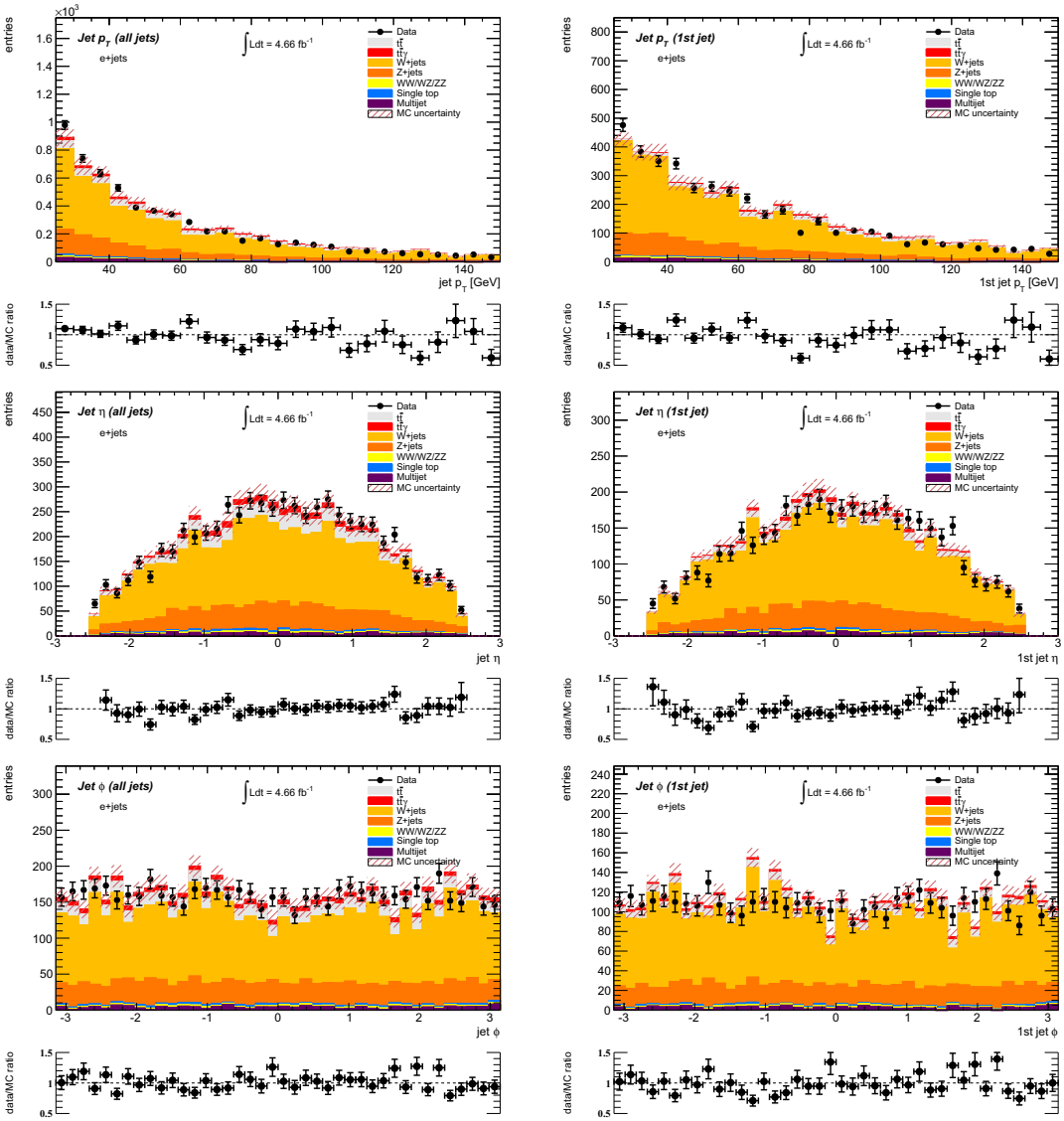

Figure B.13: Comparison between data and the expectation from Monte Carlo simulation for events passing the event selection of the W+jets+γ control region in the electron channel. p_T (upper row), η (middle row) and ϕ distributions are shown for all selected jets (left column) and jets with the highest p_T (right column). Data points are shown in black with statistical uncertainties, while the stacked histogram includes the Monte Carlo expectation of the signal process and all background contributions. Each plot also illustrates systematic uncertainties on the Monte Carlo prediction. Further, a data to Monte Carlo ratio plot is included in each figure with statistical uncertainties.

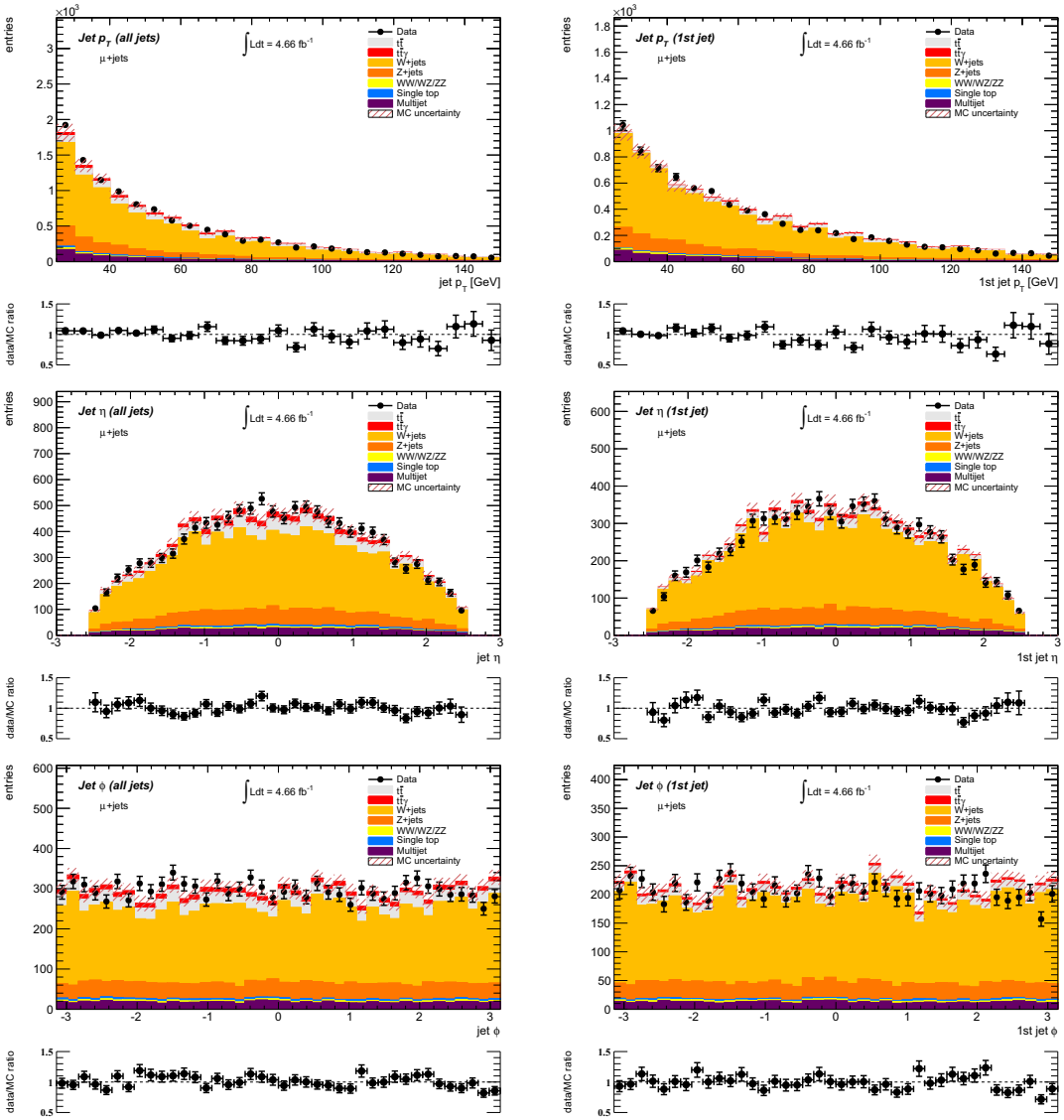

Figure B.14: Comparison between data and the expectation from Monte Carlo simulation for events passing the event selection of the W+jets+γ control region in the muon channel. p_T (upper row), η (middle row) and ϕ distributions are shown for all selected jets (left column) and jets with the highest p_T (right column). Data points are shown in black with statistical uncertainties, while the stacked histogram includes the Monte Carlo expectation of the signal process and all background contributions. Each plot also illustrates systematic uncertainties on the Monte Carlo prediction. Further, a data to Monte Carlo ratio plot is included in each figure with statistical uncertainties.

B.5 Additional plots of Chapter 12

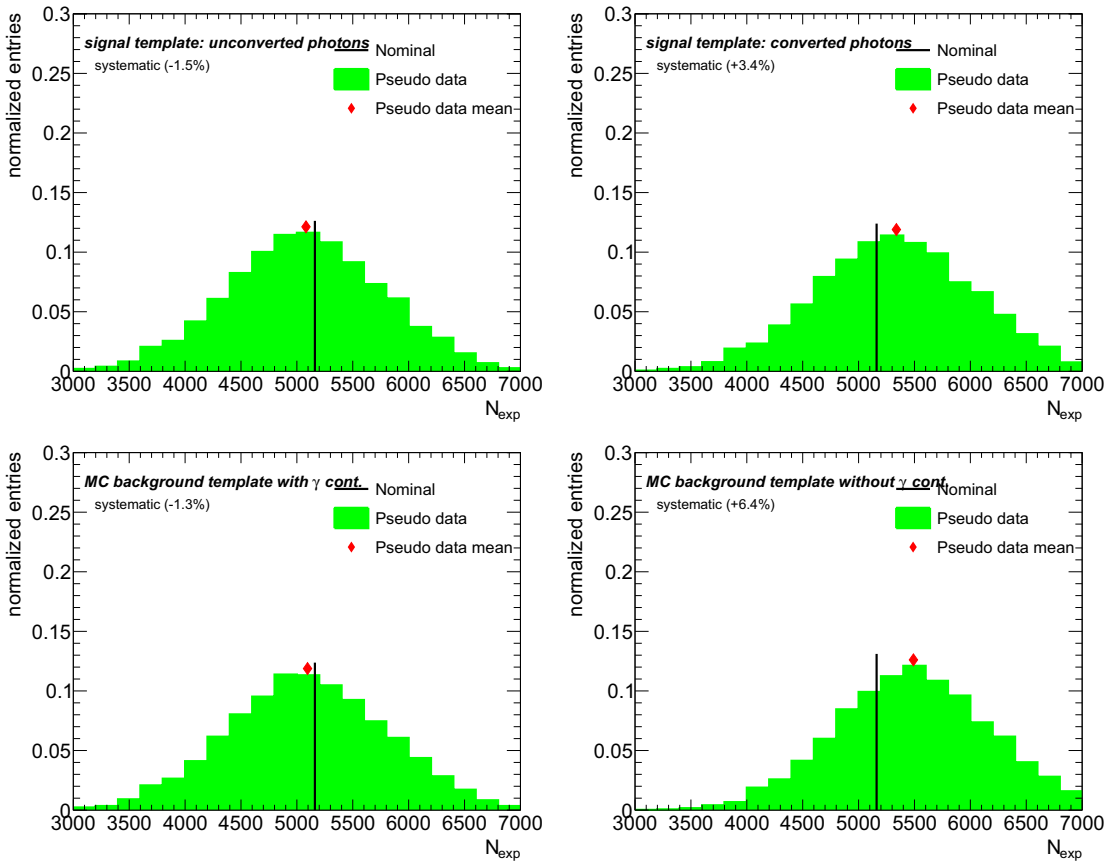

Figure B.15: Distribution of the expected number of signal events N_{exp} for 5000 pseudo experiments to evaluate various systematic uncertainties. The upper row shows the result using the signal template derived from unconverted photons (left) and converted photons (right) The lower row are the resulting distributions using background templates from dijet simulation, using all selected events (left) and excluding γ+jet events. The mean of the distribution is marked in red, while the vertical black line shows the nominal result. The difference between the two markers is considered as systematic uncertainty.

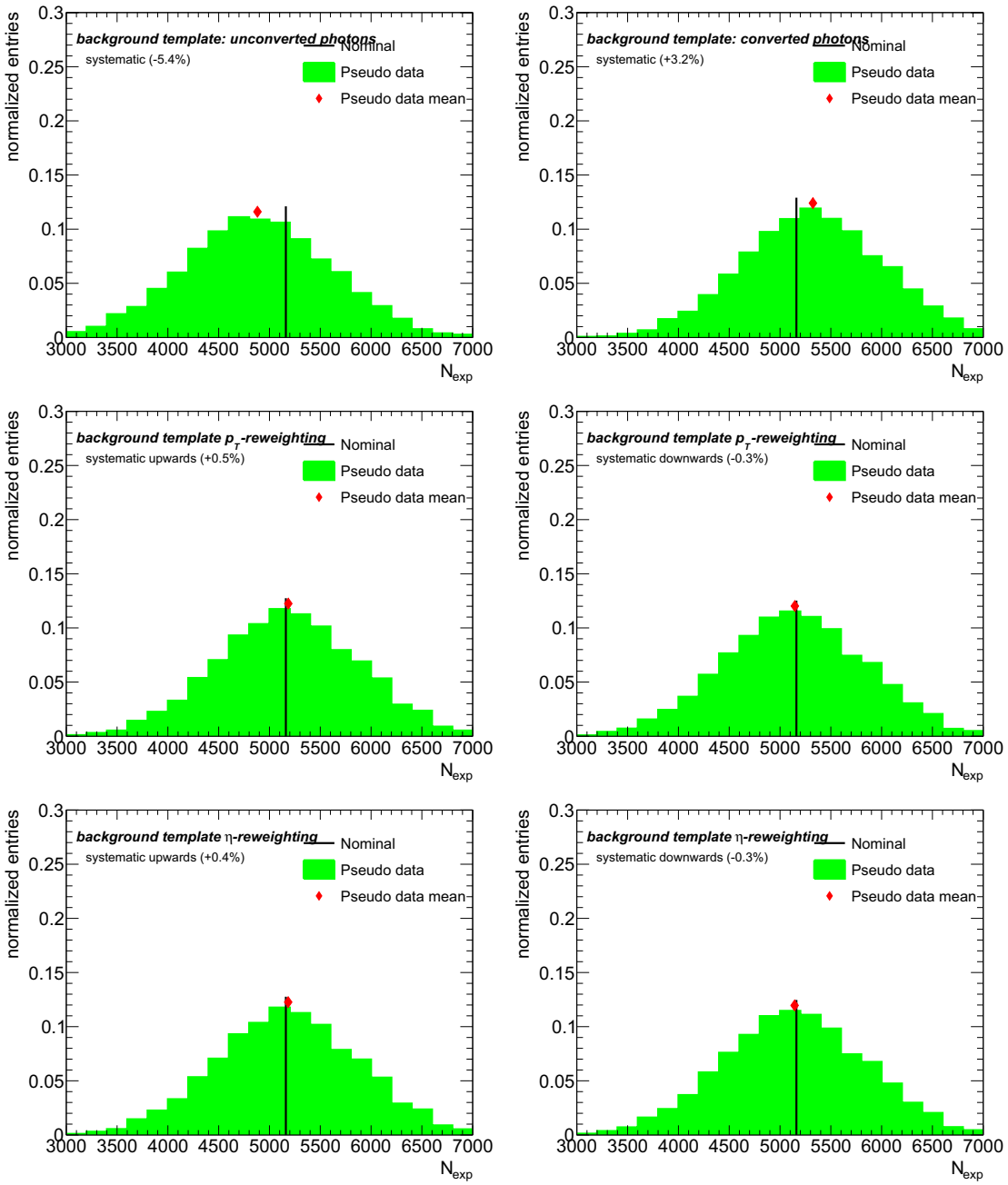

Figure B.16: Distribution of the expected number of signal events N_{exp} for 5000 pseudo experiments to evaluate various systematic uncertainties of the background template. The upper row shows the result using the template derived from unconverted photons (left) and converted photons (right). The other distributions include uncertainties from p_T (middle row) and $|\eta|$ reweighting (lower row). The mean of the distribution is marked in red, while the vertical black line shows the nominal result. The difference between the two markers is considered as systematic uncertainty.

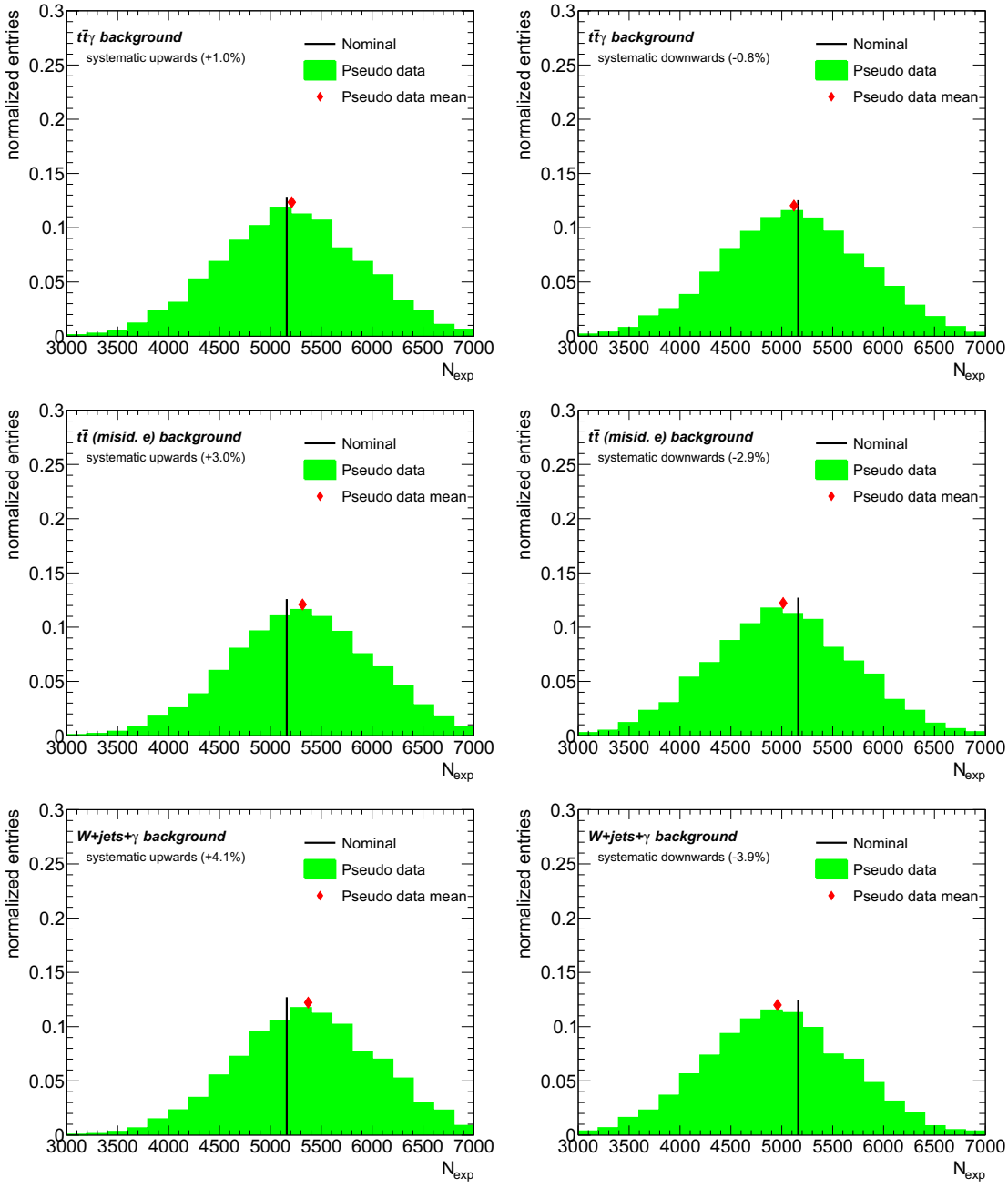

Figure B.17: Distribution of the expected number of signal events N_{exp} for 5000 pseudo experiments to evaluate various systematic uncertainties of the prompt photon background. The results are shown for the $t\bar{t}\gamma$ background (upper row), $t\bar{t}$ processes with a misidentified electron (middle row) and the W+jets+γ background contribution (lower row). The mean of the distribution is marked in red, while the vertical black line shows the nominal result. The difference between the two markers is considered as systematic uncertainty.

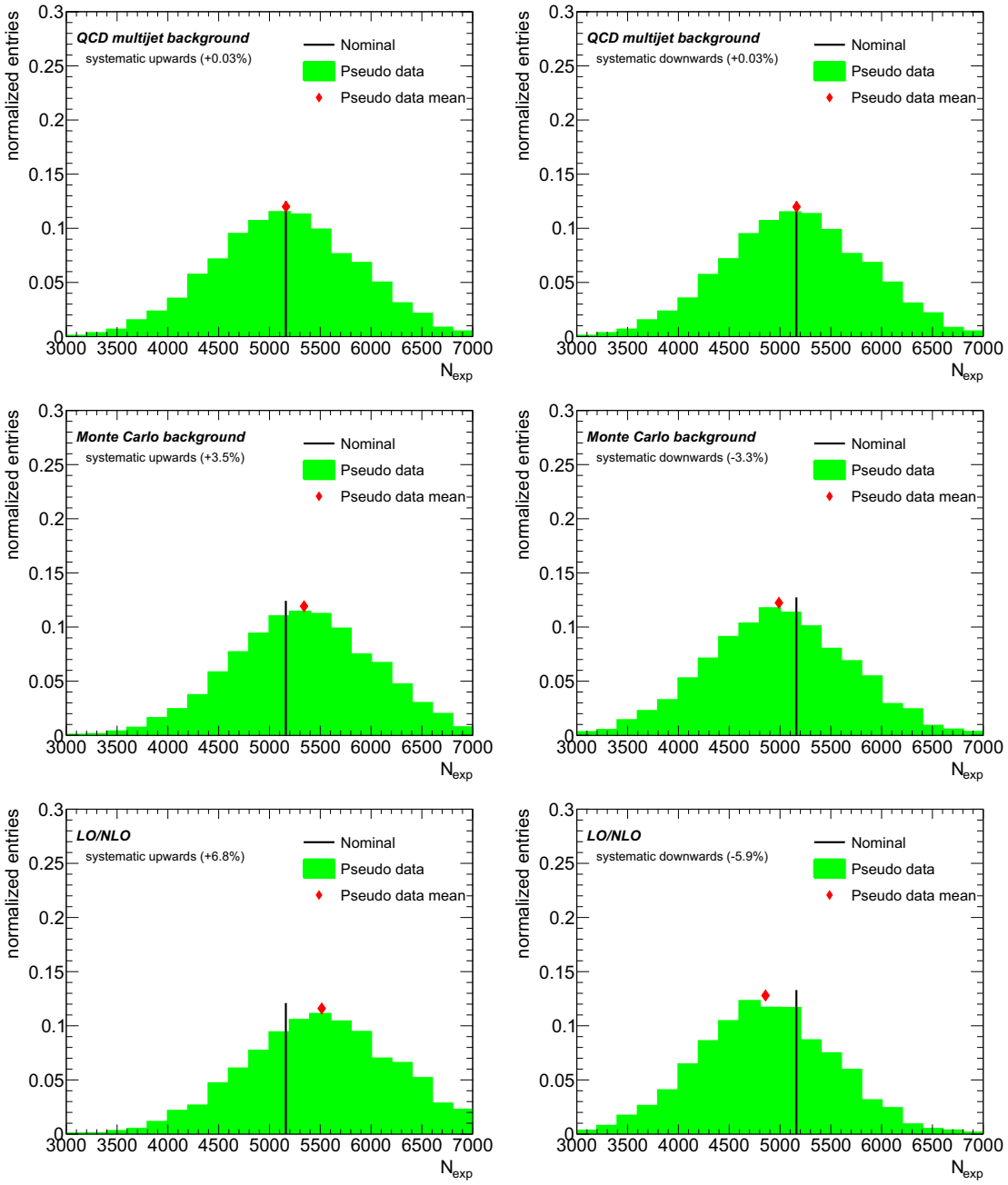

Figure B.18: Distribution of the expected number of signal events N_{exp} for 5000 pseudo experiments to evaluate various systematic uncertainties of the prompt photon background and Monte Carlo generators. The results are shown for the QCD multijet background (upper row) and the remaining background contributions estimated from Monte Carlo simulation (middle row). The lower row include the uncertainty using a leading order or next-to-leading order generator. The mean of the distribution is marked in red, while the vertical black line shows the nominal result. The difference between the two markers is considered as systematic uncertainty.

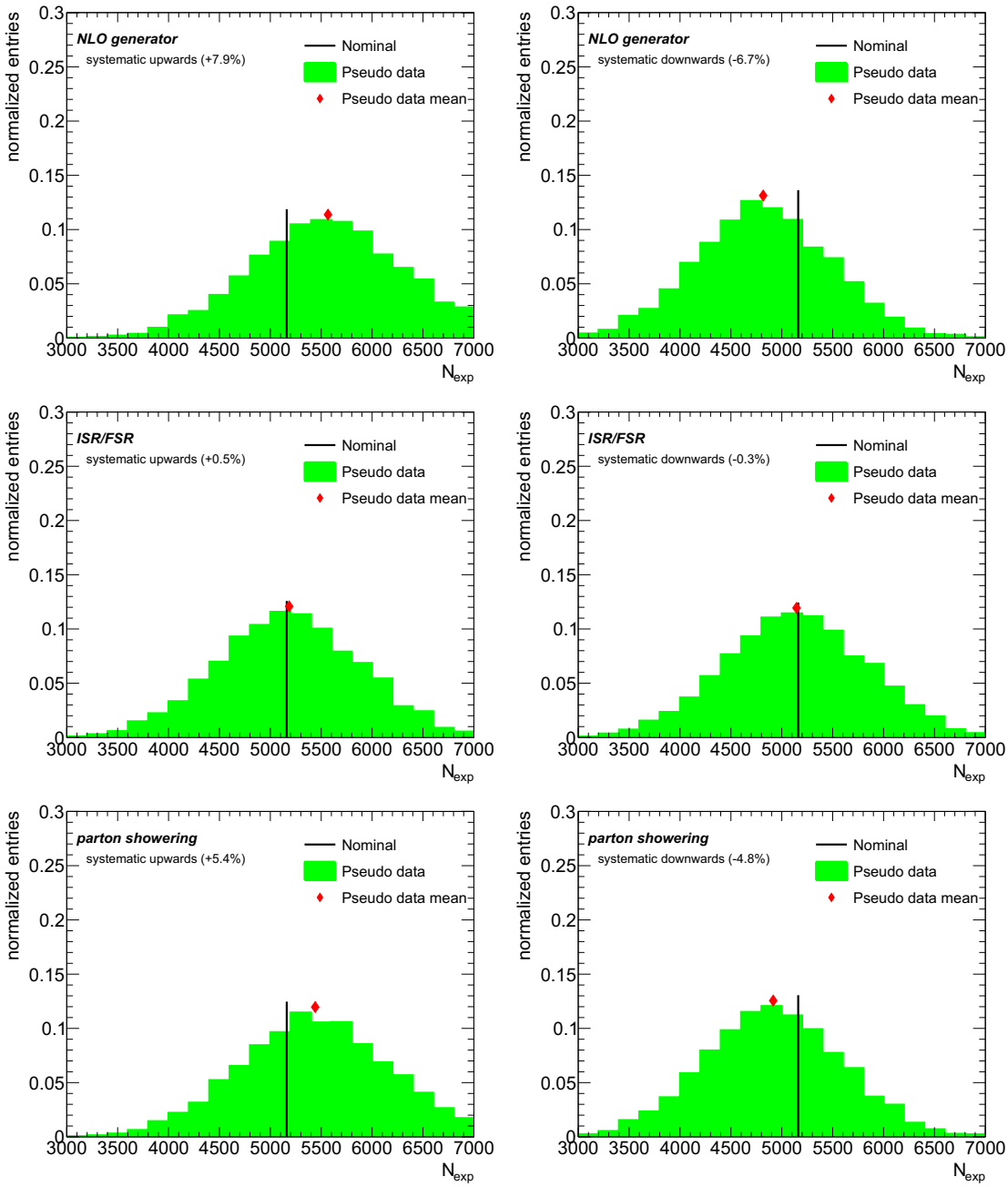

Figure B.19: Distribution of the expected number of signal events N_{exp} for 5000 pseudo experiments to evaluate various Monte Carlo generator uncertainties. The results are shown using a different next-to-leading generator (upper row), different initial and final state raditation conditions (middle row) and different parton showering programs (lower row). The mean of the distribution is marked in red, while the vertical black line shows the nominal result. The difference between the two markers is considered as systematic uncertainty.

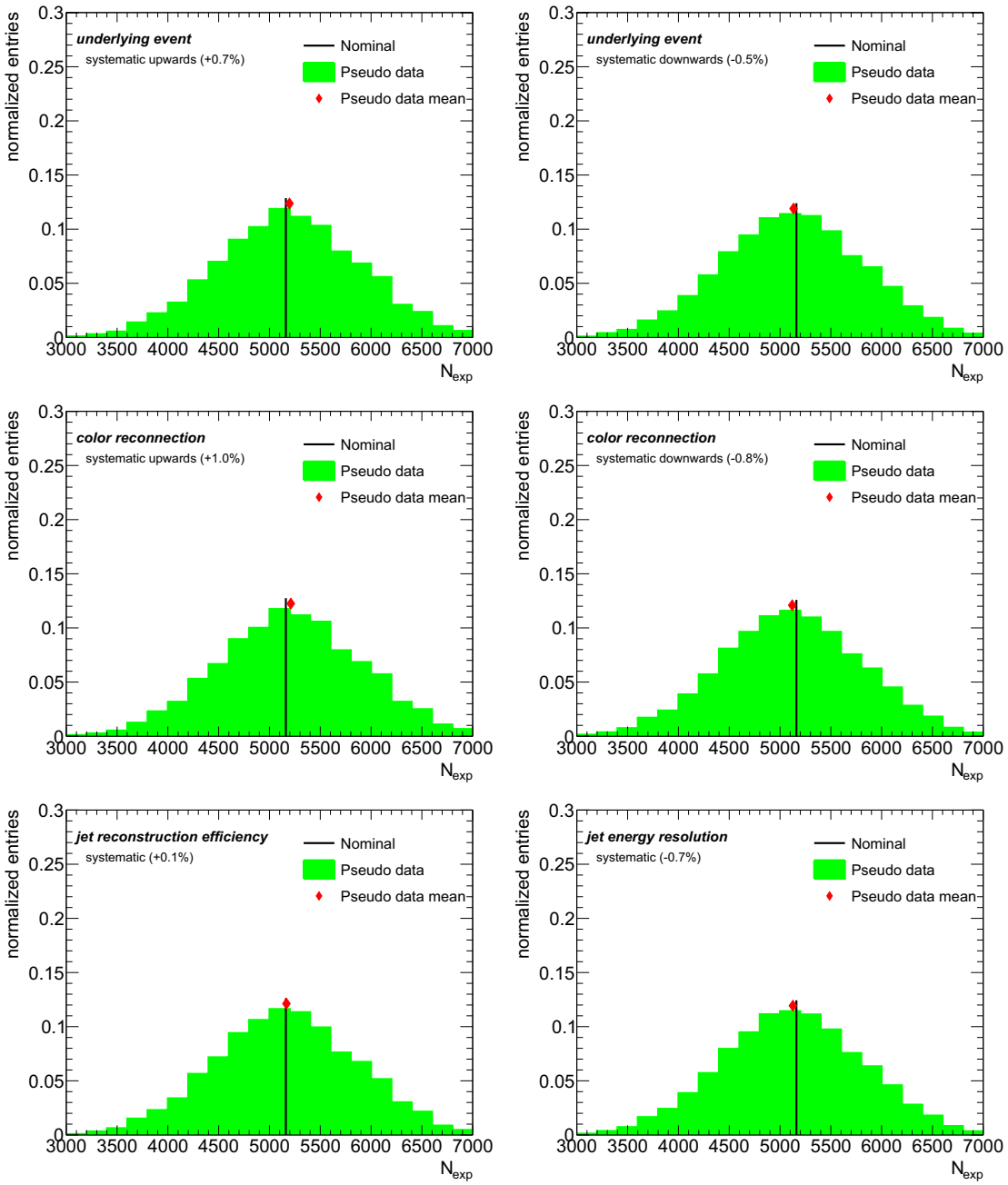

Figure B.20: Distribution of the expected number of signal events N_{exp} for 5000 pseudo experiments to evaluate various Monte Carlo generator and jet modeling uncertainties. The results are shown using different underlying event (upper row) and color reconnection conditions (middle row). The lower row include systematic uncertainties due to the jet reconstruction efficiency (left) and jet energy resolution (right). The mean of the distribution is marked in red, while the vertical black line shows the nominal result. The difference between the two markers is considered as systematic uncertainty.

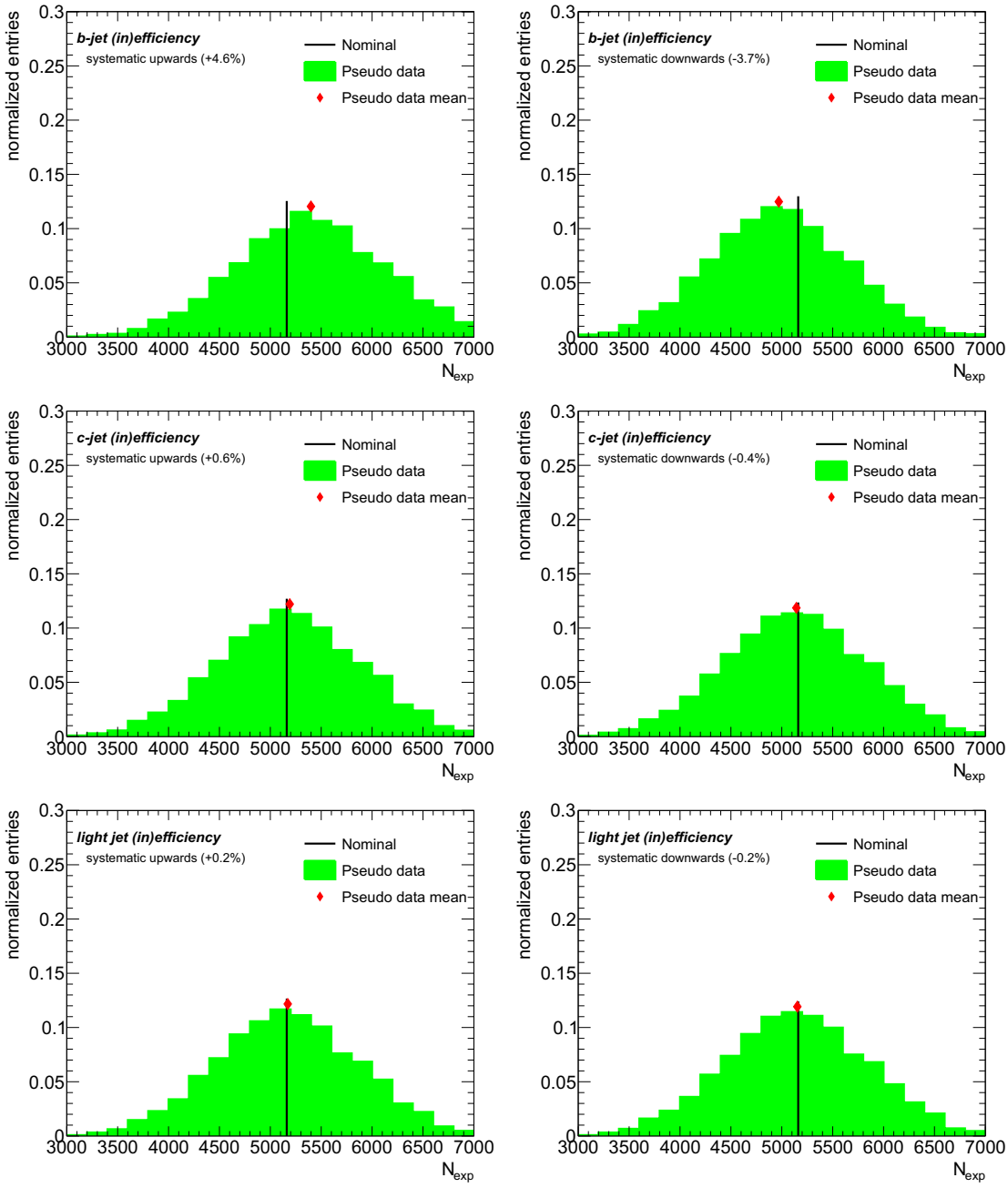

Figure B.21: Distribution of the expected number of signal events N_{exp} for 5000 pseudo experiments to evaluate the b-tagging uncertainty. The results include uncertainties of the b-jet (upper row), c-jet (upper row) and light jet scale factors (lower row). The mean of the distribution is marked in red, while the vertical black line shows the nominal result. The difference between the two markers is considered as systematic uncertainty.

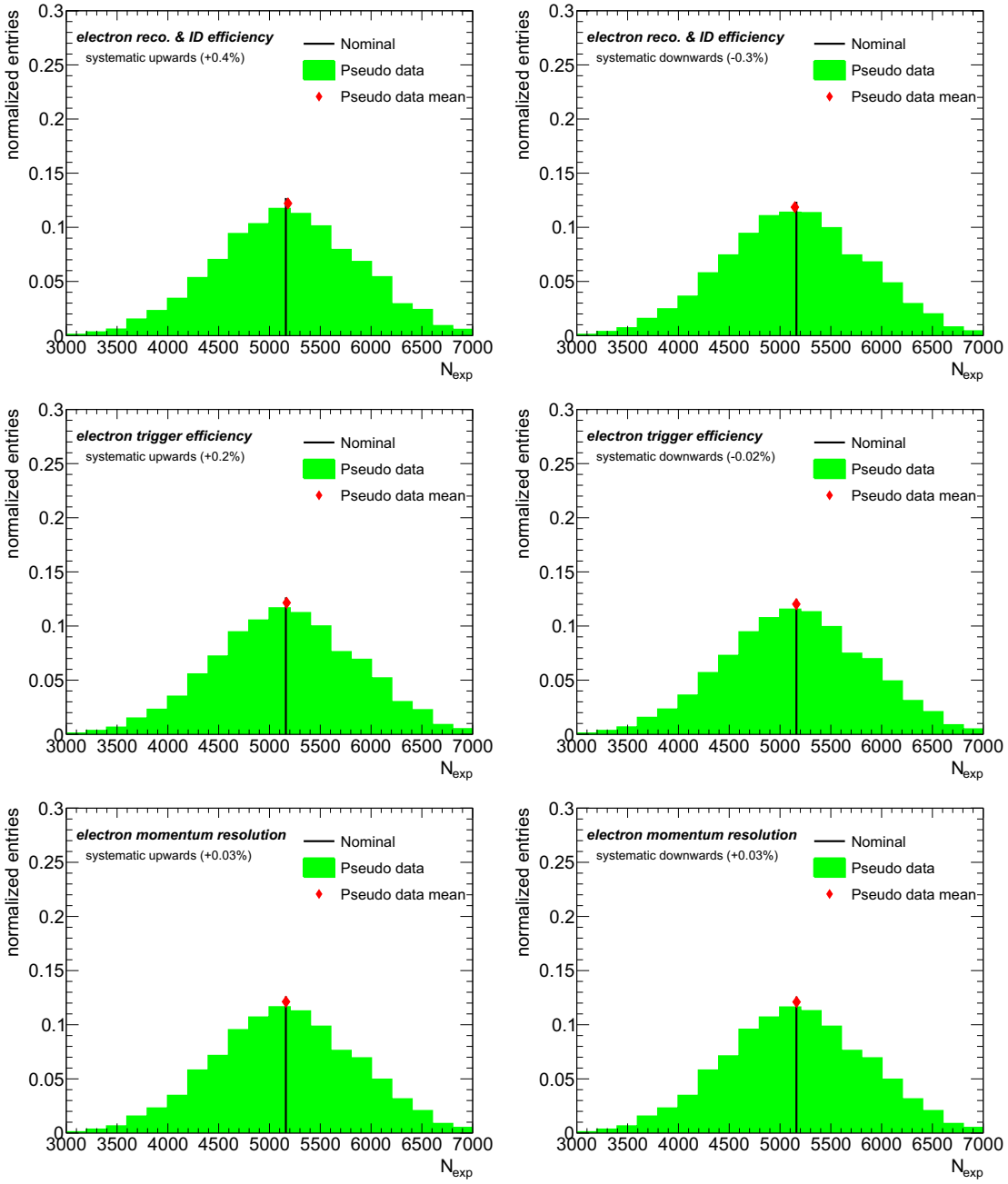

Figure B.22: Distribution of the expected number of signal events N_{exp} for 5000 pseudo experiments to evaluate various electron modeling uncertainties. The results include uncertainties of the reconstruction and identification scale factors (upper row), trigger scale factors (middle row) and energy resolution (lower row). The mean of the distribution is marked in red, while the vertical black line shows the nominal result. The difference between the two markers is considered as systematic uncertainty.

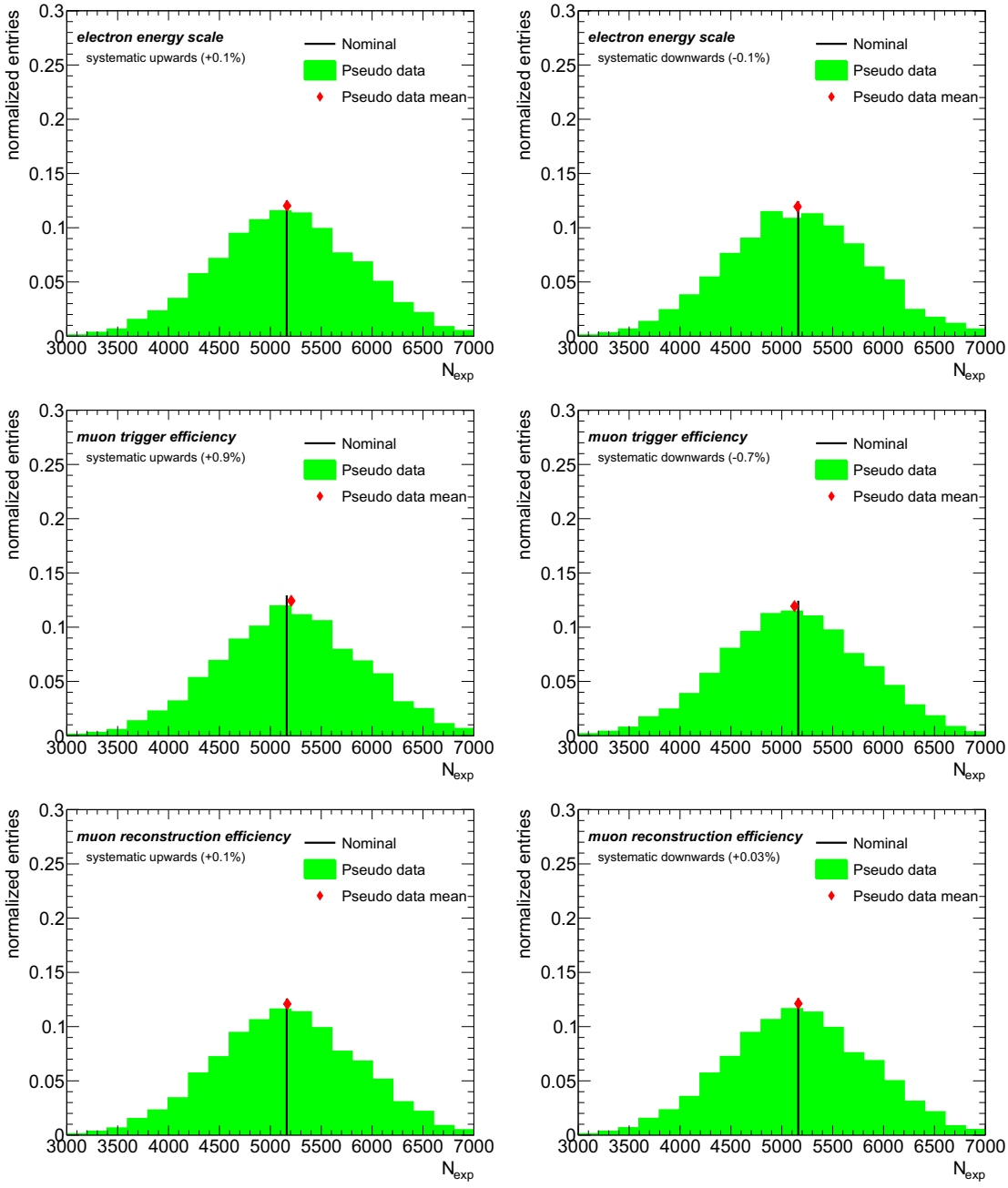

Figure B.23: Distribution of the expected number of signal events N_{exp} for 5000 pseudo experiments to evaluate various electron and muon modeling uncertainties. The results include uncertainties of the electron energy scale (upper row), as well as muon trigger (middle row) and reconstruction scale factors (lower row). The mean of the distribution is marked in red, while the vertical black line shows the nominal result. The difference between the two markers is considered as systematic uncertainty.

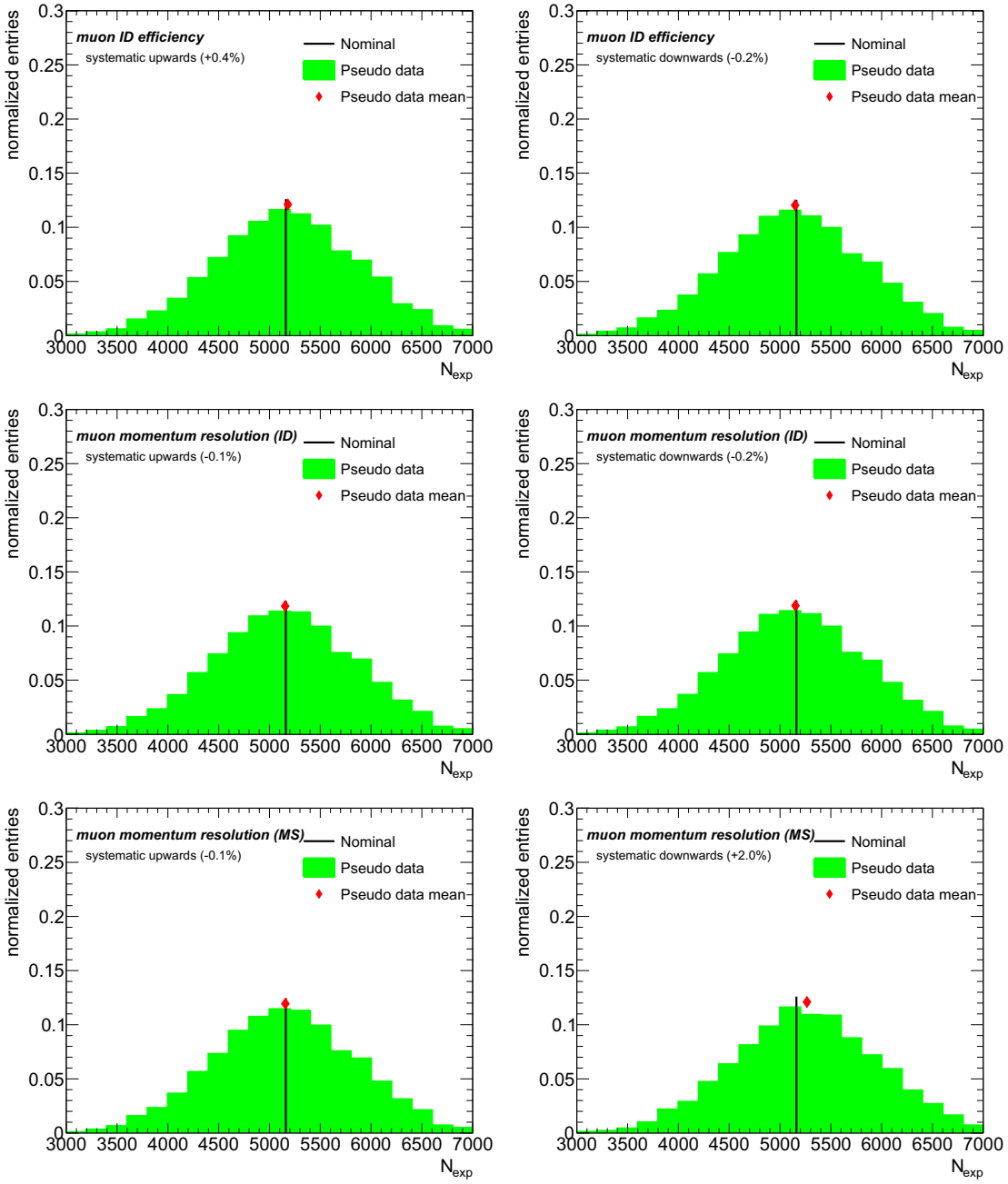

Figure B.24: Distribution of the expected number of signal events N_{exp} for 5000 pseudo experiments to evaluate various muon modeling uncertainties. The results include uncertainties of the identification scale factors (upper row), as well as muon momentum smearing by varying different components (middle and lower row). The mean of the distribution is marked in red, while the vertical black line shows the nominal result. The difference between the two markers is considered as systematic uncertainty.

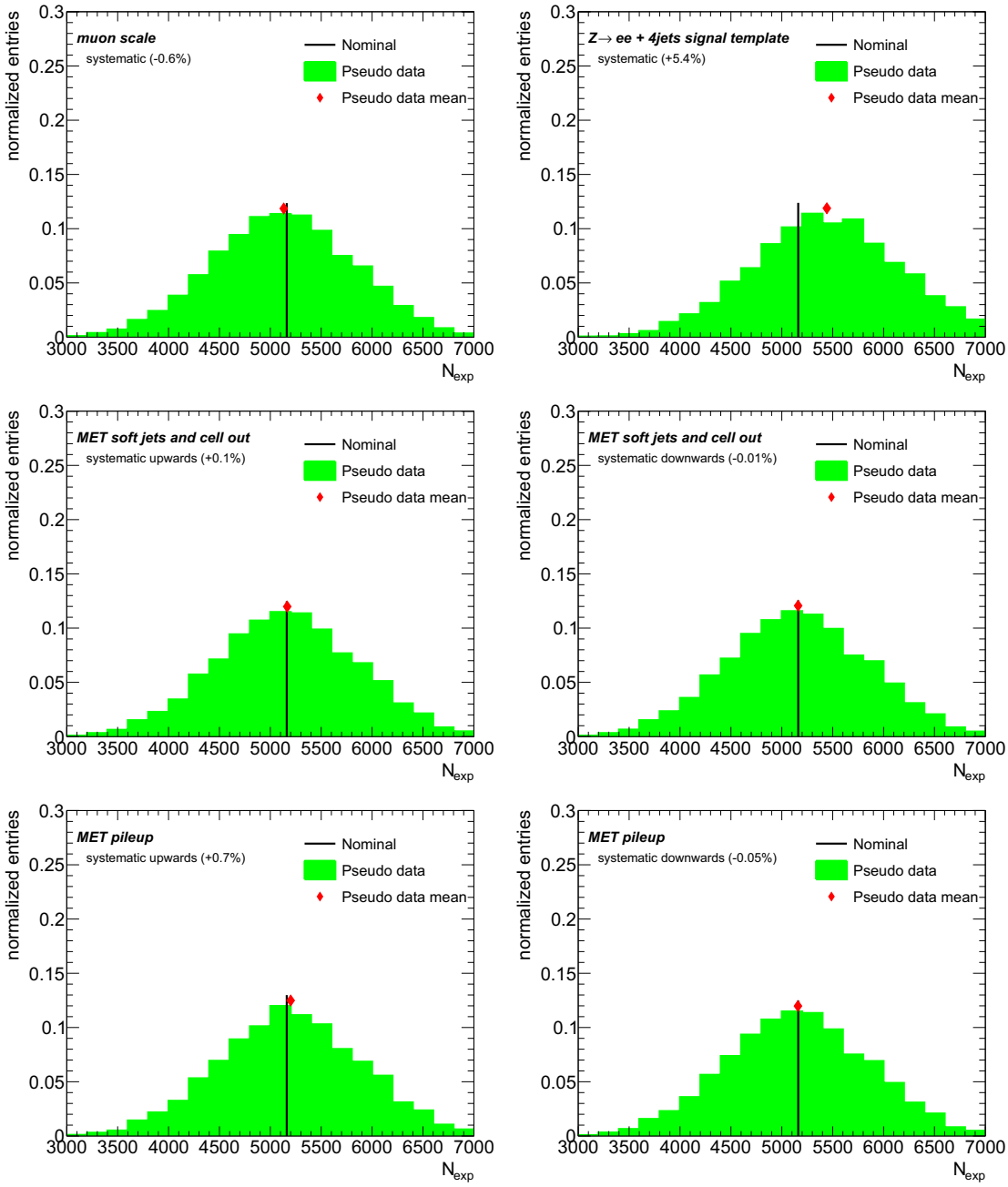

Figure B.25: Distribution of the expected number of signal events N_{exp} for 5000 pseudo experiments to evaluate various muon and $\not\!\!E_T$ modeling uncertainties as well as an uncertainty on the signal template. The results include uncertainties from the muon energy scale (upper left) and deviations from the nominal result using the electron isolation distribution from data as signal template (upper right). $\not\!\!E_T$ uncertainties arise from its cell out and soft jet components (middle row) and pileup (lower row). The mean of the distribution is marked in red, while the vertical black line shows the nominal result. The difference between the two markers is considered as systematic uncertainty.

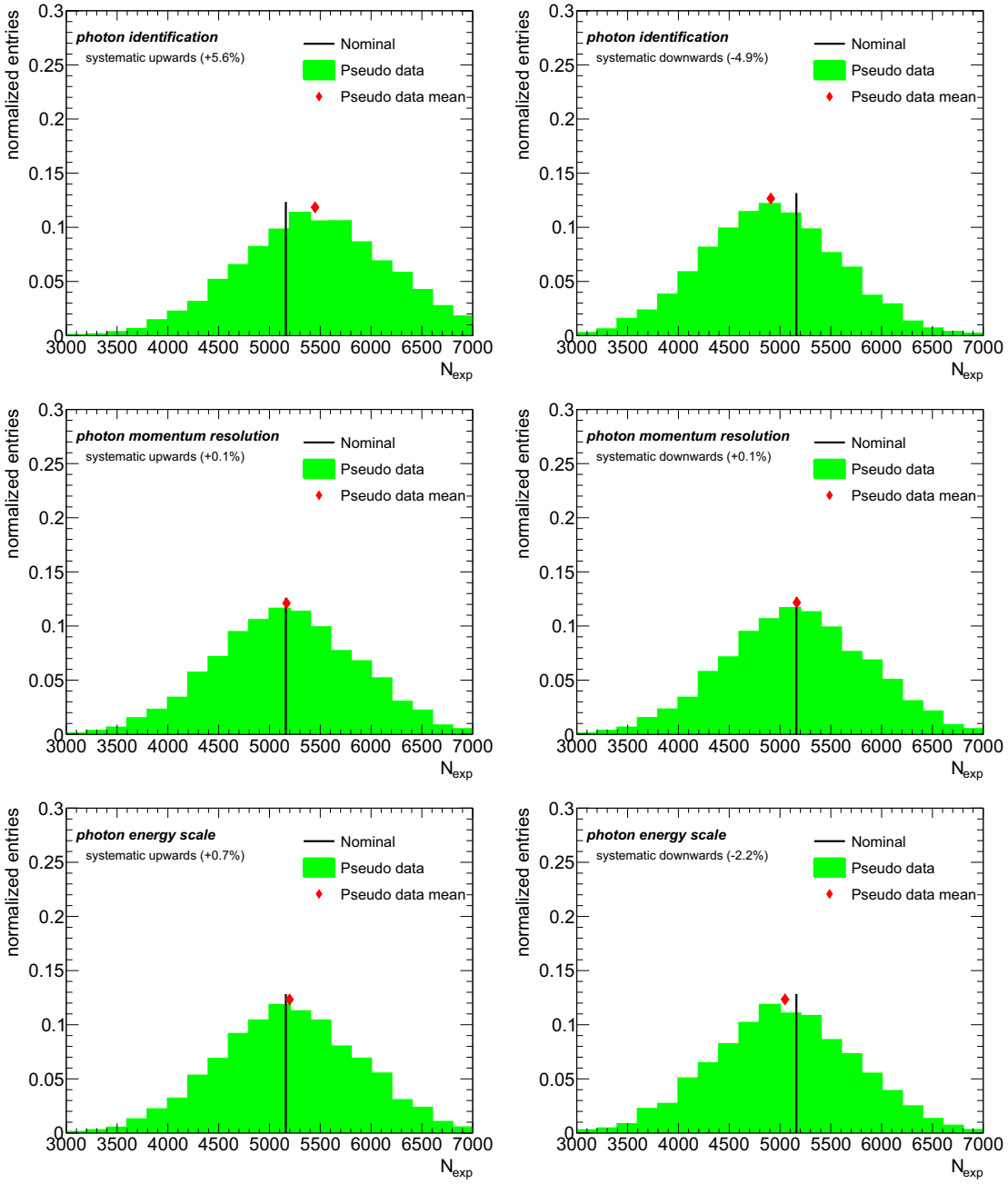

Figure B.26: Distribution of the expected number of signal events N_{exp} for 5000 pseudo experiments to evaluate various photon modeling uncertainties. The results include uncertainties from photon identification (upper row), momentum resolution (middle row) and the photon energy scale (lower row). The mean of the distribution is marked in red, while the vertical black line shows the nominal result. The difference between the two markers is considered as systematic uncertainty.

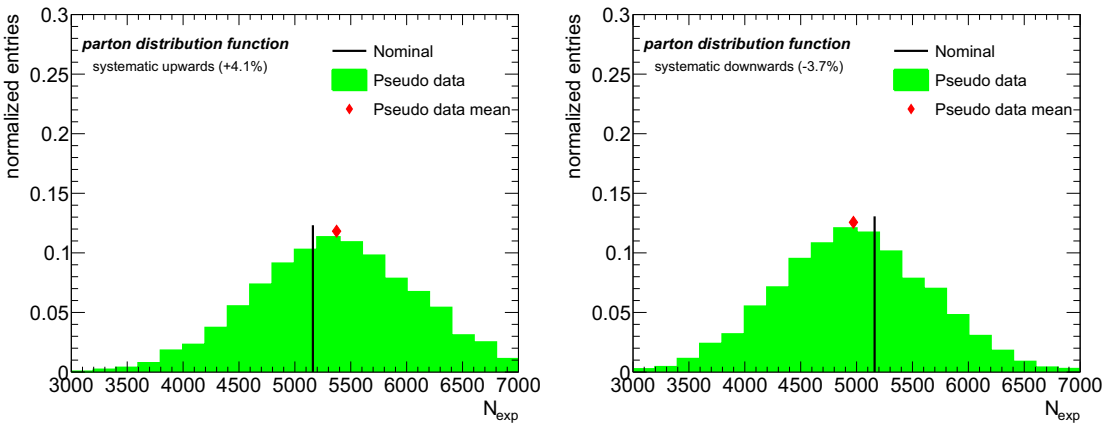

Figure B.27: Distribution of the expected number of signal events N_{exp} for 5000 pseudo experiments to evaluate the uncertainties due to the parton distribution function. The mean of the distribution is marked in red, while the vertical black line shows the nominal result. The difference between the two markers is considered as systematic uncertainty.

Bibliography

[1] D. Griffiths. Introduction to Elementary Particles. *John Wiley & Sons*, 2008. (Cited on page 3.)

[2] F. Halzen and A.D. Martin. Quarks and leptons: an introductory course in modern particle physics. *Wiley & Sons*, 1984. (Cited on page 3.)

[3] M. K. Gaillard, P. D. Grannis, and F. J. Sciulli. The Standard model of particle physics. *Rev.Mod.Phys.*, 71:S96–S111, 1999. (Cited on page 3.)

[4] P. Langacker. Introduction to the Standard Model and Electroweak Physics. pages 3–48, 2009. (Cited on page 3.)

[5] E. Noether. Invariante Variationsprobleme. *Nachrichten von der Gesellschaft der Wissenschaften zu Göttingen, Mathematisch-Physikalische Klasse*, 1918:235–257, 1918. (Cited on page 3.)

[6] J. Beringer et al. Review of Particle Physics (RPP). *Phys.Rev.*, D86:010001, 2012. (Cited on pages 4, 5, 7, 8, 10 and 17.)

[7] S. L. Glashow. Partial Symmetries of Weak Interactions. *Nucl.Phys.*, 22:579–588, 1961. (Cited on page 6.)

[8] A. Salam. Weak and Electromagnetic Interactions. *Conf.Proc.*, C680519:367–377, 1968. (Cited on page 6.)

[9] S. Weinberg. A Model of Leptons. *Phys.Rev.Lett.*, 19:1264–1266, 1967. (Cited on page 6.)

[10] UA1 Collaboration. Experimental Observation of Isolated Large Transverse Energy Electrons with Associated Missing Energy at $\sqrt{s} = 540\,\mathrm{GeV}$. *Phys.Lett.*, B122:103–116, 1983. (Cited on page 7.)

[11] UA2 Collaboration. Observation of Single Isolated Electrons of High Transverse Momentum in Events with Missing Transverse Energy at the CERN $\bar{p}p$ Collider. *Phys.Lett.*, B122:476–485, 1983. (Cited on page 7.)

[12] UA1 Collaboration. Experimental Observation of Lepton Pairs of Invariant Mass Around $95\,\mathrm{GeV/c^2}$ at the CERN SPS Collider. *Phys.Lett.*, B126:398–410, 1983. (Cited on page 7.)

[13] UA2 Collaboration. Evidence for $Z^0 \to e^+e^-$ at the CERN $\bar{p}p$-Collider. *Phys.Lett.*, B129:130–140, 1983. (Cited on page 7.)

[14] M. Kobayashi and T. Maskawa. CP-Violation in the Renormalizable Theory of Weak Interaction. *Progress of Theoretical Physics*, 49:652–657, 1973. (Cited on page 7.)

[15] N. Cabibbo. Unitary Symmetry and Leptonic Decays. *Phys. Rev. Lett.*, 10:531–533, 1963. (Cited on page 7.)

[16] L. Wolfenstein. Parametrization of the Kobayashi-Maskawa Matrix. *Physical Review Letters*, 51, 1983. (Cited on page 8.)

[17] CKM Fitter Group. Preliminary results as of Summer 2012 (ICHEP 12 conference). http://ckmfitter.in2p3.fr/www/results/plots_ichep12/ckm_res_ichep12.html. Accessed August 6th, 2013. (Cited on page 9.)

[18] P. W. Higgs. Broken symmetries, massless particles and gauge fields. *Phys.Lett.*, 12:132–133, 1964. (Cited on page 9.)

[19] F. Englert and R. Brout. Broken Symmetry and the Mass of Gauge Vector Mesons. *Phys.Rev.Lett.*, 13:321–323, 1964. (Cited on page 9.)

[20] G. S. Guralnik, C. R. Hagen, and T. W. B. Kibble. Global Conservation Laws and Massless Particles. *Phys.Rev.Lett.*, 13:585–587, 1964. (Cited on page 9.)

[21] A. Djouadi. The Anatomy of electro-weak symmetry breaking. I: The Higgs boson in the standard model. *Phys.Rept.*, 457:1–216, 2008. (Cited on pages 9 and 10.)

[22] ATLAS Collaboration. Observation of a new particle in the search for the Standard Model Higgs boson with the ATLAS detector at the LHC. *Phys.Lett.*, B716:1–29, 2012. (Cited on page 10.)

[23] CMS Collaboration. Observation of a new boson at a mass of 125 GeV with the CMS experiment at the LHC. *Phys.Lett.*, B716:30–61, 2012. (Cited on page 10.)

[24] LHC Higgs Cross Section Working Group. LHC Higgs Cross Section Working Group. https://twiki.cern.ch/twiki/bin/view/LHCPhysics/CrossSections. Accessed August 6th, 2013. (Cited on page 11.)

[25] ATLAS Collaboration. Combined coupling measurements of the Higgs-like boson with the ATLAS detector using up to 25 fb^{-1} of proton-proton collision data. ATLAS-CONF-2013-034, 2013. (Cited on page 12.)

[26] ATLAS Collaboration. Combined measurements of the mass and signal strength of the Higgs-like boson with the ATLAS detector using up to 25 fb^{-1} of proton-proton collision data. ATLAS-CONF-2013-014, 2013. (Cited on page 11.)

[27] ATLAS Collaboration. Measurements of the properties of the Higgs-like boson in the two photon decay channel with the ATLAS detector using 25 fb^{-1} of proton-proton collision data. ATLAS-CONF-2013-012, 2013. (Cited on page 13.)

[28] ATLAS Collaboration. Measurements of the properties of the Higgs-like boson in the four lepton decay channel with the ATLAS detector using 25 fb^{-1} of proton-proton collision data. ATLAS-CONF-2013-013, 2013. (Cited on pages 12 and 13.)

[29] C. N. Yang. Selection Rules for the Dematerialization of a Particle into Two Photons. *Phys. Rev.*, 77:242–245, 1950. (Cited on page 12.)

[30] ATLAS Collaboration. Study of the spin of the new boson with up to $25\,\text{fb}^{-1}$ of ATLAS data. ATLAS-CONF-2013-040, 2013. (Cited on page 12.)

[31] ATLAS Collaboration. Search for the Standard Model Higgs boson in the $H \to Z\gamma$ decay mode with pp collisions at $\sqrt{s} = 7$ and $8\,\text{TeV}$. ATLAS-CONF-2013-009, 2013. (Cited on page 12.)

[32] ATLAS Collaboration. Search for a Standard Model Higgs boson in $H \to \mu\mu$ decays with the ATLAS detector. ATLAS-CONF-2013-010, 2013. (Cited on page 12.)

[33] G. Karagiorgi et al. Leptonic CP violation studies at MiniBooNE in the (3+2) sterile neutrino oscillation hypothesis. *Phys.Rev.*, D75:013011, 2007. (Cited on page 13.)

[34] Super-Kamiokande Collaboration. Measurements of the solar neutrino flux from Super-Kamiokande's first 300 days. *Phys.Rev.Lett.*, 81:1158–1162, 1998. (Cited on page 13.)

[35] P. Minkowski. $\mu \to e\gamma$ at a Rate of One Out of 1-Billion Muon Decays? *Phys.Lett.*, B67:421, 1977. (Cited on page 13.)

[36] M. Gell-Mann, P. Ramond, and R. Slansky. Complex Spinors and Unified Theories. *Conf.Proc.*, C790927:315–321, 1979. (Cited on page 13.)

[37] T. Yanagida. Horizontal Symmetry and Masses of Neutrinos. *Prog.Theor.Phys.*, 64:1103, 1980. (Cited on page 13.)

[38] R. N. Mohapatra and G. Senjanovic. Neutrino Masses and Mixings in Gauge Models with Spontaneous Parity Violation. *Phys.Rev.*, D23:165, 1981. (Cited on page 13.)

[39] H. Fritzsch, M. Gell-Mann, and H. Leutwyler. Advantages of the Color Octet Gluon Picture. *Phys.Lett.*, B47:365–368, 1973. (Cited on page 14.)

[40] D0 Collaboration. Determination of the strong coupling constant from the inclusive jet cross section in $p\bar{p}$ collisions at $\sqrt{s} = 1.96\,\text{TeV}$. *Phys. Rev. D*, 80:111107, 2009. (Cited on page 15.)

[41] S. W. Herb et al. Observation of a Dimuon Resonance at 9.5 GeV in 400 GeV Proton-Nucleus Collisions. *Phys.Rev.Lett.*, 39:252–255, 1977. (Cited on page 17.)

[42] UA2 Collaboration. Search for top quark production at the CERN $\bar{p}p$ collider. *Z.Phys.*, C46:179, 1990. (Cited on page 17.)

[43] CDF Collaboration. Top quark search in the electron + jet channel in $p\bar{p}$ collisions at $\sqrt{s} = 1.8\,\text{TeV}$. *Phys.Rev.*, D43:664–686, 1991. (Cited on page 17.)

[44] CDF Collaboration. Observation of Top Quark Production in $\bar{p}p$ Collisions. *Phys.Rev.Lett.*, 74:2626–2631, 1995. (Cited on page 17.)

[45] D0 Collaboration. Observation of the Top Quark. *Phys.Rev.Lett.*, 74:2632–2637, 1995. (Cited on page 17.)

[46] H1 and ZEUS Collaboration. Combined Measurement and QCD Analysis of the Inclusive $e^+ - p$ Scattering Cross Sections at HERA. *JHEP*, 1001:109, 2010. (Cited on page 18.)

[47] J. Pumplin et al. New Generation of Parton Distributions with Uncertainties from Global QCD Analysis. *JHEP*, 0207:012, 2002. (Cited on pages 18 and 79.)

[48] The Durham HepData Project. On-line Unpolarized Parton Distribution Calculator with Graphical Display. http://hepdata.cedar.ac.uk/pdf/pdf3.html. Accessed August 6th, 2013. (Cited on page 18.)

[49] S. Moch and P. Uwer. Theoretical status and prospects for top-quark pair production at hadron colliders. *Phys.Rev.*, D78:034003, 2008. (Cited on page 19.)

[50] U. Langenfeld, S. Moch, and P. Uwer. New results for $t\bar{t}$ production at hadron colliders. 2009. (Cited on page 19.)

[51] M. Beneke et al. Threshold expansion of the $gg(q\bar{q}) \to Q\bar{Q} + X$ cross section at $\mathcal{O}(\alpha_s^4)$. *Phys.Lett.*, B690:483–490, 2010. (Cited on page 19.)

[52] ATLAS Collaboration. Combination of ATLAS and CMS top-quark pair cross section measurements using up to $1.1\,\text{fb}^{-1}$ of data at 7 TeV. ATLAS-CONF-2012-134, 2012. (Cited on pages 20 and 21.)

[53] ATLAS Collaboration. Statistical combination of top quark pair production cross-section measurements using dilepton, single-lepton and all-hadronic final states at $\sqrt{s} = 7\,\text{TeV}$ with the ATLAS detector. ATLAS-CONF-2012-024, 2012. (Cited on pages 20 and 159.)

[54] D0 Collaboration. Observation of Single Top Quark Production. *Phys.Rev.Lett.*, 103:092001, 2009. (Cited on page 21.)

[55] CDF Collaboration. First Observation of Electroweak Single Top Quark Production. *Phys.Rev.Lett.*, 103:092002, 2009. (Cited on page 21.)

[56] N. Kidonakis. Next-to-next-to-leading-order collinear and soft gluon corrections for t-channel single top quark production. *Phys.Rev.*, D83:091503, 2011. (Cited on pages 22 and 82.)

[57] N. Kidonakis. NNLL resummation for s-channel single top quark production. *Phys.Rev.*, D81:054028, 2010. (Cited on pages 22 and 82.)

[58] N. Kidonakis. Two-loop soft anomalous dimensions for single top quark associated production with a W^- or H^-. *Phys.Rev.*, D82:054018, 2010. (Cited on pages 22 and 82.)

[59] ATLAS Collaboration. Evidence for the associated production of a W boson and a top quark in ATLAS at $\sqrt{s} = 7\,\text{TeV}$. *Phys.Lett.*, B716:142–159, 2012. (Cited on page 22.)

[60] ATLAS Collaboration. Measurement of the t-channel single top-quark and top-antiquark production cross-sections and their ratio in pp collisions at $\sqrt{s} = 7\,\text{TeV}$. ATLAS-CONF-2012-056, 2012. (Cited on page 22.)

[61] ATLAS Collaboration. Search for s-Channel Single Top-Quark Production in pp Collisions at $\sqrt{s} = 7\,\text{TeV}$. ATLAS-CONF-2011-118, 2011. (Cited on page 22.)

[62] R Schwienhorst and D Hirschbühl. Summary of ATLAS single top analyses Status: June 2012. ATL-COM-PHYS-2012-860, 2012. (Cited on page 23.)

[63] CDF Collaboration. Measurement of $R = B(t \to Wb)/B(t \to Wq)$ in the SecVtx tagged lepton plus jets sample with $8.7\,\text{fb}^{-1}$ of Data. CDF note 10887, 2012. (Cited on page 23.)

[64] CMS Collaboration. Measurement of the ratio $B(t \to Wb)/B(t \to Wq)$. CMS-PAS-TOP-12-035, 2013. (Cited on page 23.)

[65] A. Quadt. Top Quark Physics at Hadron Colliders. *Springer-Verlag*, 2007. (Cited on page 23.)

[66] M. Jezabek and Johann H. Kuhn. QCD Corrections to Semileptonic Decays of Heavy Quarks. *Nucl.Phys.*, B314:1, 1989. (Cited on page 23.)

[67] D0 Collaboration. An Improved determination of the width of the top quark. *Phys.Rev.*, D85:091104, 2012. (Cited on pages 23 and 24.)

[68] CDF Collaboration. A Direct Top Quark Width Measurement at CDF. CDF note 10936, 2012. (Cited on page 24.)

[69] ATLAS Collaboration. Determination of the Top Quark Mass with a Template Method in the All Hadronic Decay Channel using $2.04\,\text{fb}^{-1}$ of ATLAS data. ATLAS-CONF-2012-030, 2012. (Cited on page 24.)

[70] ATLAS Collaboration. Measurement of the $t\bar{t}$ production cross section in the all-hadronic channel in ATLAS with $\sqrt{s} = 7\,\text{TeV}$ data. ATLAS-CONF-2012-031, 2012. (Cited on page 24.)

[71] D0 Top Quark Group. Useful Diagrams of Top Signals and Backgrounds. http://www-d0.fnal.gov/Run2Physics/top/top_public_web_pages/top_feynman_diagrams.html. Accessed August 6th, 2013. (Cited on page 25.)

[72] ATLAS Collaboration. Measurement of the $t\bar{t}$ production cross section in the τ+jets channel using the ATLAS detector. *Eur.Phys.J.*, C73:2328, 2013. (Cited on page 25.)

[73] CMS Collaboration. Measurement of the top-antitop production cross section in the τ+jets channel in pp collisions at $\sqrt{s} = 7\,\text{TeV}$. 2013. (Cited on page 25.)

[74] J. Stirling. Parton luminosity and cross section plots. http://www.hep.ucl.ac.uk/wstirlin/plots/plots.html. Accessed August 6th, 2013. (Cited on page 27.)

[75] D0 Collaboration CDF Collaboration. Combination of the top-quark mass measurements from the Tevatron collider. *Phys.Rev.*, D86:092003, 2012. (Cited on page 29.)

[76] ATLAS Collaboration. Combination of ATLAS and CMS results on the mass of the top quark using up to $4.9\,\text{fb}^{-1}$ of data. ATLAS-CONF-2012-095, 2012. (Cited on page 29.)

[77] CDF Collaboration. The CDF Measurement of the Top Quark Charge using the Top Decay Products in Lepton+Jet channel. CDF note 10460, 2011. (Cited on page 30.)

[78] ATLAS Collaboration. Measurement of the top quark charge in pp collisions at $\sqrt{s} = 7\,\text{TeV}$ in the ATLAS experiment. ATLAS-CONF-2011-141, 2011. (Cited on pages 30 and 34.)

[79] A. Czarnecki, J.G. Korner, and J.H. Piclum. Helicity fractions of W bosons from top quark decays at NNLO in QCD. *Phys.Rev.*, D81:111503, 2010. (Cited on page 30.)

[80] ATLAS Collaboration. Combination of the ATLAS and CMS measurements of the W-boson polarization in top-quark decays. ATLAS-CONF-2013-033, 2013. (Cited on pages 30 and 31.)

[81] D0 Collaboration CDF Collaboration. Combination of CDF and D0 measurements of the W boson helicity in top quark decays. *Phys.Rev.*, D85:071106, 2012. (Cited on pages 30 and 31.)

[82] W. Bernreuther, A. Brandenburg, Z. G. Si, and P. Uwer. Top quark pair production and decay at hadron colliders. *Nucl.Phys.*, B690:81–137, 2004. (Cited on page 31.)

[83] D0 Collaboration. Evidence for spin correlation in $t\bar{t}$ production. *Phys.Rev.Lett.*, 108:032004, 2012. (Cited on page 32.)

[84] CDF Collaboration. Measurement of ttbar Spin Correlations Coefficient in $5.1\,\text{fb}^{-1}$ Dilepton Candidates. CDF note 10719, 2011. (Cited on page 32.)

[85] CMS Collaboration. Measurement of Spin Correlations in $t\bar{t}$ production. CMS-PAS-TOP-12-004, 2012. (Cited on page 32.)

[86] ATLAS Collaboration. Observation of spin correlation in $t\bar{t}$ events from pp collisions at $\sqrt{s} = 7\,\text{TeV}$ using the ATLAS detector. *Phys.Rev.Lett.*, 108:212001, 2012. (Cited on page 32.)

[87] CDF Collaboration. Measurement of the top quark forward-backward production asymmetry and its dependence on event kinematic properties. *Phys.Rev.*, D87:092002, 2013. (Cited on pages 32 and 33.)

[88] D0 Collaboration. Measurement of Leptonic Asymmetries and Top Quark Polarization in $t\bar{t}$ Production. *Phys.Rev.*, D87:011103, 2013. (Cited on page 32.)

[89] CMS Collaboration. Inclusive and differential measurements of the $t\bar{t}$ charge asymmetry in proton-proton collisions at 7 TeV. *Phys.Lett.*, B717:129–150, 2012. (Cited on page 32.)

[90] CMS Collaboration. Top charge asymmetry measurement in dileptons at 7 TeV. CMS-PAS-TOP-12-010, 2012. (Cited on page 32.)

[91] ATLAS Collaboration. Measurement of the charge asymmetry in top quark pair production in pp collisions at $\sqrt{s} = 7$ TeV using the ATLAS detector. *Eur.Phys.J.*, C72:2039, 2012. (Cited on page 32.)

[92] F. Deliot and U. De Sanctis. Measurement of the charge asymmetry in dileptonic decay of top quark pairs in pp collisions at $\sqrt{s} = 7$ TeV using the ATLAS detector. ATLAS-COM-CONF-2012-060, 2012. (Cited on page 32.)

[93] U. Baur, A. Juste, L. H. Orr, and D. Rainwater. Probing electroweak top quark couplings at hadron colliders. *Phys.Rev.*, D71:054013, 2005. (Cited on page 33.)

[94] U. Baur, M. Buice, and L. H. Orr. Direct measurement of the top quark charge at hadron colliders. *Phys.Rev.*, D64:094019, 2001. (Cited on page 34.)

[95] M. Ciljak, M. Jurcovicova, S. Tokar, and U. Baur. Top charge measurement at ATLAS detector. ATL-PHYS-2003-035, 2003. (Cited on page 34.)

[96] CMS Collaboration. Measurement of associated production of vector bosons and $t\bar{t}$ at $\sqrt{s} = 7$ TeV. *Phys.Rev.Lett.*, 110:172002, 2013. (Cited on page 34.)

[97] M. V. Garzelli, A. Kardos, C. G. Papadopoulos, and Z. Trocsanyi. $t\bar{t}W^{\pm}$ and t $\bar{t}Z$ Hadroproduction at NLO accuracy in QCD with Parton Shower and Hadronization effects. *JHEP*, 1211:056, 2012. (Cited on page 34.)

[98] CDF Collaboration. Evidence for $t\bar{t}\gamma$ Production and Measurement of $\sigma_{t\bar{t}\gamma}/\sigma_{t\bar{t}}$. *Phys.Rev.*, D84:031104, 2011. (Cited on page 34.)

[99] O. Bruning et al. LHC design report. Vol. I: The LHC main ring. CERN-2004-003-V-1, 2004. (Cited on page 37.)

[100] M. Benedikt et al. LHC design report. Vol. III: The LHC Injector Chain. CERN-2004-003-V-3, 2004. (Cited on page 37.)

[101] ATLAS Collaboration. The ATLAS Experiment at the CERN Large Hadron Collider. *JINST*, 3:S08003, 2008. (Cited on pages 37, 41, 42, 43, 44, 45, 46 and 48.)

[102] CMS Collaboration. The CMS Physics Technical Design Report, Volume 1. *CERN/LHCC*, 2006-001, 2006. (Cited on page 37.)

[103] LHCb Collaboration. LHCb reoptimized detector design and performance: Technical Design Report. *CERN/LHCC*, 2003-030, 2003. (Cited on page 37.)

[104] ALICE Collaboration. ALICE Physics Performance Technical Design Report. *CERN/LHCC*, 2005-030, 2005. (Cited on page 37.)

[105] C. Lefèvre. The CERN accelerator complex. 2008. (Cited on page 38.)

[106] AC Team. The four main LHC experiments. 1999. (Cited on page 39.)

[107] ATLAS Collaboration. Luminosity Public Results. https://twiki.cern.ch/twiki/bin/view/AtlasPublic/LuminosityPublicResults. Accessed August 6th, 2013. (Cited on pages 40, 75 and 76.)

[108] ATLAS Collaboration. ATLAS Magnet System: Technical Design Report. *CERN/LHCC*, 97-018, 1997. (Cited on page 42.)

[109] ATLAS Collaboration. ATLAS Inner Detector: Technical Design Report Vol.1. *CERN/LHCC*, 97-016, 1997. (Cited on page 43.)

[110] ATLAS Collaboration. ATLAS Inner Detector: Technical Design Report Vol.2. *CERN/LHCC*, 97-017, 1997. (Cited on page 43.)

[111] ATLAS Collaboration. ATLAS Pixel Petector: Technical Design Report. *CERN/LHCC*, 98-013, 1998. (Cited on page 43.)

[112] A. Ahmad et al. The Silicon microstrip sensors of the ATLAS semiconductor tracker. *Nucl.Instrum.Meth.*, A578:98–118, 2007. (Cited on page 43.)

[113] E. Abat et al. The ATLAS Transition Radiation Tracker (TRT) proportional drift tube: Design and performance. *JINST*, 3:P02013, 2008. (Cited on page 43.)

[114] ATLAS Collaboration. ATLAS Calorimeter Performance: Technical Design Report. *CERN/LHCC*, 96-040, 1996. (Cited on page 45.)

[115] ATLAS Collaboration. ATLAS Calorimeter Performance: Technical Design Report. *CERN/LHCC*, 1996-041, 1996. (Cited on page 45.)

[116] ATLAS Collaboration. ATLAS Calorimeter Performance: Technical Design Report. *CERN/LHCC*, 96-042, 1996. (Cited on page 45.)

[117] ATLAS Collaboration. ATLAS Muon Spectrometer: Technical Design Report. *CERN/LHCC*, 97-022, 1997. (Cited on page 46.)

[118] ATLAS Collaboration. ATLAS Level 1 Trigger: Technical Design Report. CERN-LHCC-98-014, 1998. (Cited on page 48.)

[119] ATLAS Collaboration. ATLAS Trigger Performance: Status Report. CERN-LHCC-98-015, 1998. (Cited on page 48.)

[120] ATLAS Collaboration. ATLAS High Level Trigger, Data Acquisition and Controls: Technical Design Report. CERN-LHCC-2003-022, 2003. (Cited on page 48.)

[121] M. Elsing et al. Configuration of the ATLAS Trigger System 062. ATL-DAQ-2003-038, 2003. (Cited on page 49.)

[122] ATLAS Collaboration. Physics objects definition by ATLAS top quark anaylsis group. https://twiki.cern.ch/twiki/bin/viewauth/AtlasProtected/TopCommonObjects2011. Accessed August 6th, 2013. (Cited on page 51.)

[123] ATLAS Collaboration. Object selection and calibration, background estimations and MC samples for the Autumn 2012 Top Quark analyses with 2011 data. ATL-COM-PHYS-2012-1197, 2012. (Cited on pages 51, 55, 56, 64, 68, 119, 120, 121, 128, 149, 151, 152 and 153.)

[124] M. Cacciari and G. P. Salam. Dispelling the N^3 myth for the k_T jet-finder. *Phys.Lett.*, B641:57–61, 2006. (Cited on page 51.)

[125] M. Cacciari, G. P. Salam, and G. Soyez. The Anti-k_T jet clustering algorithm. *JHEP*, 0804:063, 2008. (Cited on page 51.)

[126] ATLAS Collaboration. Jet energy measurement with the ATLAS detector in proton-proton collisions at $\sqrt{s} = 7\,\text{TeV}$. *Eur.Phys.J.*, C73:2304, 2013. (Cited on page 51.)

[127] ATLAS Collaboration. Pile-up corrections for jets from proton-proton collisions at $\sqrt{s} = 7\,\text{TeV}$ in ATLAS in 2011. ATLAS-CONF-2012-064, 2012. (Cited on page 52.)

[128] ATLAS Collaboration. Jet energy scale and its systematic uncertainty in proton-proton collisions at $\sqrt{s} = 7\,\text{TeV}$ with ATLAS 2011 data. ATLAS-CONF-2013-004, 2013. (Cited on page 53.)

[129] D. W. Miller, A. Schwartzman, and D. Su. Pile-up jet energy scale corrections using the jet-vertex fraction method. ATL-COM-PHYS-2009-180, 2009. (Cited on page 53.)

[130] ATLAS Collaboration. Commissioning of the ATLAS high-performance b-tagging algorithms in the 7 TeV collision data. ATLAS-CONF-2011-102, 2011. (Cited on page 54.)

[131] M. zur Nedden et al. Measuring the b-tag efficiency in a top-pair sample with $5\,\text{fb}^{-1}$ of data from the ATLAS detector. ATL-COM-PHYS-2012-128, 2012. (Cited on pages 56 and 151.)

[132] ATLAS Collaboration. Electron performance measurements with the ATLAS detector using the 2010 LHC proton-proton collision data. *Eur.Phys.J.*, C72:1909, 2012. (Cited on pages 56 and 152.)

[133] ATLAS Collaboration. Expected electron performance in the ATLAS experiment. ATL-PHYS-PUB-2011-006, April 2011. (Cited on pages 56 and 60.)

[134] A. Ahmad and M. Boonekamp. Calibrated $Z \to e^- e^+$ invariant mass with 2011 data. ATL-COM-PHYS-2011-1637, 2011. (Cited on pages 57 and 58.)

[135] M. Hance, D. Olivito, and H. Williams. Performance Studies for e/γ Calorimeter Isolation. ATL-COM-PHYS-2011-1186, 2011. (Cited on page 59.)

[136] ATLAS Collaboration. Performance of the ATLAS Electron and Photon Trigger in pp Collisions at $\sqrt{s} = 7\,\text{TeV}$ in 2011. ATLAS-CONF-2012-048, 2012. (Cited on pages 61 and 62.)

[137] ATLAS Collaboration. Muon Performance in Minimum Bias pp Collision Data at $\sqrt{s} = 7\,\text{TeV}$ with ATLAS. ATLAS-CONF-2010-036, 2010. (Cited on page 64.)

[138] ATLAS Collaboration. Muon Momentum Resolution in First Pass Reconstruction of pp Collision Data Recorded by ATLAS in 2010. ATLAS-CONF-2011-046, 2011. (Cited on pages 64 and 152.)

[139] Salvucci A. Measurement of muon momentum resolution of the ATLAS detector. ATL-PHYS-PROC-2012-013, 2012. (Cited on pages 64 and 65.)

[140] ATLAS Collaboration. Performance of the ATLAS Trigger System in 2010. *Eur.Phys.J.*, C72:1849, 2012. (Cited on page 66.)

[141] ATLAS Collaboration. Performance of the ATLAS muon trigger in 2011. ATLAS-CONF-2012-099, 2012. (Cited on page 66.)

[142] Combined Muon Performance Group. Combined Muon Performance Public Results. https://twiki.cern.ch/twiki/bin/view/AtlasPublic/MuonPerformancePublicPlots. Accessed August 6th, 2013. (Cited on page 68.)

[143] ATLAS Collaboration. Performance of Missing Transverse Momentum Reconstruction in Proton-Proton Collisions at 7 TeV with ATLAS. *Eur.Phys.J.*, C72:1844, 2012. (Cited on pages 68 and 153.)

[144] A. Canepa et al. Missing Transverse Energy for Top Physics analyses with early ATLAS data at $\sqrt{s} = 7\,\text{TeV}$. ATL-COM-PHYS-2010-821, 2010. (Cited on page 68.)

[145] ATLAS Collaboration. Electron and Photon Reconstruction and Identification in ATLAS: Expected Performance at High Energy and Results at 900 GeV. ATLAS-CONF-2010-005, 2010. (Cited on page 69.)

[146] ATLAS Collaboration. Expected Photon Performance in the ATLAS Experiment. ATL-PHYS-PUB-2011-007, 2011. (Cited on pages 69 and 72.)

[147] L. Carminati et al. Reconstruction and Identification Efficiency of Inclusive Isolated Photons. ATL-PHYS-INT-2011-014, 2011. (Cited on pages 71 and 73.)

[148] ATLAS Collaboration. Measurements of the photon identification efficiency with the ATLAS detector using $4.9\,\text{fb}^{-1}$ of pp collision data collected in 2011. ATLAS-CONF-2012-123, 2012. (Cited on pages 71 and 74.)

[149] Q. Buat et al. Definition of the photon cleaning procedure for 2011 data. ATL-COM-PHYS-2012-134, 2012. (Cited on page 73.)

[150] J. Adelman et al. ATLAS Offline Data Quality Monitoring. *J. Phys.: Conf. Ser.*, ATL-SOFT-PROC-2009-003:042018. 6 p, 2009. (Cited on page 75.)

[151] C. Cuenca Almenar et al. ATLAS online data quality monitoring. *Nucl.Phys.Proc.Suppl.*, 215:304–306, 2011. (Cited on page 75.)

[152] T. Sjostrand, S. Mrenna, and P. Z. Skands. PYTHIA 6.4 Physics and Manual. *JHEP*, 0605:026, 2006. (Cited on page 78.)

[153] G. Corcella et al. HERWIG 6.5: an event generator for Hadron Emission Reactions With Interfering Gluons (including supersymmetric processes). *JHEP*, 0101:010, 2001. (Cited on page 78.)

[154] J. M. Butterworth, J. R. Forshaw, and M. H. Seymour. Multiparton Interactions in Photoproduction at HERA. *Z. Phys.*, C72:637–646, 1996. (Cited on page 78.)

[155] P. Golonka and Z. Was. PHOTOS Monte Carlo: A Precision Tool for QED Corrections in Z and W Decays. *Eur.Phys.J.*, C45:97–107, 2006. (Cited on page 78.)

[156] J. Allison et al. Geant4 developments and applications. *IEEE Trans.Nucl.Sci.*, 53:270, 2006. (Cited on page 78.)

[157] S. Agostinelli et al. GEANT4: A Simulation toolkit. *Nucl.Instrum.Meth.*, A506:250–303, 2003. (Cited on page 78.)

[158] ATLAS Collaboration. The ATLAS Simulation Infrastructure. *Eur.Phys.J.*, C70:823–874, 2010. (Cited on page 78.)

[159] K. Melnikov, M. Schulze, and A. Scharf. QCD corrections to top quark pair production in association with a photon at hadron colliders. *Phys.Rev.*, D83:074013, 2011. (Cited on page 79.)

[160] A. Scharf. Private communication. 2011. (Cited on page 79.)

[161] W. Kilian, T. Ohl, and J. Reuter. WHIZARD: Simulating Multi-Particle Processes at LHC and ILC. *Eur.Phys.J.*, C71:1742, 2011. (Cited on page 79.)

[162] M. Moretti, T. Ohl, and J. Reuter. O'Mega: An Optimizing Matrix Element Generator. 2001. (Cited on page 79.)

[163] C Schwinn. Top quark couplings at ILC : six and eight fermion final states. Top quark couplings to Higgs and gauge bosons at a linear collider: 6 and 8 fermion final states. hep-ph/0412028. MZ-TH-2004-21:15 p, Dec 2004. (Cited on page 79.)

[164] T. Ohl. Vegas Revisited: Adaptive Monte Carlo Integration Beyond Factorization. *Comput.Phys.Commun.*, 120:13–19, 1999. (Cited on page 79.)

[165] M. Bosman et al. Understanding Monte Carlo Generators for Top Physics. ATL-COM-PHYS-2009-334. (Cited on page 80.)

[166] S. Allwood-Spires et al. Monte Carlo Samples Used for Top Physics. ATL-PHYS-INT-2010-132, 2010. (Cited on pages 80 and 81.)

[167] S. Frixione and B. R. Webber. Matching NLO QCD computations and parton shower simulations. *JHEP*, 0206:029, 2002. (Cited on page 80.)

[168] S. Frixione et al. The MC@NLO 4.0 Event Generator. CERN-TH-2010-216, 2010. (Cited on page 80.)

[169] H. Lai et al. New parton distributions for collider physics. *Phys.Rev.*, D82:074024, 2010. (Cited on pages 80 and 148.)

[170] ATLAS Collaboration. First tuning of HERWIG/JIMMY to ATLAS data. ATL-PHYS-PUB-2010-014, 2010. (Cited on page 80.)

[171] M. Aliev et al. HATHOR - HAdronic Top and Heavy quarks crOss section calculatoR. *Computer Physics Communications*, 182(4):1034–1046, 2011. (Cited on page 80.)

[172] Frixione, S. and Nason, P. and Oleari, C. Matching NLO QCD Computations with Parton Shower Simulations: the POWHEG Method. *JHEP*, 0711:070, 2007. (Cited on page 80.)

[173] Kersevan, B. P. and Richter-Wąs, E. The Monte Carlo Event Generator AcerMC Version 2.0 with Interfaces to PYTHIA 6.2 and HERWIG 6.5. TPJU-6-2004, 2004. (Cited on page 80.)

[174] P. Z. Skands. Tuning Monte Carlo Generators: The Perugia Tunes. *Phys.Rev.*, D82:074018, 2010. (Cited on pages 80 and 148.)

[175] M. L. Mangano et al. ALPGEN, a Generator for Hard Multiparton Processes in Hadronic Collisions. *JHEP*, 0307:001, 2003. (Cited on page 80.)

[176] C. Anastasiou, L. J. Dixon, K. Melnikov, and F. Petriello. High precision QCD at hadron colliders: Electroweak gauge boson rapidity distributions at NNLO. *Phys.Rev.*, D69:094008, 2004. (Cited on page 81.)

[177] R. Hamberg, W.L. van Neerven, and T. Matsuura. A Complete calculation of the order α_s^2 correction to the Drell-Yan k factor. *Nucl.Phys.*, B359:343–405, 1991. (Cited on page 81.)

[178] J. Butterworth et al. Single Boson and Diboson Production Cross Sections in pp Collisions at $\sqrt{s} = 7\,\text{TeV}$. ATL-COM-PHYS-2010-695, 2010. (Cited on page 81.)

[179] ATLAS Collaboration. Measurements of $W\gamma$ and $Z\gamma$ production in pp collisions at $\sqrt{s} = 7\,\text{TeV}$ with the ATLAS detector at the LHC. 2013. (Cited on page 81.)

[180] T. Gleisberg et al. Event generation with SHERPA 1.1. *JHEP*, 0902:007, 2009. (Cited on page 81.)

[181] S. D. Ellis, R. Kleiss, and W. J. Stirling. W's, Z's and Jets. *Phys.Lett.*, B154:435, 1985. (Cited on pages 81 and 126.)

[182] Frits A. Berends, H. Kuijf, B. Tausk, and W. T. Giele. On the production of a W and jets at hadron colliders. *Nucl.Phys.*, B357:32–64, 1991. (Cited on page 81.)

[183] S. Frixione et al. Single-top hadroproduction in association with a W boson. *JHEP*, 0807:029, 2008. (Cited on page 82.)

[184] J. M. Campbell and R. K. Ellis. MCFM for the Tevatron and the LHC. *Nucl.Phys.Proc.Suppl.*, 205-206:10–15, 2010. (Cited on page 82.)

[185] ATLAS Collaboration. Measurement of the $t\bar{t}$ production cross-section in pp collisions at $\sqrt{s} = 7\,\text{TeV}$ using kinematic information of lepton+jets events. ATLAS-CONF-2011-121, 2011. (Cited on pages 85 and 159.)

[186] ATLAS Collaboration. Measurement of the top quark pair production cross-section with ATLAS in pp collisions at $\sqrt{s} = 7\,\text{TeV}$ in the single-lepton channel using semileptonic b decays. ATLAS-CONF-2012-131, 2012. (Cited on pages 85 and 159.)

[187] ATLAS Collaboration. Measurement of the top quark-pair cross-section with ATLAS in pp collisions at $\sqrt{s} = 7\,\text{TeV}$ in the single-lepton channel using b-tagging. ATLAS-CONF-2011-035, 2011. (Cited on page 87.)

[188] ATLAS Collaboration. Measurement of the top quark pair production cross-section with ATLAS in the single lepton channel. *Phys.Lett.*, B711:244–263, 2012. (Cited on page 87.)

[189] A. Caldwell, D. Kollár, and K. Kröninger. BAT - The Bayesian Analysis Toolkit. *Computer Physics Communications*, 180:2197–2209, 2009. (Cited on page 94.)

[190] H. Abreu et al. Purity Estimates for the Inclusive Isolated Photons. ATL-PHYS-INT-2011-015, 2011. (Cited on page 99.)

[191] ATLAS Collaboration. QCD multijet background recommendation by ATLAS top quark anaylsis group. https://twiki.cern.ch/twiki/bin/viewauth/AtlasProtected/TopFakesICHEP2012. Accessed August 6th, 2013. (Cited on pages 119, 120 and 121.)

[192] F. A. Berends, W. T. Giele, H. Kuijf, R. Kleiss, and W. J. Stirling. Multijet production in W, Z events at $p\bar{p}$ colliders. *Phys.Lett.*, B224:237, 1989. (Cited on page 126.)

[193] ATLAS Collaboration. W+jets background estimates by ATLAS top quark anaylsis group. https://twiki.cern.ch/twiki/bin/viewauth/AtlasProtected/WplusJetsBackgroundsforTopAnalyses. Accessed August 6th, 2013. (Cited on page 128.)

[194] M. Botje et al. The PDF4LHC Working Group Interim Recommendations. 2011. (Cited on page 148.)

[195] PDF4LHC. Recommendation for LHC cross section calculations. http://www.hep.ucl.ac.uk/pdf4lhc/. Accessed August 6th, 2013. (Cited on page 148.)

[196] A.D. Martin et al. Parton distributions for the LHC. *Eur.Phys.J.*, C63:189–285, 2009. (Cited on page 148.)

[197] NNPDF Collaboration. Unbiased global determination of parton distributions and their uncertainties at NNLO and at LO. *Nucl.Phys.*, B855:153–221, 2012. (Cited on page 148.)

[198] ATLAS Collaboration. Jet energy scale and its systematic uncertainty in proton-proton collisions at $\sqrt{s} = 7\,\text{TeV}$ in ATLAS 2010 data. ATLAS-CONF-2011-032, 2011. (Cited on page 149.)

[199] ATLAS Collaboration. ATLAS Calorimeter Response to Single Isolated Hadrons and Estimation of the Calorimeter Jet Scale Uncertainty. ATLAS-CONF-2011-028, 2011. (Cited on page 149.)

[200] ATLAS Collaboration. In-situ pseudorapidity intercalibration for evaluation of jet energy scale uncertainty using dijet events in proton-proton collisions at $\sqrt{s} = 7\,\text{TeV}$. ATLAS-CONF-2011-014, 2011. (Cited on page 150.)

[201] ATLAS Collaboration. In-situ jet energy scale and jet shape corrections for multiple interactions in the first ATLAS data at the LHC. ATLAS-CONF-2011-030, 2011. (Cited on page 150.)

[202] ATLAS Collaboration. Close-by Jet Effects on Jet Energy Scale Calibration in pp Collisions at $\sqrt{s} = 7\,\text{TeV}$ with the ATLAS Detector. ATLAS-CONF-2011-062, 2011. (Cited on page 150.)

[203] ATLAS Collaboration. Light-quark and Gluon Jets in ATLAS. ATLAS-CONF-2011-053, 2011. (Cited on page 150.)

[204] G. Romeo et al. Jet Energy Resolution from In-situ Techniques with the ATLAS Detector Using Proton-Proton Collisions at a Center of Mass Energy $\sqrt{s} = 7\,\text{TeV}$. ATL-COM-PHYS-2011-240, 2011. (Cited on page 151.)

[205] ATLAS Collaboration. Jet energy resolution in proton-proton collisions at $\sqrt{s} = 7\,\text{TeV}$ recorded in 2010 with the ATLAS detector. *Eur.Phys.J.*, C73:2306, 2013. (Cited on page 151.)

[206] ATLAS Collaboration. Jet energy resolution and selection efficiency relative to track jets from in-situ techniques with the ATLAS Detector Using Proton-Proton Collisions at a Center of Mass Energy $\sqrt{s} = 7\,\text{TeV}$. ATLAS-CONF-2010-054, 2010. (Cited on page 151.)

[207] ATLAS Collaboration. Measurement of the charge asymmetry in dileptonic decay of top quark pairs in pp collisions at $\sqrt{s} = 7\,\text{TeV}$ using the ATLAS detector. ATLAS-CONF-2012-057, 2012. (Cited on page 151.)

[208] Combined Egamma Performance Group. Photon identification efficiencies with 2011 data. https://twiki.cern.ch/twiki/bin/viewauth/AtlasProtected/PhotonID2011#2011_Council_Moriond_Recommendat. Accessed August 6th, 2013. (Cited on page 152.)

[209] S. van der Meer. Calibration of the effective beam height in the ISR. CERN-ISR-PO-68-31. ISR-PO-68-31, 1968. (Cited on page 153.)

[210] ATLAS Collaboration. Luminosity Determination in pp Collisions at $\sqrt{s} = 7\,\text{TeV}$ Using the ATLAS Detector at the LHC. *Eur.Phys.J.*, C71:1630, 2011. (Cited on page 153.)

[211] ATLAS Luminosity Group. Improved Luminosity Determination in pp Collisions at $\sqrt{s} = 7\,\text{TeV}$ using the ATLAS Detector at the LHC. ATL-COM-PHYS-2012-821, 2012. (Cited on page 153.)

[212] ATLAS Collaboration. Measurement of the top quark pair production cross section in the single-lepton channel with ATLAS in proton-proton collisions at 8 TeV using kinematic fits with b-tagging. ATLAS-CONF-2012-149, 2012. (Cited on page 159.)